Karlsruhe Institute of Technology

Tobias Frenzel

On 3D Chiral Mechanical Metamaterials

2020
Dissertation

On 3D Chiral Mechanical Metamaterials

Zur Erlangung des akademischen Grades eines
DOKTORS DER NATURWISSENSCHAFTEN
von der KIT-Fakultät für Physik des
Karlsruher Instituts für Technologie (KIT)

genehmigte

DISSERTATION

von

M. Sc. Tobias Frenzel
geboren in Nürtingen

Tag der mündlichen Prüfung: 4. Dezember 2020
Referent: Prof. Dr. Martin Wegener
Korreferent: Prof. Dr. Peter Gumbsch

Contents

Publications

Parts of this thesis have already been published ...
... in scientific journals:

- T. Frenzel, M. Kadic, and M. Wegener, "Three-dimensional mechanical metamaterials with a twist", *Science* **358**, 1072-1074 (2017).

- J. Reinbold, T. Frenzel, A. Münchinger, and M. Wegener, "The Rise of (Chiral) 3D Mechanical Metamaterials", *Materials* **12**, 3527 (2019).

- T. Frenzel, J. Köpfler, E. Jung, M. Kadic, and M. Wegener, "Ultrasound experiments on acoustical activity in chiral mechanical metamaterials", *Nat. Commun.* **10**, 1-6 (2019).

- T. Frenzel, V. Hahn, P. Ziemke, J. L. G. Schneider, C. Yi, P. Kiefer, P. Gumbsch, and M. Wegener, "Large characteristic lengths in 3D chiral elastic metamaterials: modeling and experiments", *Comms. Mater.*, accepted.

... at scientific conferences (only own presentations):

- T. Frenzel, C. Findeisen, M. Kadic, P. Gumbsch, and M. Wegener "Mechanical metamaterials beyond classical continuum mechanics" (invited talk), 3D Printing Materials Conference, Netherlands, Sittard-Geleen, February 2017.

- T. Frenzel, M. Kadic, and M. Wegener "Observation of mechanical activity in a 3D chiral metamaterial", MRS Fall Meeting, United States of America, Boston, November 2018.

- T. Frenzel, J. Köpfler, E. Jung, J. Reinbold, A. Münchinger, M. Kadic, and M. Wegener, "Observation of acoustical activity in a 3D metamaterial", Metamaterials Conference, Italy, Rome, September 2019.

ADDITIONAL RELATED WORK HAS ALREADY BEEN PUBLISHED ...
... in scientific journals:

- T. Frenzel, J. D. Brehm, T. Bückmann, R. Schittny, M. Kadic, and M. Wegener, "Three-dimensional labyrinthine acoustic metamaterials", *Appl. Phys. Lett.* **103**, 061907 (2013).
- L. Alloatti, C. Kieninger, A. Frölich, M. Lauermann, T. Frenzel, W. Freude, J. Leuthold, M. Wegener, and C. Koos, "Second-order nonlinear optical metamaterials: ABC-type nanolaminates", *Appl. Phys. Lett.* **107**, 121903 (2015).
- T. Frenzel, C. Findeisen, M. Kadic, P. Gumbsch, and M. Wegener, "Tailored buckling microlattices as reusable light-weight shock absorbers", *Adv. Mater.* **28**, 5865-5870 (2016).
- M. Kadic, T. Frenzel, and M. Wegener, "Mechanical metamaterials: When size matters", *Nat. Phys.* **14**, 8-9 (2018).
- P. Ziemke, T. Frenzel, M. Wegener, and P. Gumbsch, "Tailoring the characteristic length scale of 3D chiral mechanical metamaterials", *Extreme Mech. Lett.* **32**, 100553 (2019).
- M. Kadic, A. Diatta, T. Frenzel, S. Guenneau, and M. Wegener,"Static chiral Willis continuum mechanics for three-dimensional chiral mechanical metamaterials", *Phys. Rev. B* **99**, 214101 (2019).
- I. Fernandez-Corbaton, C. Rockstuhl, P. Ziemke, P. Gumbsch, A. albiez, R. Schwaiger, T. Frenzel, M. Kadic, and M. Wegener,"New twists of 3D chiral metamaterials", *Adv. Mater.* **31**, 1807742 (2019).
- J. Köpfler, T. Frenzel, M. Kadic, J. Schmalian, and M. Wegener,"Topologically Protected Twist Edge States for a Resonant Mechanical Laser-Beam Scanner", *Phys. Rev. Appl.* **11**, 034059 (2019).
- V. Hahn, P. Kiefer, T. Frenzel, J. Qu, E. Blasco, C. Barner-Kowollik, and M. Wegener,"Rapid Assembly of Small Materials Building Blocks (Voxels) into Large Functional 3D Metamaterials", *Adv. Funct. Mater.*, 1907795 (2020).
- Y. Chen, T. Frenzel, S. Guenneau, M. Kadic, and M. Wegener,"Mapping acoustical activity in 3D chiral mechanical metamaterials onto micropolar continuum elasticity", *J. Mech. Phys. Solids* **137**, 103877 (2020).

- T. Frenzel, J. Köpfler, A. Naber, and M. Wegener, "Detecting atomic-scale displacements by optical-image cross-correlations analysis and 3D printed marker arrays", *Sci. Rep.*, accepted.

... at scientific conferences (only own presentations):

- T. Frenzel, C. Findeisen, M. Kadic, V. Schuster, P. Gumbsch, and M. Wegener, "Metamaterials using buckling instabilities for reusable energy absorption", DPG-Frühjahrstagung, Regensburg, Germany, March 2016.

- T. Frenzel, C. Findeisen, M. Kadic, V. Schuster, P. Gumbsch, and M. Wegener, "Tailored Buckling 3D Metamaterials as Reusable Light-Weight Shock Absorbers", Metamaterials Conference, Crete, Greece, September 2016.

Chapter 1

1 Introduction

Once after a seminar talk, I received a rather peculiar question. A colleague asked: *'What is the difference between your work and one of my childhood toys, a humming top?'*[1] Although meant jokingly, his remark left me both baffled and stunned at the same time. Is our research outperformed by a simple toy? Unsurprisingly, my follow up response was pretty unconvincing.

To put this into perspective, the talk I gave dealt with our most recent work on push-to-twist coupling in mechanical metamaterials, which is also the subject of this thesis. The related paper was published just a couple of days prior to said talk in a quite prestigious journal. In this, we presented a 3D printed material which twists when being compressed. So technically, the colleague's assessment was accurate. Our material twisted upon compression, just like the humming top starts rotating when pushing down the pole. One could even argue that the humming top is in fact more advanced, since it continues spinning and starts making music when releasing the pole.

The intriguing part my colleague's question was of course its subtext: How could a mechanism so simple that even toys have exploited it for decades, resonate so well in the scientific community? At the time, I had no good answer to that. Thus, after a while I figured that my colleague and I thought of the 3D printed material in totally different terms. He thought of it in terms of a structure. And in fact, there are plenty of structures converting a linear motion or deformation into a rotation or twist. Just think of crankshafts in car engines, the coupling rods of a locomotive, or the spiral pole of the mentioned humming top.

In contrast, we thought of our 3D printed structure as a material. For these to deform like that is a very particular property. As a matter of fact, this trait

[1] Paraphrased question of Prof. Dr. Heinz Kalt, Seminar of the Institute of Applied Physics, Karlsruhe Institute of Technology, Karlsruhe, December 2017.

is so unusual that the classical Cauchy theory describing the deformation of bodies forbids such deformations for homogeneous materials altogether. Within the scope of Cauchy mechanics, homogeneous bodies are allowed to deform in a multitude of different ways. They can shear, expand, and even contract laterally when being compressed [1]. Yet, a twist deformation is strictly prohibited. So from this point of view, a twist deformation is highly surprising. Even more so since the observed effects were not only a small correction, but were as big as the common deformation modes of the body [2].

So, should our 3D printed structure be considered a material? And what distinguishes a material from a structure? I would argue now that structures are materials, if one can describe and use them like regular materials. Take ordinary glass as an example, which is nothing but an amorphous structure of atoms. Yet, everybody would consider it a material. Usually, we do not care about the position of every atom, the direction of every bond, or the mobility of every electron. Instead, we use material parameters like the refractive index to describe its optical properties or the Young's modulus for its elastic traits. The same holds true e.g. for concrete. There, the ingredients can be centimeter sized stones. Still, nobody would object to calling concrete a material. So whether the substructure of the material is on the atomic scale or on the macroscopic scale does not influence our perception of materials either. The only thing that matters is that we can use and describe the structure as a regular constituent material. Hence, being able to assign such material parameters, or at least locally defined intensive quantities that describe the response is key.

One might argue that one can still assign effective material parameters to any structure. Yet, our understanding of material goes along with a specific expectation of its scaling behavior. Material parameters are always intensive quantities [3]. Once again exploiting glass as an example: the refractive index does not change whether the thickness of a pane is one centimeter or one meter. Likewise, every other property we would refer to as a material trait stays the same. In essence, this is the key difference between the humming top and our 3D printed material. When stacking multiple humming tops or crankshafts together as you would do with a material, the intended working mechanism will fail. The coupled crankshafts will not drive a car and the humming tops will not form one big rotating top. Yet, the material we conceived will twist and its effective material parameters will be independent of the sample size.

Obviously, this generalized notion of materials is not new. So called

metamaterials have been around for decades already. These man-made rationally designed structures [4] exhibit properties that can go well beyond the properties of its constituents, hence the prefix 'meta' [5]. Metamaterial research is a fast growing field and giving a sufficient overview is a nearly impossible task for this introduction. Not least because the metamaterial idea is a broad and versatile concept, which has been applied in optics [6, 7], photonics [4], acoustics [8–10], heat conduction [11–13], or continuum mechanics [14–16], just to mention a few.

With their versatility, metamaterials enable a multitude of applications. The one attracting most attention might be the invisibility cloak [17, 18]. Therein, metamaterials smoothly guide light around an object. Yet, in case somebody hopes to be able to buy Harry Potter's cloak of invisibility soon, that person would have to be be reminded that the proposed devices only operate in a small frequency range [19, 20]. Broadband devices are forbidden by causality. Hence, perfect invisibility remains a science fiction for now. Yet, cloaking devices for antennas to avoid coupling between different frequency bands are promising applications [21–23].

Surprisingly, designing cloaks for mechanical waves is amongst the most challenging processes [24]. Not least because transverse and longitudinal polarized waves, as well as mixing and conversion between those, have to be taken into account. Therefore, many cloak designs rely on so called Cosserat materials. These materials are named after the Cosserat brothers, who developed a theory involving additional degrees of freedom in 1909 [25]. As a result, Cosserat materials possess broken minor symmetries of the elasticity tensors by definition [26].

This raised some question for us: How does a Cosserat metamaterial look like and which qualitatively new effects can be expected? Can we use metamaterials to enhance these effects? Some questions were already answered theoretically. In the 1960s, Eringen formulated the micropolar theory of elasticity [27–31], which explicitly assumed elasticity tensors lacking minor symmetries. Therefore, his theory is sometimes also referred to as Cosserat continuum mechanics and will be used as a continuum model for Cosserat materials throughout this thesis. Yet, the micropolar generalization is just one approach amongst many [32].

As a matter of fact, in contrast to the classical Cauchy theory, the micropolar theory can describe chiral media [30, 33]. It has been shown that in chiral materials qualitatively new effects like acoustical activity [34–36], the elastic counterpart of optical activity, and the push-to-twist coupling [33] mentioned at the beginning can occur.

The main goal of this thesis is to achieve a chiral Cosserat metamaterial. Therefore, I will introduce and discuss different blueprints for metamaterial unit cells. Their properties beyond Cauchy elasticity will be proven by characterizing both the push-to-twist coupling in these materials and their acoustical activity.

Outline of this thesis

This thesis is generally split into two parts. Part I focuses on the elastostatic push-to-twist coupling in chiral metamaterials. I will begin with a recapitulation of the classical Cauchy continuum theory in chapter 2. From that, it will become clear that the Cauchy theory is fundamentally not capable of describing chiral material. Consequently, I will introduce a generalization of the Cauchy continuum theory, the so called micropolar continuum theory. Therewith, I will outline the analytical solution derived by Roderic Lakes, which predicts qualitatively new twist deformations for a strained chiral bar. In chapter 3, I will sketch the basic principles of the finite element method, which was used for all numerical calculations in this thesis. The measurement setup and the fabrication methods are presented in chapter 4. Therein, I will present our basic sample design and give details on the setup to measure the push-to-twist coupling. Furthermore, I will present the 3D printers used for sample fabrications. In chapter 5, I will depict the mechanism and unit cells that lead to push-to-twist coupling. Subsequently, I will present the realization, as well as the numerical and experimental characterization of a certain cubic metamaterial design. Based on that, I will present our findings of a modified version of this unit cell that showed remarkably large twist deformations and characteristic lengths scales in chapter 6. Furthermore, I will introduce a simple analytical model, which helps understanding the inner mechanisms of this modified metamaterial.

Part II deals with the propagation of elastic waves in chiral metamaterial. In chapter 7, I will give a brief overview of elastic waves in the different continuum theories. Additionally, I will introduce the notion of acoustical activity. The necessary numerical and experimental methods will be mentioned in chapter 8 and chapter 9. In chapter 10, I will present the numerical and experimental results for two different unit cell designs. Additionally, I will compare these results to calculations of a micropolar continuum. Finally, I will summarize and discuss the thesis in chapter 11, followed by a brief outlook.

Part I

ELASTOSTATICS: PUSH-TO-TWIST COUPLING

Chapter 2

2 Fundamentals of Continuum Mechanics

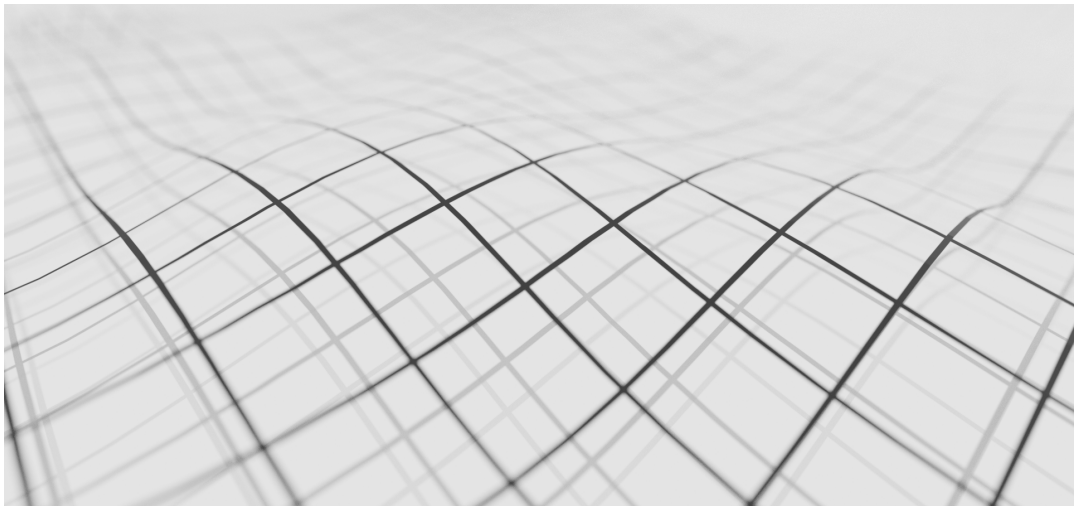

Artistic illustration of a deformed continuum

"Ut tensio, sic vis"[37] or "as the extension, so the force." This law was formulated by Robert Hooke in 1678, when he described the deformation of springs for the first time. Little did he know that this simple statement was going to be the guiding principle of every linear theory of elastic materials until today. In this chapter, I will give a short introduction to different continuum theories of elastic bodies that generalize Hooke's law into three dimensions and which will be used later in this thesis to model our metamaterials. In that, I will show that a qualitatively new push-to-twist coupling emerges when considering chiral material. Finally, I will define the term metamaterial and give a brief overview of the field of mechanical metamaterials.

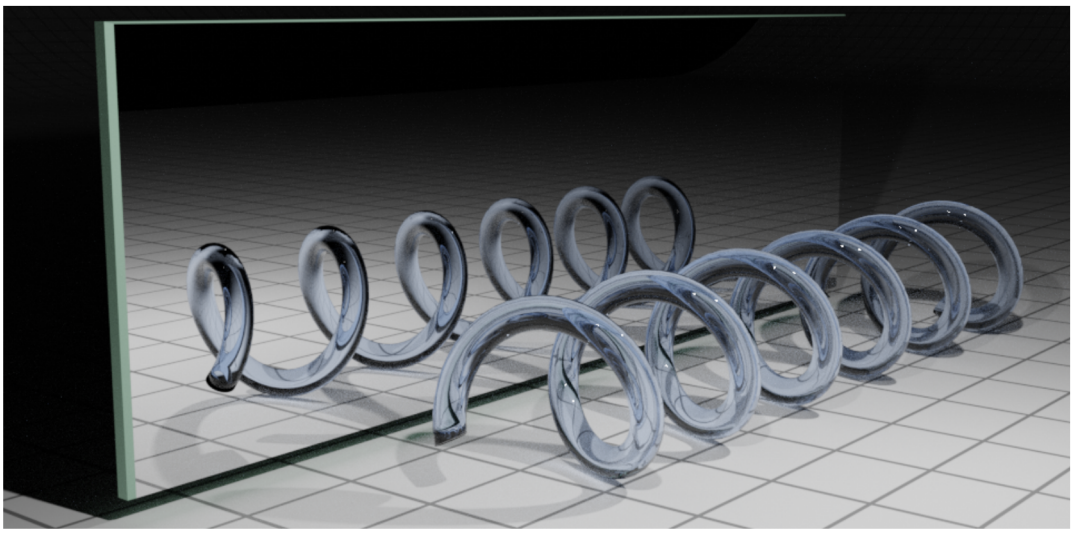

Figure 2.1: Illustration of a spiral and its mirror image. Spirals are chiral objects, since a spiral and its mirror image cannot be superimposed by only using rotations and translations.

2.1 Chirality

The first definition of chirality was brought forward by Kelvin in 1894. He wrote:

> *"I call any geometrical figure, or group of points, 'chiral', and say that it has chirality if its image in a plane mirror, ideally realized, cannot be brought to coincide with itself."*[38]

It is important to know that bringing two objects to coincide implies that only translations and rotations are allowed operation. Maybe the most prominent example of chiral objects are human hands. No matter how one would turn them, they are non-superimposable. Another example is the spiral and its mirror image depicted in Figure 2.1. In analogy to our hands, the original spiral can be called right-handed, whereas the mirror image is left-handed. These terms are quite commonly used when distinguishing chiral molecules. Notably, the right- and left-handed version of a molecule can have totally different effects. The sedative thalidomide, better known by its trade name Contergan, can serve as an example. One handedness had the desired sedative effects, whereas the other caused major birth defects [39].

In 1957 and 1958 [40, 41], in an effort to sharpen the definition of chirality, Whyte formulated a set of conditions any object or system has to fulfill to be chiral.

> *"The necessary and sufficient condition for the presence of chirality is the absence of all three of the following symmetry elements: a plane of symmetry, a centre of symmetry, and any 4n-fold inversion axis. The definition applies both to mathematical forms and to observed phenomena, and does not presuppose their representation in any particular manner..."* [41]

Although chiral objects and materials play a major role in chemistry and physics, e.g. optical activity is caused by chiral media, chiral elastic materials have only recently sparked the interest of a wider scientific community. One of the reasons for that might be that chiral effects were considered to be rather small and therefore negligible for macroscopic objects. Consequently, the classical Cauchy theory of elasticity cannot distinguish between materials of different handedness, as will be shown in the following section.

2.2 Cauchy Theory of Elastic Solids

Continuum mechanics deals with the deformation of bodies and the related forces and stresses within these bodies. The origins of the classical Cauchy Theory traces back to the 18th century mathematician Augustin-Louis Cauchy and is subject of many standard textbooks. Here, I am closely following the didactic approaches of Slaughter [42], and of Timoshenko and Goodier [43]. Since this is meant as a short introduction only, I refer the interested reader to one of these books for more insights.

In continuum theories, a body $\mathbb{B}$ consist of an infinite number of material points or infinitesimal material elements, each occupying a unique position in space. If all points lie inside a continuous region with only a finite number of regular surfaces, this is called a configuration $\mathcal{R}$ of the body $\mathbb{B}$. Deformations of the body $\mathbb{B}$ are characterized by comparing a current configuration $\mathcal{R}_t$ at time t and boundary $\partial\mathcal{R}_t$ to a reference configuration $\mathcal{R}$ with boundary $\partial\mathcal{R}$. The reference configuration usually represents the natural state of the body, i.e. a state without external stimuli.

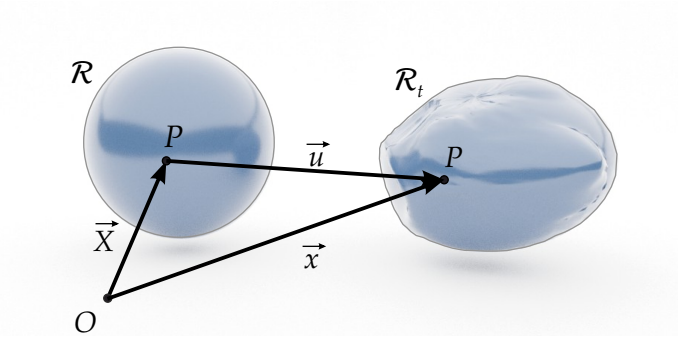

Figure 2.2: Illustration of the body $\mathbb{B}$ in the reference configuration $\mathcal{R}$ and current configuration $\mathcal{R}_t$. The position of a certain material point P in $\mathcal{R}$ is given by $\vec{X}(P)$ and by $\vec{x}$ in $\mathcal{R}_t$ respectifly. The displacement vector $\vec{u}$ connects P in the reference system to its position in the current system.

2.2.1 *Kinematics*

In a fist step, measures to characterize deformations in these two configurations of the same body are introduced. The position of point P in the reference system $\mathcal{R}$ relative to an origin O is given by the vector $\vec{X}(P)$. Likewise, $\vec{x}(P)$ denotes the position of P in the current configuration $\mathcal{R}_t$, as depicted in Figure 2.2. As already mentioned above, each material point occupies a unique position for a given time t, meaning that two different material points cannot be at the same position at the same time. Of course, different material points can occupy the same positions at different times. Therefore an isomorphic vector operator $\vec{\chi}(\bullet, t)$ exists, which maps all points of the reference configuration $\mathcal{R}$ onto the current one $\mathcal{R}_t$.

$$\vec{\chi}(\bullet, t) : \mathcal{R} \to \mathcal{R}_t \tag{2.1}$$

Hence, every position of P in the current configuration can be expressed as a function of its position in the reference configuration

$$\vec{x} = \vec{\chi}(\vec{X}, t). \tag{2.2}$$

Due to the isomorphism of the mapping, the inverse relation $\vec{\chi}^{-1}(\bullet, t) : \mathcal{R}_t \to \mathcal{R}$ also exists, yielding the position $\vec{X}$ of P in the reference configuration as a function of the position in the current configuration

$$\vec{X} = \vec{\chi}^{-1}(\vec{x}, t). \tag{2.3}$$

With this, it is possible to define the displacement vector $\vec{u}$

$$\vec{u} = \vec{\chi}(\vec{X}, t) - \vec{X}, \tag{2.4}$$

$$\vec{u} = \vec{x} - \vec{\chi}^{-1}(\vec{x}, t), \tag{2.5}$$

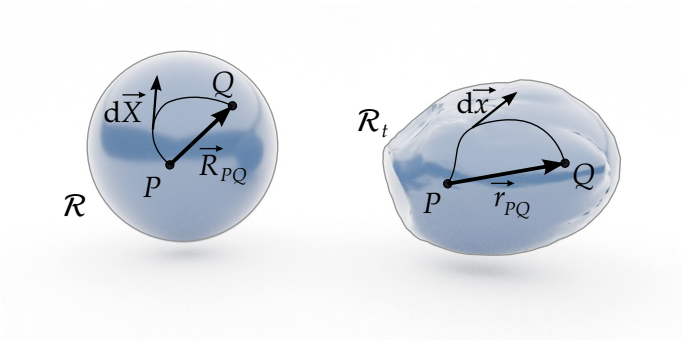

Figure 2.3: The two points P and Q are connected by the material curve $\mathcal{C}$ in the reference and by $\mathcal{C}_t$ in the current configuration. Using these curves, the vectors $\vec{R}_{PQ}$ and $\vec{r}_{PQ}$ can be defined, describing the distance between P and Q in the respective configuration.

which connects the position of P in the current configuration with the reference. Intuitively, $\vec{u}$ describes the positional change of P when changing between the configurations $\mathcal{R}$ and $\mathcal{R}_t$. Both definitions Equation 2.4 and Equation 2.5 are equivalent. Merely different view points are chosen, either the reference system $\vec{X} = X_A \hat{e}_A$ or the current system $\vec{x} = x_i \hat{e}_i$ to describe all quantities. Nevertheless, the result does not depend on the particular choice of the base, only the representation of physical quantities does. The material or Lagrangian description chooses the reference coordinates $\vec{X}$, whereas the spatial or Eulerian description chooses the current position $\vec{x}$. When considering solid bodies, the material description seems the natural choice, whereas in fluid mechanics, the spatial representation is more favorable.

The displacement vector field $\vec{u}$ is a state function in linear elasticity. Hence, it only depends on the current and reference configuration and not on the history of the system. Consequently, every solution $\vec{u}$ must fulfill

$$\oint_{\mathcal{P}} \mathrm{d}\vec{u} = 0, \tag{2.6}$$

for every closed path $\mathcal{P}$. Although the body is completely described by its displacement vector field $\vec{u}(\vec{X}, t)$, for deformations, only the change of the distance between neighboring points P and Q is important. Current configurations, where all distances between points of the body are equal to the distances in the reference configuration are so called rigid body motions. For the scope of this thesis, these are of lesser importance.

A measure for deformation of a body can be derived by considering two arbitrary paths $\mathcal{C}$ and $\mathcal{C}_t$, which connect the points P and Q in $\mathcal{R}$ and $\mathcal{R}_t$ as depicted in Figure 2.3. The vector R_{QP} connecting the two points in $\mathcal{R}$ can

be expressed in terms of a path integral along the curve $\mathcal{C}$

$$\vec{R}_{QP} = \int_{\mathcal{C}} \mathrm{d}\vec{X}, \tag{2.7}$$

in the reference system. Equivalently, the vector r_{QP} in the current configuration is given by

$$\vec{r}_{QP} = \int_{\mathcal{C}_t} \mathrm{d}\vec{x}. \tag{2.8}$$

Both are illustrated in Figure 2.3. Again, by exploiting the isomorphism of the mapping, a non-singular, second-order tensor $\mathbf{F}$ must exist, that uniquely links $\mathrm{d}\vec{x}$ and $\mathrm{d}\vec{X}$ via

$$\mathrm{d}\vec{x} = \mathbf{F}\,\mathrm{d}\vec{X} \quad \Longleftrightarrow \quad \mathrm{d}x_i = F_{iA}\mathrm{d}X_A. \tag{2.9}$$

The second-order tensor $\mathbf{F}$ is called the deformation gradient tensor. It is defined as

$$F_{iA} = \frac{\partial x_i}{\partial X_A}. \tag{2.10}$$

Likewise, the inverse deformation gradient tensor $\mathbf{F}^{-1}$ is given by

$$F^{-1}_{Ai} = \frac{\partial X_A}{\partial x_i}, \tag{2.11}$$

and fulfills

$$\mathrm{d}X_A = F_{Ai}\,\mathrm{d}x_i. \tag{2.12}$$

The deformation-gradient tensor $\mathbf{F}$ contains all information about the body's rotations and deformations, whilst neglecting pure translations. More precisely, it describes only the changes in length and direction of an infinitesimal vector $\mathrm{d}\vec{X}$ as a function of the the position $\vec{X}$.

2.2.2 *Strain Tensor*

Although pure translations are not captured by the deformation-gradient tensor, it still contains rigid body rotations, which is not desirable either. Thus, yet another quantity need to be introduced, the so called strain tensor. A simple derivation starts by calculating the length of the material lines $\mathcal{C}$ and $\mathcal{C}_t$ depicted in Figure 2.3

$$S = \int_{\mathcal{C}} \mathrm{d}S, \qquad s = \int_{\mathcal{C}_t} \mathrm{d}s. \tag{2.13}$$

Therein, the infinitesimal path lengths $\mathrm{d}s$ and $\mathrm{d}S$ are defined by

$$\mathrm{d}\vec{X} = \hat{\mathrm{Y}}\,\mathrm{d}S, \qquad \mathrm{d}\vec{x} = \hat{v}\,\mathrm{d}s, \tag{2.14}$$

where $\hat{\mathrm{Y}}$ and $\hat{v}$ are unit tangent vectors. Using this, it follows

$$\begin{aligned}(\mathrm{d}s)^2 &= \mathrm{d}\vec{x}\cdot\mathrm{d}\vec{x} && (2.15)\\ &= (\mathbf{F}\cdot\mathrm{d}\vec{X})\cdot(\mathbf{F}\cdot\mathrm{d}\vec{X}) && (2.16)\\ &= \mathrm{d}\vec{X}\cdot(\mathbf{F}^{\mathrm{T}}\cdot\mathbf{F})\cdot\mathrm{d}\vec{X} && (2.17)\\ &= \left[\hat{\mathrm{Y}}\cdot(\mathbf{F}^{\mathrm{T}}\cdot\mathbf{F})\cdot\hat{\mathrm{Y}}\right](\mathrm{d}S)^2. && (2.18)\end{aligned}$$

This can be rewritten using the symmetric and positive definite right Cauchy-Green deformation tensor $\mathbf{C} = \mathbf{F}^{\mathrm{T}}\cdot\mathbf{F}$

$$\mathrm{d}s = (\hat{\mathrm{Y}}_A C_{AB}\hat{\mathrm{Y}}_B)^{1/2}\mathrm{d}S. \tag{2.19}$$

The Cauchy-Green deformation tensor $\mathbf{C}$ correctly grasps the local deformations of a material, and neglects rigid body translations and rotations. Yet, in case of such a rigid body motion, the Cauchy-Green deformations tensors yields $\mathbf{C} = \mathbb{1}$ for all points in $\mathcal{C}_t$. Therefore, the Lagrangian strain tensor is defined as

$$\mathbf{E} = \frac{1}{2}(\mathbf{C} - \mathbb{1}) \quad \Longleftrightarrow \quad E_{AB} = \frac{1}{2}(C_{AB} - \delta_{AB}). \tag{2.20}$$

In contrast to the Cauchy-Green deformation tensor, it is zero for undeformed bodies. As a final step, the Lagrangian strain tensor will be expressed as a function of the displacement field $\vec{u}$. By exploiting the relations Equation 2.5 and Equation 2.10, the deformation gradient $\mathbf{F}$ can be rewritten as

$$F_{iA} = \delta_{iA} + \frac{\partial u_i}{\partial X_A}. \tag{2.21}$$

Together with the definition of the Lagrangian strain tensor Equation 2.20, a representation depending on the displacement field in the material frame can be derived

$$E_{AB} = \frac{1}{2}\left(\frac{\partial u_A}{\partial X_B} + \frac{\partial u_B}{\partial X_A} + \frac{\partial u_A}{\partial X_B}\frac{\partial u_B}{\partial X_A}\right). \tag{2.22}$$

Totally equivalent considerations in the spatial coordinates yield an expression for the Almansi-Hamel strain tensor

$$e_{AB} = \frac{1}{2}\left(\frac{\partial u_i}{\partial x_j} + \frac{\partial u_j}{\partial x_i} + \frac{\partial u_i}{\partial x_j}\frac{\partial u_j}{\partial x_i}\right). \tag{2.23}$$

Considering only small displacements, the last term in Equation 2.22 vanishes and the infinitesimal strain tensor ε can be defined as

$$\varepsilon_{ij} = \frac{1}{2}\left(\frac{\partial u_i}{\partial X_j} + \frac{\partial u_j}{\partial X_i}\right). \tag{2.24}$$

This linearizion procedure is sometimes referred to as the geometrical linearization of the strain tensor and is distinct from the linearization of the constitutive equations later on.

At this point, it is worth introducing a commonly used short notation for the partial derivatives. The derivative of the k-th element of an arbitrary physical quantity $\vec{\zeta}$ with respect to the coordinate X_i is defined as

$$\frac{\partial \zeta_k}{\partial X_i} = \zeta_{k,i}. \tag{2.25}$$

By applying this definition to Equation 2.22, the infinitesimal strain tensor reads

$$\varepsilon_{ij} = \frac{1}{2}\left(u_{i,j} + u_{j,i}\right). \tag{2.26}$$

In the following, the infinitesimal strain tensor of Equation 2.26 will simply be referred to as the strain tensor.

2.2.3 *Forces and Stresses*

So far, only the description of the motion of points and the deformation of a body $\mathbb{B}$ has been established. Now, measures of forces and stresses inside $\mathbb{B}$ will be introduced. Generally, two types of forces can be distinguished. External forces are stimuli that act on the boundary of the body (surface force) or the volume. Common examples are contact forces from interaction with other objects or the gravitational field. On the other hand, there are internal forces that arise form the interaction of the body with itself.

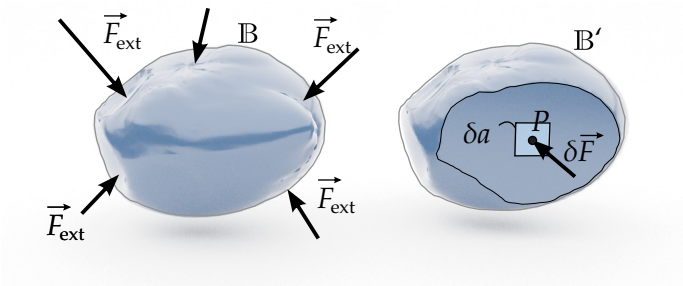

Figure 2.4: An arbitrary deformed body $\mathbb{B}$ with a set of external forces $\vec{F}_{\text{ext}}$ action on the outer surfaces. The self-interaction of $\mathbb{B}$ is illustrated by virtually cutting $\mathbb{B}$ in half and examine the forces $\delta\vec{F}$ acting on a infinitesimal area δa.

To grasp these internal forces, the small gedankenexperiment depicted in Figure 2.4 has been considered. A body $\mathbb{B}$ in the current state $\mathcal{R}_t$ with a set of external forces $\vec{F}_{\text{ext}}$ acting on its outer surface is cut into two separate bodies $\mathbb{B}'$ and $\mathbb{B}''$. The former internal forces of $\mathbb{B}$, arising from the interacting of the subparts $\mathbb{B}'$ and $\mathbb{B}''$, can now be interpreted as external forces acting on the surface $\partial\mathbb{B}'$ of the body $\mathbb{B}'$. In other words, it is possible to represent the internal forces as set of external forces $\delta\vec{F}_i$ acting on each area δa of an imaginary surface $\partial\mathbb{B}'$ inside the body. When choosing a point $P \in \delta a$, the set of external forces acting on δa can be rewritten in terms of a total force $\vec{F}_{\delta a}$ and a total angular momentum $\vec{M}_{\delta a}$, both acting on P.

The classical Cauchy continuum theory now makes the following fundamental assumptions about the total angular momentum $\vec{M}_{\delta a}$ and the total force $\vec{F}_{\delta a}$:

1) The total angular momentum $\vec{M}_{\delta a}$ per area vanishes when reducing δa to P

$$\lim_{\delta a \to P} \frac{\vec{M}_{\delta a}}{\delta a} = 0. \tag{2.27}$$

2) The total force $\vec{F}_{\delta a}$ per area tends to a definite limit, the so called traction vector $\vec{t}$

$$\lim_{\delta a \to P} \frac{\vec{F}_{\delta a}}{\delta a} = \vec{t}\,(\vec{X}, \hat{n}, t), \tag{2.28}$$

with $\hat{n}$ being the face normal of δa.

These expressions are explicitly formulated in the spatial frame. For body forces, analogous assumptions yield that the total angular momentum vanishes and that the total force per volume element is finite. At this point it is worth mentioning that requiring the total angular momentum to vanish is a drastic simplification and limits the applicability of the Cauchy theory.

So-called generalized theories relax this assumption, *i.e.* couple-stress theory [44–46] and all micro-mechanical theories [27, 28, 31]. The latter will be discussed in greater detail in section 2.3.

Although the traction vector already contains all information about the forces within the body, it is an ill-suited quantity, since it depends on the normal vector $\hat{n}$ of a virtual plane. However, the second order Cauchy stress tensor $\mathbf{T}(\vec{X}, t)$ can be defined as a measure independent of the cutting plane

$$t_i(\vec{X}, \hat{n}, t) = \hat{n}_j T_{ji}(\vec{X}, t). \tag{2.29}$$

The Cauchy stress tensor has a straight forward physical interpretation. It describes the current force $\delta\vec{F}$ acting on the point P as

$$\delta F_i = \hat{n}_j T_{ji} \delta a. \tag{2.30}$$

2.2.4 *Equations of Motion*

The relations between accelerations and stresses is grasped by the equations of motion. A straight forward way of deriving them is considering the equation for the balance of linear momentum of a body $\mathbb{B}'$ occupying the area $\mathcal{R}'_t$ with external boundary $\partial\mathcal{R}'_t$

$$\int_{\partial\mathcal{R}'_t} t_i \mathrm{d}a + \int_{\mathcal{R}'_t} \rho b_i \mathrm{d}v = \int_{\mathcal{R}'_t} \rho a_i \mathrm{d}v. \tag{2.31}$$

Thereby, $\vec{b}$ denotes the force vector, the body force equivalent of the traction vector $\vec{t}$. ρ is called the mass density, a_i the acceleration. The equation of motion in integral form is derived by inserting the definition for the Cauchy stress tensor Equation 2.29 into Equation 2.31 and applying Gauss's theorem

$$\int_{\mathcal{R}'_t} \rho a_i \mathrm{d}v = \int_{\mathcal{R}'_t} \left(T_{ji,j} + \rho b_i\right) \mathrm{d}v. \tag{2.32}$$

The more commonly used differential form is given by

$$\rho a_i = T_{ji,j} + \rho b_i. \tag{2.33}$$

A second equation of motion can be derived by considering the condition for the balance of angular momentum. It reads

$$\int_{\partial\mathcal{R}'_t} \epsilon_{ijk} x_j t_k \mathrm{d}a + \int_{\mathcal{R}'_t} \rho \epsilon_{ijk} x_j b_k \mathrm{d}v = \int_{\partial\mathcal{R}'_t} \rho \epsilon_{ijk} x_j a_k \mathrm{d}v, \tag{2.34}$$

with the Levi-Civita symbol ϵ_{ijk}. Again, by exploiting Equation 2.31 and applying Gauss's theorem in integral form, the second equation of motion is found

$$\epsilon_{ijk} T_{jk} = 0. \tag{2.35}$$

Equation 2.35 implies that the Cauchy stress tensor is generally symmetric

$$T_{ji} = T_{ij}. \tag{2.36}$$

From similar considerations in the reference configuration, the second Piola-Kirchhoff tensor $\tilde{\mathbf{S}}$ can be derived. It can be shown that for small deformations

$$F_{iJ} \approx \delta_{iJ}, \tag{2.37}$$

the Piola-Kirchhoff tensor $\tilde{\mathbf{S}}$ and the Cauchy tensor $\mathbf{T}$ are identical.

$$\tilde{S}_{ij} \approx T_{ji} = \sigma_{ij}. \tag{2.38}$$

To emphasis this approximation, the kinematically infinitesimal stress tensor σ is defined. In the following, this infinitesimal stress tensor σ will simply be referred to as the Cauchy tensor or stress tensor. Finally, the equations of motion read

$$\sigma_{ji,j} + f_i = \rho a_i \tag{2.39}$$

$$\sigma_{ij} = \sigma_{ji} \tag{2.40}$$

Note that after this linearizion, the material and spatial frame are approximately the same. Therefore, all quantities will be represented in the material frame implicitly and instead of distinguishing between upper and lower case indices, only the latter will be used.

2.2.5 *Linear Constitutive Model*

The constitutive relation establishes a connection between the stress and strain measures introduced before. In general, this can be a complicated and highly nonlinear relation. Nevertheless, for infinitesimal strains and stresses, a linear ansatz is reasonable. The most general of these is given by

$$\sigma_{ij} = C_{ijkl} \varepsilon_{kl}, \tag{2.41}$$

where $\mathbf{C}$ denotes the rank four elasticity tensor. Equation 2.41 is also referred to as the generalized Hooke's law.

Generally, the elasticity tensor $\mathbf{C}$ has $3^4 = 81$ elements, but not all of them are independent. In fact the number is significantly reduced by symmetry. Since both the stress and the strain tensor are symmetric, the elasticity tensor must also be symmetric with respect to a permutation of the indices ij and kl respectively

$$C_{ijkl} = C_{jikl}, \qquad C_{ijkl} = C_{ijlk}. \tag{2.42}$$

These minor symmetries of the elasticity tensor already reduce the number of independent entries to only 36. Additionally, the strain energy should only depend on the strain in the deformed configuration, but not an the history of the deformation. This is equivalent to the condition

$$C_{ijkl} = C_{klij}. \tag{2.43}$$

Equation 2.43 defines the so called major symmetries of the elasticity tensor. These reduce the number of independent entries to only 21. However, by exploiting material symmetries, this number drops even further.

Using this, the elastic energy or strain energy U can be defined as

$$U = \frac{1}{2} C_{ijkl} \varepsilon_{ij} \varepsilon_{kl}. \tag{2.44}$$

2.2.6 *Voigt Notation*

To take full advantage of the major and minor symmetries when writing down these tensor equations, the Voigt notation rearranges the 3×3 stress and strain tensor into vectors with 6 elements

$$\bar{\sigma}_1 = \sigma_{11}, \quad \bar{\sigma}_2 = \sigma_{22}, \quad \bar{\sigma}_3 = \sigma_{33}, \quad \bar{\sigma}_4 = \sigma_{23}, \quad \bar{\sigma}_5 = \sigma_{31}, \quad \bar{\sigma}_6 = \sigma_{12}, \tag{2.45}$$

$$\bar{\varepsilon}_1 = \varepsilon_{11}, \quad \bar{\varepsilon}_2 = \varepsilon_{22}, \quad \bar{\varepsilon}_3 = \varepsilon_{33}, \quad \bar{\varepsilon}_4 = 2\varepsilon_{23}, \quad \bar{\varepsilon}_5 = 2\varepsilon_{31}, \quad \bar{\varepsilon}_6 = 2\varepsilon_{12}. \tag{2.46}$$

Consequently, instead of a $3 \times 3 \times 3 \times 3$ tensor, the elasticity tensor is represented by a symmetric 6×6 matrix $\bar{\boldsymbol{C}}$

$$\bar{\boldsymbol{C}} = \begin{pmatrix} C_{1111} & C_{1122} & C_{1133} & C_{1123} & C_{1113} & C_{1112} \\ C_{2211} & C_{2222} & C_{2233} & C_{2223} & C_{2213} & C_{2212} \\ C_{3311} & C_{3322} & C_{3333} & C_{3323} & C_{3313} & C_{3312} \\ C_{2311} & C_{2322} & C_{2333} & C_{2323} & C_{2313} & C_{2312} \\ C_{1311} & C_{1322} & C_{1333} & C_{1323} & C_{1313} & C_{1312} \\ C_{1211} & C_{1222} & C_{1233} & C_{1223} & C_{1213} & C_{1212} \end{pmatrix}, \tag{2.47}$$

without losing information or generality.

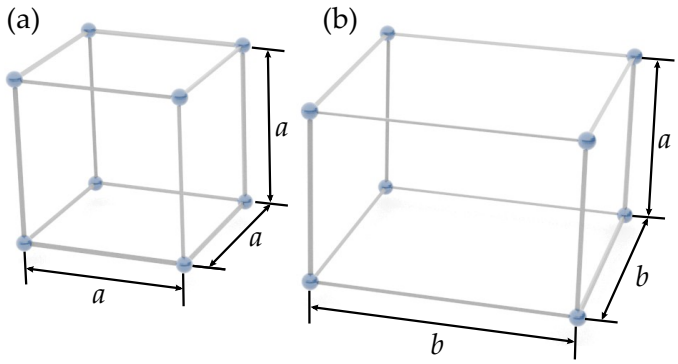

Figure 2.5: Illustration of the Bravais lattices of (a) a cubic material system and (b) a tetragonal material system.

2.2.7 *Material Symmetry*

Considering symmetries of the material enforces further restrictions on the entries of the elasticity tensor. Generally speaking, the higher the symmetry of a material, the less independent entries remain in the elasticity tensor. Here, only the symmetry classes and their respective elasticity tensors that are going to be used later are introduced. Illustrations of the corresponding Bravasi lattice are depicted in Figure 2.5 when possible.

TETRAGONAL MATERIALS:

Tetragonal materials only have one fourfold rotation axis and the Bravais lattice is characterized by $a = b \neq c$ and $\alpha = \beta = \varphi = 90$. The corresponding elasticity tensor has 6 independent entries and is given in its most general form by

$$\bar{\boldsymbol{C}}_{\text{tet}} = \begin{pmatrix} C_{1111} & C_{1122} & C_{1133} & 0 & 0 & 0 \\ C_{1122} & C_{1111} & C_{1133} & 0 & 0 & 0 \\ C_{1133} & C_{1133} & C_{3333} & 0 & 0 & 0 \\ 0 & 0 & 0 & C_{1313} & 0 & 0 \\ 0 & 0 & 0 & 0 & C_{1313} & 0 \\ 0 & 0 & 0 & 0 & 0 & C_{1212} \end{pmatrix}. \tag{2.48}$$

CUBIC MATERIALS:

Cubic materials have three mutual orthogonal fourfold rotation axis and the Bravais lattice is characterized by $a = b = c$ and $\alpha = \beta = \varphi = 90$. The corresponding elasticity tensor has 3 independent entries and is

given in its most general form by

$$\bar{C}_{\text{cub}} = \begin{pmatrix} C_{1111} & C_{1122} & C_{1122} & 0 & 0 & 0 \\ C_{1122} & C_{1111} & C_{1122} & 0 & 0 & 0 \\ C_{1122} & C_{1122} & C_{1111} & 0 & 0 & 0 \\ 0 & 0 & 0 & C_{1212} & 0 & 0 \\ 0 & 0 & 0 & 0 & C_{1212} & 0 \\ 0 & 0 & 0 & 0 & 0 & C_{1212} \end{pmatrix}. \tag{2.49}$$

ISOTROPIC MATERIALS:

The physical properties of an isotropic material do not depend on its orientation. Hence, it can be rotated around an arbitrary axis by an arbitrary angle, whilst leaving the elasticity tensor unchanged. Hence, the elasticity tensor $\bar{C}_{\text{iso}}$ has only 2 independent entries. Its general structure is the same as for cubic case, but additionally $C_{1212} = (C_{1111} - C_{1122})/2$. Often, the isotropic elasticity tensor is expressed in terms of the Lamé-constants λ and μ. They are related to the elasticity tensors entries by $C_{1212} = \mu$, $C_{1111} = \lambda + 2\mu$, and $C_{1122} = \lambda$ and allow for a compact notation of the generalized Hooke's law for isotropic material:

$$\sigma_{ij} = \lambda \delta_{ij} \varepsilon_{kk} + 2\mu \varepsilon_{ij} \tag{2.50}$$

2.2.8 *Material Moduli*

Each entry C_{ijkl} relates a certain strain component to a specific stress component. Hence, these entries do not have an easy physical interpretation and cannot directly be related to any measurable quantity in a real word experiment. Instead, the following set of material moduli is commonly used to describe elastic solids. Illustration for their interpretation are shown in Figure 2.6. In principle, they can be defined for any symmetry classes, but for the sake of clarity, only the definitions in the isotropic case are given.

BULK MODULUS B:

Measure of the rigidity against hydrostatic pressure as depicted in Figure 2.6(a)

$$B = \lambda + \frac{2\mu}{3}. \tag{2.51}$$

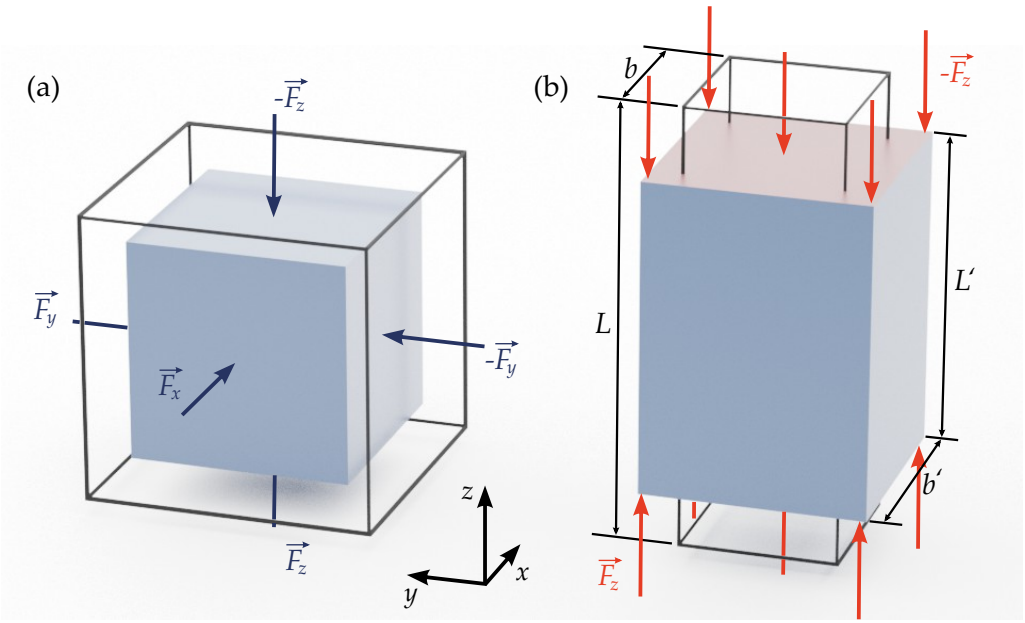

Figure 2.6: Exemplary deformation modes related to the definition of material moduli. (a) For a deformation under hydrostatic pressure ($F_x = F_y = F_z$), the bulk modulus is the ratio between relative volume decrease of an object and external pressure increase. (b) The Young's modulus is the ratio between axial force and relative length change of a bar for uniaxial loading. For the same boundary conditions, the Poisson's ratio relates length decrease to the increase of the width of the bar.

YOUNG'S MODULUS E:

Measure for the rigidity against uniaxial deformation as shown Figure 2.6(b). It relates the axial force F_z to the axial strain via $F_z = E(L' - L)A/L$. It is related to the entries of the elasticity tensor by

$$E = \frac{\mu(3\lambda + 2\mu)}{\lambda + \mu}. \tag{2.52}$$

POISSON'S RATIO ν:

Ratio between lateral and transverse strain $\nu = -\frac{(b'-b)L}{((L'-L)b}$ for a uniaxial deformation as depicted in Figure 2.6(b). It is related to the entries of the elasticity tensor by

$$\nu = \frac{\lambda}{2(\lambda + \mu)}. \tag{2.53}$$

For less symmetric materials, the material moduli have to be defined for every direction individually. For example in the tetragonal case with z-axis as symmetry axis, there are two distinct Young's moduli $E_1 = E_2$ and E_3. Thereby, E_3 corresponds to a rigidity against a uniaxial compression or elongation in z-direction, E_1 and E_2 the rigidity along the x- and y-axis, respectively.

2.2.9 *Limits of the Cauchy Theory*

The classical Cauchy theory has proven to be a suitable approximation for most materials. Yet, due to its simplifying assumptions, important effects drop out.

For example, the history of a deformation is neglected entirely. The strains and stresses in a Cauchy material only depend on its current configurations and its reference, but not on how it got there. Due to viscoelastic effects, this assumption often does not hold true for polymers. There, effects like hysteresis, relaxation, and creep play a major role.

Most importantly for the scope of this thesis, Cauchy elasticity is inherently centrosymmetric. Hence, it cannot distinguish between a right- and left-handed material. This has been pointed out by Lakes [33]. He showed that an inversion has no effect on the elasticity tensor of a Cauchy continuum

$$C_{ijkl} = \frac{\partial x_m}{\partial x_i}\frac{\partial x_n}{\partial x_i}\frac{\partial x_o}{\partial x_k}\frac{\partial x_p}{\partial x_l}C_{mnop} = (-1)^4 C_{ijkl} = C_{ijkl}. \tag{2.54}$$

More precisely, he argues that tensors of even rank are generally invariant under inversion and hence, cannot describe chiral effects.

2.3 Micropolar Theory of Elastic Solids

Although the classical Cauchy theory has proven to be a mighty and versatile tool to describe deformations and stresses in a body, it remains a first and sometimes crude approximation. As discussed at the end of the previous section, the classical theory even fails to describe some material symmetries and the related effects entirely. The micropolar theory that is going to be introduced in this chapter solves some of these problems by introducing new degrees of freedom and thereby generalizing the equations of motion and the constitutive model of the classical theory. Most importantly, for the scope of this thesis, it can properly describe chiral media and predicts

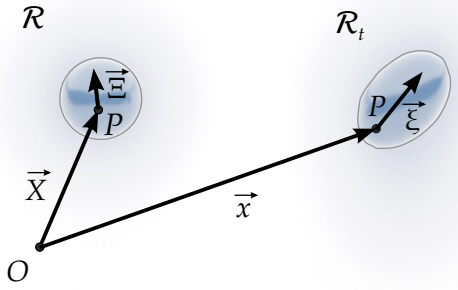

Figure 2.7: A micropolar continuum is a continuum of point particles. One of these is sketched here in the reference $\mathcal{R}$ and current configuration $\mathcal{R}_t$. The additional degrees of freedom of such a point particle are described by the vectors $\vec{\Xi}$ and $\vec{\xi}$, respectively.

new effects related to them. The explanations closely follow the text books of Eringen [31], as well as the work of Dyszlewicz and Altenbach [47, 48]. This section is merely intended to be a brief introduction. For a profound derivation of the theory, I refer the interested reader to one of these text books, as well as to Eringen's original publications [27–30].

2.3.1 *Kinematics*

Some of the problems of the Cauchy theory are rooted in the definition of a continuum itself. Each material point P is unambiguously and completely characterized by the displacement vector $\vec{u}$. In other words, the classical Cauchy continuum is a collection of undeformable points particles. It has been shown that this assumption is insufficient if the deformation is dominated by effects related to the substructure like in bones [49, 50] or grid structures [51–53]. The latter often serve as toy models for real crystals. Therefore, Eringen starts his derivations of the micropolar continuum theory for elastic solids with a definition of a microcontinuum:

> *"A microcontinuum is a continuous collection of deformable point particles."*[31]

As before, every point P is going to be characterized by its coordinate vector $\vec{X}$, but additionally, a vectorial quantity $\vec{\Xi}$ is attached to P, that describes the orientation and the deformation state of the point particle

$$\vec{X}'(\vec{X}, t) = \vec{X}(t) + \vec{\Xi}(\vec{X}, t), \tag{2.55}$$

$$\vec{x}'(\vec{X}, t) = \vec{x}(\vec{X}, t) + \vec{\xi}(\vec{X}, \vec{\Xi}, t). \tag{2.56}$$

An illustration of such a point particle is given in Figure 2.7. As in the Cauchy continuum, the deformations are expressed as mappings between the reference and the current configuration

$$\vec{\chi} : \vec{X} \to \vec{x}, \qquad \vec{\zeta} : \vec{\Xi} \to \vec{\xi}. \tag{2.57}$$

Note that the motions of $\vec{X}$ and $\vec{\Xi}$ are represented by independent mappings. Therefore, $\vec{\Xi}$ represents additional degrees of freedom of the motion that characterizes the inner structure of P. As depicted in Figure 2.7, $\vec{X}$ and $\vec{\Xi}$ describe the material particle $P \in \mathbb{B}$ in the reference configuration $\mathcal{R}$, whereas $\vec{x}$ and $\vec{\xi}$ refer to the current configuration $\mathcal{R}_t$.

$$\vec{x} = \vec{\chi}(\vec{X}, t) \qquad \Longleftrightarrow \qquad x_k = \chi_k(X_K, t), \tag{2.58}$$

$$\vec{\xi} = \vec{\zeta}(\vec{X}, \vec{\Xi}, t) \qquad \Longleftrightarrow \qquad \xi_k = \zeta_k(X_K, \Xi_K, t). \tag{2.59}$$

Equation 2.58 defines the macrodeformations and in analogy to the reasoning in section 2.2b the deformation gradients are defined accordingly

$$x_{k,K} = \frac{\partial x_k}{\partial X_K}, \qquad X_{K,l} = \frac{\partial X_k}{\partial x_l}. \tag{2.60}$$

The micromotions, defined by Equation 2.59, are considered to be small compared to the macromotions in Equation 2.58, since the material particles are generally considered small compared to the overall body $\mathbb{B}$. Therefore, a linear ansatz for the mapping $\zeta_k(X_K, \Xi_K, t)$ is reasonable

$$\xi_k = \zeta_{kK}(X_K, t)\Xi_K, \tag{2.61}$$

$$\Xi_K = \mathfrak{X}_{Kk}(X_K, t)\xi_k, \tag{2.62}$$

with the microdeformation tensor ζ_{kK} and the inverse microrotation tensor $\mathfrak{X}_{Kk}$. When multiplied with Cartesian base vectors $\hat{I}$ and $\hat{\imath}$, the independent directors ζ_K and $\mathfrak{X}_k$ can be defined

$$\zeta_K = \zeta_{kK} i_k, \qquad \mathfrak{X}_k = \mathfrak{X}_{Kk} I_K. \tag{2.63}$$

These deformable directors are depicted in Figure 2.8. In a simplified picture, the directors can be imagined as a tripod attached to P. In the most general case, these directors can be rotated and stretched with respect to arbitrary axes independently from each other. This means that the relative angles and relative lengths of the directors can change arbitrarily. Obviously, this

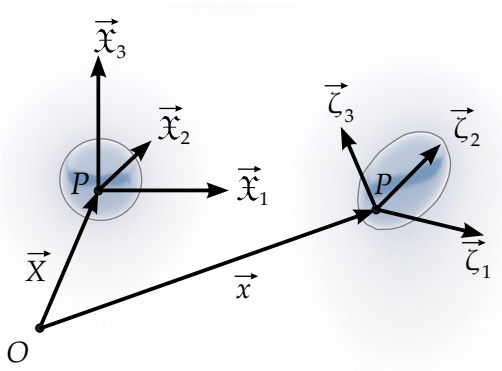

Figure 2.8: The maps relating the new degrees of freedom in the current to those in the reference, and vis versa, can be expressed as two sets of directors ζ_i and $\mathfrak{x}_i$. In principle, the length and direction of each director ζ_i and $\mathfrak{x}_i$ can be deformed individually.

can lead to a large number of additional degrees of freedom. Yet, in the micropolar theory as considered here, only a subclass of deformations are taken into account. In essence, the directors are considered to be a set of orthonormal vectors with fixed lengths and fixed relative angles. Therefore, microdeformations are restrained to rigid body rotations and only three additional degrees of freedom are introduced. This directly implies

$$\zeta_{kK}\zeta_{lK} = \delta_{kl}, \qquad \mathfrak{x}_{Kk}\mathfrak{x}_{Lk} = \delta_{KL}. \tag{2.64}$$

Using this, it can easily be shown that

$$\zeta_{kK} = \mathfrak{x}_{Kk}, \tag{2.65}$$

$$j = \det \zeta_{kK} = 1, \tag{2.66}$$

with the Jakobian determinate j.

2.3.2 *Strain Measures*

Suitable strain measures are again found, when calculating the arc lengths $\mathrm{d}S$ in the reference frame. Equation 2.56 yields

$$\mathrm{d}x'_k = x_{k,K}\mathrm{d}X_K + \zeta_{kK}\mathrm{d}\Xi_K + \zeta_{kK,L}\Xi_K\mathrm{d}X_L. \tag{2.67}$$

With that, the arc length is given by

$$\begin{aligned}(\mathrm{d}s)^2 = (\mathrm{d}x'_k)^2 = [&x_{k,K}x_{k,L} + 2(x_{k,K}\zeta_{k,L} + x_{kM,L}\zeta_{kM,K})\Xi_M \\ &+\zeta_{kM,K}\zeta_{kN,L}\Xi_M\Xi_N]\mathrm{d}X_K\mathrm{d}X_L + \\ 2(x_{k,K}\zeta_{kL} + \zeta_{kL}\zeta_{kM,K}&\Xi_M)\mathrm{d}X_K\mathrm{d}\Xi_L + \zeta_{kK}\zeta_{kL}\mathrm{d}\Xi_K\mathrm{d}\Xi_L.\end{aligned} \tag{2.68}$$

According to [27–31], the Cosserats' deformation tensor $\mathfrak{C}_{KL}$ and the wryness tensors φ_{KL} are appropriate strain measures, which fulfill Equation 2.68, as well as the conditions Equation 2.64, Equation 2.65, and Equation 2.66

$$\mathfrak{C}_{KL} = x_{k,K}\zeta_{kL}, \qquad \varphi_{KL} = \frac{1}{2}\epsilon_{KNM}\zeta_{kM,L}\zeta_{kN}. \tag{2.69}$$

The Cosserat deformation tensor $\mathfrak{C}_{KL}$ can be interpreted as the micropolar generalization of the Cauchy-Green deformation tensor defined in Equation 2.19. Again, in case of a rigid body motion, the Cosserats' deformation tensor is equal to the identity matrix. Therefore, the Lagrangian deformation tensors are defined as

$$\mathfrak{E}_{KL} = \mathfrak{C}_{KL} - \delta_{KL}, \qquad \varphi_{KL} = \frac{1}{2}\epsilon_{KNM}\zeta_{kM,L}\zeta_{kN}. \tag{2.70}$$

Finally, these strain tensors should be linearized and rewritten as a function of the displacement vector $\vec{u}$ and the microdisplacement vector $\vec{\phi}$

$$\vec{u} = \vec{x} - \vec{X}, \qquad \vec{\phi} = \vec{\xi} - \vec{\Xi}. \tag{2.71}$$

First, the deformation gradient is kinematically linearized following the reasoning of section 2.2. Furthermore, the microdeformations are approximated by a rotation matrix $R(\phi)$ for infinitely small rotations. This can be expressed in terms of the microdisplacement vector $\vec{\phi}$

$$R_{kl}(\phi) = \delta_{kl} - \epsilon_{klm}\phi_m. \tag{2.72}$$

Using this, the gradients of deformation read

$$x_{k,K} = \delta_{kK} + u_{k,K}, \qquad \zeta_{kK} = \delta_{kK} - \epsilon_{kKl}\phi_l. \tag{2.73}$$

Ultimately, by exploiting Equation 2.73, the Lagrangian strain tensors defined in Equation 2.70 are given in their linearized form

$$\varepsilon_{kl} = u_{l,k} + \epsilon_{klm}\phi_m, \qquad \varphi_{kl} = \phi_{k,l}. \tag{2.74}$$

Once again, to emphasis the difference between the linearized tensors and the strain tensors of Equation 2.70, these are denoted by lower case Greek letters. Also, since the material and spatial frame are equivalent in this approximation, the distinction between upper and lower case indicis becomes obsolete.

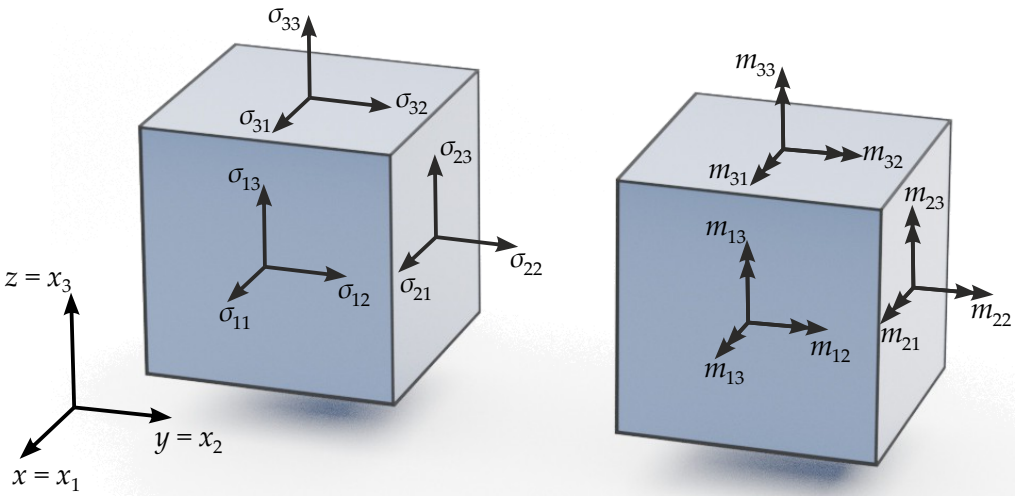

Figure 2.9: Depiction of an infinitesimal cubic volume element. The tripods illustrate the directions of the stress (left) and couple stress tensors (right). Note that the stresses and couple stresses related to these tripods only act on the surfaces the tripods are resting on.

The most important finding of this subsection is, that the strain tensor ε_{kl} is inherently nonsymmetric. This becomes immediately clear, when considering the second term in the definition $\epsilon_{klm}\phi_m$, since the Levi-Civita tensor is a skew-symmetric tensor.

As a result, in contrast to the classical Cauchy continuum, the micropolar continuum introduces point particles that have additionally rotational degrees of freedom. Therefore, points are not only characterized by a position vector $\vec{X}$, but also have a microdisplacement vector $\vec{\phi}$. Consequently, deformations in a micropolar material are defined by two tensors, the strain tensor ε_{kl} and the microdeformation tensor φ_{kl}.

2.3.3 *Stress measures*

In the previous subsection, the concept of point particles lead to additional degrees of freedom due to their deformability. When considering forces, it becomes immediately clear that a particle can be subject to momenta and couple stresses in contrast to the infinitesimal points in Cauchy elasticity. This is in sharp contrast to the postulations of Cauchy mechanics in section 2.2. Therefore, the postulations for micropolar continua are reformulated:

1) The total angular momentum $\vec{M}_{\delta a}$ per area tends to a definit limit, the so called coupled stress vector $\vec{m}$, when reducing δa to P

$$\lim_{\delta a \to P} \frac{\vec{M}_{\delta a}}{\delta a} = \vec{m}(\vec{X}, \hat{n}, t). \tag{2.75}$$

2) The total force $\vec{F}_{\delta A}$ per area tends to a definite limit, the so called traction vector $\vec{t}$, when reducing δA to P

$$\lim_{\delta a \to P} \frac{\vec{F}_{\delta a}}{\delta a} = \vec{t}\,(\vec{X}, \hat{n}, t), \tag{2.76}$$

with $\hat{n}$ being the face normal of δa.

Once more, following the reasoning of section 2.2, δA is meant to be part of a virtual cut plane through the body $\mathbb{B}$. To eliminate the cut plane dependency, the stress tensor σ and couple stress tensor $\mathbf{m}$ are defined as

$$t_i(\vec{X}, \hat{n}, t) = \hat{n}_j \sigma_{ji}(\vec{X}, t), \qquad m_i(\vec{X}, \hat{n}, t) = \hat{n}_j m_{ji}(\vec{X}, t). \tag{2.77}$$

Illustrations of these tensors are depicted in Figure 2.9. As for the strain measures, one additional stress measure is needed in micropolar elasticity, the couple stress tensor $\mathbf{m}$. Together, these two tensors completely characterize the forces and momenta in a micropolar material. Note that both the stress and the couple stress tensor are generally not symmetric.

2.3.4 *Equations of Motion*

The equations of motion can be derived from the energy balance law, as well as the balance of momentum and angular momentum. Yet, these are lengthy calculations with only little insights. Therefore, only the results are presented here. More details are given in [27–31]. The equations of motion of a micropolar continuum are

$$\rho a_l = \sigma_{kl,k} + \rho b_l \tag{2.78}$$

$$\rho \sigma_l = m_{kl,k} + \epsilon_{lmn} \sigma_{mn} + \rho l_l, \tag{2.79}$$

with mass density ρ, body forces $\vec{b}$, body moments $\vec{l}$, the acceleration $\vec{a}$, and the microacceleration σ_l.

2.3.5 Constitutive Model

When considering only small displacements $\vec{u}$ and microdisplacements $\vec{\phi}$, it is reasonable to assume a linear relation between the strain tensors and the stress tensors. As it can be shown, the most general definition of the total elastic energy U for a micropolar material is given by

$$U = \frac{1}{2} C_{klmn} \varepsilon_{kl} \varepsilon_{mn} + \frac{1}{2} A_{klmn} \varphi_{kl} \varphi_{mn} + B_{klmn} \varepsilon_{kl} \varphi_{mn}. \tag{2.80}$$

With the three rank-four tensors **A**, **B**, and **C**. From that, the constitutive equations can de derived

$$\frac{\partial U}{\partial \varepsilon_{kl}} = \sigma_{kl} = C_{klmn} \varepsilon_{mn} + B_{klmn} \varphi_{mn} \tag{2.81}$$

$$\frac{\partial U}{\partial \varphi_{lk}} = m_{kl} = A_{klmn} \varphi_{mn} + B_{mnlk} \varepsilon_{mn}. \tag{2.82}$$

In principle, each tensor **A**, **B**, and **C** has 81 entries, leading to a total number of 243 tensor elements. Since both the strain measures ε_{kl} and φ_{kl} as well as the the stress measures σ_{kl} and m_{kl} are nonsymmetric tensors, the elasticity tensors presented here do not have minor symmetries. Only the major symmetries persist, yielding

$$C_{klmn} = C_{mnkl}, \qquad A_{klmn} = A_{mnkl}. \tag{2.83}$$

This reduces the number of independent entries of both **C** and **A** to 45, leaving a total of 171 independent entries. These are significantly more than have previously been found for Cauchy elasticity. Generally speaking, this complicates a complete experimental characterization of micropolar materials, since the number of independent experimental observables has to be equal to the number of independent tensor entries.

2.3.6 Voigt Notation and Material Symmetries

Although not as many symmetries can be exploited to reduce the number of parameters in the micropolar theory, it is useful to go to a representation where the elasticity tensors **C**, **A**, and **B** are represented as a 9×9 matrix. The strain tensor is written as

$$\begin{aligned} &\bar{\varepsilon}_1 = \varepsilon_{11}, \quad \bar{\varepsilon}_2 = \varepsilon_{22}, \quad \bar{\varepsilon}_3 = \varepsilon_{33}, \quad \bar{\varepsilon}_4 = \varepsilon_{(23)}, \quad \bar{\varepsilon}_5 = \varepsilon_{(31)}, \\ &\bar{\varepsilon}_6 = \varepsilon_{(12)}, \quad \bar{\varepsilon}_4 = \varepsilon_{[23]}, \quad \bar{\varepsilon}_8 = \varepsilon_{[31]}, \quad \bar{\varepsilon}_9 = \varepsilon_{[12]}, \end{aligned} \tag{2.84}$$

with the symmetric $\varepsilon_{(kl)}$ and antisymmetric $\varepsilon_{[kl]}$ parts of the strain tensor

$$\varepsilon_{(kl)} = \frac{1}{2}(\varepsilon_{kl} + \varepsilon_{lk}), \qquad \varepsilon_{[kl]} = \frac{1}{2}(\varepsilon_{kl} - \varepsilon_{lk}). \tag{2.85}$$

The stress tensors σ_{kl} and m_{kl}, as well es the microdeformation tensor φ_{kl} are treated equivalently.

Yet again, the number of independent parameters are significantly reduced, when taking material symmetries into account. The general shape of an arbitrary 9×9 tensor $\mathbf{T}$ is given here. Keep in mind that for $\mathbf{C}$ and $\mathbf{A}$ additional elements might be equal due to their major symmetries $C_{klmn} = C_{mnkl}$ and $A_{klmn} = A_{mnkl}$. This time, for the sake of readability, the indicis of the tensor are also contracted.

TETRAGONAL MATERIALS:

Tetragonal materials have a total of 32 independent material parameters.

$$\bar{\boldsymbol{T}}_{\text{tet}} = \begin{pmatrix} T_{11} & T_{12} & T_{13} & 0 & 0 & 0 & 0 & 0 & 0 \\ T_{12} & T_{11} & T_{13} & 0 & 0 & 0 & 0 & 0 & 0 \\ T_{13} & T_{13} & T_{33} & 0 & 0 & 0 & 0 & 0 & 0 \\ 0 & 0 & 0 & T_{44} & 0 & 0 & T_{47} & 0 & 0 \\ 0 & 0 & 0 & 0 & T_{44} & 0 & 0 & T_{47} & 0 \\ 0 & 0 & 0 & 0 & 0 & T_{66} & 0 & 0 & 0 \\ 0 & 0 & 0 & T_{74} & 0 & 0 & T_{77} & 0 & 0 \\ 0 & 0 & 0 & 0 & T_{74} & 0 & 0 & T_{77} & 0 \\ 0 & 0 & 0 & 0 & 0 & 0 & 0 & 0 & T_{99} \end{pmatrix} \tag{2.86}$$

CUBIC MATERIALS:

Cubic materials have a total of 12 independent material parameters.

$$\bar{\boldsymbol{T}}_{\text{cub}} = \begin{pmatrix} T_{11} & T_{12} & T_{12} & 0 & 0 & 0 & 0 & 0 & 0 \\ T_{12} & T_{11} & T_{12} & 0 & 0 & 0 & 0 & 0 & 0 \\ T_{12} & T_{12} & T_{11} & 0 & 0 & 0 & 0 & 0 & 0 \\ 0 & 0 & 0 & T_{44} & 0 & 0 & 0 & 0 & 0 \\ 0 & 0 & 0 & 0 & T_{44} & 0 & 0 & 0 & 0 \\ 0 & 0 & 0 & 0 & 0 & T_{44} & 0 & 0 & 0 \\ 0 & 0 & 0 & 0 & 0 & 0 & T_{77} & 0 & 0 \\ 0 & 0 & 0 & 0 & 0 & 0 & 0 & T_{77} & 0 \\ 0 & 0 & 0 & 0 & 0 & 0 & 0 & 0 & T_{77} \end{pmatrix} \tag{2.87}$$

ISOTROPIC MATERIALS:

The tensor of an isotropic material looks the same as for the cubic case, but additionally $T_{44} = \frac{1}{2}(T_{11} - T_{21})$. It has a total of 9 independent material parameters. Another compact representation of the isotropic tensors is given by

$$C_{klmn} = \lambda\delta_{kl}\delta_{mn} + (\mu + \kappa)\delta_{km}\delta_{ln} + \mu\delta_{kn}\delta_{lm}, \tag{2.88}$$

$$A_{klmn} = \alpha\delta_{kl}\delta_{mn} + \beta\delta_{km}\delta_{ln} + \gamma\delta_{kn}\delta_{lm}, \tag{2.89}$$

$$B_{klmn} = B_1\delta_{kl}\delta_{mn} + B_2\delta_{km}\delta_{ln} + B_3\delta_{kn}\delta_{lm}. \tag{2.90}$$

The parameters μ and λ are related to the Lamé-parameters introduced in section 2.2.

CHIRAL AND ACHIRAL MATEIALS

This generalized elasticity was discussed in the scope of this thesis only to be able to describe chiral materials. The following example will shine a light on how micropolar elasticity deals with chirality. It has been defined before that a material is chiral, if its mirror image cannot be brought into congruence with the original material. Equivalently, equations describing a chiral material should not recover their original form after performing a mirror operation on the coordinate system, e.g. $z \to -z$. As an illustration, the transformation of a single element of the stress tensor σ_{33} of an isotropic material is examined for said mirror

operation.

$$\begin{aligned}\sigma_{33} =&\lambda(\varepsilon_{11}+\varepsilon_{22}+\varepsilon_{33})+(2\mu+\kappa)\varepsilon_{33}\\ &+B_1(\varphi_{11}+\varphi_{22}+\varphi_{33})+(B_2+B_3)\varphi_{33}, \qquad (2.91)\\ \Leftrightarrow \sigma_{33} =&\lambda(u_{1,1}+u_{2,2}+u_{3,3})+(2\mu+\kappa)u_{3,3}\\ &+B_1(\phi_{1,1}+\phi_{2,2}+\phi_{3,3})+(B_2+B_3)\phi_{3,3}, \qquad (2.92)\end{aligned}$$

Performing the mirror operation $z \to -z$ is equivalent to $u_3 \to -u_3$ and $\partial/\partial z \to -\partial/\partial z$. Therefore, the second order tensors $\boldsymbol{\sigma}$ and $\boldsymbol{\varepsilon}$ remain unchanged. On the other hand, $\vec{\phi}$ is a rotation vector and therefore a pseudovector. Hence, it transforms as $\phi_1 \to -\phi_1$, $\phi_2 \to -\phi_2$, and $\phi_3 \to \phi_3$

$$\begin{aligned}\sigma_{33} =&\lambda(u_{1,1}+u_{2,2}+u_{3,3})+(2\mu+\kappa)u_{3,3}\\ &+B_1(-\phi_{1,1}-\phi_{2,2}-\phi_{3,3})-(B_2+B_3)\phi_{3,3}. \qquad (2.93)\end{aligned}$$

Obviously, due to the sign in front of the $\phi_{i,i}$ components, Equation 2.93 and Equation 2.92 are not equivalent. Thus, this equations describes a chiral medium. Yet, the equations are equal for arbitrary mirror operations or inversions, and in consequence the material would be achiral, for the special case of $B_1 = B_2 = B_3 = 0$.

In general, chiral material have $\mathbf{B} \neq 0$, whereas achiral, hence centrosymmetric material, exhibit $\mathbf{B} = 0$. Evidently, chirality is introduced in micropolar elasticity by mixing vectorial and pseudovectorial (tensorial and pseudotensorial) quantities.

THE CAUCHY LIMIT

It becomes obvious from Equation 2.88, Equation 2.89, and Equation 2.90 that for $\kappa = \alpha = \beta = \gamma = B_1 = B_2 = B_3 = 0$, a form equivalent to the isotropic Cauchy continuum is recovered. Generally speaking, it can be shown that any Cauchy material can be modeled by setting some parameters of $\mathbf{C}$ to zero and $\mathbf{A} = \mathbf{B} = 0$. Hence, the Cauchy limit is contained as a special parameter configuration in the micropolar theory. As a result, the micropolar continuum is indeed a generalization of a Cauchy continuum.

Note that the nomenclature in this section slightly deviates from the one in [31] or other text books and publications. The author chose this representation to point out similarities between the micropolar and the

Cauchy theory. Therefore, the tensor connecting σ_{kl} and ϵ_{kl} is called $\mathbf{C}$. Others might call this tensor $\mathbf{A}$ instead. Generally speaking, a commonly used notation is not yet fully established and directly comparing results from different authors has to be done with caution. Not least, since even the definition of Voigt's notation is done inconsistently.

2.3.7 *Material Moduli*

To ease physical interpretation, a set of technical constants is derived from tensor entries, the so-called material moduli. For an achiral isotropic medium, they are defined as follows [31, 54, 55]:

Young's modulus	$E = \frac{(2\mu+\kappa)(3\lambda+2\mu+\kappa)}{2\lambda+2\mu+\kappa}$
shear modulus	$G = \frac{2\mu+\kappa}{2}$
Poisson's ratio	$\nu = \frac{\lambda}{2\lambda+2\mu+\kappa}$
characteristic length for torsion	$l_\mathrm{t} = \sqrt{\frac{\beta+\gamma}{2\mu+\kappa}}$
characteristic length for bending	$l_\mathrm{b} = \sqrt{\frac{\gamma}{2(2\mu+\kappa)}}$
coupling number	$N = \sqrt{\frac{\kappa}{2(\mu+\kappa)}}$
polar ratio	$\Psi = \frac{\beta+\gamma}{\alpha+\beta+\gamma}$

The Young's modulus E, shear modulus G, and Poisson's ratio ν have the same meaning as their classical counterparts. Interestingly, two of the material moduli are lengths with unit meters. Loosely speaking, they are connected to the size of the point particles, or to the structural elements in the material that couple the microdeformational degrees of freedom to the usual ones. This is in sharp contrast to the classical Cauchy continuum, where all material moduli either have the dimension of a stress or none at all.

The occurrence of material moduli carrying information about a length scale has far reaching consequences and eventually leads to the breakdown of scale invariance. Meaning that some physical properties will not only

Material	E(MPa)	G(MPa)	ν	l_t(mm)	l_b(mm)	N^2	Ψ
Human bone [49, 50]	12000	4000	-	0.22	0.45	≤ 0.5	1.5
Graphite [56]	4500	-	0.06	1.6	2.8	1	-
Polyurethane foam [58]	300	104	0.4	0.62	0.33	0.04	1.5

Table 2.1: Examples of experimentally determined micropolar material parameters for some selected materials.

depend on the outer dimensions of the sample, but also how these relate to characteristic lengths scales of the material. An example pointing out this length scale dependency of the torsional rigidity of a cylindrical bar will be discussed in the next subsection.

It has been shown experimentally that micropolar effects and the corresponding degrees of freedom are present in a multitude of materials. Especially human bone [49, 50], graphite [56], and foams [57, 58] showed deviations from the classical behavior. A couple of exemplary material moduli are given in Table 2.1.

For the case of a chiral isotropic medium, Lakes defines yet another set of nine material parameters [33]. Those especially relevant for chiral effects are:

$$K_0 = \frac{B_1 + B_2 + B_3}{\sqrt{(\alpha+\beta+\gamma)(\lambda+2\mu+\kappa)}},$$
$$K_3 = \frac{B_1}{B_1 + B_2 + B_3},$$
$$l_1 = \frac{B_1 + B_2 + B_3}{2\mu + \kappa}.$$

l_1 has the dimension of a length. K_0 is related to the strength of the noncentrosymmetric coupling and K_3 plays the role of a Poisson's ratio [33].

For passive media, meaning media that do not have an internal energy source, the entries to the elasticity tensor are not independent from each other. Instead, they can only be varied within strict bounds. A passive material basically means that every possible deformation of a body leads to an increased total elastic energy U compared to the undeformed or natural

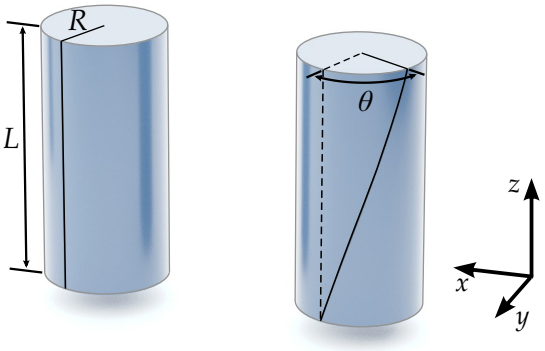

Figure 2.10: Illustration of an undeformed cylinder (left) and of the same cylinder subjected to a twist (right). Thereby, the bottom of the cylinder is fixed and the top surface is rotated by an angle θ around the z-axis.

configuration of the body. Assuming every arbitrary deformation can be decomposed into eigendeformations of the material, a material is passive if all corresponding eigenenergies are positive. These eigenstates and the according energies can be derived by rewriting Equation 2.80. Thereby, the three 9×9 elasticity tensors $\mathbf{A}$, $\mathbf{B}$, and $\mathbf{C}$ are rearranged into a single 18×18 tensor $\tilde{\mathbf{C}}$

$$\tilde{\mathbf{C}} = \begin{pmatrix} \mathbf{C} & \mathbf{B} \\ \mathbf{B}^{\mathrm{T}} & \mathbf{A} \end{pmatrix}. \tag{2.94}$$

The reasoning above implies that for all passive material, $\tilde{\mathbf{C}}$ is positive definite. From that, restrictions on the tensor elements can be derived, both for the micropolar [33, 59, 60] and Cauchy mechanics [1, 61–63]. Consequently, the material moduli cannot have arbitrary values. Instead, strict bounds can be derived.

2.3.8 *Torsion of an Achiral Circular Cylinder*

When a cylinder with circular footprint or radius R and height L is subjected to a small torsion θ as illustrated in Figure 2.10, the resulting shear stresses τ assuming Cauchy elasticity are simply given by

$$\tau = \theta G \frac{R}{L}, \tag{2.95}$$

with shear modulus G [42]. It only depends on the cylinder's aspect ratio R/L and the constant material moduli. The torsional stiffness Ω, the ratio between total torque at the end of the bar T and torsion angle θ is defined as

$$\Omega = \frac{T}{\theta} = G \frac{J}{L}, \tag{2.96}$$

with the polar momentum $J = \int_A r^2 \mathrm{d}A$. In 1975, Gauthier and Jahsman solved the same problem of a circular cylinder, but this time considering a micropolar material. Their expression derived in [54] for the torsional stiffness reads

$$\Omega = G\frac{J}{L}\left(1 + 6\left(\frac{l_\mathrm{t}}{R}\right)^2 \frac{1 - \frac{4}{3}\Psi\mathcal{F}}{1 - \Psi\mathcal{F}}\right). \tag{2.97}$$

The lengthy analytical expressions for $\mathcal{F}$ are given in [54]. Although $\mathcal{F}$ also depends on l_t and R, one can directly tell from the prefactor that the result not only depends on the aspect ration of the bar as before, but also on the ratio between characteristic length and cylinder radius l_t/R. Furthermore, the deviations from the classical result increase for cylinders that are small compared to the characteristic length. In the large sample limit $R \to \infty$ the last term on the right hand side vanishes and the Cauchy limit is recovered.

These findings are the crucial novelties of micropolar mechanics and can be summarized as follows:

1) Micropolar media have intrinsic characteristic length scales. When sample dimensions are in the same order of magnitude as these length scales, deviations from the classical behavior are expected.

2) In the large sample limit, the Cauchy elasticity and micropolar elasticity are equal. In this limit, the dimensions of the point particle become neglectable and can be treated as ordinary points.

Now the key questions are: What determines the magnitude of characteristic lengths scales? And can these characteristic length scales be much larger than the building blocks the material is made of? Our design efforts for chiral micropolar metamaterials, that are presented later, directly foot on these questions.

Gauthier and Jahsman also showed that not all experiments show deviations from the classical behavior. Especially simple tension experiments yield no length scale dependency of the effective material moduli, nor of the displacement fields [54]. Instead, they only find deviations for boundaries involving torsion or bending deformations.

2.3.9 *Twist-to-Push Coupling in Chiral Materials*

Apart from these rather quantitative deviations in achiral material, qualitatively new effects have been found in chiral media. Lakes and Benedict

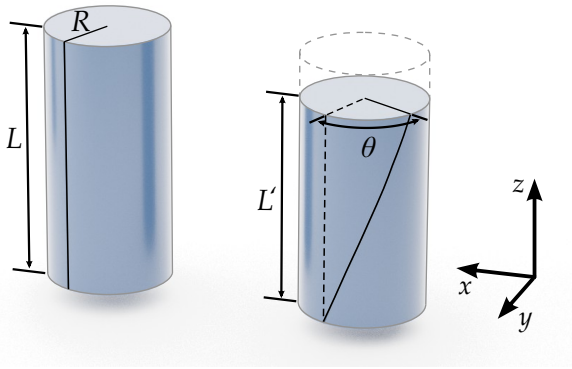

Figure 2.11: Illustration of an undeformed cylinder (left) out of a chiral constituent material. When subjected to an axial strain along the z-axis, the cylinder twist by an angle θ around this axis (right). The bottom of the cylinder is fixed and otherwise no external torques or forces are applied.

showed in [33] that a chiral isotropic cylinder with circular foot print twists when subject to an axial compression. Thereby, the twisting occurs in a plane orthogonal to the axial strains as illustrated in Figure 2.11. In their paper [33], they were able to solve the static problem analytically in polar coordinates (z, r, θ) and arrived at the following solutions

$$u_z = \varepsilon_{zz} z, \qquad \phi_z = b_0 z,$$
$$u_\theta = b_0 r z, \qquad \phi_\theta = 0.$$

In that, b_0 is a twist angle per unit length which depends on the radius R of the cylinder. The rather complex radial dependency of the displacement fields are not shown here and are of minor importance for the discussions later. They found that the twist angle increases linearly with the sample height and that this angle is constant in every plane orthogonal to the pushing direction. As in the classical case, the axial strain ε_{zz} is constant along the axis of the external compression.

Lakes and Benedict also give analytical expressions for b_0 for different assumptions on the material moduli. Here, the most general case will be skipped, since it is difficult to gain any physical insights from this expression. Assuming, $B_1 = 0$, $\lambda = 0$, $\alpha = 0$ they found a rather compact expression

$$b_0 = -\frac{K_0 l_t}{l_t^2 + \frac{R^2}{4} + \frac{R^2 I_2(pR) N}{(pR)^2 I_0(pR) - pR I_1(pR)}} \varepsilon_{zz}, \tag{2.98}$$

with $p = (2\kappa)/((\alpha + \beta + \gamma)(1 - K_0^2))$ and the Bessel functions I_0, I_1, and I_2 [33]. Importantly, the twist per unit length b_0 is proportional to the strain ε_{zz} and the chiral coupling K_0. Interestingly, when changing the sign in

front of the tensor $\mathbf{B}$, K_0 also changes sign, and hence the twisting direction. Yet, the magnitude stays the same. Therefore, by changing the sign of $\mathbf{B}$, the material is switched from a right-handed to a left-handed material, or vice versa. Furthermore, Lakes and Benedict show that for large sample radii R the twist per unit length b_0 decreases proportional to the inverse square of the radius and approaches a constant for sufficiently small radii ($R \ll l_t$). This means that for a sample with fixed aspect ratio R/L the twist angle, meaning the difference in rotation angle between the ends of the bar, decreases $\propto 1/R$. Hence, for large samples the twist deformation u_θ vanishes and the Cauchy limit is recovered again. These findings will be of utmost importance in later chapters.

2.4 Other Generalized Theories

Of course, the micropolar approach is not the only generalization of Cauchy elasticity, that describes chiral effects and chiral materials. The author simply chose this theory since it is a linear generalization, that already shows good agreement with the simulations and experiments shown later. In doing so, it additionally requires comparatively few independent material parameters (9 in the isotropic case). In this section, a short overview is given over alternative theories, without going into the details. This is by no means a complete list of existing theories.

2.4.1 Microstretch and Micromorphic Elasticity

In fact, micropolar elasticity is only an edge case of the more general microstretch and micromorphic elasticity. Whilst starting from the same assumptions of a microcontinuum made up out of deformable point particles, microstretch elasticity allows not only for rigid body rotations of the directors, but also length changes. Thereby, a microstretch continuum possesses even more degrees of freedom and therefore requires even more material parameters.

The micromorphic theory even goes one step further and also allows for a change of the relative angles between the directors. This actually leads to the definition of an additional strain and stress tensor and five additional elasticity tensors.

In both microstretch and micromorphic elasticity, the chiral coupling results from mixing tensorial and pseudotensorial quantities. These theories

are also summarized by Eringen in [27–30].

2.4.2 *Gradient-Theories*

Within the framework of these theories which have been established by Toupin [44] and Mindlin [64, 65], the elastic energy does not only depend on the elastic strains, but also explicitly on the gradients of the strain. Therefore, a third-ranked tensor appears in the constitutive equations making the previous reasoning for tensors of even rank obsolete [66] (compare section 2.1). Hence, chiral material can be described using gradient-theories.

2.4.3 *Willis-Elasticity*

The Willis elasticity [67–69] is mostly used in the context of elastic waves. It is somewhat related to a dielectric medium [69] in a sense that the frequency dependency of effective mass resembles the frequency dependency of the dielectric constant. In the past it has been shown that this theory can describe chiral effects [69] for time dependent problems. Again, this is related to tensors of odd rank appearing in the constitutive relations. In 2019, Kadic derived equations for the static regime [70]. This approach seems especially promising, since it needs only a minimum number of independent material parameters to describe a chiral medium. Yet, further studies are needed to validate and expand this theory.

2.5 Mechanical Metamaterials

2.5.1 *Definition of Metamaterials*

The term metamaterial was introduced by Walser in 2001 [71] in the context of electromagnetic laminates that showed *"previously unattained properties"* [71]. The prefix meta (ancient Greek for beyond) should emphasize that the observed properties go beyond the mere average of atoms and chemical bonds constituting the material. Unfortunately, there is not a clear definition of metamaterials that all researchers could relate to [15]. Kadic, Wegener, and colleagues therefore formulated this loose definition, within most of today's metamaterials fall:

> *"Metamaterials are rationally designed composites made of tailored*

> *building blocks that are composed of one or more constituent bulk materials. The metamaterial properties go beyond those of the ingredient materials, qualitatively or quantitatively."[15]*

The rational design is key to metamaterials and makes them distinct from alloys, mixtures or foams, which are patterned in a random process. Usually, metamaterials consist of material building blocks, or in case of crystals unit cells, much bigger than the atomic scale, but small compared to a crucial experimental length scale like wavelength or sample size. These building blocks are sometimes also referred to as metaatoms, in analogy to atoms - the building blocks of regular materials.

In a way, metamaterials turn the traditional approaches of material science on its head. Instead of trying to describe what can be found in nature, metamaterials present us with the creative challenge of finding the building blocks or unit cells that lead to the desired material properties. Therefore, laying down a strategic roadmap of how to arrive at a certain design is notoriously difficult. It often starts with the idea of a certain micro-mechanism on the unit cell level [14, 72], like coinciding a magnetic and electric resonance [73–75], or the bending of a bi-material beam [76, 77], that will result in the desired properties of the material. Other approaches exploit topological optimization techniques [78–81].

It has been argued in the past that metamaterials only gain relevance for real world applications, if their complex microstructure can be mapped on effective material parameters referring to a fictitious continuum [15]. For elastic materials, this might be an effective Young's modulus, for optical materials, an effective electric permittivity might be an appropriate representation. In this homogenization procedure, the complexity of the microstructure is represented by only a couple of parameters [82–84]. Engineers then might use these effective parameters for modeling and planing, just as they use the material parameters for every ordinary material. Yet, retrieving these parameters is notoriously difficult. Currently, there is no straight forward routine to extract effective parameters for arbitrary structures [15].

In general, the metamaterial concept is very versatile, and is of course not restricted to a single discipline [11, 85]. Instead, numerous metamaterials have been realized not only for mechanical applications, but for optical [4, 18, 86] and acoustical applications [8, 87, 88], seismic protection [89–91], or even Hall effect metamaterials [92–95], only to mention a few examples. A mechanical metamaterial is tailored to exhibit special mechanical properties. Meaning, they seek to control deformations, mechanical forces, or stresses.

2.5.2 *Brief Overview of Mechanical Metamaterials*

Metamaterials in general, and the field of mechanical metamaterials in particular, has been a thriving discipline with new design proposals and experimental studies appearing on a weekly basis. Therefore, a complete discourse of prior work is illusive and only selected examples are presented. A broad overview of the state of the art is also given in these review papers [14–16].

Linear Mechanical Metamaterials

Many metamaterial designs of the past targeted the realization of arbitrary, and sometimes exotic, Cauchy elasticity tensors and material moduli. Maybe the most prominent example is the so-called pentamode material. This solid effectively behaves like a liquid in the sense that it is easy to deform, but hard to compress hydrostatically [61, 96]. Such pentamode structures also led to the design of unfeelability cloaks [97].

Auxetic metamaterials on the other hand exhibit a negative Poisson's ratio. In contrast to most ordinary materials, which expand laterally when being compressed axially, auxetic materials contract laterally upon axial compression. Many different designs have been proposed in the past [98, 99], some even approaching the most extreme case of a Poisson's ratio of $\nu = -1$ [100].

Other metamaterials that might become important for many engineering applications exhibit extraordinary high stiffnesses, whilst having a low mass density [101, 102].

Other Mechanical Metamaterials

But the properties of mechanical metamaterial already go well beyond what can be described by the classical Cauchy elasticity tensors. For example, structures with highly nonlinear responses based on mechanical instabilities have been proposed for shock and energy absorption [103, 104]. Such mechanical instabilities also led to the development of programmable metamaterials, whose properties can be adjusted even after fabrication [105].

Topologically protected edge states have been discussed to provide robust functionalities. The concept originated from condensed matter physics, yet, exciting mechanical counterparts have been proposed recently [106–108].

Chapter 3

3 Numerical Methods for Elastostatic Problems

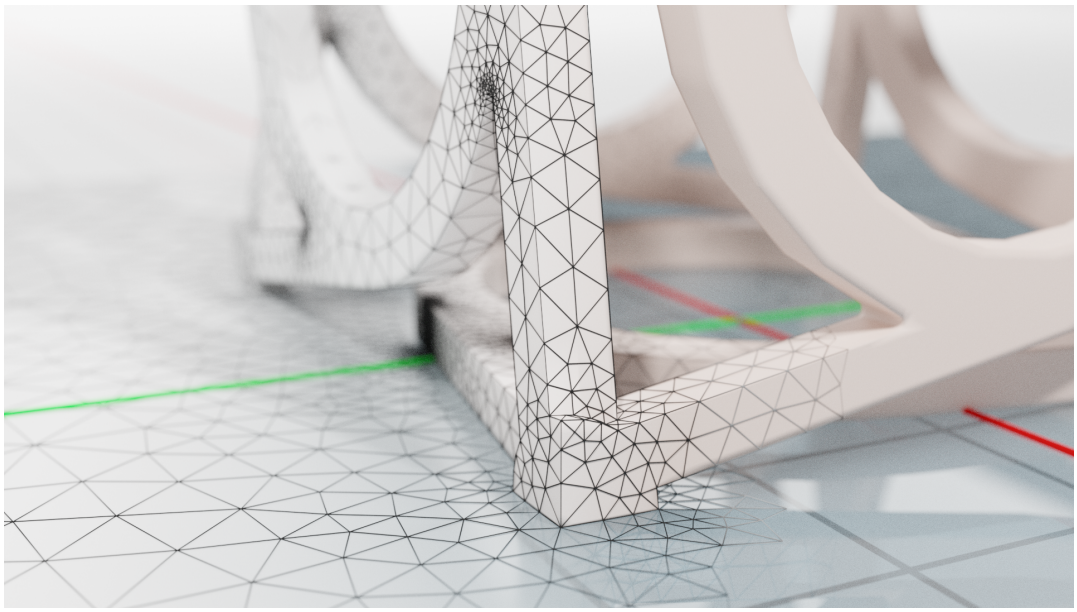

Artistic illustration: from numerics to real world samples

Designing metamaterials for a specific purpose without numeric models is a nearly impossible task. Not least, because numerics enables us to test and precharacterizer a huge number of structures with only little effort, compared to time consuming and sometimes expensive experiments. On the basis of the numerical modeling, we pick the best performing structures that will be fabricated and put to test. Due to its versatility, the so-called finite element method is a suitable tool. In this chapter, I will give a short introduction to the method. Furthermore, I will discuss the implementation of the Cauchy and micropolar equations.

3.1 The Finite Element Method

The finite element method (FEM) is a well established numerical routine to find approximate solutions to partial differential equations (PDE). As such, it is already subject of many textbooks like [109, 110]. Therefore, this is only meant as a short introduction to the method. The author closely follows the didactic approach by Bower [111].

First, the domain Ω on which a PDE should be solved is separated into non-overlapping subdomains Ω_i, the so-called finite elements

$$\Omega = \bigcup_{i=1}^{e} \Omega_i. \tag{3.1}$$

The solution $u(x)$ is approximated by a linear combination of ansatz functions $\psi_a(x)$, each of them is nonzero only on one subdomain Ω_i. At the same time, the field of the desired quantity u is discretized, meaning it will only be calculated at a number of nodes at x_a. These nodes are the characteristic points of finite elements. For example, in case of a tetrahedral element, the nodes are simply the four corners of the tetrahedron. Hence, elements share common nodes. Therefore, the ansatz is chosen as follows

$$u^h(x_a) = \sum_{a=1}^{n} c_a \psi_a(x), \tag{3.2}$$

with real coefficients c_a. The superscript h denotes that a discretization and approximation took place and is called the discretization parameter. It is assumed that for $h \to 0$, the approximated solution converges to the exact solution $u_h \to u$. Note that a is not only the summation index, but at the same time denotes the index of the node. Therefore, $\psi_a(x_b) = 0$ for $a \neq b$, since the subdomains do not overlap. By applying the principle of virtual work [109], the PDE are expressed as integral equations, the so-called weak form. Since the ansatz functions are nonoverlapping, the integrals can be solved for each domain individually and yield conditions for the coefficients c_a. These can be expressed as a system of linear equations

$$\mathbf{M}\vec{c} = \vec{q}, \tag{3.3}$$

with the quadratic matrix $\mathbf{M}$, the vector $\vec{c}$ containing linear combinations of the coefficients c_a, and the vector $\vec{q}$ representing the boundary conditions. Since the functions $\psi_a(x)$ are only nonzero on a couple of elements, $\mathbf{M}$ is a

sparse matrix with most of its entries being zero. If $\vec{q}$ is a linear function of the coefficients c_a, which holds true for linear elastic problems, the system of linear equations is simply solved using a direct or iterative solver.

3.2 Cauchy Mechanics in Finite Elements

Now, the previously described method is applied to describe the Cauchy elastic properties of the object represented by the domain Ω. The principle of virtual work is a calculus of variations method and as such, a different form of expressing the equations of motion [111]. It states, if for all virtual displacements δv the stress field σ_{ij} satisfies

$$\int_{\Omega} \sigma_{ij}\delta\varepsilon_{ij}\mathrm{d}V - \int_{\Omega} b_i\delta v_i\mathrm{d}V - \int_{\partial\Omega} t_i\delta v_i\mathrm{d}A = 0, \tag{3.4}$$

the equations of motions are also satisfied. In that, the virtual strain tensor $\delta\varepsilon_{ij}$ is defined as $\delta\varepsilon_{ij} = 1/2(\delta v_{i,j} + \delta v_{j,i})$. By utilizing the symmetries of both strain and virtual strain tensor, as well as the symmetry of the stress tensor, and inserting the constitutive relations, the weak form is derived as

$$\int_{\Omega} C_{ijkl}u_{i,j}\delta v_{i,j}\mathrm{d}V - \int_{\Omega} b_i\delta v_i\mathrm{d}V - \int_{\partial\Omega} t_i\delta v_i\mathrm{d}A = 0. \tag{3.5}$$

Another way to derive this weak form, is multiplying the equations of motion with a test function and subsequently integrating over the domain Ω and its boundary $\partial\Omega$.

Every component of the displacement vector u_i and virtual displacement vector δv_i is replaced by the ansatz given in Equation 3.2

$$u_i^h(x) = \sum_{a=1}^{n} c_{ai}\psi_a(x), \qquad v_i^h(x) = \sum_{b=1}^{n} c_{bi}\psi_b(x). \tag{3.6}$$

After some algebraic transformations, the weak form Equation 3.5 can be represented by

$$K_{aibk}c_{bk} = F_{ai}, \tag{3.7}$$

with

$$K_{aibk} = \int_{\mathfrak{R}} C_{ijkl}\psi_{a,j}\psi_{b,l}\mathrm{d}V; \qquad F_{ai} = \int_{\mathfrak{R}} b_i\psi_a\mathrm{d}V + \int_{\mathfrak{R}} t_i\psi_a\mathrm{d}A. \tag{3.8}$$

K is called the stiffness matrix, $\vec{c}_b$ is a vector containing the degrees of freedom of the system. Note that the result does not depend on the test function δv anymore. A more detailed derivation can be found in [111].

3.3 Micropolar Mechanics in Finite Elements

For a micropolar continuum, Joeng and coworkers [112] found the following expression for the weak form

$$\int_\Omega (\sigma_{ij}\delta\varepsilon_{ij} + m_{ij}\delta\varphi_{ij})\mathrm{d}V - \int_\Omega (b_i\delta v_i + d_i\delta\eta_i)\mathrm{d}V - \int_{\partial\Omega} (t_i\delta v_i + m_i\delta\eta_i)\mathrm{d}A = 0, \tag{3.9}$$

with the body microdisplacements vector $\vec{d}$, and the virtual strain tensors $\delta\varepsilon_{ij} = \delta u_{j,i} - \epsilon_{ijk}\delta\eta_k$ and $\delta\varphi_{ij} = \delta\eta_{i,j}$ [112]. Actually, all information concerning the physics of a system are already contained in the weak form. The following treatment to arrive at the matrix equation is totally equivalent to the case discussed before and will therefore be skipped here.

3.4 Implementation of the Finite Element Method

For all FEM calculations performed by the author in this thesis, the commercial software COMSOL Multiphysics has been used, unless explicitly state otherwise. The geometry was split up, or mashed, into tetrahedral elements and the displacement fields were discretized using quadratic ansatz functions. The resulting matrix equation was solved using the multifrontal massively parallel sparse direct solver (MUMPS). Detailed information are given in the COMSOL user manual [113].

In the first part of this thesis, only static experiments are considered. Therefore, forces connected to the accelerations, ρa_i and $\rho\sigma_i$, vanish in Equation 2.39, Equation 2.78, and Equation 2.78.

Cauchy Continuum

The Cauchy elasticity as introduced in section 2.2 is already implemented in the solid mechanics module [113]. It also offers the possibility to account for geometrical nonlinearities. When doing so, instead of the linear strain and stress tensors ε_{ij} and σ_{ij}, COMSOL uses the Lagrangian strain tenor **E** and the second Piola-Kirchhoff stress tensor **S**.

Micropolar Continuum

The micropolar theory is not predefined in COMSOL. Yet, the program allows the user to implement any desired physical model by entering the weak form [113]. Therefore, Equation 3.9 was implemented using the weak form PDE module. Two independent models have been set up that gave matching results. The fist model was set up by the author using a linear isotropic constitutive model. The second by Yi Chen, who implemented the most general linear constitutive relations, was used to treat cubic and tetragonal materials. Additional details about implementing a micropolar model in COMSOL are given in [112, 114, 115].

Chapter 4

4 Setups and Fabrication Methods

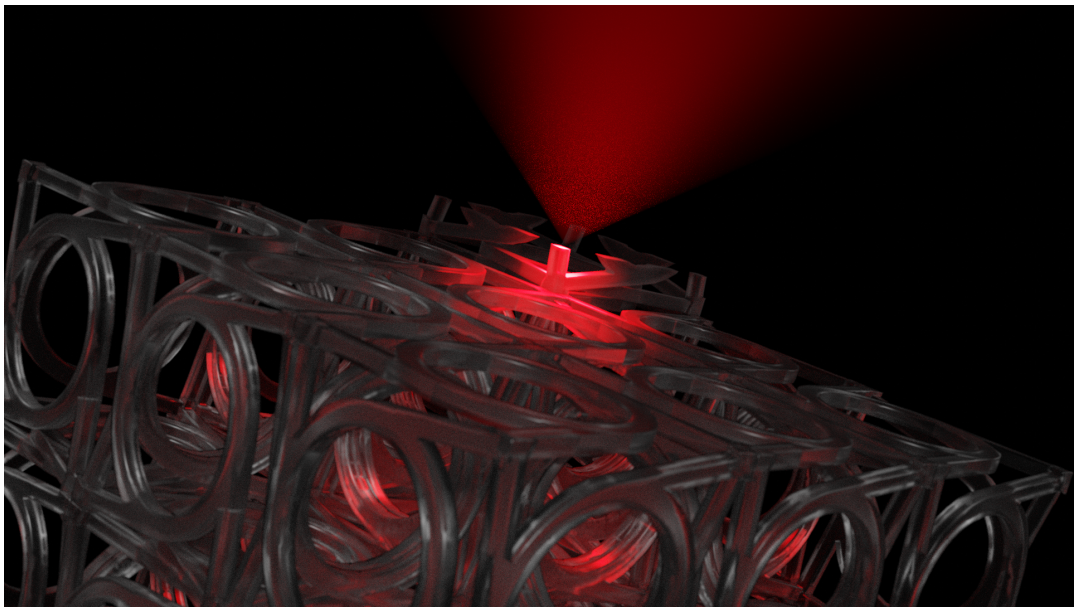

Artistic illustration of the 3D-printing process

In this chapter, I will introduce a self-build measurement setup that characterizes the push-to-twist coupling and the Young's modulus of our metamaterial samples. Before, I will present a clever sample design facilitating the experimental boundary conditions drastically. Afterwards, I will introduce the image cross-correlation routine, which tracks displacements as small as a couple of nanometers. Finally, I will describe the two three-dimensional laser printers used for sample fabrication.

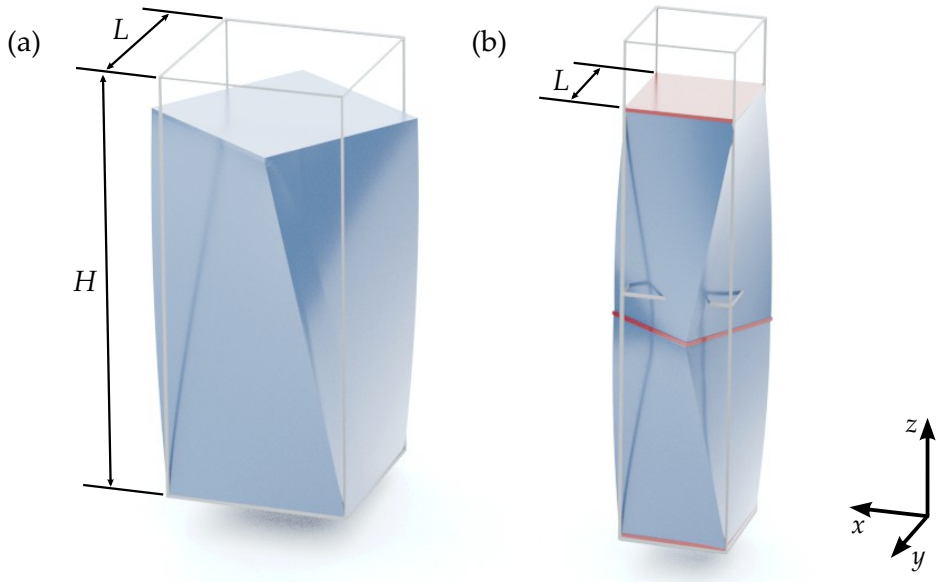

Figure 4.1: (a) Illustration of the twist-to-push coupling in a square bar with a single handedness. (b) Two chiral bars stacked on top of each other with opposite handedness. Thereby, the interface between the two bars can twist freely without the need to realize sliding boundary conditions. To facilitate the measurement, a plate (red) with markers will be added for the experiments in between the bars with different handedness, which will be tracked using digital image cross-correlation. The plates at both ends (red) ensure a properly defined contact of the sample with the substrate and the measurement setup, respectively.

4.1 General Sample Design

As has been shown in previous chapters, upon pushing, a chiral rod twists around the pushing direction as illustrated in Figure 4.1(a). To characterize the metamaterials, the magnitude of this twisting angle is going to be extracted and will be the key measure for both the chirality and the characteristic length scale. Therefore, it is crucial that the experimental setup does neither alter nor disturb this twisting motion. Meaning, the x- and y-components of the displacement need to move as freely as possible for a prescribed strain along the z-direction. Yet, these so called sliding boundary conditions, where only one component of the displacement vector is prescribed, are notoriously difficult to realize experimentally. Some residual

friction between a sample and the stamp of the measurement setup will always distort the twist angle, since it will act as a counter moment to the sample movement. This becomes especially challenging when performing experiments on the microscale as presented later, where adhesion forces to surfaces can play a dominant role, compared to the relatively small forces of the sample.

Nevertheless, the necessity of sliding boundary conditions can be circumvented by exploiting material symmetries. Namely, by stacking a right- and left-handed version of the structure on top of each other. As has been shown in subsection 2.3.9, by flipping the handedness only the direction of the twisting changes, but not the magnitude of the twist angles. This means, by stacking chiral bars of left- and right-handedness on top of each other, the top bar would reverse the twisting of the bottom bar. Thereby, both ends of the sample would not rotate and can be fixed, such that all components of the displacement vector can be prescribed. A schematic arrangement is depicted in Figure 4.1(b). Similar sample geometries have been used in [2].

To facilitate the extraction of displacement vectors using an image cross-correlation method, a plate with markers is added between the two parts of opposite handedness (plate thickness 10 µm). Additionally, to ensure well-defined contact, another set of plates with 10 µm thickness are added to the top and the bottom of the sample.

Despite these efforts to minimize the influence of the boundaries, for some samples the results are still heavily influenced by the boundaries and the finite size of the sample. Not least because the plates at the end prevents a lateral expansion or contraction of the metamaterial caused by its nonzero Poisson's ratio. Furthermore, these plates enforce the same displacement for all points at the boundary even within a unit cell. Unfortunately, these imperfect boundaries are hard to bypass experimentally. An estimation of the magnitude of their influence is given in [116]. This problem is somewhat similar to the influence of sample geometry when determining material moduli, like Young's modulus or the Poisson's ration, in classical tensile test [117].

Such boundary effects tend to get smaller for elongated samples. Therefore, a large sample aspect ratio H/L is desirable, assuming a sample height H and a square footprint with side length L. On the other hand, large aspect ratios increase the sample production time significantly. Hence, for each handedness an aspect ratio of $H/L = 2$ has been chosen leading to an aspect ratio of the total sample of $2H/L = 4$.

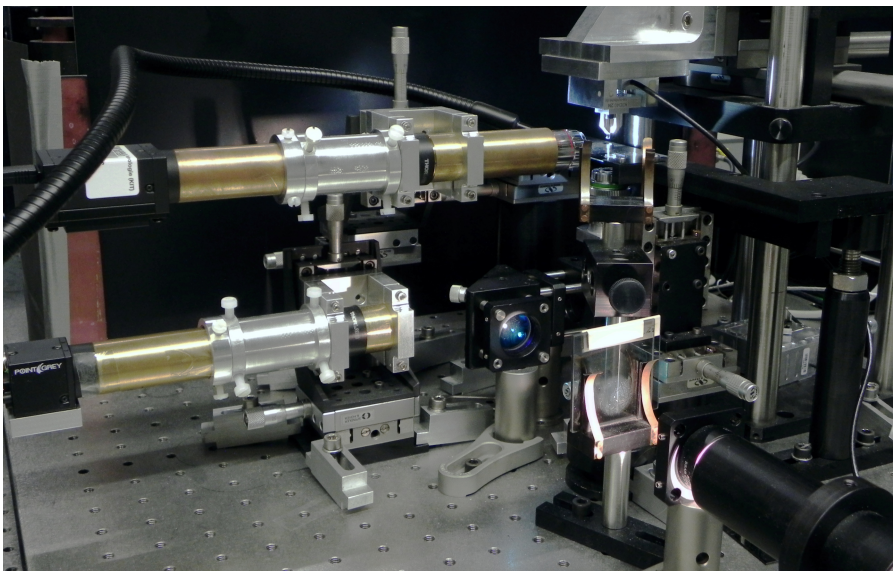

Figure 4.2: Photo of the self-made measurement setup. A detailed scheme is given in Figure 4.3. The major components are two microscopes, an automated stage with a force sensor attached, and the sample holder.

4.2 Measurement Setup

The sample design presented in the previous section and depicted in Figure 4.1(b) drastically simplifies the measurement setup, since sliding boundaries do not need to be realized. The remaining requirements are:

1) Prescribe a given displacement along one direction with micrometer precision.

2) Record the azimuthal displacements occurring in the middle of the sample with micrometer precision.

3) Record the forces to compute the effective Young's modulus of the material with micronewton precision.

The self-build setup depicted in Figure 4.2 fulfills exactly these demands. It consists of four major components: two optical microscopes capable of imaging the sample both from the bottom and from the side, a 3D automated stage, a sample holder that is fixed to the optical table, and a force sensor

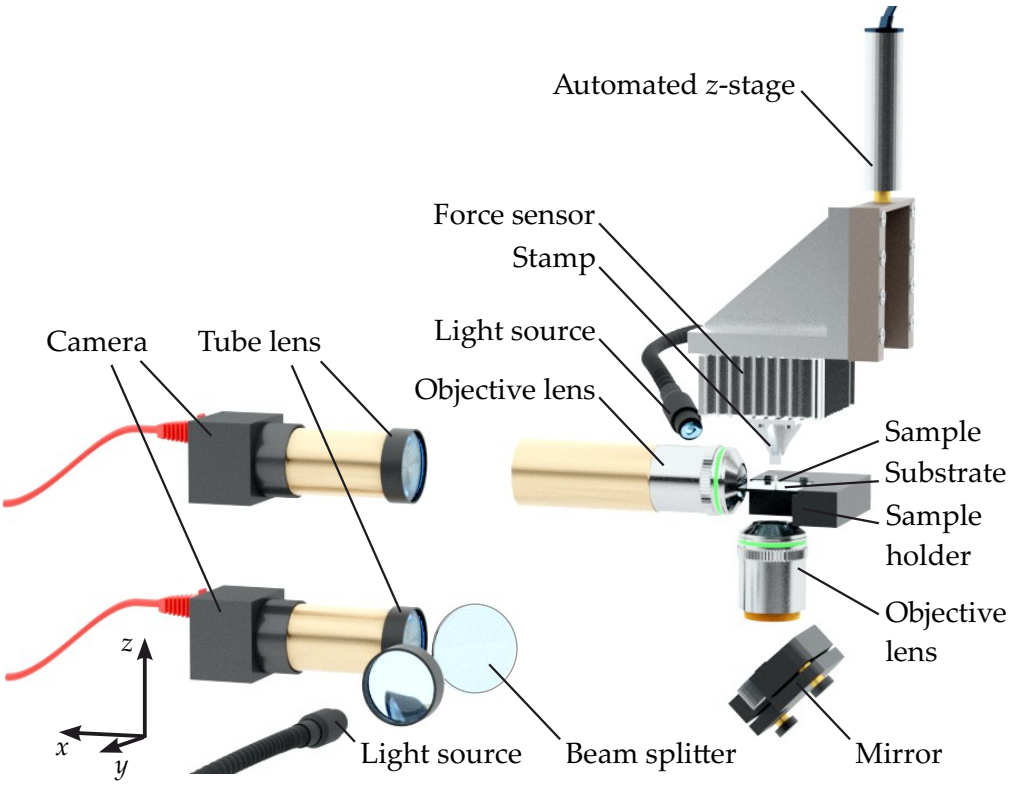

Figure 4.3: Scheme of the self-made measurement setup. Quasi-static displacements are prescribed using an automated z-stage, whilst measuring the axial forces. The deformation of the samples is monitored by two microscopes.

attached to the automated stage. A scheme of the setup highlighting these parts is given in Figure 4.3.

The setup's operation principle is as follows. A metamaterial sample is placed and tightly fixed on the sample holder directly underneath a stamp. This stamp prescribes a displacement normal to the sample's substrate by moving the motorized stages along the z-direction. The stamp itself is fixed to the force sensor to measure the force arising form the compression of the sample between the sample holder and translation stage. Both components, as well as the optical table and the force sensor, can be regarded as incompressible compared to the soft metamaterial samples.

The camera looking from the side is used to ensure proper initial contact between the sample and stamp and also for monitoring during the measurement. The second microscope looking from the bottom through the sample's substrate focuses onto the marker plate between the right- and left-handed

part of the metamaterial sample (also compare Figure 4.1). Thereby, the twist-to-push coupling can directly be observed in the camera images as a rotation of this plate. Using image cross-correlation, displacements of individual points in the focal plane are measured.

The recorded forces as function of the prescribed displacement, as well as the in plane displacements of the markers on the middle plate, are going to be the basis of all further data analysis.

Details on the individual components are given below. This setup was already used in [2, 118], and parts of it were used previously in [97, 100, 104, 119].

Translation Stages

Three motorized stages (Newport TRA-CC), mounted orthogonally with respect to each other, are used to move around freely in three dimensions. The lateral degrees of freedom are used to place the stamp above the sample. The bi-directional repeatability of the stages is specified by the manufacturer as $\Delta u = \pm 1.5\,\mu m$. The maximum stage velocities are $v_{max} = 0.4\,mm/s$. Every stage is addressed by a Newport SMC100CC motion controller. All positioning commands are generated using MATLAB and sent to the motion controller via a serial port.

Microscopes

Two simple microscopes were build, each consisting of a camera, an objective lens and a $f = 150\,mm$ tube lens. One of these microscopes monitors the sample from the side, the other one from the bottom through the glass substrate. To end up with a compact setup, the beam path of the second microscope includes a mirror tilted by 45°. Illumination both from an external light emitting diode and through the objective lens from the bottom are available. Therefore, a glass wedge is introduced to the beam path of the second microscope as a beam splitter.

The following cameras were used interchangeably: FLIR BFLY-PGE-50S5M-C, FLIR BFLY-PGE-50H5C-C, FLIR GS3-U3-41C6M, FLIR BFLY-PGE-31S4M-C. To record pictures of the measurement, all cameras were addressed using the software FlyCapture by FLIR Systems.

Depending on the required magnification, one of the following objective lenses was used: 2.5× NA = 0.075 Zeiss Epiplan-NEONFLUAR, 5× NA =

0.15 Zeiss EPIPlan, 5× NA = 0.13 Olympus MSPlan, 10× NA = 0.2 Zeiss EPIPlan, or 20× NA = 0.4 Zeiss LD Achroplan. These objective lenses have been chosen for their comparatively long working distances in air, which are needed due to geometrical limitations.

Force Sensor

Although the used sensor (10N K3D60, ME-Messsysteme) is capable of measuring three independent axes simultaneously, only the component normal to the sensor's surface is read out. The signal of the sensor is amplified (GSV-1A4 SubD37/2, Me-Messsysteme) and read out using a national instrument card at a frequency of $f = 0.3\,\mathrm{MHz}$. Electrical noise was significantly reduced by immediately averaging over 1000 measurements. In order to improve the sensitivity for the characterization of the metamaterials with tetragonal symmetry, the force sensor was replaced by a 2N K3D40 sensor (ME-Messsysteme).

4.3 Digital Image Cross-Correlation

The setup introduced in the previous section basically produces a video of the rotation of the middle plate, not only of the strained and unstrained position, but also of the loading and unloading process. Yet, to quantify the rotation angle, the displacements of the marker on this plate need to be extracted. For tracking such features, digital image cross-correlation has proven to be a useful tool in the past [120], especially in the context of metamaterial characterization [2, 76, 97, 118, 121, 122]. In the scope of this thesis, the freely available digital image cross-correlation library for MATLAB implemented by Eberl [123] was used.

4.3.1 Basic Principle

The image cross-correlation analysis generally compares a feature, or region of interest (ROI), in two different pictures $I_1(x, y)$ and $I_2(x, y)$. The coordinates are discretized, $x = n_x p$ and $y = n_y p$, due to pixelation, with pixel size p and the pixel number n_x and n_y. Usually, the ROI is only a small area compared to $I_1(x, y)$, reaching from x_1 to x_2 and from y_1 to y_2, and centered at (x_0, y_0). In a first step, the two-dimensional cross-correlation function is

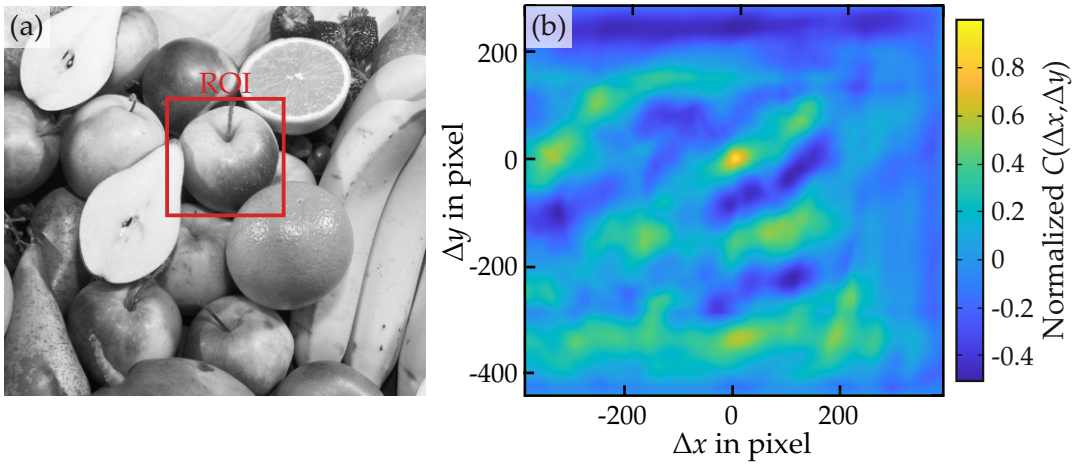

Figure 4.4: (a) Exemplary picture $I_1(x, y)$ with a region of interest (ROI) marked by a red box. Adapted from [124] (CC BY 3.0) (b) The calculated cross-correlation function $C(\Delta x, \Delta y)$ of the ROI with $I_1(x, y)$. $C(\Delta x, \Delta y)$ exhibits a clear maximum, where the ROI and $I_1(x, y)$ are similar, or in this case, equal.

calculated as

$$C(\Delta x, \Delta y) = \int_{x_1}^{x_2} \int_{y_1}^{y_2} I_1(x, y) I_2(x + \Delta x, y + \Delta y) \mathrm{d}x \mathrm{d}y. \tag{4.1}$$

$C(\Delta x, \Delta y)$ has a maximum, whenever the feature in I_2 at the position $(x_0 + \Delta x, y_0 + \Delta y)$ resembles the ROI. Figure 4.4 shows an example, where a ROI in $I_1(x, y)$ has been correlated with the picture $I_1(x, y)$ itself. Therefore, $C(\Delta x, \Delta y)$ exhibits a maximum at $\Delta x = \Delta y = 0$. Figure 4.4(b) exhibits additional local maxima. For sufficiently good image quality, as in the experiments presented later, selecting the global maximum of $C(\Delta x, \Delta y)$ is adequate as the position of the ROI. Yet, unfavorably chosen ROI with low contrast or pictures with identical features can lead to equally pronounced side peaks. Selecting the right maximum has to be done with caution then. In [125], some of these errors are illustrated nicely.

Obviously, when taking the maximum of $C(\Delta x, \Delta y)$ as the displacement of the ROI, Δx and Δy are always integer multiples of the pixel size. Especially, when the displacements are much smaller than the pixel size, the maximum will not change at all and will stay at $\Delta x = 0$, $\Delta y = 0$. To further increase the accuracy of the displacements towards subpixel precision $(\delta x, \delta y)$, a two-dimensional parabola is fitted to an area of 3×3 values of the correlation

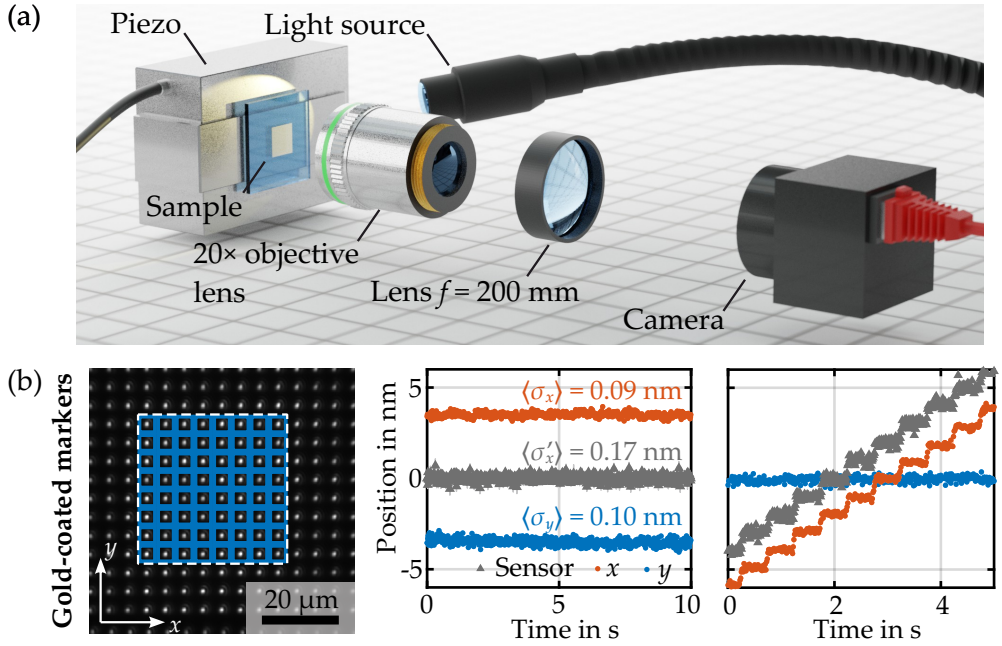

Figure 4.5: (a) Scheme of the setup for displacement measurements with subnanometer precision. (b) In the left panel, an exemplary measurement of a gold coated marker array is shown. The ROI are marked by blue boxes. In the middle panel, average localization errors as small as $\langle\sigma_x\rangle = 0.09\,\text{nm}$ were deduced in measurements (blue and red dots) with nominally zero prescribed displacement. Thereby, these results even surpass the accuracy of the internal capacitive sensor of the piezo stage (gray). In the right panel, prescribed steps of 1 nm can clearly be identified. Taken from [120] with permission.

function with the maximum at its center. The vertex of the parabola defines the displacement with subpixel precision $(\delta x, \delta y)$. Depending on the image quality, precisions down to 1/100 of a pixel can regularly be achieved for a single region of interest [120, 125].

4.3.2 *Subnanometer Precision from Digital Image Cross-Correlation*

Julian Köpfler and the author of this thesis showed in their paper [120], that by averaging over multiple regions of interest the mean localization error can get as small as $\langle\sigma_x\rangle = 0.09\,\text{nm}$. Of course this assumes that all ROI in a picture move in the same way. This is not true for the measurements conducted in the elastostatic part of this thesis, but will be exploited for the

elastodynamic measurements in the second part of this thesis.

In [120], the setup depicted in Figure 4.5(a) was used, which is comparable to the microscopes presented in section 4.2 and in the setup that will be introduced in section 9.2. Hence, the setups used in the scope of this thesis are expected to perform comparably.

To demonstrate the subnanometer localization capability, a piezoelectric stage prescribed both a constant displacement and a step functions with 1 nm step size as a function of time. The best case of a gold-coated marker array with 8×8 regions of interest is depicted in Figure 4.5. The step function can be clearly identified in the output of the image cross-correlations, meaning that subnanometer precision has been achieved, indeed.

4.4 3D Laser Printing

Most metamaterials, and the ones that are presented later on in particular, have very complex architectures, which makes them difficult and often even impossible to manufacture using conventional techniques. Therefore, it is not surprising that the development of new additive manufacturing techniques and the progress in the field of metamaterials are linked closely [15]. It is notoriously difficult to choose the fitting 3D printer from the wide range of techniques on the market. A brief introduction and comparisons between different techniques are given in [126, 127].

The defining challenge of the metamaterial samples presented here is the relatively large ratio between the smallest features inside a unit cell and the overall sample size. The smallest printable volume elements are called voxels, in analogy to pixels, the smallest building blocks of a picture. Having the large sample size to feature ratio requires that voxel need to be printed at a hight rate to end up with reasonable short fabrication times. [126, 127] suggest that there are only three viable option at the moment: continuous liquid interphase printing, inkjet 3D printing, and 3D laser printing. For the scope of this thesis, the latter was chosen. Originally developed in the nanophotonics community [128–130], this technique is now well established and has been studied in great detail already. It has enabled various material applications, ranging from 3D photonic crystals [128, 129], photonic metamaterials [4], and microscaffolds for cell examination [131, 132], just to mention a few.

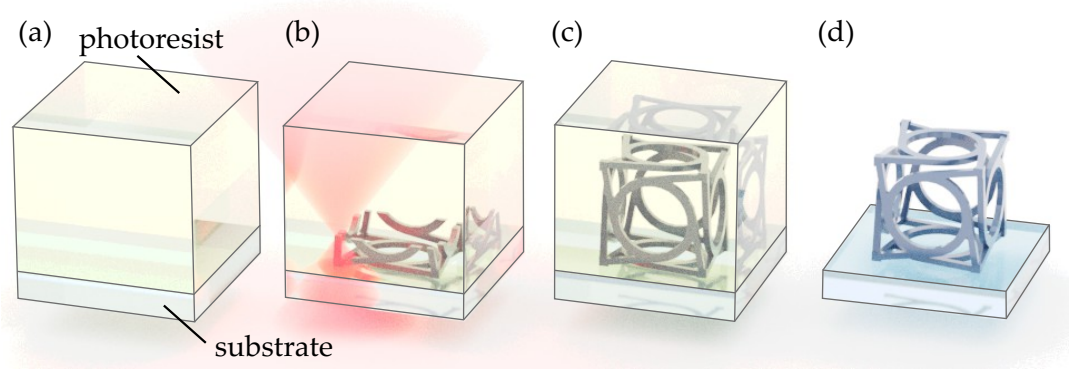

Figure 4.6: Illustration of a work flow typical for 3D direct laser printing: (a) substrate with photoresist, (b) writing process, (c) exposed structure, (d) structure after development. Adapted from [133].

4.4.1 Basic Principle

3D laser printing, 3D laser micro printing, two-photon printing, two-photon lithography, direct laser writing, and combinations of these terms are different names for essentially the same technique. It enables the printing of nearly arbitrary 3D polymer structures by scanning a focused laser through a liquid photoresist. Via two- or multi-photon absorption [134], a photochemical reaction is triggered in the focus of the laser, leading to the formation of a solid polymer network. After exposure, the remaining liquid photoresist is washed away using solvents. A typical work flow is depicted in Figure 4.6.

The laser focus is scanned along precomputed lines and thereby the entire volume of a desired 3D geometry gets exposed one line after the other. At first, this sequential approach sounds very slow. Yet, a laser beam can be moved very fast, especially compared to a clunky extrusion nozzle, making this printing technique one of fastest in terms of voxels per second, despite its serial character. In this work, the underlying geometry data for the printed structures was created using the computer-aided design (CAD) module of COMSOL Multiphysics, exported as an STL-file, and subsequently converted into machine code using the software Describe (Nanoscribe GmbH).

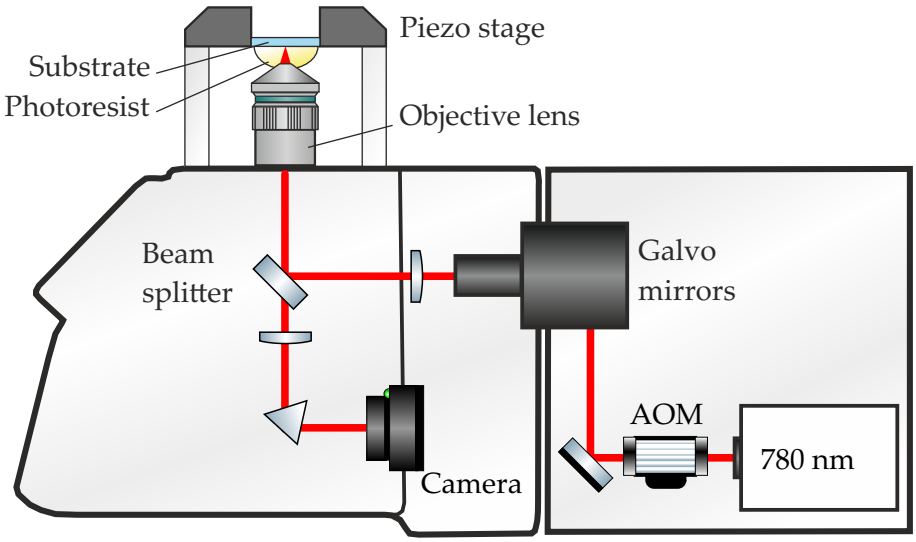

Figure 4.7: Scheme of the Nanoscribe system. Reproduced from [135]

4.4.2 *Nanoscribe Setup*

Most of the samples in the scope of this thesis have been fabricated using the commercially available system Photonic Professional GT (Nanoscribe GmbH), in combination with a $25 \times \mathrm{NA} = 0.8$ objective (LCI Plan-NEOFLUAR, Zeiss), and the commercially available photoresist IP-S (Nanoscribe GmbH). A schematic of this setup is depicted in Figure 4.7. The laser light is created by a frequency doubled erbium fiber laser (wavelength 780 nm) and its power is regulated by an acousto-optic modulator (AOM). During printing, the objective lens is dipped directly into the liquid photoresist. Thereby, the possible printing height is only limited by the range of the microscope z-drive. Due to the finite numerical aperture of the objective lens, the voxels are elongated along the z-axis. Typical dimensions of the voxel for this configuration are $0.5 - 1\,\mu\mathrm{m}$ laterally and $2 - 3\,\mu\mathrm{m}$ in height. When writing structures bigger than the field of view of the objective lens (approximately circular with a diameter of 400 µm), the substrate is shifted using a mechanical stage. A pair of galvo mirrors scans the laser beam with up to 0.2 m/s in the focal plane.

Substrate Preparation

Substrates with a thin layer of indium tin oxide on top are used to facilitate the alignment by increasing the index contrast between the photoresist and

the substrate. A silanization of the substrate's surfaces enables the formation of chemical bonds between the printed polymer [136]. Thereby, printed samples are fixed to the substrate and do not fall off easily. For the silanization, the properly cleaned glass substrate is treated with air plasma for $\sim$ 30 min, before being placed in a 1 mM solution of of 3-(trimethoxysilyl)propylmethacrylate in toluene for $\sim$ 60 min. Subsequently, the substrates are cleaned in deionized water and dried.

Sample Development

The residual liquid photoresist is washed out of the printed structure in a bath of mr-Dev 600 (Micro Resist Technology), where it rests for $\sim$ 10 min. Afterwards, the samples are immersed in acetone for $\sim$ 20 min. It is important to never let the samples fall dry, since capillary forces would destroy the fragile polymer structures. Therefore, in a final step, the samples are supercritically dried in CO_2 using the Leica EM CPD030 (Leica Microsystems).

4.4.3 Multifocus 3D Laser Printing Setup

Fabricating the largest samples characterized in this thesis was only possible using an even faster 3D printer. This was developed and build by Vincent Hahn over the course of his doctoral work. A scheme of the setup is shown in Figure 4.8. The operation principle of the setup is discussed in great detail in [118, 127]. Apart from the improved galvo mirrors and faster electronics, the key difference compared to the Nanoscribe system is a diffractive optical element (DOE), which splits the laser beam into nine equal subbeams. Thereby, nine foci are printing simultaneously. Obviously, these foci cannot be controlled individually, which is not a problem for periodic structures. All in all, these improvements led to a 30-fold increase in printing rate. For all samples produced with this setup, the commercial photoresist IP-dip (Nanoscribe GmbH) and a 40×, NA = 1.4 objective (Plan-Apochroma, Zeiss) was used.

Substrate Preparation

Printing large structures requires large volumes of photoresists. Since this setup does not offer a resist dispenser, all the resist must be present on the objective lens right from the start. Unfortunately, due to the geometry of the

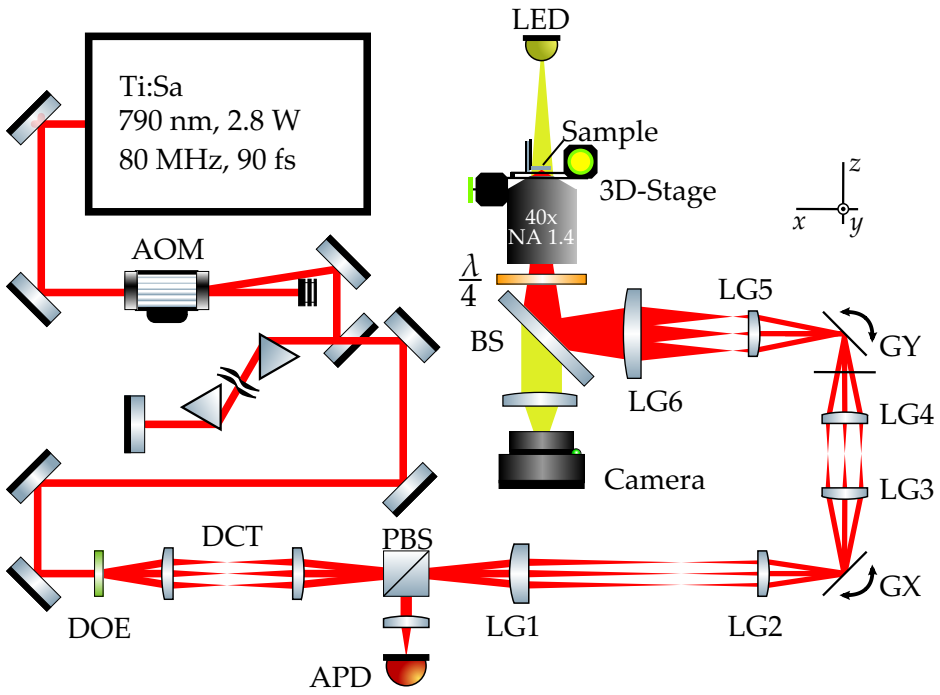

Figure 4.8: Scheme of the multifocus 3D laser printing system [127]. In contrast to the Nanoscribe system, a diffractive optical element (DOE) splits the laser beam into 9 equivalent foxi. These are scanned simultaneously using two galvo mirrors (GX and GY).

objective lens, the volume between the objective and the substrate is very narrow. Thus, samples were printed onto an additional glass pedestal. To ensure proper bonds between the pedestal and the polymer structure, the pedestal has been silanized.

Sample Development

In contrast to the samples printed with the Nanoscribe system, samples from the multifocus system were only treated in acetone for $\sim 20\,\text{min}$ and subsequently supercritically dried in CO_2 using a Leica EM CPD300 (Leica Microsystems).

Chapter 5

5 Push-to-Twist Coupling in Cubic Metamaterials

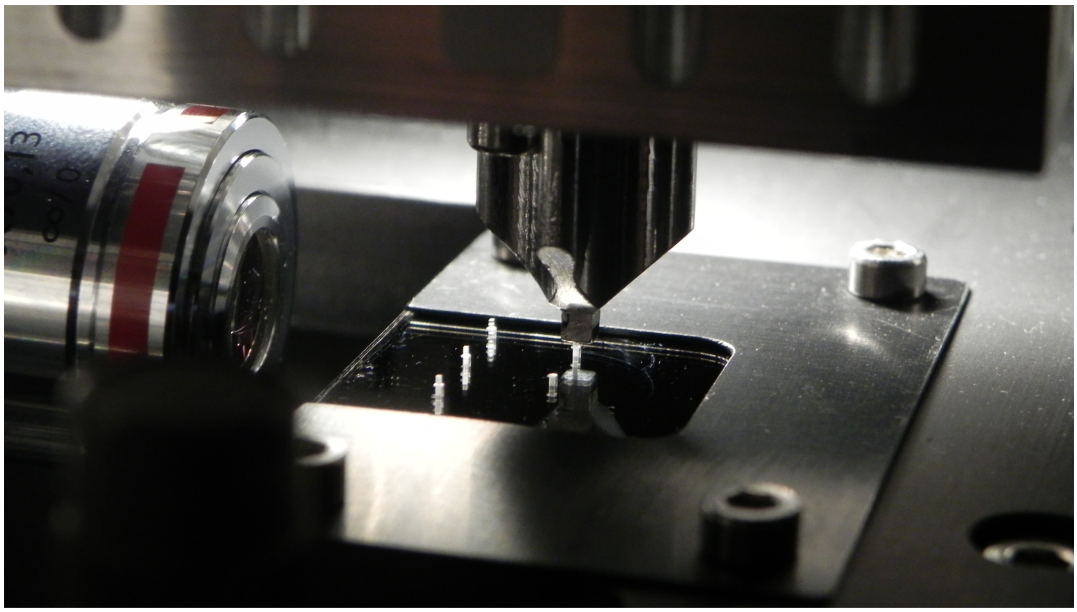

Photograph of the setup during measurement

In this chapter, the unit cell Muamer Kadic and I designed will be revealed and its basic working principle will be introduced. Furthermore, I will present my original numerical characterization and optimization of the chiral samples. Subsequently, the fabricated samples will be presented and fabricational challenges will be discussed briefly. Afterwards, these samples will be characterized and the rotation angle resulting from the push-to-twist coupling will be calculated. Finally, I will introduce a set of micropolar material parameters, which reproduces the metamaterial's properties nicely. The main findings of this chapter were published in [2].

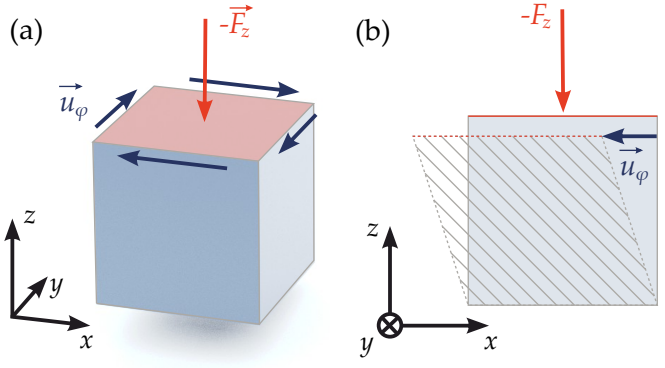

Figure 5.1: (a) Chiral cube subjected to an infinitesimal axial force. The resulting infinitesimal twist deformation is equivalent to a shear deformation of every side of the cube (b).

Although chirality leads to qualitatively new effects, like a push-to-twist coupling in bars (see section 2.3), the concept played little to no role for a long time. Mainly, since these new effects only arrise in the static regime, when sample dimensions are in the same order of magnitude as the characteristic length scales of the materials. For ordinary materials, these length scales are usually related to the size of the molecules, grains, pores, or other substructures of the materials. Hence, chiral effects tend to vanish for macroscopic samples (also see Table 2.1). Metamaterials, on the other hand, can extend the material properties far beyond the properties of its constituents. Therefore, the aim is to design metamaterials, which show pronounced push-to-twist coupling, preferably even for macroscopic sample sizes.

5.1 Mechanisms of Push-to-Twist Coupling in Metamaterials

In a straight forward design approach, unit cells, which individually twist upon pushing, are stacked up into a crystal. In that, the twist-to-push coupling hopefully persists in the crystal. Additionally, twists of the individual unit cells around their own center of mass should somehow add up to a macroscopic push-to-twist coupling of the sample. As will be shown later, the inter-unit-cell-coupling, when stacking up the crystal, is as important for the material properties of the metamaterial as the intra-unit-cell-coupling. For a moment, only the mechanisms in the unit cell shall be relevant.

To begin with, a mechanism building block shall be identified, which shows a push-to-twist coupling. In a second step, these building blocks

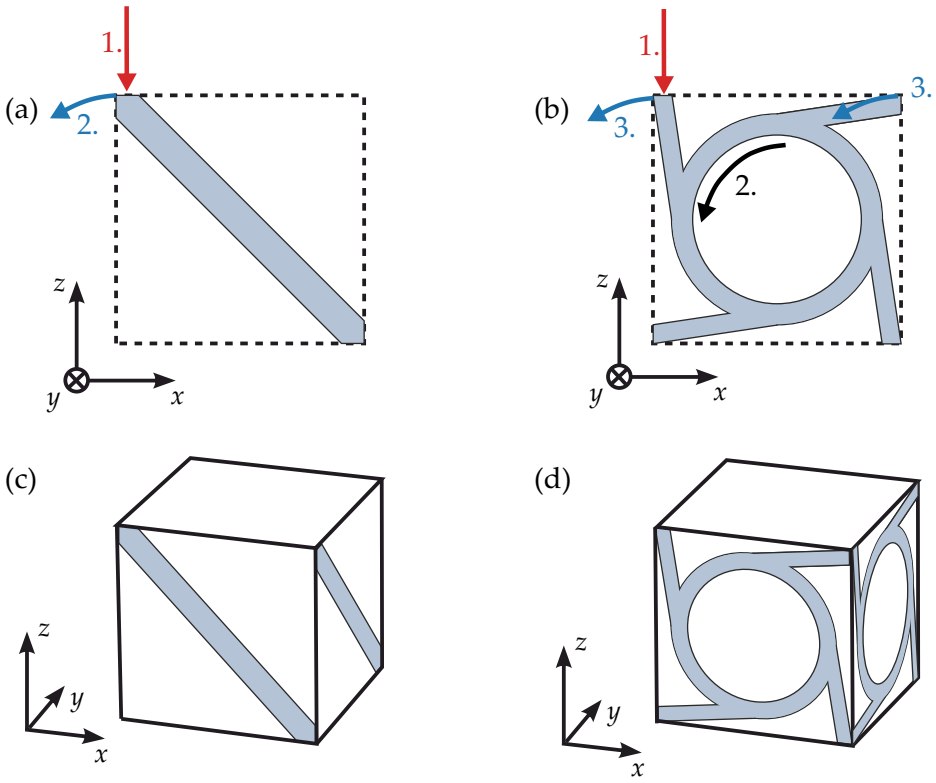

Figure 5.2: Exemplary 2D motives that shear along x upon pushing along z-axis with two-fold (a) and four-fold (b) rotational symmetry. These motives can be arranged into the building blocks (c) and (d), which exhibit the desired twist deformation upon axial deformation along the z-axis.

can be integrated into the unit cell design. Consider the block depicted in Figure 5.1, which is fixed at the bottom. This block shall serve as a black box, meaning it has some substructure that creates the wanted push-to-twist coupling and therefore twists infinitesimally (red arrow) upon an infinitesimal compression along the z-direction (blue arrow). When examining any side plane of this block individually, it becomes clear that the infinitesimal twist corresponds to an infinitesimal shearing of this plane (compare Figure 5.1(b)). The magnitude of the shear is equal for all side planes, but opposite planes move in opposite directions. Hence, the push-to-twist coupling in a 3D building block can be realized by finding a 2D motive that shears upon compression.

The most simplistic motive is filling the plane with a diagonal bar as

depicted in Figure 5.2(a). Upon pushing from the top (1), the bar will be bent (2) and thereby the effective plane will not only be compressed along z, but also sheared. The corresponding building block is depicted in Figure 5.2(b). Another possible motive, which is inspired by previous work on 2D chiral lattices [100, 137–139] is depicted in Figure 5.2(c) and (d). The mechanism at work is a bit more complex than the one of the first motive. Upon pushing from the top (1), the upright bar induces a rotation of the ring (2), which in turn pulls the horizontal bar inwards(3). Once again, the effective boundaries of the side plane are compressed along z and sheared. This motive has a higher symmetry (4-fold rotational symmetry) than the first motive (2-fold rotational symmetry), which will facilitate the construction of a highly symmetric unit cell in the next section. This motive can be called chiral in 2D, since by only using in-plane rotations, the mirror image cannot be superimposed on the original motive. Obviously, there is an infinite number of possible motives that would have the desired push-to-shear coupling. Also, there are other principles to create building blocks with a push-to-twist coupling. Here, only those used later in this thesis are presented.

5.2 Blueprints of Cubic Chiral Metamaterials

In a next step, the building blocks of the previous section will be spatially arranged in crystal unit cells. In this chapter, the aim is to design a metamaterial that behaves similar along any of the three principle directions x, y, and z. Therefore, cubic unit cells are implemented. Ideally, the properties of the metamaterial would be isotropic, meaning that independent of the direction of compression, a twist would occur in the plane perpendicular to the compression. Yet, achieving isotropic properties with a crystalline structure is considerably difficult in elasticity. This is due to the fact that the highest crystalline symmetry (cubic symmetry) has more independent material parameters than the isotropic case (also see section 2.2 and section 2.3). Therefore, crystalline structures are only isotropic, if an accidental degeneration of the tensor elements can be achieved. This is in great contrast to the electrodynamic case, where the electric permittivity and the magnetic susceptibility tensor of an isotropic and a cubic material are formally equal [140].

A simple cubic unit cell can easily be realized using the building block of

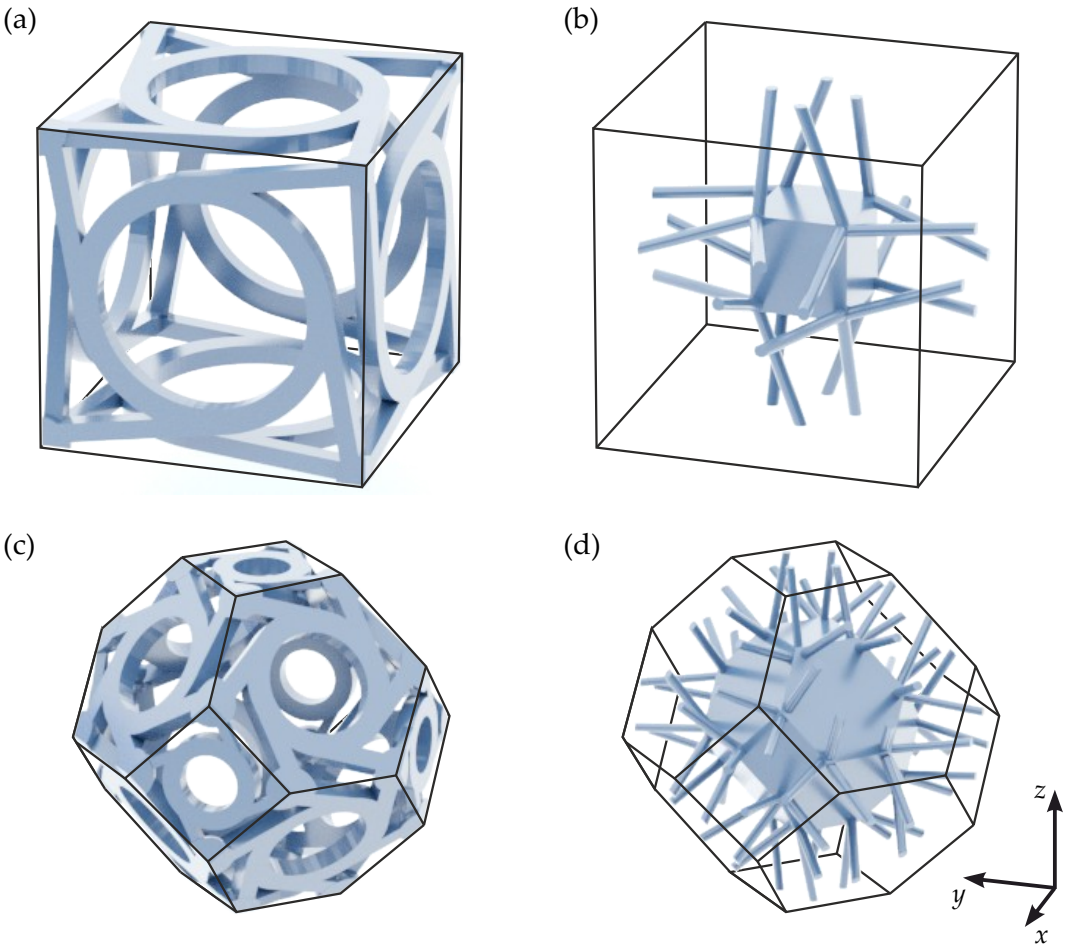

Figure 5.3: Gallery of 3D cubic unit cells, which were constructed on the basis of the building blocks depicted in Figure 5.2. (a) and (b) are simple cubic unit cells. (c) and (d) are body centered cubic unit cells. This figure is adapted from [2].

Figure 5.2(d) by adding two additional motives of correct handedness at the top and bottom of the cube, as depicted in Figure 5.3(a). This unit cell was brought forward in [2]. Yet, exploiting these construction principles, even more complex unit cell symmetries can be achieved. An example of a body-centered cubic unit cell is depicted in Figure 5.3(c). There, chiral motives with four- or six-fold rotational symmetry were added to the boundary planes of the Wigner-Seitz cell.

Due to the lack of symmetry, creating a simple cubic unit cell from the building block depicted in Figure 5.2(c) is more challenging. Nevertheless,

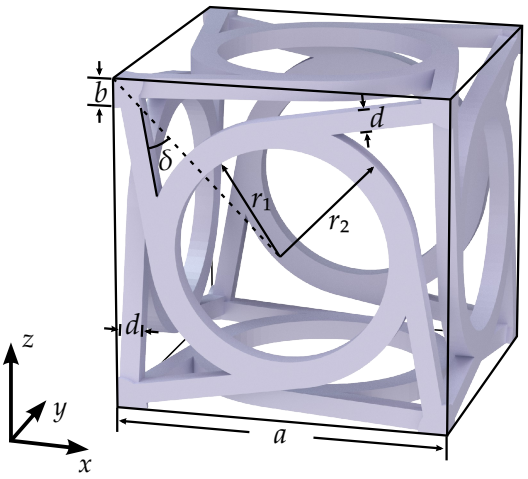

Figure 5.4: Blueprint of the studied simple cubic unit cell with lattice constant a. The parameters were optimized to yield high twist angles per axial strain, whilst taking fabricational restrictions into account. For the experiments, the following set of parameters was used: $d = 0.06a$, $r_2 = 0.4a$, $\delta = \delta_{\max} \approx 35°$, $b = \sqrt{2}d$, and $r_1 = 0.32a$. Crucially, when setting $\delta = 0$, an achiral unit cell showing no push-to-twist coupling is recovered. This figure is adapted from [2].

it can be done by placing a cube in the middle of the unit cell and adding the building block on each side of the cube. This unit cell depicted in Figure 5.3(b) was brought forward by Lakes [141, 142]. Again, other unit cell symmetries can be achieved by placing a shrinked version of the Wigner-Seitz cell in the middle of the unit cell and adding the building blocks with the correct rotational symmetry to each of the faces as depicted in Figure 5.3(d).

The unit cell depicted in Figure 5.3(a) was chosen for further characterization. Its crucial advantage is that the simple cubic unit cells generally exhibited the largest rotation angles in preliminary numerical studies (not depicted). Furthermore, first numerical studies suggested a slightly bigger characteristic length scale of the unit cell depicted in (a), compared to the unit cell (b). Still, the latter yielded generally larger rotation. Most importantly, unit cell (a) is the easiest to fabricate and resulted in more stable samples, since it does not rely on a large number of slender bars.

5.3 Numerical Characterization of Chiral Cubic Metamaterials

In this section, the metamaterial is optimized to show a maximum twist angle per percent strain and subsequently characterized numerically. Therefore, finite element calculations were performed using the commercial software COMSOL Multiphysics. For all simulations in this section, the metamaterial's constituent material was modeled as a Cauchy material, as introduced in section 2.2 and section 3.2. Unless explicitly stated otherwise, the kinemat-

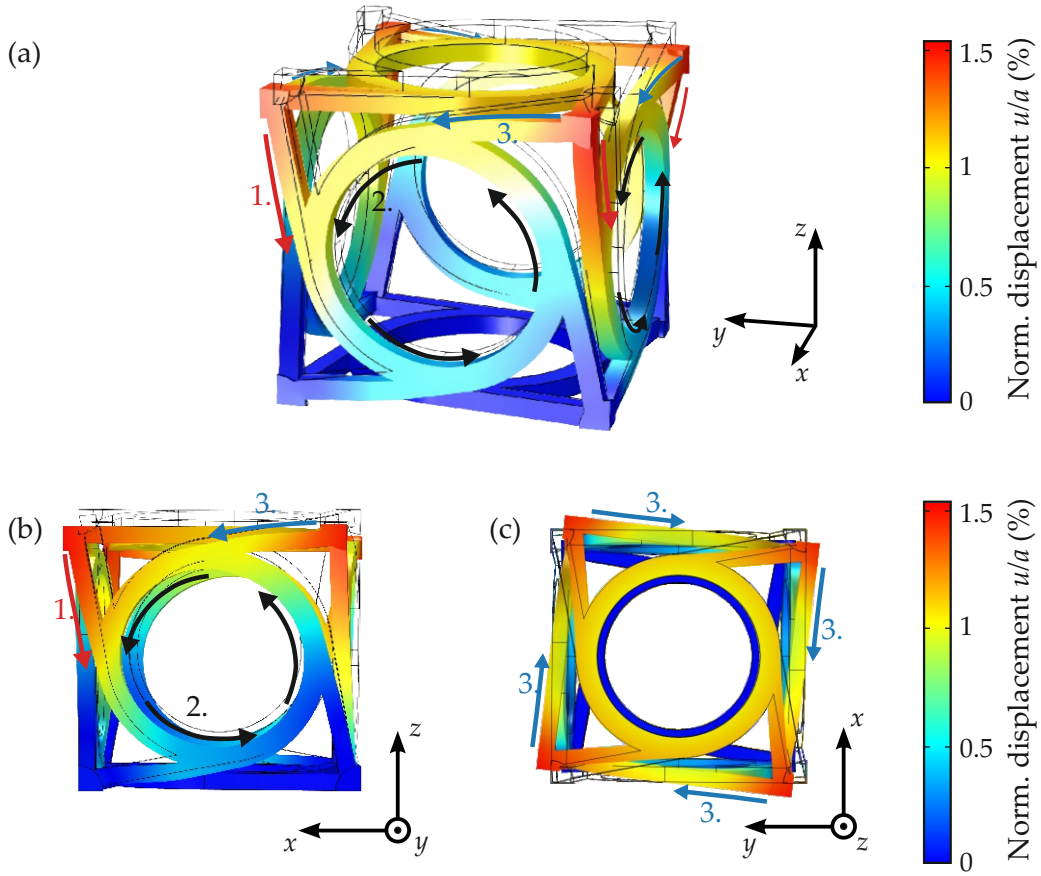

Figure 5.5: Calculated deformation of a single unit cell under an oblique view (a), and viewing along the (b) y- and (c) z-direction. The intended mechanism as already introduced in Figure 5.2 can be observed clearly: the vertical bar (1) induces a rotation of the ring (2), which in turn pulls in the corner connected to the horizontal bar (3). This figure is adapted from [2].

ically linearized equations were used, meaning, geometrical nonlinearities were neglected.

5.3.1 *Basic Mechanism*

Using the construction principles of the previous sections, the unit cell depicted in Figure 5.4 was derived. In a first step, the functional principle predicted in the previous sections shall be verified. For this purpose, a single unit cell was implemented with fixed boundaries at the bottom of the unit

cell ($\vec{u} = 0$). A displacement u_z along the z-direction was prescribed to the top surface of the unit cell, whereas the remaining boundaries were left open. The result is depicted in Figure 5.5. It proves nicely that the unit cells shows the desired push-to-twist coupling. Especially the intended mechanism, with the vertical bar (1) inducing a rotation of the ring (2), which in turn pulls the corner connected to the horizontal bar inwards (3), is functioning as planned.

5.3.2 *Maximization of the Twist Angle per Axial Strain*

In the second step, the geometrical parameters d, δ, and r_2 were varied individually in order to find a parameter set that yields the largest rotation angle φ per axial strain ε_{zz}. In other words, the contribution of the chiral micropolar effect should be maximized. This was done on structures containing $1 \times 1 \times 2$ unit cells. The structure was fixed at the bottom ($\vec{u} = 0$) and a plate out of the same constituent material as the unit cell was added at the top. A displacement u_z was prescribed along the z-direction to the top surface of that plate. A comparable sample is depicted later in Figure 5.7(a). This sample geometry was chosen to mimic the experimental boundaries that are going to be introduced in more detail in section 5.4 (also see section 4.1 and subsection 5.3.3).

Since the top plate is stiff compared to the filigree unit cell underneath, it stays essentially undeformed. Hence, the average rotation angle of the plate is equal to the rotation angle at any position of the plate. At the same time, the plate averages over the different local rotations that might occur in the structure below. Therefore, by probing the displacement vector of one of the corners of the top plate, the average twist angle φ per axial strain $\varepsilon_{zz} = u_z/H$ of the metamaterial can be calculated by

$$\frac{\varphi}{\varepsilon_{zz}} = \operatorname{asin}\left(u_x \sin\left(\operatorname{atan}\left(\frac{y}{x}\right)\right) - u_y \cos\left(\operatorname{atan}\left(\frac{y}{x}\right)\right)\right) \frac{180^\circ}{\pi} \frac{H}{u_z}. \tag{5.1}$$

First, the twist angle φ per axial strain ε_{zz} was calculated as a function of the angle δ. As can be seen in Figure 5.6(b), φ/ε_{zz} increases monotonously, meaning that the unit cell becomes more chiral with increasing δ. Due to geometrical restrictions, δ has an upper bound given by

$$\delta_{\max} = \operatorname{asin}\left(\frac{\sqrt{2}\,(r_2 - d/2))}{a - b}\right). \tag{5.2}$$

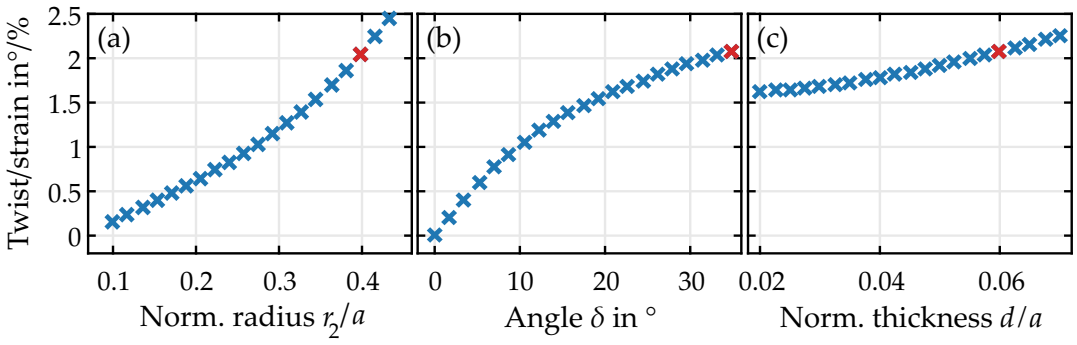

Figure 5.6: Calculated twist per axial strain of samples containing $1 \times 1 \times 2$ unit cells as a function of (a) the radius r_2, (b) the angle δ, and (c) the bar thickness d. The geometrical parameters are defined in Figure 5.4. This figure is adapted from [2].

Notably, the structure does not twist at all for $\delta = 0$. In this case, a centrosymmetric, hence achiral unit cell is recovered. Therefore, all entries of the elasticity tensor $\mathbf{B}$ are zero and in accordance with the findings of Gauthier [54] and Lakes [33] no deviation from the classical Cauchy behavior is expected. Hence, the twist has to vanish. The unit cell with $\delta = 0$ will serve as the achiral reference structure in the following.

At the same time, φ/ε_{zz} increases monotonously both as a function of d and r_2, for the parameter range depicted in Figure 5.6(a) and (c). For these simulations, r_1 was not kept constant, but rather $r_2 - r_1 = \text{const.} \approx 0.08a$. Both b and r_1 show no significant influence on the twist per strain, when varied within reasonable bounds (not depicted).

As a result, maximizing r_2, δ, and d yields the highest rotations angles per axial strain. On the other hand, geometrical restrictions prevent arbitrarily high values for either of these parameters. At some point, parts of the unit cell begin to overlap or get in contact during compression and thereby, make the desired mechanism obsolete. Furthermore, extremely narrow gaps between seperated parts, like the gap between neighboring rings in a unit cell, cannot be fabricated. The so called proximity effect [126, 143] would connect these rings during the 3D printing process, which would also alter the functionality of the unit cell. In an effort to balance between the desirably large twist angles and experimental feasibility, the parameters marked in red in Figure 5.6 were selected for further characterization. These are: $d = 0.06a$, $r_2 = 0.4a$, $\delta = \delta_{\max} \approx 35°$, as well as $b = \sqrt{2}d$, and $r_1 = 0.32a$.

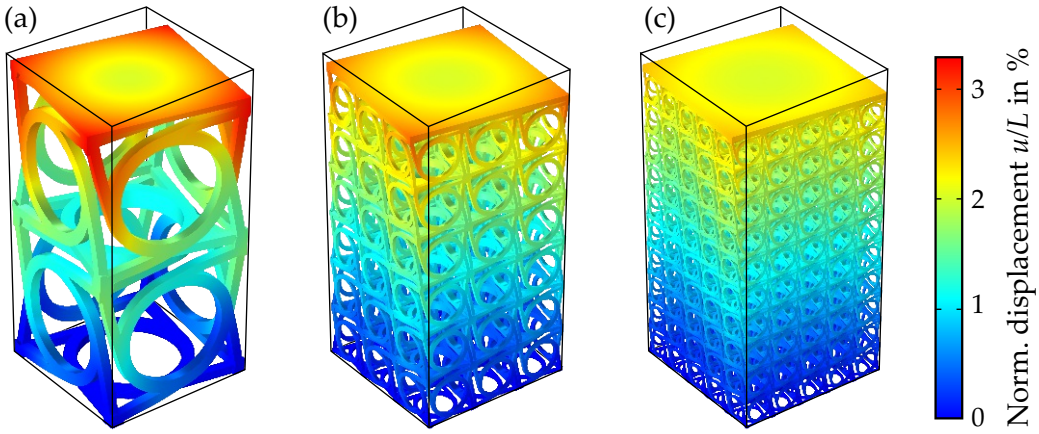

Figure 5.7: Gallery of calculated displacements for structures with scaling factors of (a) $N = 1$, (b) $N = 3$, and (c) $N = 5$. The samples contain a total of $N \times N \times 2N$ unit cells. Each sample was fixed at the bottom and subjected to a prescribed displacement corresponding to $\varepsilon_{zz} = -1\%$ at the top plate. For clarity, the deformations are enhanced by a factor of 5.

5.3.3 *Twist per Strain of the Metamaterial Samples*

It has been shown in section 2.3 and [33] that cylindrical bars from a chiral constituent material twist upon axial compression. Furthermore, this twist angle does not only depend on the sample's aspect ratio, but also on the ratio between the characteristic length scale l_t and the bar's radius R. Hence, examining the twist per axial strain as a function of R/l_t, whilst keeping the sample's aspect ratio constant, is the crucial study to extract estimates for the characteristic length. For crystal structures, the characteristic length scale is necessarily proportional to the lattice constant a. Meaning, that by simply doubling the size of the unit cell and hence doubling a, the characteristic length scales will also double. In this context, changing the ratio R/l_t is equivalent to changing the ratio R/a between the cylinder radius and the lattice constant.

Due to the cubic symmetry of the unit cell, samples with circular footprints cannot be realized easily. Instead, square footprint and outer sample dimensions of $L \times L \times H$ were used, with the side length L and sample height H. Yet, the reasoning above can be transferred, yielding that the twist per strain has to be studied as a function of the ratio between sample side length L and lattice constant a. In the following, this ratio is referred to as

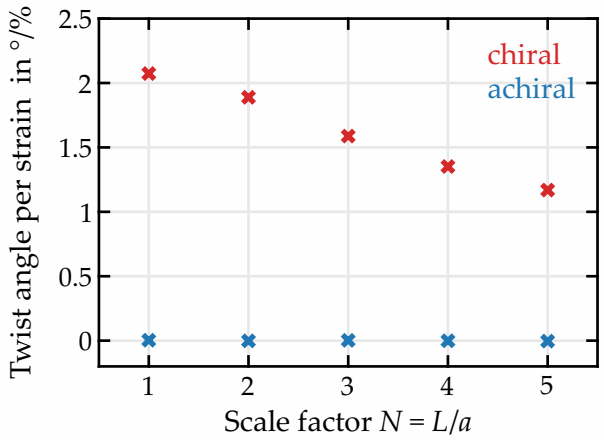

Figure 5.8: Calculated twist angles per axial strain for different scale factors N, both for chiral and achiral ($\delta = 0$) samples. Clearly, the chiral samples twist, whereas no twist could be observed for the achiral structures within the margins of numerical precision. This figure is adapted from [2].

the scale factor $N = L/a$. For crystalline structures, N is an integer.

There are two equivalent ways of conducting this study. Either by keeping the lattice constant a constant and changing the sample's side length L, or by keeping L constant, whilst adjusting a. For the calculations performed here, the latter option was chosen. Thereby, special care has to be taken concerning the size of the mesh elements. When scaling the unit cell, the discretization of the individual unit cells should not change. Yet, both approaches, scaling the lattice constant and the sample size, yield identical results and will be used at some point in the following.

As in the experiments, samples containing $N_x \times N_y \times N_z = N \times N \times 2N$ unit cells have been implemented, with $N = 1, 2, 3, 4, 5$. Therefore, the absolute metamaterial size is given by $L_x \times L_y \times H = Na \times Na \times 2Na$. Samples with $N > 5$ are out of reach, due to the high memory consumption of the finite element method. For the calculations, each sample was fixed ($\vec{u} = 0$) at the bottom and a plate with outer dimensions $Na \times Na \times 0.17H$ was added to the top of the metamaterial. At the top of this plate, a displacement $u_z = -0.01H$ was prescribed along the z-direction, leading to a compressional strain of $\varepsilon_{zz} = u_z/H = -1\%$. Exemplary raw data for $N = 1, 3, 5$ are depicted in Figure 5.7(a)-(c). The magnitude of the displacement vector is plotted in false colors and for better visibility, the deformations are enhanced by a factor of 5.

Figure 5.7(a)-(c) clearly shows that all structures exhibit a pronounced twist. The rotation angle φ of the metamaterial sample is calculated, as introduced in subsection 5.3.2, from the displacement components of a corners of the top plate according to Equation 5.1. The resulting twist angle

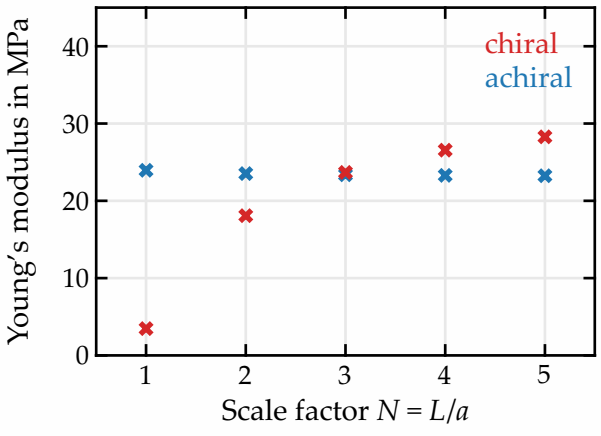

Figure 5.9: Calculated effective Young's moduli of the metamaterial samples for different scale factors N, both for chiral and achiral ($\delta = 0$) samples. For the chiral samples the Young's modulus depends on the scale factor N, whereas a constant Young's modulus is observed for the achiral structures. This figure is adapted from [2].

per axial strain φ/ε_{zz} is plotted as a function of N in Figure 5.8, both for the chiral structures and the achiral control structure.

Clearly, only the chiral structures exhibit a twist, whereas all achiral structures show zero twist within the margins of numerical precision. For $N = 1$, a maximum twist angle of $\varphi/\varepsilon_{zz} = 2.1°/\%$ was found. It then decreases monotonously as a function of N. Interestingly, when going from $N = 1$ to $N = 5$, the twist merely decreases by less than a factor of 2. Hence, it can already be concluded that the characteristic scale factor $N_c = l_t/a$ is in the same order or magnitude as the scaling factors investigated. Since for $N \gg N_c$, a faster decay $\propto 1/N$ is expected (see section 2.3 and [33]).

5.3.4 *Effective Young's Modulus*

The effective Young's modulus was probed numerically by applying the same boundary conditions as above. Yet, instead of a displacement, a boundary force of $-F_z$ was prescribed along the z-direction to the top plate. The resulting displacement u_z of the top plate was probed at a corner of the plate. Using this, the effective Young's modulus is calculated using

$$E = \frac{F_z H}{L^2 u_z}. \tag{5.3}$$

The calculated effective Young's moduli are plotted in Figure 5.9. The effective Young's moduli also show a pronounced N-dependency. It increases monotonously by approximately a factor of 6 from $N = 1$ to $N = 5$ and

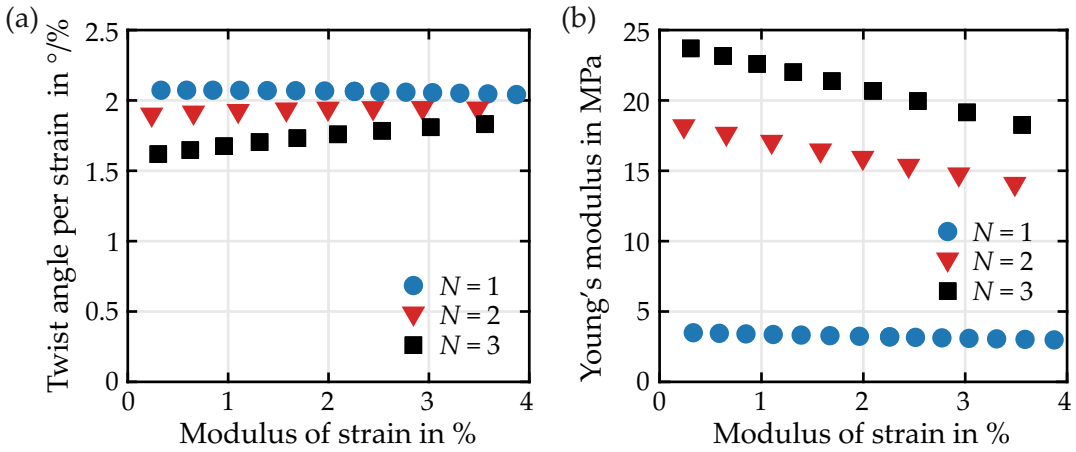

Figure 5.10: Calculated twist angles per axial strain (a) and effective Young's modulus (b) as a function of the axial strain ε_{zz}. In contrast to the previous calculations, geometrical nonlinearities were taken into account. This figure is adapted from [2].

seems to converge towards an upper bound. Yet, larger values of N need to be calculated to draw any definite conclusion on its numerical value.

5.3.5 *Geometrical Nonlinearities*

The micropolar theory predicts a linear relation between the twist angle φ and the axial strain ε_{zz}. To check the range of validity of this linear assumption, the simulations above were repeated, but this time, geometrical nonlinearities where taken into account. The boundary conditions were equivalent to the ones in subsection 5.3.4. Additionally, the boundary force was varied to achieve axial strains between 0 and -4%. Due to the increased memory consumption of the nonlinear approach, only structures with $N = 1, 2, 3$ were calculated. The results of these nonlinear calculations are depicted in Figure 5.10. They predict only little influence of the strain for the case of $N = 1$, both for the twist per strain as for the effective Young's modulus. Yet, with increasing N the nonlinearity increases as well. For $N = 3$ the twist increases by approximately 12% for the depicted strain values. The effect on the effective Young's modulus is even larger. A decrease by more than 23% can be observed.

5.4 Experiments on Chiral Cubic Metamaterials

In this section, the fabricated samples and the results from the experimental characterization are presented. At first, the challenges of the sample fabrication and strategies to solve these are presented. Afterwards, mathematical details of the data evaluation are given. Finally, the measured sample twists and Young's moduli are shown and compared to the numerical predictions of the previous section.

5.4.1 Printing Strategy

Although 3D printing is often sold as a quick and easy manufacturing technique, producing the desired structure accurately can cause major problems. For example, many techniques have difficulties printing overhanging parts. Often, special scaffoldings are added, which need to be removed later in the development step. Using 3D laser printing, such scaffolds can often be avoided by developing a dedicated printing sequence. Another challenge is the asymmetry and finite size of the voxel, the smallest printable volume element. For all samples produced in this chapter, the Nanoscribe system was used. All numerical values given here are specifically adjusted to the used instrumentation.

Voxel Correction

Before printing, the 3D geometry is split into lines, along which the laser focus is scanned. In a very simplified picture, the 3D printer lines up voxels along these paths. Yet, in case of 3D laser printing, these voxels are asymmetric. For the components used here, the voxel's height can range from $2-3\,\mu m$, and its width from $0.5-1\,\mu m$. This finite size and asymmetry distorts the printed structure decisively, especially when the geometry's features and the voxel size are comparable. This is illustrated in Figure 5.11(a) and (b). The finite voxel size can be accounted for by adjusting the geometrical parameters of the input geometry, as depicted in Figure 5.11(c) and (d). Unfortunately, there is no straight forward correction procedure. Instead, this needs to be done for each set of printing parameters, each geometry, and each structure size individually in a trial and error procedure. A complete list of the geometry corrections which compensate the voxel size is given in subsection A.1.1.

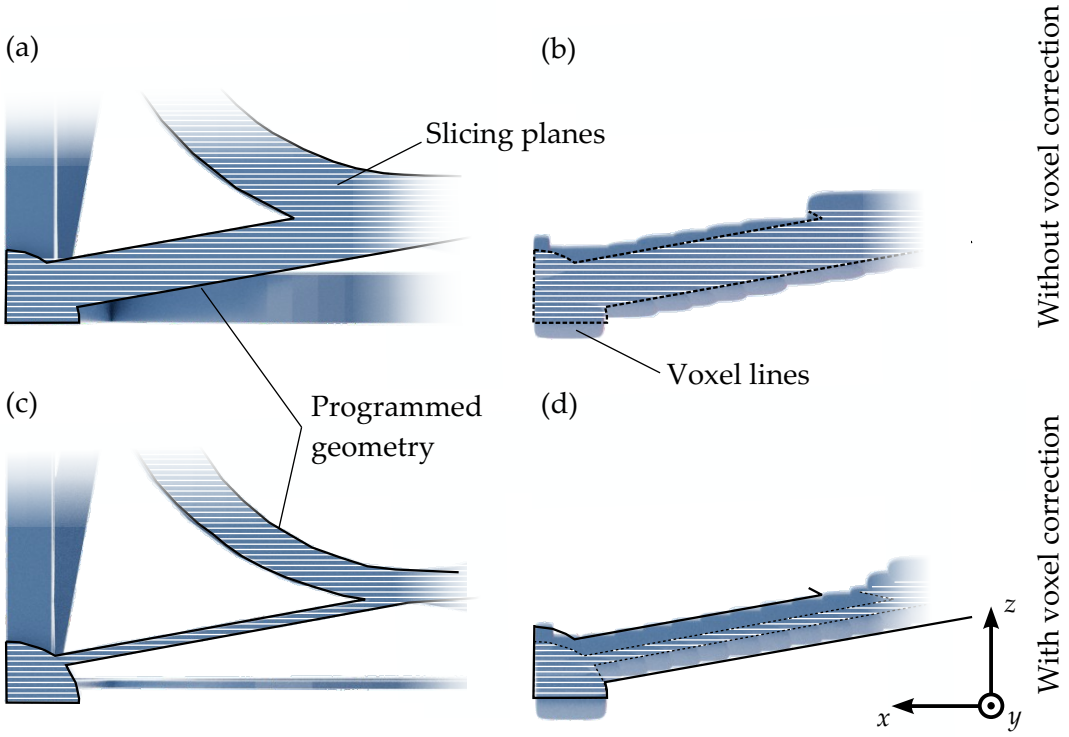

Figure 5.11: (a) Cut through the unit cell along the x-y-plane. The white lines represent the laser trajectories when slicing the intended geometry. (b) Voxels of finite size have been placed along the laser trajectories. Obviously, the resulting structure is much larger than the intended structure (black dashed line). (c) Programmed structures accounting for the finite size of the voxel and the deduced laser trajectories. (d) The voxel lines along the shortened trajectories reproduce the desired geometry (black line) more accurately compared to (b). This scheme roughly resembles the case of $N = 5$ with lattice constant $a = 100\,\mu\text{m}$ (compare Figure 5.13).

Splitting into Multiple Printing Fields

Due to the finite field of view of the objective lens, structures can only be printed simultaneously in an area with a diameter of 400 µm. This is less than the intended sample footprint of about 500 µm × 500 µm. In order to still be able to print the whole sample, it was split in smaller blocks, which were printed sequentially. The sizes of these blocks were adapted according to the unit cell size.

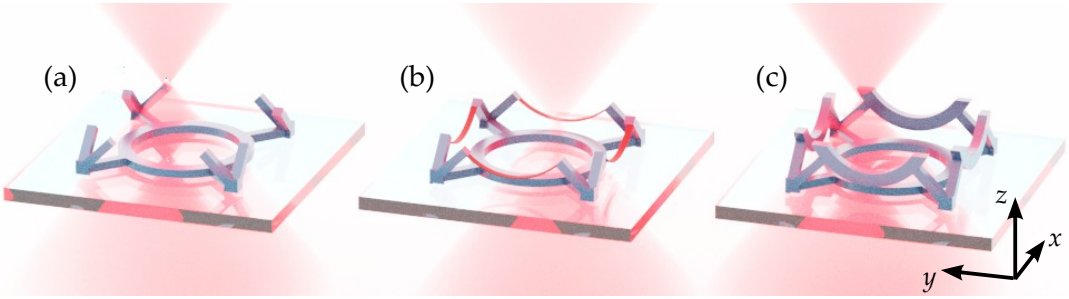

Figure 5.12: Printing strategy to avoid flying objects. (a) First, the outer bars of the unit cells are printed along the $+z$-direction. The rings are intentionally left out. (b) A slender support structure (red) is printed starting from the previously written structure along the $-z$-direction. (c) Subsequently, the rings are printed along $+z$-direction in contact to the support structure. Therefore, the rings are immediately connected to the substrate and do not float away.

Avoiding Flying Objects

Overhanging and flying objects are notoriously difficult to print. The term flying object usually refers to parts of the geometry that are not connected to the substrate or any previously printed parts. Since these flying objects float in the liquid photoresist, any small flow inside the resist will make them float away. This is particularly problematic for the achiral control structures. There, the bottom of the rings is initially not connected to any previously written structure, when building up the structure in planes along the z-direction. This was avoided by first writing only the bars that connect the ring to the corners of the unit cell. Subsequently, a slender support structure was printed from top to bottom, i.e. the printing direction was inverted. This support, which is essentially the bottom edge of the ring, is sufficient to hold the rest of the ring that is printed in a third step at its desired position. This time again using the normal printing direction. The whole procedure is sketched in Figure 5.12.

5.4.2 *Fabricated Samples*

As has been pointed out before, probing the characteristic length scale of the metamaterial can either be done by keeping the lattice constant a fixed and changing the sample's side length L, or vice versa. As for the numerical studies, the latter was also chosen for the experimental characterization.

In doing so, the same optical setup can be used for the measurement of samples having different scale factors N. At the same time, forces due to the compression of the samples are increased for small scale factors N, hence become easier to measure. In general, by using this approach, possible systematic errors of the measurement setup do not depend as much on N, since the prescribed displacements u are equal and the measured forces are comparable for all samples.

Figure 5.13 gives an overview over the fabricated samples. As elaborated in section 4.1, a right- and a left-handed metamaterial bar was printed on top of each other with plates added at the bottom, middle, and top of the sample. Markers that facilitate the image-cross-correlation are printed onto the overhanging part of the middle plate. In order to achieve reasonably short fabrication times, a side length of $L = 500\,\mu m$ was chosen. Samples with scale factors reaching from $N = 1$ to $N = 5$ were realized, containing up to 500 unit cells in total. Higher scale factors were out of reach, due to excessively long printing times of these structures and the limited resolution of the used setup.

As mentioned before, scaling the unit cell size reduces sources of systematical errors of the measurement setup. On the downside, scaling the unit cell size makes the fabrication of the samples even more challenging. Merely the size of the unit cell should be changed by up to factor of 5, yet the geometrical proportions with respect to a must stay equal. Extensive experimental optimization was needed to find suitable voxel corrections. Close ups of single unit cells for different scale factors N are depicted in Figure 5.14. It proves that the scaling was done with remarkable accuracy.

5.4.3 *Extracting Rotation Angles from the Digital Image Cross-Correlation*

For the experiments, the samples were compressed axially using the setup introduced in section 4.2, whilst being monitored with two cameras. One camera was focused to the side of the sample, the other observed the marker plate in the middle from the bottom. Videos were recorded during the compression. Using the image-cross-correlation method introduced in section 4.3, the position $\vec{x}_i(t)$ of the i-th marker on the middle plate was calculated as a function of time t. By subtracting the initial position $\vec{x_i}(t_0 = 0)$, the

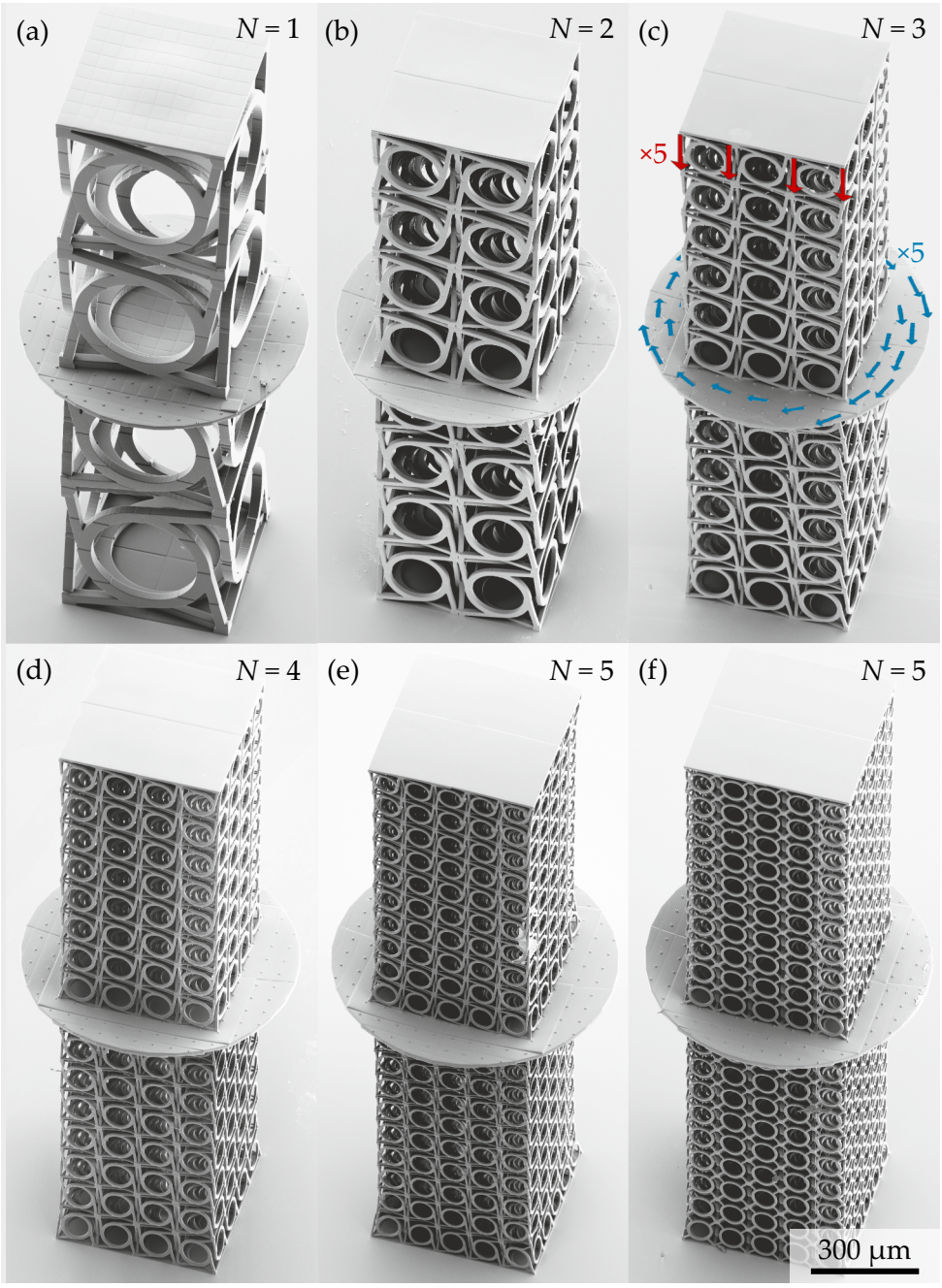

Figure 5.13: Scanning electron micrographs of 3D printed samples using the Nanoscribe instrumentation. (a)-(e) are chiral structures with scale factors of $N = 1, 2, 3, 4, 5$. (f) is an achiral control structure with $N = 5$. Additionally, raw measurement data are plotted in (c). For clarity, the displacements are enhanced by a factor of 5 compared to the image scale bar. This figure is adapted from [2].

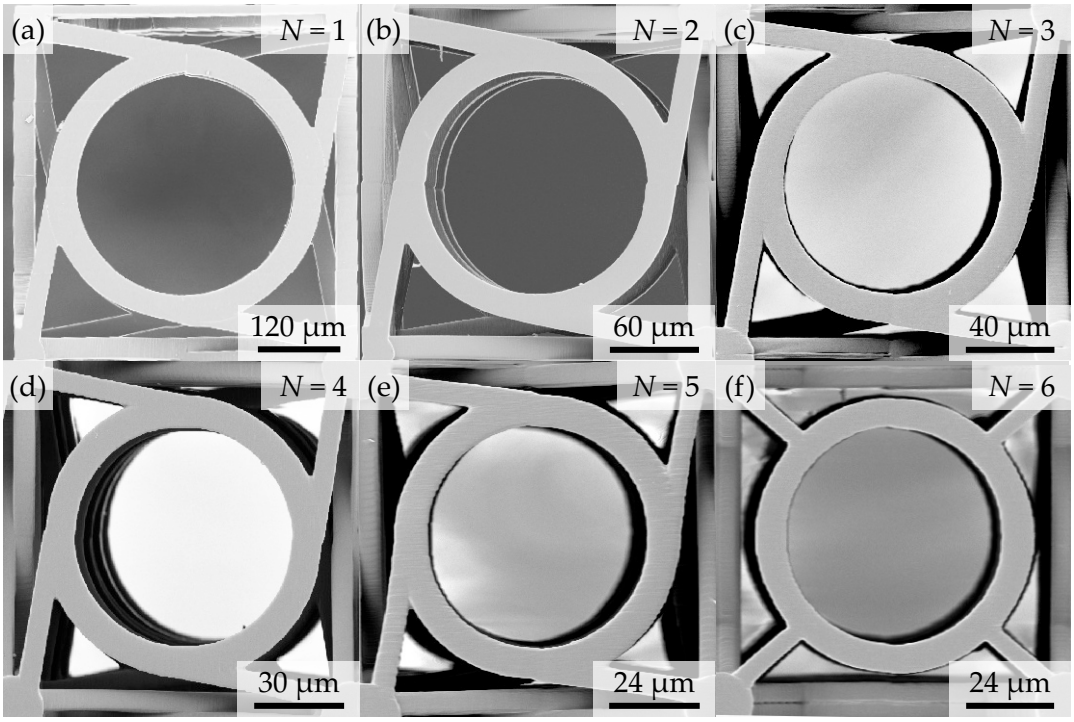

Figure 5.14: Gallery of unit cell close-ups of the samples depicted in Figure 5.13. (a)-(e) are chiral structures with scale factors of $N = 1, 2, 3, 4, 5$. (f) is an achiral control structure with $N = 5$. Note that from (a) to (e) the scale bar changes by a factor of five. These close-ups were taken with a scanning electron microscope and demonstrate the generally high printing quality. This figure is adapted from [2].

displacement vectors $\vec{u}_i(t)$ were calculated as

$$\vec{u}_i(t) = \vec{x}_i(t) - \vec{x}_i(t_0). \tag{5.4}$$

Note that these vectors refer to positions in a 2D image, hence they have only two components. The x- and y-components of a single marker are plotted as a function of time in Figure 5.15(b). (a) shows the displacement vectors for all tracked markers of the chiral sample with $N = 3$ at a time t_1, for which the axial strain was $\varepsilon_{zz} = -1.5\%$. From these data, the azimuthal components $u_{\varphi i}$ of the displacement vectors, and hence the rotation angle φ, shall be computed.

In the most general case, the tracked middle plate can be translated and

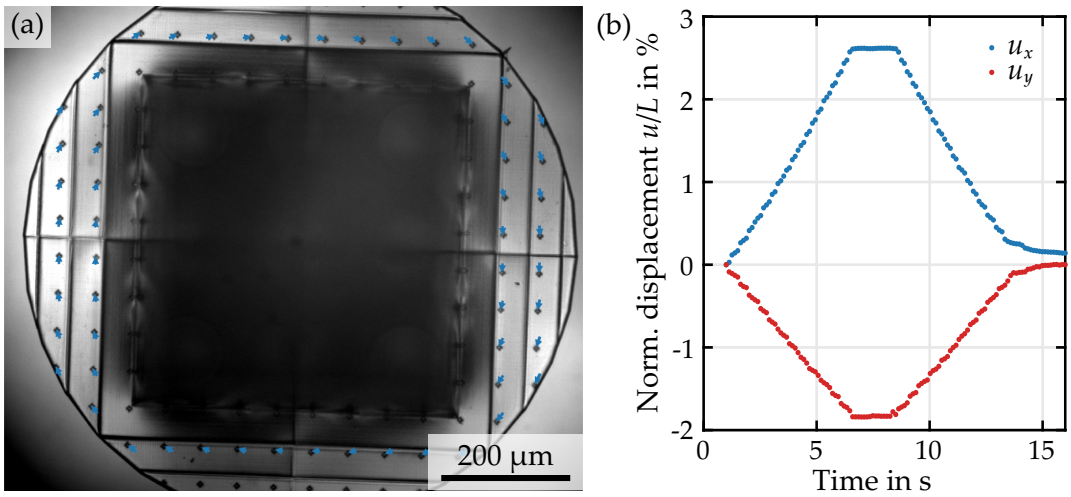

Figure 5.15: (a) Optical micrograph of a sample wit $N = 3$ during measurement. An axial strain of $\varepsilon_{zz} = -1.5\%$ was prescribed. The photo was taken through the substrate and focuses on the marker plate in between the right- and left-handed parts of the structure. The displacement vectors (blue) extracted by digital image cross-correlation are depicted on the same scale. (b) x- and y-component of the displacement vector $\vec{u}_i$ of a single marker as a function of time. A whole loading and unloading cycle is depicted. Panel (a) is adapted from [2].

rotated in the x-y plane. Yet, only the latter is of interest. Translation can be caused by a misalignment of the optical system and the sample axis or by sample imperfections. Hence, the azimuthal displacement was calculated by subtracting the movement of the center of gravity $\langle u(t)\rangle_i = \langle x_i(t)\rangle_i - \langle x_i(t_0)\rangle_i$ from the measured displacements

$$u_{\varphi i}(t) = u_i(t) - \langle u(t)\rangle_i. \tag{5.5}$$

In this context, $\langle\bullet\rangle_i$ denotes the average over all markers at a given time t. Later, $\langle\bullet\rangle_t$ will be used as a time average of a single marker.

The rotation angle $\varphi_i(t)$ was then calculated by

$$\varphi_i(t) = \frac{u_{\varphi i}(t)}{r_i}, \tag{5.6}$$

with $r_i = |\vec{O} - \vec{x}_i(t_0)|$ being the distance between the marker's reference position and the center of rotation $\vec{O}$. In turn, $\vec{O}$ was calculated by first fitting a linear function $f_i(x)$ to the corrected positions $x_{\mathrm{corr},i} = x_i(t) - \langle u_i(t)\rangle_i$ for

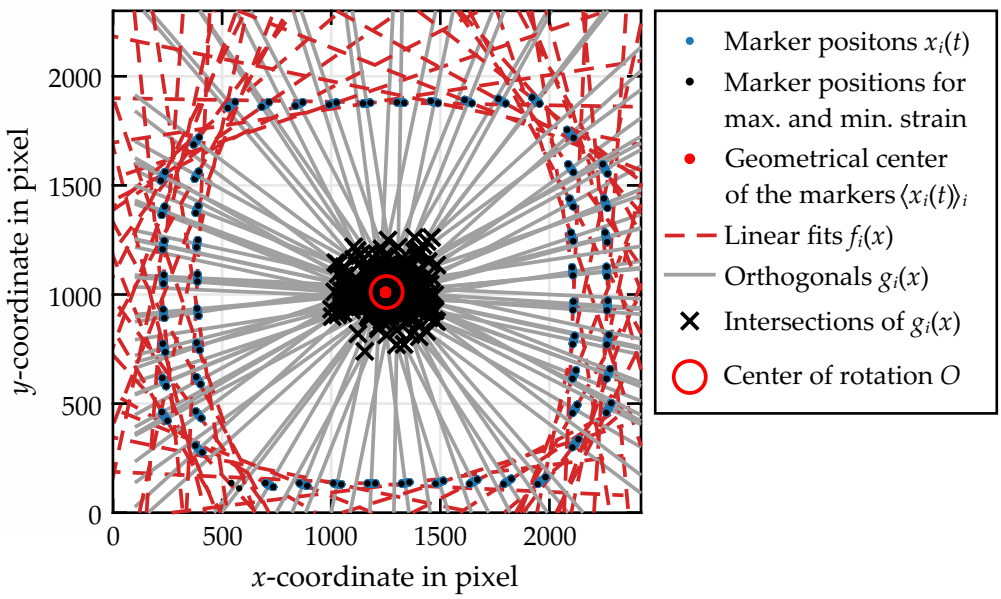

Figure 5.16: The extracted marker positions $x_i(t)$ of the same measurement as depicted in Figure 5.15 are plotted as blue dots. The black markers indicate the positions of minimum and maximum strain. The movement of the geometrical center of the marker array $\langle x_i(t) \rangle_i$ is in the order of the marker size (red dots). The linear fits $f_i(x)$ are depicted as red dashed lines. The center of rotation (red circle) is calculated as the average position of the intersections of all $g_i(x)$ within an area surrounding $\langle x_i(t) \rangle_i$.

every marker (red lines in Figure 5.16). The positions $x_{\mathrm{corr},i}$ are plotted for an exemplary measurement of a sample with $N = 3$ and $\varepsilon_{zz} = -1.5\%$ in Figure 5.16 as blue dots. Secondly, a line $g_i(x)$ orthogonal to $f_i(x)$ through the point $\langle x_{\mathrm{corr},i}(t) \rangle_t$ is calculated (gray lines in Figure 5.16). The center of rotation $\vec{O}$ is then given as the mean value of all intersections (black crosses in Figure 5.16) of the functions $g_i(x)$ within a predetermined range.

5.4.4 *Twist per Strain of the Metamaterial Samples*

Twist angles were measured for samples containing $(N \times N \times 2N) \times 2$ unit cells with $N = 1, 2, 3, 4, 5$, both for chiral and achiral structures. Therefore, displacements corresponding to axial strains of $\varepsilon_{zz} = -0.5\%, -1.0\%, -1.5\%$ have been prescribed. In each experimental cycle, the strain was ramped up slowly to its maximum, kept at this state for approximately 2 s, and sub-

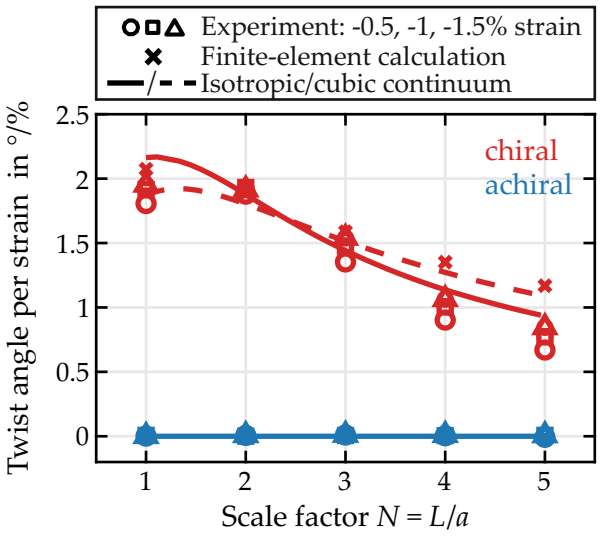

Figure 5.17: Summary of the measured and calculated twist angles per axial strain. Results both for chiral (red) and achiral samples (blue) are depicted. Experimentally, strains of $\varepsilon_{zz} = -0.5\%, -1\%, -1.5\%$ have been probed. Additionally, the twist angles deduced from structural finite-element calculations and from effective continuum models are plotted. Both were performed in the linear regime. This figure is adapted from [2].

sequently released to its unstrained configuration again. Every experiment was repeated six times, with pauses of at least 20 s in between consecutive loading cycles. For each experiment, the twist angle per axial strain was calculated as stated in the previous subsection. The mean rotation angle for every strain is plotted as a function of N in Figure 5.17. The statistical errors are within the size of the symbols, and therefore not depicted. For comparison, the results from the finite element calculations described in the previous section are also depicted.

For all chiral samples, a pronounced twist angle per axial strain was measured. The qualitative trend also agrees well with the predictions from finite-element calculations. For $N = 1, 2, 3$, an exceptionally good quantitative agreement was found. Generally smaller twist angles were measured for the cases of $N = 4, 5$. Furthermore, for all samples larger strains led to higher twists per strain. In Figure 5.13(c), a scanning electron micrograph is shown together with the measured displacement vectors for the axial (red arrows) and azimuthal displacements (blue arrows). For better visibility, all vectors have been scaled by a factor of 5. From this it becomes clear that the axial and azimuthal displacements are comparable in magnitude. Hence, the effects due to the new degrees of freedom are as large as the ordinary ones. On the other hand, the achiral control structures show no twist within the margins of error as expected.

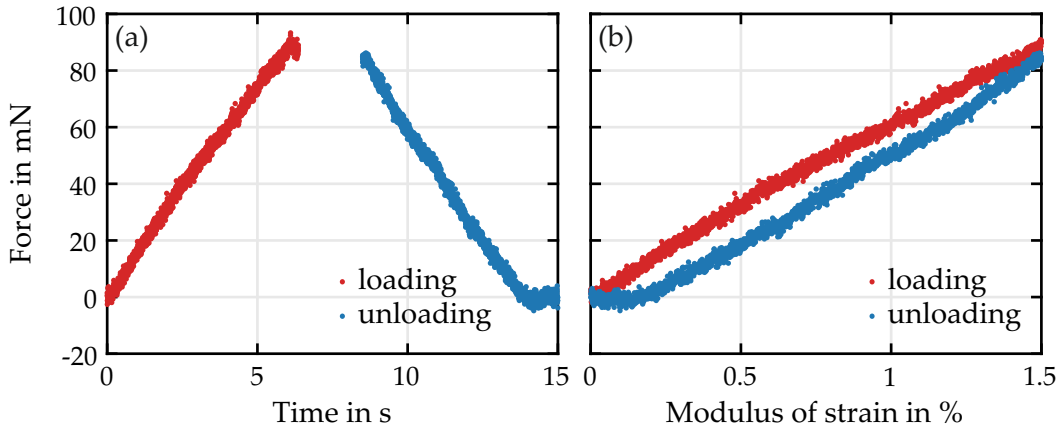

Figure 5.18: Exemplary force measurement of a chiral metamaterial sample with $N = 3$ subjected to a maximal axial strain of $\varepsilon_{zz} = -1.5\%$. The loading (blue) and unloading curves are depicted both as a function of time (a) and external strain (b). In (b), only small deviations from linearity are recognizable. Additionally, a small hysteresis can be observed. This is most likely caused by the viscoelastic properties of the used constituent polymer.

5.4.5 *Effective Young's Modulus*

Simultaneously to the twist measurement, the counteracting force F_z of the sample was recorded as a function of time, and hence as a function of the external strain. Exemplary data of the force measurement of the sample with $N = 3$ and a prescribed maximum strain of $\varepsilon_{zz} = -1.5\%$ is depicted in Figure 5.18.

Using this data, the effective Young's modulus was extracted using a linear fit. To compare these values to the finite-element calculations of the structures, a Young's modulus of $E = 2.6\,\mathrm{GPa}$ and a Poisson's ration of $\nu = 0.4$ was assumed for the constituent material in the simulations.

As for the twist per strain, the qualitative trends of the numerical calculations are reproduced well by the experiments. Again, larger deviations are present for the chiral samples with $N = 4, 5$. As expected from classical Cauchy elasticity, the Young's modulus of the achiral control sample does not show a N dependency within the margins of error.

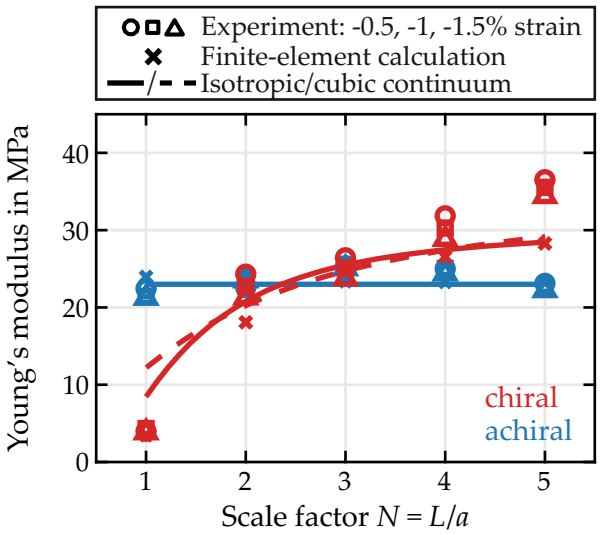

Figure 5.19: Summary of the measured and calculated effective Young's moduli. Results both for chiral (red) and achiral samples (blue) are depicted. Experimentally, strains of $\varepsilon_{zz} = -0.5\%, -1\%, -1.5\%$ were probed. Additionally, the effective Young's moduli deduced from structural finite-element calculations and from effective continuum models are plotted. Both were performed in the linear regime. This figure is adapted from [2].

5.5 The Quest for Effective Material Parameters

The title of this section is based on the title of Gauthier's and Jahsman's 1975 article *"A Quest for Micropolar Elastic Constants"*[54], where they already pointed out the difficulties of completely characterizing the micropolar elasticity tensors for an achiral and isotropic cylinder. Surely, the additional parameters for a chiral material do not facilitate the task. Furthermore, to the best knowledge of the author, there is no closed analytical solution describing the axial compression of a chiral bar with square footprint using micropolar elasticity. Although Lakes derived equations for the axial compression of a chiral cylinder [33], these solutions in their most general form can barely be used as a fit function for a parameter retrieval. Furthermore, it is questionable, whether the samples with square footprints discussed in this thesis can be approximated by a round cylinder.

On the other hand, without a proper continuum description and the corresponding effective material parameters, metamaterials are of little use for real world applications (compare section 2.5 and [15]). Since a proper parameter retrieval is out of reach, a set of material parameters was found in [2] that mimics the scaling behavior of the metamaterial by a systematic parameter variation. These parameters are also given in subsection B.1.1. Unfortunately, these original parameters do not describe a passive material, since not all eigenvalues of the elasticity tensor were positive, eventhough all bounds on the material parameters derived in [33] are fulfilled.

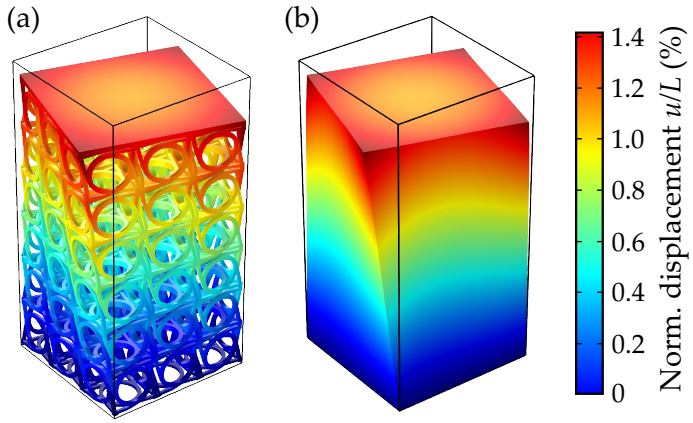

Figure 5.20: Calculated displacements for the chiral structure (a) and the cubic micropolar continuum (b). Both correspond to a scale factor of $N = 3$ and a prescribed axial strain of $\varepsilon_{zz} = -1\%$. The general behavior of the structure is nicely captured by the continuum model. This figure is adapted from [2].

Yet, Yi Chen showed in [60] that the metamaterial behavior can be reproduced using micropolar material parameters of a passive, cubic material. By solving the micropolar wave equation analytically, he was able to retrieve some of the micropolar parameters. The remaining ones were found by a numerical optimization procedure. The derived set of material parameters are given in subsection B.1.2 and [60].

The static push-to-twist coupling for both the isotropic and cubic micropoar continuum was derived numerically by prescribing a displacement to the top surface of a cuboid with outer dimensions of $L \times L \times H$. A chiral cubic micropolar material was assumed for the cuboid's constituent material. For a fixed set of material parameters, the effective Young's modulus and the resulting twist per strain were evaluated as a function of the sample side length L, whilst keeping the cuboid's aspect ratio constant. In this fashion, only the ratio between characteristic length and sample dimension L/l_t is varied.

Figure 5.20 shows a comparison between the structural calculations of a sample with $N = 3$ and a cuboid out of the cubic micropolar continuum with $L = 3a$. It illustrates that the twist effect is indeed nicely captured by the micropolar continuum. This becomes yet clearer, when extracting the twist angle per strain and the effective Young's modulus for different scale factors N as depicted in Figure 5.17 and Figure 5.19. The results of the isotropic medium are plotted as solid lines and those of the cubic as dashed

lines. Both, the qualitative trends and the absolute values for both quantities are well reproduced. Obviously, the width of the cuboid L is not restricted to integer multiples of the lattice constant a. Hence, values in between can be calculated and actually have a physical meaning.

The characteristic length scales l_t and l_1 have previously been defined for an isotropic medium (compare [33] and subsection 2.3.7). These can also be expressed in terms of the entries of the elasticity tensor

$$l_t = \sqrt{\frac{A_{44} + A_{47}}{C_{44} + C_{47}}}, \tag{5.7}$$

$$l_1 = \frac{B_{11}}{C_{44} + C_{47}}. \tag{5.8}$$

Using the isotropic material parameters given in [2] and subsection B.1.1, the characteristic lengths scales are

$$l_t = 177\,\mu m, \tag{5.9}$$

$$l_1 = 188\,\mu m. \tag{5.10}$$

Assuming that Equation 5.7 and Equation 5.8 also define material moduli for the cubic symmetry, the characteristic length scales for the cubic material parameters (compare subsection B.1.2 and [60]) are given by

$$l_t = 69\,\mu m, \tag{5.11}$$

$$l_1 = 571\,\mu m. \tag{5.12}$$

Due to the ways the scaling was conducted in the micropolar calculations, this has to be compared to a lattice constant of $a = 500\,\mu m$ in the experiments. The lattice constant and the characteristic length scales are of similar order of magnitude. This fits nicely to the finding, that the twist angle per axial strain only decreases by a factor of 2 when going from $N = 1$ to $N = 5$. Once again, these material parameters were not found in a proper parameter retrieval, but rather found in a numerical optimization. This explains the big difference in the characteristic length scales found for the cubic and isotropic case. On top of that, it should be stressed once again that the isotropic material parameters unfortunately do not describe a passive material.

Within the scope of this continuum calculations, large values for N can be calculated with ease. Figure 5.17 shows the twist per strain of the cubic micropolar continuum for scale factors as big as $N = 110$ (red curve) in a

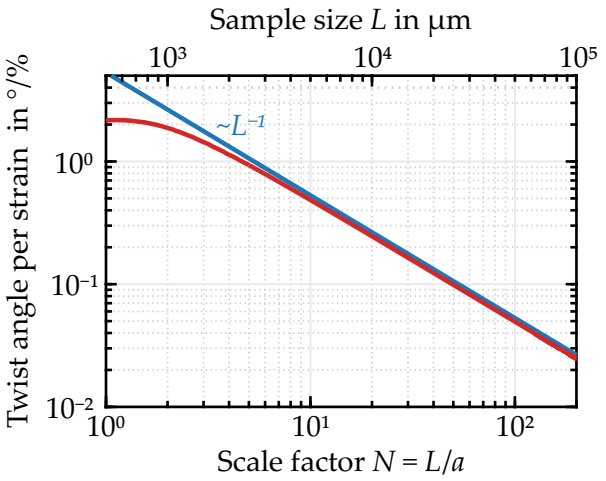

Figure 5.21: The calculated twist per axial strain of the cubic micropolar continuum model (red) is depicted as a function of the scale factor N. With this continuum model, scale factors $N > 10^2$ can easily be calculated. For comparison, a curve $\propto L^{-1}$ is plotted (blue). For large N, the twist per axial strain approaches this characteristic. This figure is adapted from [2].

double logarithmic plot. For these calculations, the cubic material parameters were used. Additionally, the blue line is proportional to a $1/N$-decay. For $N > 10$, the twist per strain approaches the blue line, meaning that it scales as $\propto 1/L$, as has been predicted in subsection 2.3.9.

Note that [60] and the parameters given in subsection B.1.2, use a different definition of the Voigt's notation. Thus, results have to be compared with caution. Furthermore, the parameters given there refer to a lattice constant of only $a = 250\,\mu\text{m}$ and a constituent material of $a = 4.18\,\text{GPa}$. To still be able to compare the results from [60] and the results presented here and in [2], the parameters have been scaled.

5.6 Discussion

First and foremost, a 3D chiral mechanical metamaterial was realized successfully, exhibiting degrees of freedom unprecedented in the classical Cauchy continuum. This is demonstrated both by the pronounced push to twist coupling and by the scale factor dependent Young's modulus. The maximum twist angles exceeded 2% per percent of axial strain. This also demonstrates that the new degrees of freedom are not only small corrections to the classical Cauchy continuum, but in fact, its related effects are as pronounced as the classical ones. Strikingly, the twist angle and the length scale dependency vanish when examining an achiral version of the metamaterial. Meaning, the classical Cauchy limit is recovered.

Furthermore, the twist angle per axial strain only decreases by a factor of 2 for the chiral samples when going from $N = 1$ to $N = 5$, both for the FEM calculations of the structures, the experiments, and the continuum model. This suggests that characteristic length scales on the order of the size of the unit cell are involved. The calculated numeric values of l_t and l_1 from the micopolar tensor elements affirm this finding.

The FEM simulations of the structure and the experiments show convincing agreements both qualitatively and quantitatively. Especially for the samples with $N = 1, 2, 3$, both the twist per axial strain and the Young's modulus match excellently. Most certainly, the deviations of the Young's modulus and the twist angle for $N = 4$ and $N = 5$ are related to residual sample imperfections. For these samples, certain geometrical features become very small and are already comparable to the voxel size of the 3D printing setup. Thereby, the relative fabrication error becomes more prominent for larger scaling factors N. For example for $N = 5$, the thickness of the lever arms is $d = 6\,\mu m$. Realistically, the fabrication tolerance of the used configuration of the Nanoscribe system and the accompanied voxel corrections is about 500 nm. This translates to a relative error of about 10%. Yet, the flexural rigidity of such a bar is proportional to the width of the bar and to the third power of the height of the bar. Thereby, the relatively small fabrication errors can already cause significant deviations. Thus, they can easily account for the small differences between experiments and FEM simulations. Maybe, the quantitative deviations concerning the nonlinearites of the samples can also be attributed to these fabrication limits.

The mechanism driven design use to generate the unit cell blueprint by no means guarantees to find an optimum design. Therefore, it is even more surprising that an approach based on topology optimization yielded a remarkably similar geometry with comparable twist per axial strain [81].

Finally, the FEM calculations of a micropolar elastic material illustrate nicely that the metamaterial behavior can be captured by a continuum model. Yet, the method used here is not suited to uniquely retrieve a set of material parameters. Most certainly, the ones presented above will not be suitable to represent the metamaterials behavior with sufficient accuracy for all boundary conditions possible. Instead, they should only be understood as an evidence that micropolar elasticity can mimic the specific effects studied above.

Chapter 6

6 Metamaterials with Enhanced Characteristic Length Scales

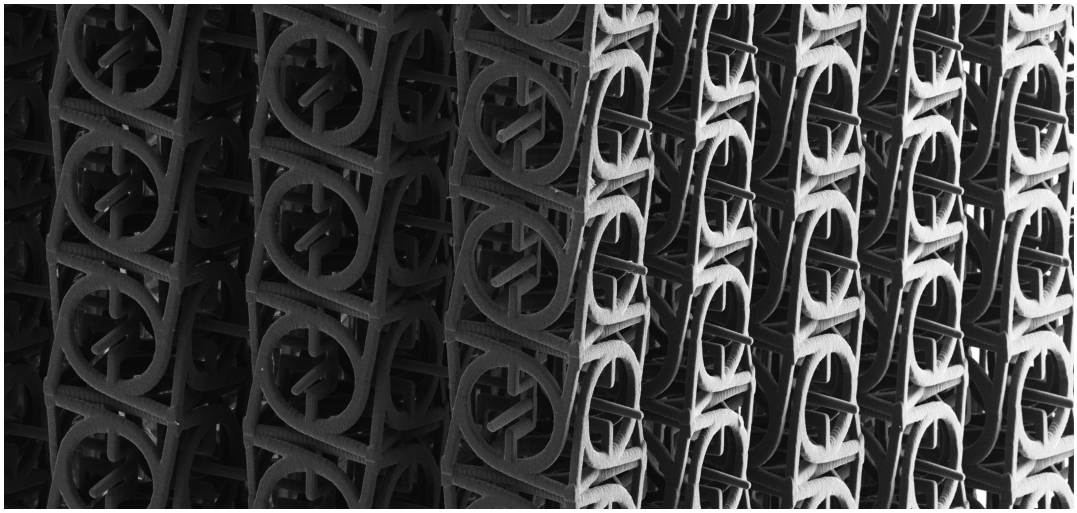

Scanning electron microscope image of a sample

In this chapter, we modify the metamaterial geometry of the previous chapter to exhibit more extreme physical properties. We not only realize higher twist angles, but also find characteristic lengths scales larger than the metamaterial's lattice constant. First, I will present a simple model that was developed by Martin Wegener and me. Afterwards, the unit cell design Patrick Ziemke and I conceptualized is presented as well as his finite element calculations based on beam theory. Finally, I will present the experimental results generated by Vincent Hahn, Jonathan Schneider and me. The major findings of this chapter have already been published in [118].

It has been shown in the previous chapter that effects beyond the limits of classical Cauchy mechanics were achieved using a chiral metamaterial. This was accompanied by a breakdown of scale invariance. Thereby, characteristic lengths on the order of the unit cell size were found, which determined the functional dependency between twist angle and scale factor N. So far, it is unclear whether the twist angle always decays monotonously and whether characteristic lengths scales are bound to be smaller or comparable to the lattice constant. Hence, the guiding questions of this chapter is: Are there unit cell designs with characteristic lengths scales much larger than the lattice constant? And, how does this influence the relation between twist and scale factor N?

6.1 Simple Model for Chiral Bars

In the considerations of the previous chapter, only little attention was paid to the role of the interaction between the chiral unit cells. Instead, the focus was on maximizing the internal push-to-twist coupling of a single unit cell. Here, the attention is shifted towards the inter unit cell coupling and how this contributes to the notion of a characteristic length scale. Therefore, a drastically simplified model of a metamaterial bar is presented that was originally brought forward by Martin Wegener and the author of this thesis. Together with Patrick Ziemke, Peter Gumbsch, Yi Chen, and Vincent Hahn this model was refined and published in [118]. Useful physical insights can be drawn from this model that will be exploited later on to modify the metamaterial's unit cell.

For this model, metamaterial crystals containing $N_x \times N_y \times N_z$ unit cells are considered, with $N = N_x = N_y$ and $N_z = 3N$ as depicted on the left of Figure 6.1. The bottom of the metamaterial should be fixed and a displacement u_z should be prescribed along the z-direction, yielding an axial strain of $\varepsilon_{zz} = u_z/H$, with sample height H. All other boundaries are considered free. Edge effects are explicitly neglected for simplicity.

Suppose, a single chiral unit cell exhibits a twist angle of $\varphi(N_x = 1, N_z = 1)$ when subjected to an axial strain ε_{zz}. For simplicity, a linear behavior $\varphi(N_x = 1, N_z = 1) \propto \varepsilon_{zz}$ is assumed. When stacking unit cells along the z-direction ($N_z > 1$) as depicted in the middle of Figure 6.1, the twist angles of the individual unit cells add up according to

$$\phi = \varphi(1, N_z) = N_z \varphi(1, 1). \tag{6.1}$$

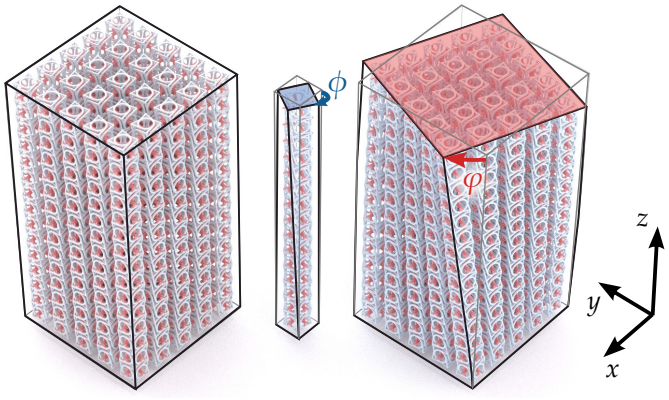

Figure 6.1: Illustration of a metamaterial crystal containing $5 \times 5 \times 15$ unit cells (left). Isolated bar of $1 \times 1 \times 15$ unit cells that twist by $\phi = \varphi(1, 15) < 0$ when subjected to an axial compression (middle). In contrast, the crystal on the right twists by $\varphi = \varphi(5, 15)$ when compressed axially. In general, ϕ and φ are distinct from one another. This figure is adapted from [118].

In that, $\phi = \varphi(1, N_z)$ describe the twist angle of a column of unit cells (compare Figure 6.1).

The same scaling behavior is assumed for the twist angles $\varphi(N_x, 1)$ of a whole plane of unit cells containing N_x^2 unit cells

$$\varphi(N_x, N_z) = N_z \varphi(N_x, 1). \tag{6.2}$$

In this spirit, $\varphi(N_x, N_z)$ denotes the twist angle of the whole metamaterial sample as depicted on the right of Figure 6.1. The scope of the simple model is finding an analytical expression for $\varphi(N_x, N_z)$ as a function of N and a couple of material parameters. To do so, an expression for the total elastic energy U is defined. Three contributing terms U_1, U_2, and U_3 were identified yielding

$$U = U_1 + U_2 + U_3. \tag{6.3}$$

In the following, each term will be introduced separately.

The first term U_1 is the usual energy related to the axial compression of the bar

$$U_1 = \frac{1}{2} c_1 N_x^2 N_z \varepsilon_{zz}^2. \tag{6.4}$$

It is proportional to the sample's volume, since every unit cell contributes equally. At this point, it might seem that Poisson's ratio ν and the other Poisson's ratio-like-quantities are explicitly zero, since only ε_{zz} appears in the energy term. Yet, due to the linear constitutive relations, all other strain tensor elements are proportional to ε_{zz}. Hence, their energy contribution is implicitly included in c_1. Therefore, c_1 is related to the material's effective

Young's modulus. For the structures studied later in this chapter, the Poisson's ratio is indeed close to zero and thus, the strain tensor components are approximately decoupled.

The second term U_2 results form the torsion of the metamaterial sample by $\varphi(N_x, N_z)$ and is related to the torsional stiffness defined in Equation 2.96

$$U_2 = \frac{1}{2} c_2 \frac{N_x^4}{N_z} \varphi(N_x, N_z)^2. \tag{6.5}$$

Keep in mind that this torsion is not a result of some external momenta, but is generated by the chiral unit cells. The N_x^4 dependency stems from the area momentum of inertia. c_2 is related to the effective shear modulus of the metamaterial.

Generally, the twist angle of a plane of unit cells $\varphi(N_x, 1)$ is distinct from the rotation angle of a single unit cell $\varphi(1,1) \neq \varphi(N_x, 1)$. In an intuitive picture, this can be explained as follows: Every unit cell wants to rotate around its own center of gravity individually. Thereby, neighboring unit cells partially counteract each other. Hence, a third energy contribution can be formulated, resulting from a difference between the twist angle of a plane $\varphi(N_x, 1)$ and the twist of an isolated unit cell $\varphi(1,1)$

$$U_3 = \frac{1}{2} c_3 N_x^2 N_z (\varphi(N_x, 1) - \varphi(1,1))^2. \tag{6.6}$$

Again, every unit cell in the volume contributes equally and therefore the energy is proportional to the sample's volume. Using Equation 6.2, the energy U_3 can be written as

$$U_3 = \frac{1}{2} c_3 \frac{N_x^2}{N_z} (\varphi(N_x, N_z) - \varphi(1, N_z))^2. \tag{6.7}$$

Therefore, the total elastic energy is given by

$$U = \frac{1}{2} c_1 N_x^2 N_z \varepsilon_{zz}^2 + \frac{1}{2} c_2 \frac{N_x^4}{N_z} \varphi(N_x, N_z)^2 + \frac{1}{2} c_3 \frac{N_x^2}{N_z} (\varphi(N_x, N_z) - \varphi(1, N_z))^2. \tag{6.8}$$

Furthermore, by assuming no external torques

$$\frac{\partial U}{\partial \varphi(N_x, N_z)} = 0, \tag{6.9}$$

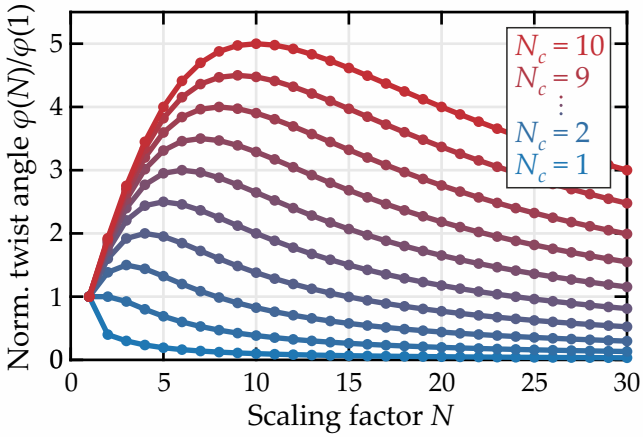

Figure 6.2: Solutions of the analytical model for various characteristic number N_c. For $N_c \geq 2$, the normalized twist angles exhibit a maximum at $N = N_c$. For $N \gg N_c$, the normalized twist again decays $\propto N^{-1}$. This figure is adapted from [118].

and a finite axial strain ε_{zz}, an expression for $\varphi(N_x, N_z)$ is derived

$$\varphi(N_x, N_z) = \varphi(1, N_z) \frac{c_3 N_x^2}{c_2 N_x^4 + c_3 N_x^2}. \tag{6.10}$$

In accordance with later experiments, the sample's aspect ratio is kept constant leading to $N_z = 3N_x = 3N$. By introducing $N_c = c_3/c_2$ and $\varphi(N) = \varphi(N, 3N)$, the twist angles is given by

$$\varphi(N > 1) = \varphi(1) \frac{N N_c^2}{N^2 + N_c^2}. \tag{6.11}$$

As a result, only two parameters $\varphi(1)$ and N_c completely determine $\varphi(N)$. The first, $\varphi(1) = 3\varphi(1,1)$, is the twist angle per strain generated by a single, isolated unit cell. It is merely a prefactor and does not influence the behavior of $\varphi(N)$. The characteristic number N_c is the ratio between the coupling strength c_3 and shear modulus c_2. N_c is the only parameter influencing the general shape of $\varphi(N)$. Interestingly, the definition of N_c somewhat resembles the definition of the material modulus l_1 (see subsection 2.3.7 and [33]).

Figure 6.2 shows $\varphi(N)$ for a fixed $\varphi(1)$ and several characteristic numbers $N_c = 1, 2, \ldots, 10$. For $N \gg N_c$, $\varphi(N)$ decays proportional to $1/N$ for all N_c depicted. For the case $N_c \gg 1$, the twist $\varphi(N)$ increases first linearly, reaches a maximum at N_c, before decreasing $\propto 1/N$. For $N_c < 1$, $\varphi(N)$ does not exhibit a maximum. The case of $N_c \approx 2$ resembles the metamaterial of the previous chapter.

This scaling behavior of $\varphi(N)$ can be understood intuitively. Consider a metamaterial beam with $N_c \gg 1$, meaning $c_3 \gg c_2$, and $N < N_c$. Here, the energy U_2 needed to twist the metamaterial bar by $\varphi(N)$ are small compared to U_3. Hence, minimizing $(\varphi(N) - \varphi(1, N_z))^2$ yields a minimum elastic energy and the metamaterial's twist angle is proportional to N

$$\varphi(N) \approx \varphi(1, N_z) = 3N\varphi(1, 1). \tag{6.12}$$

If N is now increased so that $N \gg N_c$, the situation is reversed due to the N^5 dependency of U_2 and the N^3 scaling of U_3. This means that much more energy is needed to twist the metamaterial bar by $\varphi(N)$ than is stored in U_3. Thereby, minimizing $\varphi(N)$ becomes more and more beneficial for increasing N.

This simple model suggests that the behavior of the twist per axial strain can be much richer than the previously discussed monotonous decrease as a function of N. Instead, for sufficiently large characteristic numbers N_c, and hence large characteristic length scales $l_c = aN_c$, a linear linear increase with a pronounced maximum at $N = N_c$ can be realized. It can be deduced that large characteristic length scales are realized, if

- the unit cells are coupled strongly along the z-direction, so that the twists of the individual unit cells add up according to $\varphi(1, N_z) = N_z\varphi(1, 1)$, and
- the shear modulus c_2 is small compared to the coupling constant c_3.

As a side note, the simple model does not yield reasonable results for $N \leq 1$, since in that context the macrorotation $\varphi(N_x, N_z)$ is ill-defined.

6.2 Metamaterial Blueprints with Large Characteristic Lengths

The simple model introduced in the previous section suggest that the coupling of the microrotions $\varphi(1, 1)$ in the xy-plane should be tuned independently from the coupling in z-direction. Therefore, leaving aside cubic symmetry and considering tetragonal materials is reasonable. As depicted in Figure 2.5, these materials have three mutual orthogonal axes. Yet, only two of them are equivalent.

6.2.1 *A Lattice Truss Metamaterial*

In [116], Patrick Ziemke proposed a lattice truss based tetragonal metmaterial exhibiting large characteristic lengths. Since the underlaying mechanism, that will be used later to modify the cubic unit cells of the previous chapter, can be understood more easily with this structure, his work will be summarized quickly. More details are given in [116]. The unit cell he proposed is composed of a chiral (blue), and achiral motive (gray), as depicted in Figure 6.3(a). The different colorings are for illustration purposes only. Both motives are made from the same constituent material and have a four-fold rotational symmetry around the z-axis. All beams have a square cross section with widths d_C for the chiral, and d_A for the achiral motives. A single plane of the metamerial crystal is constructed by stacking these motives as illustrated in Figure 6.3(e). The outlines of the crystal's unit cell are depicted in black. A 3D crystal is built by simply stapling these layers without intermediate motives. Thereby, a single unit cell contains effectively one chiral and three achiral motives (compare Figure 6.3(f)). As a consequence, the resulting unit cell is tetragonal.

How this arrangement yields higher twist angles per axial strain is depicted in Figure 6.3(c) and (d). First, consider a couple of isolated unit cells as depicted in (c). When subjected to an axial elongation, every unit cell twist around its own center of mass, as indicated by the red arrows. Next, these cells are brought into contact to build up a plane of unit cells without intermediate unit cells (b), as has been done before in chapter 5 and [2]. Still, every unit cell "wants" to rotate around its own center of mass, yet the contact to their neighbors forces a mutual rotation around the common center of mass. Thereby, the rotations of the single unit cells do not add up constructively, but cancel each other instead. In this very simplified picture, the only uncompensated rotation stems from the outer boundaries. In the language of the simple model this means: The directly connected unit cells have such a high shear and rotational stiffness c_2 compared to c_3, that the energy contribution U_3, due to the restricted rotation, is comparatively small. Hence, this structure has a small characteristic length l_c.

In contrast, when inserting the achiral motives (d), the rotations do not directly cancel each other. Instead, they effectively shear the achiral motives in between. Considering a low shear resistance of these achiral motives, the chiral ones can rotate around their own center of mass nearly unconstrained. Whereas for a high shear resistance, the case of directly coupled unit cells (c)

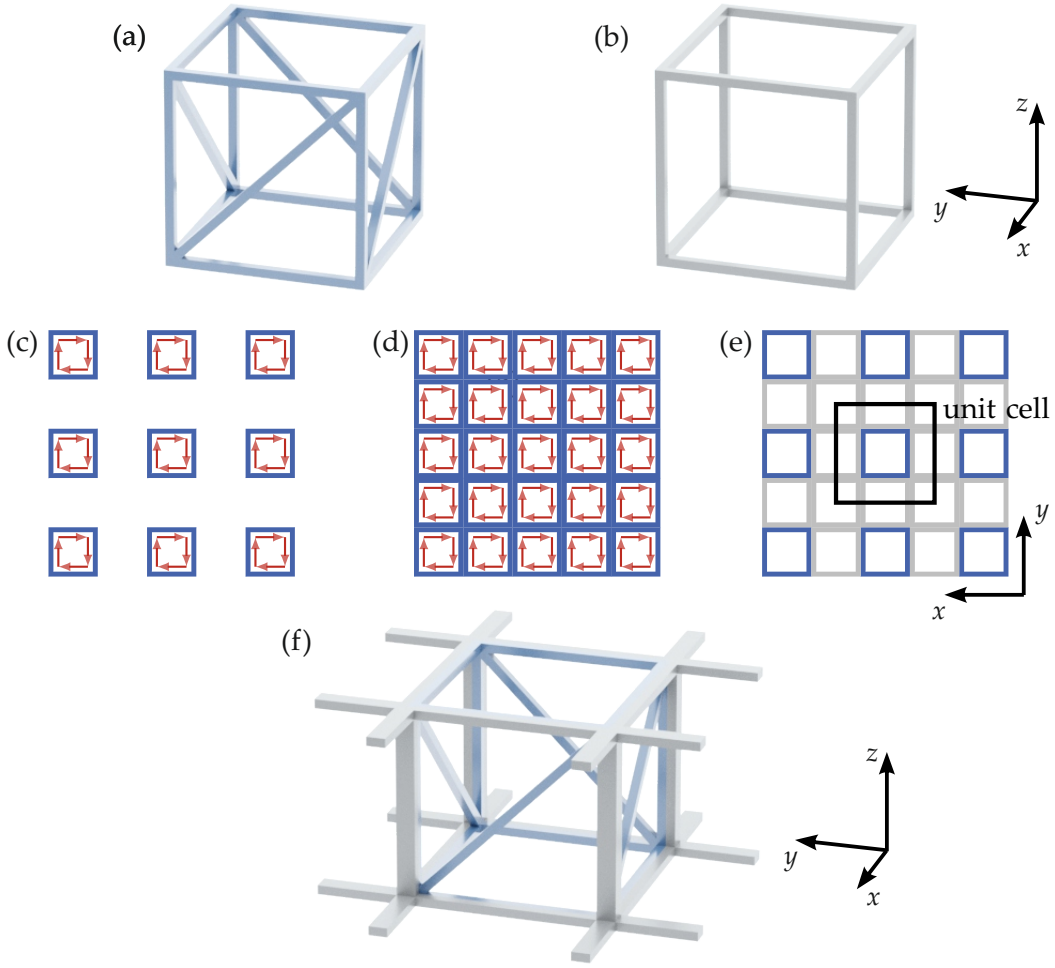

Figure 6.3: Blueprints for a metamaterial with enhanced characteristic length. It is comprised of a chiral (a) and an achiral motive (b). When elongated along the z-direction, individual chiral motives (blue) will rotate around their geometrical center individually (c). Upon constructing a crystal by bringing these chiral motives (blue) in direct contact (d), the unit cells will counteract the motions of their direct neighbors. (e) By inserting additional achiral motives (gray), the cancellations of the rotations of individual unit cells are mitigated. Thereby, a qualitatively different scaling of the twist angle per axial strain as a function of N can be expected. From these considerations, the blueprint presented in (f) can be derived. This figure is adapted from [116].

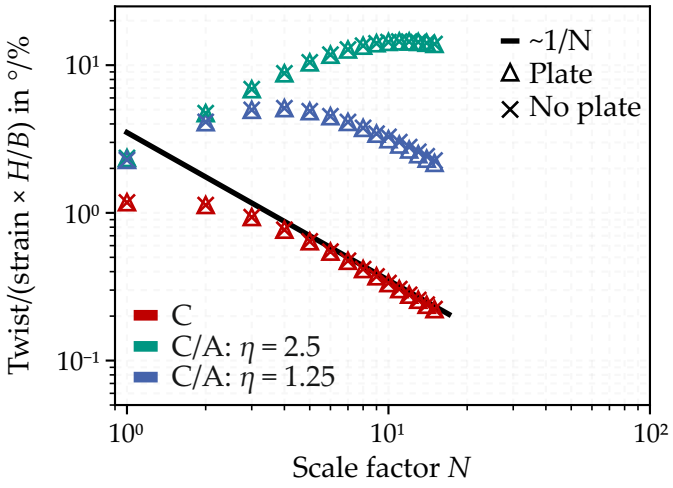

Figure 6.4: Calculated twist per axial strain for the lattice truss metamaterial normalized to the samples aspect ratio H/B. Using Timoshenko beams, crystals containing only chiral (red) and both chiral and achiral motives (green and blue) were simulated for samples containing $N \times N \times 18N$ unit cells. The coupling strength was varied by changing the thickness of the bars in the achiral motives (compare green and blue). This is quantified by the ratio of the bar thicknesses in the chiral and achiral motives $\eta = d_C/d_A$. Additionally, the influence of having plates at the sample's ends was studied. This figure is adapted from [116].

is recovered. Hence, by adjusting the effective shear modulus of the achiral unit cell with respect to the chiral ones, the coupling strength between neighboring unit cells can be tuned. In terms of the simple model this means that the achiral motives lower the twist energy U_2 with respect to U_3. Thereby, the characteristic length l_c is increased.

Using Timoshenko-beams as approximates for the bars within the unit cells, Ziemke performed finite-element calculations of metamaterial samples for different scaling factors N. This Timoshenko-beam model was implemented in ABAQUS. The calculated twists per axial strain for structures containing $N \times N \times 18N$ unit cells are depicted in Figure 6.4. The samples solely containing chiral motives (compare Figure 6.3(c)) are plotted in red. They exhibit nearly the same monotonous decay of the axial twist per strain as the metamaterial studied in chapter 5. Whereas for the samples containing both chiral and achiral motives, the twists per strain increase first, reach a maximum, and seem to decay $\propto 1/N$ for large N. This perfectly resembles

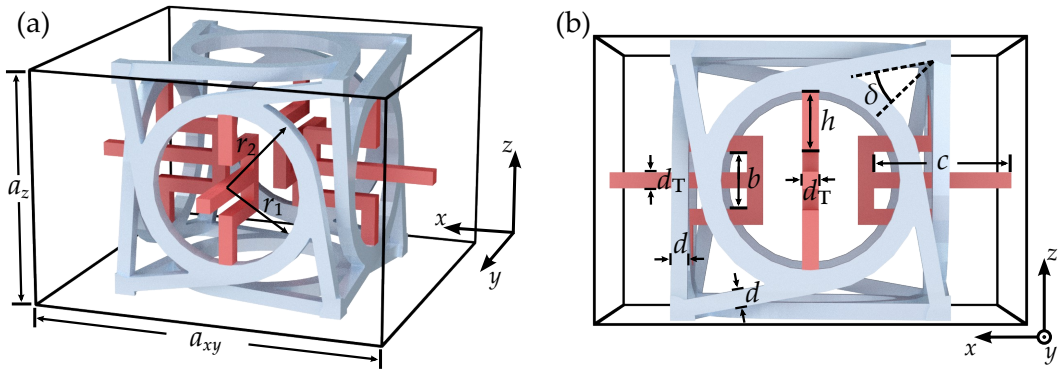

Figure 6.5: Blueprint of a chiral tetragonal unit cell. The blue parts of the unit cell are identical to the unit cell of the previous chapter. The red parts mitigate the interaction between neighboring unit cells. Both parts are made from the same constituent material, the colors are merely for illustration. (a) depicts an oblique view, (b) is a view along the y-direction. The geometrical parameters are given by $a_z = 2/3\,a_{xy}$, $d = 0.04\,a_{xy} = d_T$, $r_2 = 0.27\,a_{xy}$, $r_1 = 0.21\,a_{xy}$, $\delta = \delta_{max} \approx 35°$, $b = 0.14\,a_{xy}$, $h = 0.14\,a_{xy}$, and $c = 0.34\,a_{xy}$. This figure is adapted from [118].

the behavior predicted in the simple model. Therefore, it can be concluded that the proposed unit cell and the underlaying mechanism indeed result in structures exhibiting an enhanced characteristic length scale.

Furthermore, the simulations show (not depicted) that the metamaterials with large characteristic lengths are more susceptible to boundary effects [116]. Especially the sample's aspect ratio and its termination, whether adding a plate at the ends or not, drastically influences the resulting twist.

6.2.2 *Adapting the Cubic Unit Cell*

Yet, the lattice truss based unit cell presented in Figure 6.3 and [116] causes major experimental issues. On the one hand, having these slender bars, whilst printing samples containing thousands of unit cells, drives the 3D laser printing setup to its limits. Especially, the shrinkage during the development process rendered fabricated structures unusable. Furthermore, this lattice truss based approach was conceived for tensile test, not compressive experiments. However, the setup introduced in section 4.2 is not capable of performing such experiments.

Therefore, a new metamaterial was designed exploiting the insights gained on the lattice truss material and the simple analytical model, but based on the cubic unit cell introduced in chapter 5. The new unit cell design, which was conceived by Patrick Ziemke and the author, is depicted in Figure 6.5. This tetragonal unit cell with $a_x = a_y = a_{xy}$ and $a_z = 2/3\, a_{xy}$ is composed of a single constituent material. The colors are merely for illustration. The blue part is identical to the unit cell studied in chapter 5, allowing for direct comparison with previous results. The red parts, on the other hand, are the crucial novelties of this unit cell. These serve the same purpose as the achiral motives of the lattice truss based approach, in that the chiral unit cells are not in direct contact anymore. Instead, the unit cells can rotate around the own center of mass more easily. Thereby, the red bars, especially the one with length $2c$, are deformed. This is comparable to the shearing of the achiral motives in the lattice truss approach. Hence, a short c and thick d_T corresponds to a strong cancellation of the rotations of neighboring unit cells, whereas a long c and thin d_T corresponds to a relatively free rotation of the blue unit cell parts. To end up with sufficiently small cancellation, whilst maintaining a compact unit cell, the starting points of the elongated bar with length $2c$ were retracted into the cubic parts (blue) of the unit cell. To retain a simply connected unit cell, the red U-shaped parts are needed.

6.3 Calculated Enhanced Characteristic Length

Again, the metamaterial is first characterized numerically. Therefore, crystals are constructed with outer dimensions of $L \times L \times H$, having the same sample's aspect ratios of $H/L = 2$ as in the previous chapter. Due to the tetragonal symmetry with lattice constants a_{xy} and $a_z = 2/3\, a_{xy}$, these samples contain $N \times N \times 3N = 3N^3$ unit cells.

6.3.1 Simulations Using Volume Elements

Using COMSOL, metamaterial samples out of the unit cell depicted in Figure 6.5 were implemented for different scale factors of $N = 1, 2, 3, 4, 5, 6$. A linear elastic Cauchy constituent material has been assumed. The same boundary conditions as for the cubic unit cells have been implemented. Hence, the metamaterial was fixed at the bottom ($\vec{u} = 0$), a plate was added at the top, and a displacement of $-u_z$ was prescribed along the z-direction

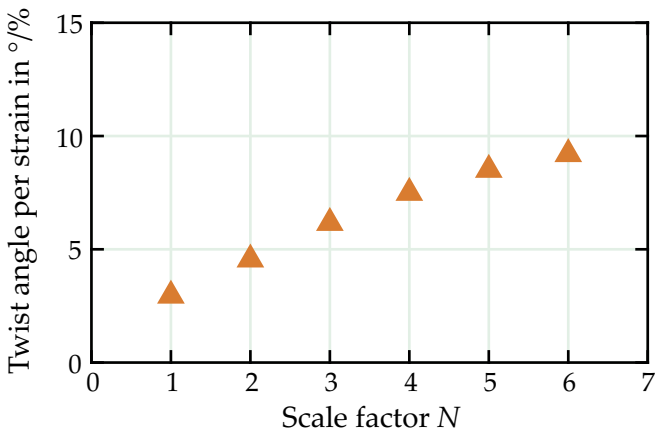

Figure 6.6: Calculated twist per axial strain of the microstructure using standard volume elements. Samples containing $N \times N \times 3N$ unit cells (as depicted in Figure 6.5) were studied. In contrast to the results of the previous chapter, the twist angle increases as a function of the scale factor N for $1 \leq N \leq 6$. This figure is adapted from [118].

to its top surface. The calculated twist angles per axial strain were extracted as before. The resulting twists per strain are depicted in Figure 6.6.

These simulations unambiguously show that the scaling behavior of the twist angles φ/ε_{zz} has been qualitatively changed, compared to the previous cubic unit cell design. Instead of a monotonous decay, an increase as a function of N is observed for the scaling factors depicted. Yet, alone from these simulations, the characteristic length l_c or the characteristic scale N_c can not be determined, since the maximum of φ/ε_{zz} is outside the computed values of N. Due to the high memory consumption of the volume elements, large values of the scaling factor N could not be calculated using this method.

6.3.2 *Simulations Using Beam Elements*

To bypass the restriction imposed by the limited accessible memory, Patrick Ziemke developed an approach based on Timoshenko beam elements [116, 118] using ABAQUS. Using these beam elements, the complex 3D geometry is replaced by simple 1D elements. Thereby, the high number of degrees of freedom needed for the volume elements is significantly reduced. This drastically simplified geometry is depicted in Figure 6.7. For clarity, not only the 1D beam elements, but the beam profile assumed in the Timoshenko beam model are depicted. More details on these calculations are given in [116, 118], and details about Timoshenko beam elements can be found in [43, 144].

Using this method, Ziemke was able to simulate the twist per axial strain

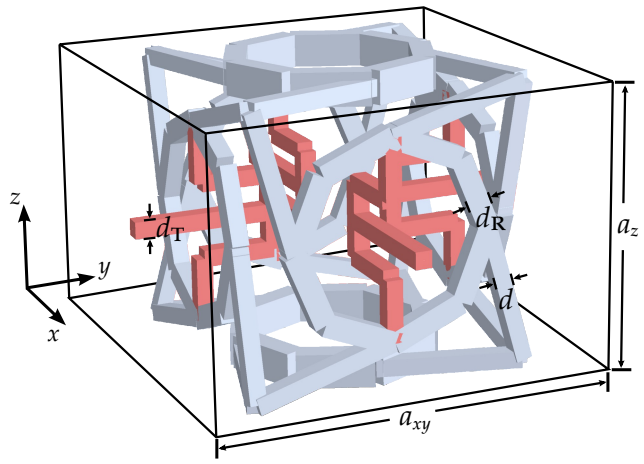

Figure 6.7: Discretization of the tetragonal unit cell using 1D Timoshenko beam elements. For illustration purposes, the beam profiles are depicted. The additional parameters are given by: $d = 0.04\,a_{xy}$, $d_R = 0.05\,a_{xy}$, and $d_T = 0.04\,a_{xy}$. This figure is adapted from [118].

φ/ε_{zz} of structures containing up to 24,000 unit cells. This corresponds to a scaling factor of $N = 20$. The extracted twist angles φ/ε_{zz} are depicted in Figure 6.8 as a function of N. Since geometrical nonlinearities were considered, φ/ε_{zz} is given for various external strains of $\varepsilon_{zz} = -0.1\%$ (solid lines), $\varepsilon_{zz} = -0.5\%$ (dashed lines), and $\varepsilon_{zz} = -1.0\%$ (dotted lines). Furthermore, the thickness d_T of the red parts in Figure 6.5 of the unit cell were varied. As laid out before, this changes the coupling between neighboring unit cells.

The general behavior of the twist angle per axial strain φ/ε_{zz} is identical for the different thicknesses d_T and strains ε_{zz} considered. First, it increases linearly, reaches a maximum, and finally decays again. Decreasing the bar thickness d_T generally shifts the maximum towards higher twist angles and higher scale factors N. For the quasi linear case of $\varepsilon_{zz} = -0.1\%$, the maximum twist angle changes from $\varphi/\varepsilon_{zz} \approx 8$ to $\varphi/\varepsilon_{zz} \approx 13$, whilst changing the thickness d_c by only $\pm 10\%$. Obviously, d_T influences φ/ε_{zz} quite sensitively.

Intuitively, increasing the bar thickness whilst keeping its length increases the bending stiffness. Thereby, more energy is needed for the deformation of the bar. In turn, this makes it harder for neighboring unit cells to twist independently and finally results in a smaller characteristic length scale.

On the other hand, for a fixed thickness $d_T = 0.036\,a_{xy}$ and external strains of $\varepsilon_{zz} = -0.1\%$, the maximum is around $N_c \approx 8$, whereas it is shifted towards larger N for higher strains. Also the maximum twist angle increases from $\varphi/\varepsilon_{zz} \approx 8^\circ/\%$ for $\varepsilon_{zz} = -0.1\%$, to $\varphi/\varepsilon_{zz} \approx 11^\circ/\%$ for $\varepsilon_{zz} = -1\%$. Hence, in the linear regime ($\varepsilon_{zz} = -0.1\%$) a characteristic scale of $N_c \approx 8$ can be deduced. Interestingly, for N smaller than this characteristic scale

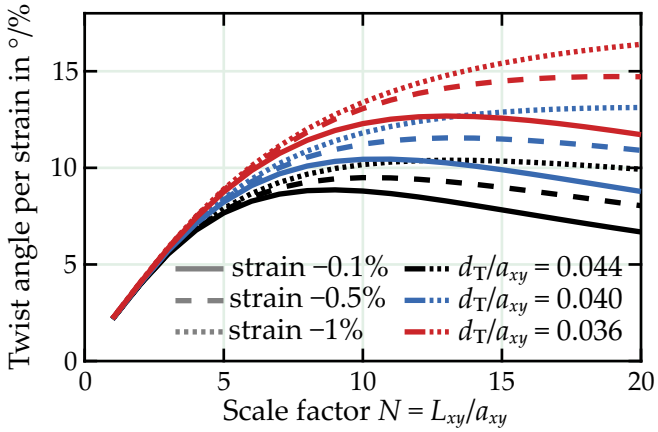

Figure 6.8: Calculated twist per axial strain using Timoshenko beam elements for different bar thicknesses d_T. Geometrical nonlinearities have been taken into account for axial strains of $\varepsilon_{zz} = -0.1\%, -0.5\%, -1\%$. Additional, the coupling of neighboring unit cells was studied by systematically varying d_T. This figure is adapted from [118].

$N_c \approx 8$, geometrical nonlinearities seem to play little to no role. Only, when N is about the size of N_c, nonlinear effects have a significant contribution and tend to increase even further with increasing N.

Another way to affect the coupling between unit cells and thereby the characteristic scale is to adjust the length c of the red bar depicted in Figure 6.5. Calculations using both Timoshenko beam and volume elements for two different bar lengths c are shown in Figure 6.9. Illustrations of the corresponding unit cell geometry are given on the right.

Obviously, a small c yields a small characteristic scale. The intuitive reasoning is equivalent to the considerations for different bar thicknesses d_T. The bending stiffness of a bar is inversely proportional to its length. Thereby, more energy is needed to bend short bars. Again, this makes it harder for neighboring unit cells to twist independently and results in a small characteristic length scale. Interestingly, nonlinearities seem to play less of a role for the smaller bar lengths c.

As can be seen in Figure 6.9, the twists per strain φ/ε_{zz} calculated using the Timoshenko beam model agree with to the twist angles calculated using standard volume elements for both bar lengths c depicted.

In conclusion, the modified unit cell exhibits a distinctive twist per axial strain indicating a significantly enhanced characteristic length scale with respect to its cubic counterpart in the finite element calculations. At the same time, the maximum twist angle is increased by nearly a factor of 5. Furthermore, by varying d_T or c, the characteristic length scale of the structure can be tuned.

Although general trends are reproduced nicely by this Timoshenko beam

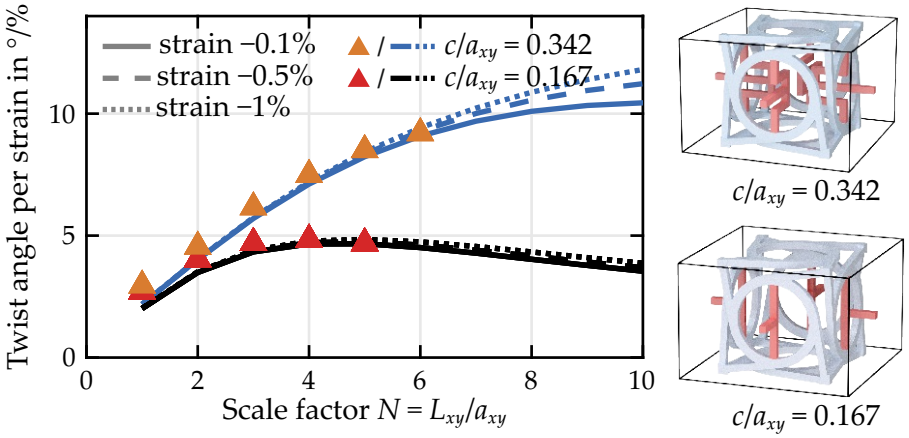

Figure 6.9: Calculated twist per axial strain using Timoshenko beam elements for different bar lengths c. Geometrical nonlinearities have been taken into account for axial strains of $\varepsilon_{zz} = -0.1\%, -0.5\%, -1\%$. Additional, the coupling of neighboring unit cells was studied by systematically varying the bar length c. All other geometrical parameters were kept constant and are given in Figure 6.5. This figure is adapted from [118].

model, the exact algebraic values should be taken with a grain of salt. For example, the Timoshenko beams grossly underestimate the effective Young's modulus of the metamaterial compared to the volume elements (not shown). This is most likely due to the fact that there is some ambiguity in converting the original 3D geometry into Timoshenko beam elements. Thereby, the lengths of bar may change or intersections of bars may not be taken into account correctly. Yet, keeping the drastic simplification of the model in mind, accompanied by the tremendous increase in accessible scaling factors N, the predictions of the Timoshenko approach are surprisingly good.

6.4 Experiments on Samples with Enhanced Characteristic Length

In this section, metamaterial samples out of the tetragonal unit cell depicted in Figure 6.5 are fabricated and characterized. Thereby, samples produced by two different 3D laser printing setups and hence made from different constituent materials are compared. Most of the samples produced by the Nanoscribe setup have been fabricated and characterized experimentally by Jonathan Schneider in the scope of his Bachelor Thesis. The samples from

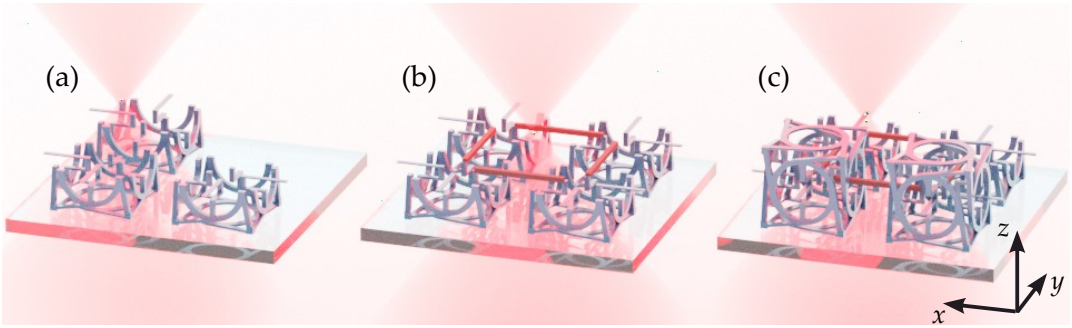

Figure 6.10: Printing strategy to avoid large overhanging objects. In a first step (a), the bottom half of the unit cell is printed, but the beams with length $2c$ are intentionally left out. Secondly, (b) only the previously left out bars (red) are printed. Thereby, both ends of the bar are connected to other parts of the unit cell at all times. Finally, (c), the writing field is shifted to its original position and the top half the unit cell is printed.

the multifocus 3D laser printer have been fabricated by Vincent Hahn and the author. The experimental characterization was also done by the author. The major findings of this section have also been published in [118].

6.4.1 *Printing Strategy*

Since the geometry of the unit cell changed compared to the one presented in chapter 5, the printing strategy also needs to be adjusted. Additionally, using the multifoucs 3D laser printer renders some of the problems and solutions conceived for the Nanoscribe systems obsolete. Especially the lattice constant can not be varied easily with this setup. Therefore, this time the experiments are conducted such that the lattice constant a_{xy} is kept constant, and thereby the sample side length L is varied accordingly.

Nanoscribe Setup

For the structures printed with the Nanoscribe setup (compare subsection 4.4.2), the lattice constant was set to $a_{xy} = 150\,\mu\text{m}$. The commercial photoresist IP-S and a $25\times$ NA $= 0.8$ objective lens was used. Thereby, 2×2 unit cells fit within a single writing field. Samples with foot prints larger than 2×2 were split along the borders of the unit cells into several writing fields containing 2×2 unit cells or less. Thus, the bar with length $2c$ is

split in half with one end being free floating till the neighboring unit cell is printed in consecutive steps. Unfortunately, this caused major structural defects. Hence, the following printing strategy was conceived. First, only the bottom halves of all unit cells in one layer was printed. The red bars with length $2c$ were intentionally left out. Secondly, these bars were added in a subsequent printing step. In doing so, the bars are supported on both ends by the previously written parts of the unit cell. In a last step, the top halves of the unit cell were printed. This strategy is illustrated in Figure 6.10. Thereby, most of the defects were avoided. Yet, the problem persists for the bars that are at the outer surface of the metamaterial sample. But since those bars are not involved in any deformation, these errors do not influence the measured results. A detailed list of the used writing parameters and voxel corrections is given in subsection A.1.2.

Multifocus 3D Laser Printing Setup

Printing samples with $N > 6$ using the Nanonscribe system would lead to infeasibly long writing times. Therefore, samples containing a large number of unit cells were fabricated using the multifocus 3D laser printing setup (compare subsection 4.4.3). For those, the lattice constant is actually predetermined by the spacing between the foci. The commercial photoresist IP-dip and a $40\times$ NA $= 1.4$ objective lens was used. Thus, the lattice constant was $a_{xy} = 74\,\mu\text{m}$. This setup could be switched between a one focus writing mode, or a mode with 3×3 foci writing in parallel. To take full advantage of the speed advantage of the multifoucs writing mode, only structures with integer multiples of three of the scale factor N were fabricated, e.g. $3 \times 3 \times 9$, $6 \times 6 \times 18$, etc. The largest samples with $N = 27$ contained 118,098 unit cells in total. The printing time for this structure was about 30 hours.

Again, the metamaterial was split up into multiple small writing fields of $3 \times 3 \times 0.5$ unit cells each. Thereby, the same connection problems of the red bar with length $2c$ occur in between writing fields as for the Nanoscribe system. Yet, similar measures to bypass this problem were not taken, since it can not be transfered easily to the multifocus setup. The plates with the markers to assist the image-cross correlation are fabricated using the single focus writing mode of the setup. A detailed list of the used writing parameters and voxel corrections is given in subsection A.1.2.

6.4.2 *Fabricated Samples*

Two sets of samples were fabricated, the first using the Nanoscribe instrumentation. For those, a lattice constant of $a_{xy} = 150\,\mu\text{m}$ was chosen and scaling factors of $N = 1, 2, 3, 4, 5, 6$ were realized. Exemplary optical micrographs and scanning electron micrographs are depicted in Figure 6.11. As for the structures of the previous chapter and as introduced in section 4.1, a right-handed structure was printed on top of a left-handed one, each containing $N \times N \times 3N$ unit cells. Due to the tetragonal symmetry of the unit cell with $a_{xy} = 2/3a_z$, this yields the same aspect ratio of the overall sample as for the cubic unit cells in the previous chapter. Plates were added both in the middle and the ends of the sample. Additionally, marker arrays were attached to the middle plate to facilitate the image cross-correlation. The samples were printed both by Jonathan Schneider in the scope of his Bachelor thesis and by the author. The pictures give evidence of the generally high printing quality.

The second set of samples was fabricated using the multifocus 3D laser printer and are depicted in Figure 6.12. The lattice constant was set to $a_{xy} = 74\,\mu\text{m}$ and different scaling factors of $N = 3, 6, 9, 12, 15, 18, 21, 27$ were printed both by Vincent Hahn and the author. Both the optical and the scanning electron micrographs demonstrate the high printing quality.

Notably, these samples are twisted right after fabrication. This can be assigned to shrinkage during the development process. Isotropic shrinkage would simply scale all dimension and hence would not lead to twisting, apart from effects due to the confinement at the glass substrate. Instead, some uniaxial stress or strain is required to induce the twist, hence the shrinkage must be asymmetric. Obviously, the printing procedure itself is highly asymmetric, since the voxel width and hight, as well as the slicing and hatching distances are different. Due to the sequential nature of the writing process, neighboring lines in a z-plane are written more or less simultaneously, whereas neighboring lines in different planes are written with some delay. All in all, this could cause local anisotropies of the constituting polymer network and thereby cause an asymmetric shrinkage. Remarkably, small differences in relative shrinkage in the axial and lateral direction can already cause large twist deformation. For example, for 10% axial and 9.9% lateral shrinkage, the relative difference of 1% is equivalent to an axial strain of the same order. Yet, as the simulation predicts, this already leads to twist

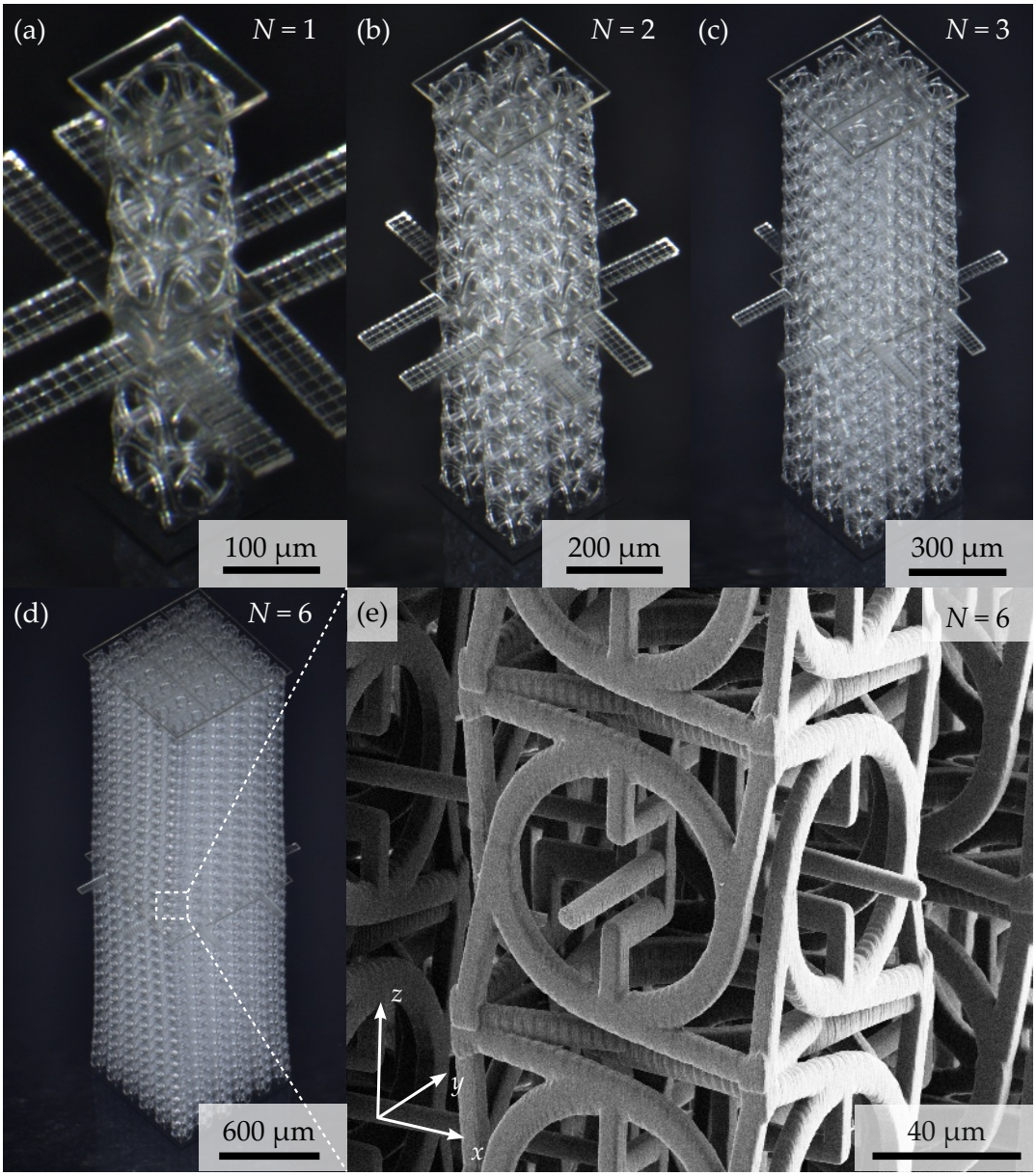

Figure 6.11: Gallery of 3D printed samples using the Nanoscribe instrumentation. Exemplary optical micrographs of samples for different scale factors $N = 1, 2, 3, 6$ are depicted in (a)-(d). Note that the scale bars change by a factor of 6. (e) shows a scanning electron micrograph of a single unit cell of the structure depicted in (d). This figure is adapted from [118].

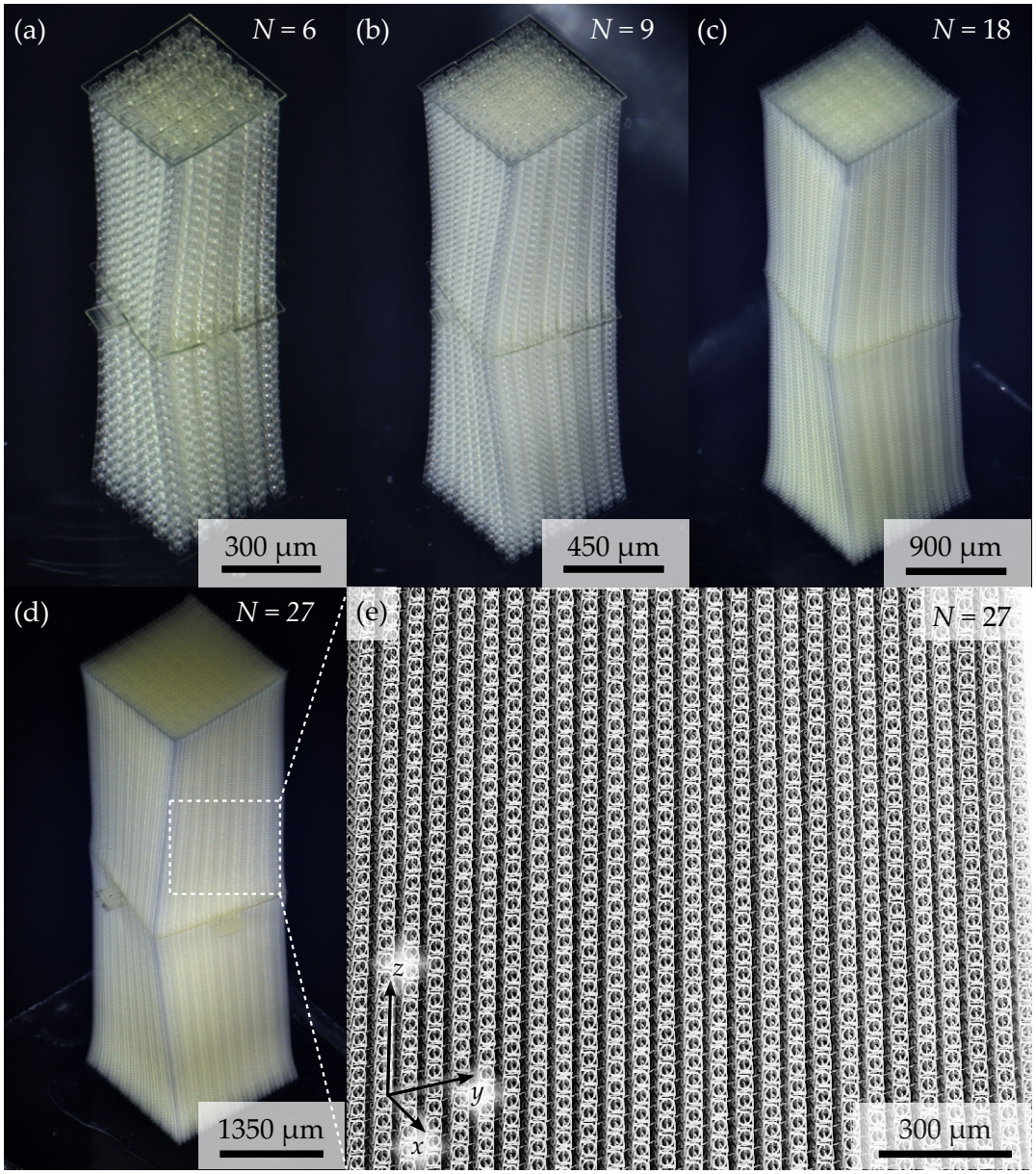

Figure 6.12: Gallery of 3D printed samples using the multifocus 3D printer. Exemplary optical micrographs of samples for different scale factors $N = 6, 9, 18, 27$ are depicted in (a)-(d). Note that the scale bars change by more than a factor of 4. (e) shows a scanning electron micrograph of a single unit cell of the structure depicted in (d). This figure is adapted from [118].

angles of up to 10°. Unfortunately, these small relative material asymmetries are unavoidable.

When examining Figure 6.12 even closer, differences between the 3×3 unit cells within one printing field can be observed. Especially bar thicknesses vary slightly and the shrinkage differs. This is caused by imperfections of the optical setup, which lead to uneven distributions of the laser power among the nine foci. Structures printed with a higher laser power appear thicker and tend to shrink less compared to structures produced with slightly less laser power. The relative power differences are on the order of 5% to 10%. Particularly, the different shrinkage factors of neighboring unit cells cause additional deformations. This also might contribute to the pretwist of the structure and might influence the performance of the structures.

6.4.3 *Twist per Strain of the Metamaterial Samples*

The measurement and post-processing of the recorded data was carried out the same way as introduced in the previous chapter. Most of the measurements of the Nanoscribe samples were conducted by Jonathan Schneider, whereas the measurements on the samples fabricated by the multifocus instrumentation were conducted by the author. The twist per axial strain φ/ε_{zz} measured for the samples fabricated by the Nanoscribe system (blue markers) and by multifocus 3D laser printer (red markers) are depicted in Figure 6.13. Each sample was probed using various external strains. Additionally, each measurement was repeated six times to examine repeatability and recoverability of the metamaterial samples. Furthermore, the reproducibility of the 3D printing precesses was checked, by carrying out experiments on multiple, nominally identical samples (dark and light marker shades).

The general trends predicted from the numerical models can be rediscovered in presented measurement data. Especially the linear increase of φ/ε_{zz} for small scaling factors N is retrieved nicely. Moreover, the samples fabricated using the Nanoscribe system and the multifocus 3D printing instrumentation yield comparable results, although different constituent materials and different lattice constants were used. For $N = 3$ and $N = 6$ the sample fabricated by the multifocus setup yield slightly smaller twist angles than the samples fabricated using the Nanoscribe system.

Considering only the measurements for the smallest strains, the maximum of φ/ϵ_{zz} is in the interval between $N = 6$ and $N = 9$. Hence, the experi-

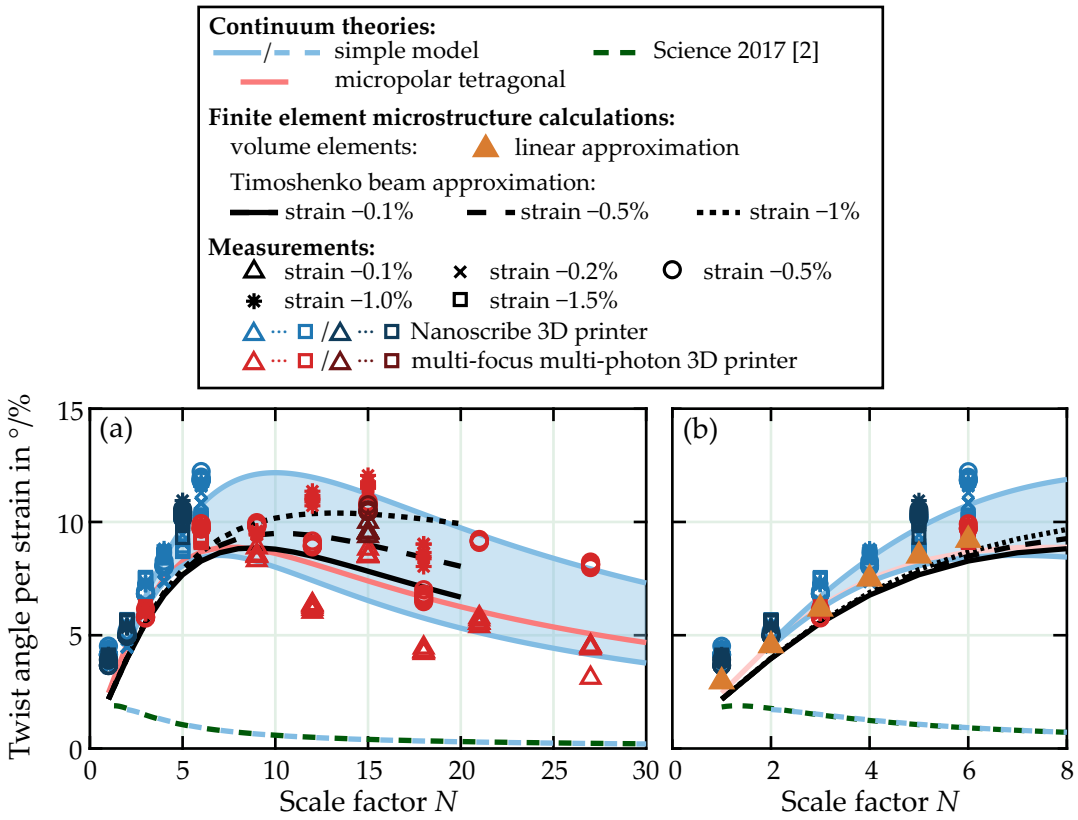

Figure 6.13: Summary of all experimental and numerical deduced twist angles per axial strain. Experimental data for scale factors ranging from $N = 1$ to $N = 27$ are depicted. Two 3D printing techniques, and thereby different constituent materials and different lattice constants a_{xy}, can be compared (red and blue marks). Experiments have been carried out for various external strains between $\varepsilon_{zz} = -0.1\%$ and $\varepsilon_{zz} = -1.5\%$ (different marker shapes). Furthermore, finite element calculations of the microstructure using standard volume (orange triangles) and Tiemoshenko beams (black lines) are presented. Additionally, the twist angles from the simple model (blue lines) for a range of characteristic numbers between $7 \leq N_c \leq 10$ is depicted, as well as the micropolar continuum calculations (pink line). For comparison, the results from the micropolar continuum of the previous chapter (dashed green line) are also plotted, as well as the simple model fitted to this curve (blue dashed line). Twist angles for scale factors N between 1 and 30 are shown in (a), whereas (b) focuses on the range between 1 and 8. This figure is adapted from [118].

mentally determined characteristic scale N_c is also in this range. Yet, the structures fabricated by the Nanoscribe system seem to suggest a slightly higher characteristic scale, but due to the limited accessible scaling factors it is difficult to draw conclusions from these samples alone.

For scale factors $N > 9$, pronounced nonlinearities can be observed. Generally, all samples show larger twist angles per axial strain for increasing strains. This fits to the general trends of the numeric calculations. Yet, the magnitude of this nonlinearity is much bigger in the experiments.

Repeating the same experiments on the same sample shows little to no difference (comparing same symbols of equal color for given N). This indicates that the samples are still functional after measurement, hence no structural damage took place. Comparing measurements of nominally equal samples (comparing different marker shades of the same color) yields relatively small deviations. Therefore, the sample fabrications seems reliable.

6.5 Effective Micropolar Material Parameters

As has been pointed out before in previous chapters and [15], being able to find effective material parameters is a key requirement to distinguish between metamaterials and ordinary structures. Hence, a set of material parameters of a micropolar tetragonal material shall be found. The corresponding tensors and constitutive relations have already been introduced in section 2.3. With the help of Yi Chen, Patrick Ziemke derived a first guess for the tensor elements following the lines of [145]. In a trial-and-error post optimization procedure, he derived the set of material parameters presented in subsection B.1.3

These parameters are chosen to mimic the behavior of a material with lattice constant $a_{xy} = 150\,\mu m$, constituent material's Young's modulus of $E = 2.6\,GPa$ and Poisson's ratio of $\nu = 0.4$. For clarification, this procedure is not suitable to retrieve theses parameters uniquely. A complete parameter retrieval would require a large number of simulations and therefore is well beyond the scope of this thesis. As illustrated in Figure 6.14, the continuum model nicely recreates the displacements field of the metamaterial calculated using the Timoshenko beam approach. Bot the radial dependency and also the magnitude of the displacements show good agreement. In Figure 6.13, the calculated twist angle per axial strain φ/ε_{zz} of the micropolar continuum is plotted as a function of N and compared to results of the Timoshenko

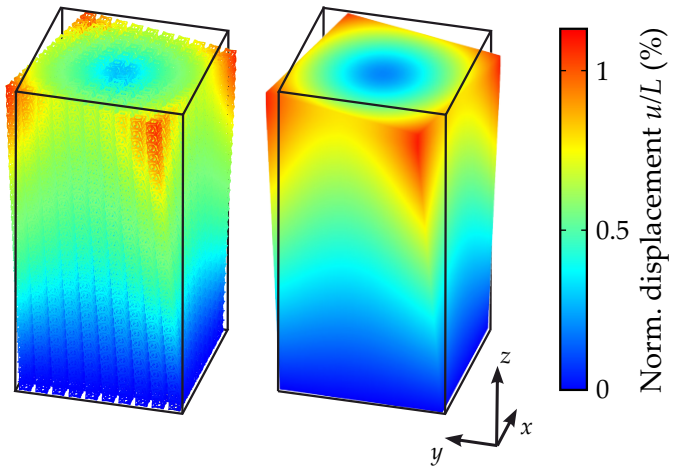

Figure 6.14: Calculated displacements for samples with $N = 10$ using Timoshenko beam elements (left) and a micropolar continuum (right) subjected to an axial strain of $\varepsilon_{zz} = -0.1\%$. For clarity, the deformation is enhanced by a factor of 15. The micropolar material nicely mimics the deformations of the Timoshenko beam approach. This figure is adapted from [118].

beam approach, the simple model, and the experiments. The qualitative scaling behavior of the metamaterial is captured excellently by the micropolar continuum theory. Only quantitatively, the maximum of φ/ε_{zz} is slightly shifted towards smaller scaling factors N. Whereas lower rotation angles are predicted for large N in the scope of the continuum model compared to the Timoshenko-beam calculations.

6.6 Discussion

In Figure 6.13 the twist per axial strain φ/ε_{zz} for all methods discussed in this chapter are summarized. These are: 1) the simple analytical model, 2) microstructure calculations using volume elements, 3) microstructure calculations using Timoshenko beams, 4) micropolar continuum calculations, and 5) experimental data. For clarity, the cases 1), 3) and 4) are depicted as continuous curves. Although for 1) and 3), only the integer values of N have physical meaning. For comparison, the results of the previous chapter are also depicted.

All data 1)-5) consistently exhibit the same qualitative behavior of φ/ε_{zz} as a function N. The twist angle increases linearly as a function of N, reaches a maximum, and decreases again. For the simple analytical model, a range for different values of $N_c = 7 - 10$ is depicted, for a fixed unit cell twist of $\varphi(1)/\varepsilon_{zz} = 2.4^\circ/\%$. Thereby, the simple model yields maximum twist angles of $8 - 12^\circ/\%$, which is $4 - 6$ times larger, than the maximum of the cubic unit cells of $\varphi/\varepsilon_{zz} \approx 2^\circ/\%$. Since φ/ε_{zz} scales $\propto N_c^2$ in the large sample

limite $N \to \infty$, the twist is 17-35 fold increased. Thereby, even for samples as large as $N = 27$, twist angles per axial strain exceeding $2^\circ/\%$ are achieved.

The red and blue data points in Figure 6.13 not only refer to different 3D printing setups, but also to different constituent materials and different lattice constants. Yet, the measured data points for $N = 3$ and $N = 6$ show good agreement. This confirms the theoretical findings that φ/ε_{zz} should neither depend on the constituent's Young's modulus, nor on the absolute value of a_{xy}. Instead, only the relative unit cell size $N = L/a_{xy}$ is relevant. The small differences most certainly trace back to imperfections of the samples fabricated with the multifoucs setup.

The Timoshenko beam calculations and the experimental data show huge nonlinearities for samples with $N > 6$, even for these generally small axial strains of $\varepsilon_{zz} \leq -1\%$. Both show an increase of the φ/ε_{zz} for increasing external strains. Yet, the nonlinearities found in the experiments are generally larger than their theoretic counterpart. This can have many reason. For instance, only geometrical nonlinearities are taken into account, but not the nonlinear response of the constituent material itself. Yet, these can become prominent for polymers, especially at locations of high stress concentration. Furthermore, it is unclear, whether the pretwist due to the shrinkage of the structure influences the geometrical nonlinearities. In case the shrinkage acts as an effective prestrain of the structure, this could also lead to an increased geometrical nonlinearity. Both, the simple model and the micropolar calculations neglect nonlinearities.

Surprisingly, the simple model with only two material parameters agrees well with the Timoshenko beam calculations for $\varepsilon_{zz} = -0.1\%$ and the micropolar continuum model. Especially, since for the latter a large number of 29 non-zero parameters is needed. By fitting the simple model to the Timoshenko beam calculations, effective values of $N_c = 7.2$ and $\varphi(1)/\varepsilon_{zz} = 2.4^\circ/\%$ have been deduced. In contrast, for the cubic unit cell of the previous sections the fitting yielded $N_c = 1.7$ and $\varphi(1)/\varepsilon_{zz} = 2.0^\circ/\%$. Obviously, the modifications of the unit cell led to an increase of the characteristic scale, and hence of the characteristic length $l_c = a_{xy}N_c$, by more than a factor of 4.

The micropolar model also describes the general behavior of the metamaterial well. Moreover, the extracted parameters are constant and do not depend on N. Hence, they can be understood as effective material parameters and the structure presented qualifies as metamaterial in the reasoning of [15].

Part II

ELASTODYNAMICS: ACOUSTICAL ACTIVITY

Chapter 7

7 Fundamentals of Elastic Waves

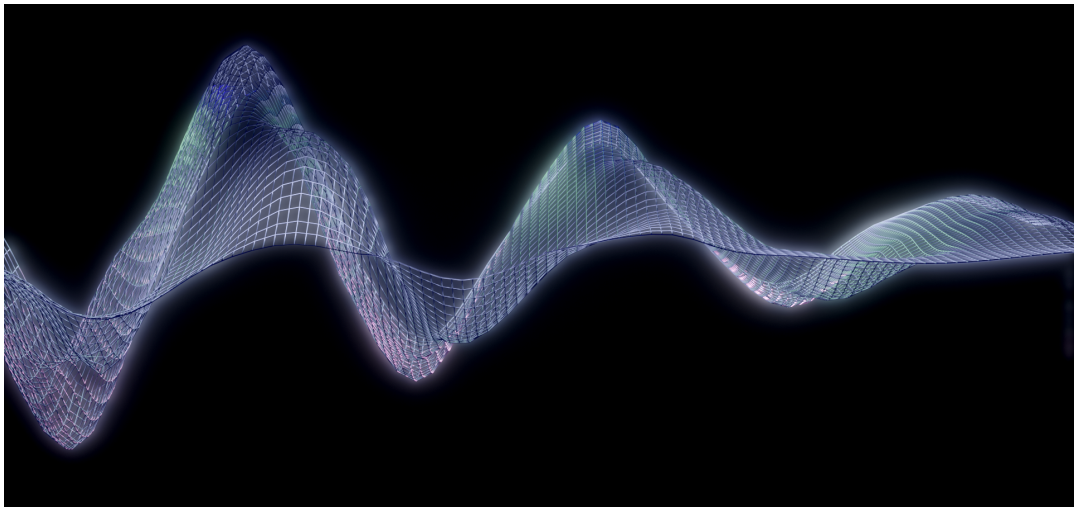

Artistic illustration of a wave package

Previously, the notion of chirality was discussed only in the context of quasi-static experiments. Meaning, velocities and accelerations were assumed to be zero. In this chapter, I will discuss the propagation of elastic waves. We start by recapitulating waves in classical Cauchy continuum. Afterwards, I will solve the wave equations for a micropolar continuum and will find nondegenerate circular polarized eigenstates. Finally, I will discuss acoustical activity, the elastic counterpart of optical activity, as a consequence of these eigenstates.

7.1 Elastic Plane Waves in Cauchy Continua

The solutions derived in the first part of this thesis all dealt with quasi static problems. Hence, the equations of motion (Equation 2.39) were solved assuming constant external forces $f_i = \text{const}$ and zero acceleration $a_i = 0$. Here, the equations of motion shall be solved for plane harmonic waves. The following is only meant as a short introduction. More details can be found in standard textbooks like in references [146, 147].

For simplicity, not the most general solution is derived. Instead, an infinitely extended cubic material is assumed and the wave should propagate along one of the principle axes, e.g. the z-axis. Therefore, the following ansatz for the components of the displacement vector is chosen:

$$u_i = U_i \exp(\mathrm{i}(k_j x_j - \omega t)). \tag{7.1}$$

Therein, ω denotes the angular frequency and is related to the ordinary frequency $f = \omega/(2\pi)$. For propagation along the z-direction, the wave vector $\vec{k}$ is given as

$$\vec{k} = \begin{pmatrix} 0 \\ 0 \\ k_z \end{pmatrix}, \tag{7.2}$$

with wave number $k_z = 2\pi/\lambda$ and wavelength λ. Be aware, that λ is commonly used both to denote the wavelength and one of the Lamé parameters.

This ansatz, together with the definition of the cubic elasticity tensor (Equation 2.49), yields three solutions of the equations of motion (Equation 2.39). The first solution with eigenvector $\vec{p}_3 = (0, 0, 1)$, has a dispersion relation $\omega_3(k_z)$ given by

$$\frac{\omega_3(k_z)}{k_z} = v_3 = \sqrt{\frac{C_{1111}}{\rho}}. \tag{7.3}$$

v_3 is the so-called phase velocity of the wave. The other two modes with eigenvectors $\vec{p}_1 = (1, 0, 0)$ and $\vec{p}_2 = (0, 1, 0)$ exhibit the same dispersion relation $\omega_{1,2}(k_z)$

$$\frac{\omega_{1,2}(k_z)}{k_z} = v_1 = v_2 = \sqrt{\frac{C_{1212}}{\rho}}. \tag{7.4}$$

The mode ω_3 refers to a longitudinal wave, since the eigenvector $\vec{p}_3$ and the wave vector $\vec{k}$ are parallel. ω_1 and ω_2 are linearly polarized transverse modes. Additionally, the latter modes are degenerate. For all modes, a linear

dispersion relation is found. Hence, the phase velocity does not depend on the wave number k_z.

7.2 Plane Elastic Waves in Micropolar Continua

To assess whether any new effects can be expected for plane waves in a chiral medium, the equations of motion (Equation 2.78 and Equation 2.78) need to be solved. This was done by Yi Chen in [60], assuming a chiral, cubic micropolar medium. There, the following ansatz for the displacement $\vec{u}$ and microdisplacement $\vec{\phi}$ was chosen

$$u_i = U_i \exp(\mathrm{i}(k_j x_j - \omega t)), \tag{7.5}$$
$$\phi_i = \Phi_i \exp(\mathrm{i}(k_j x_j - \omega t)). \tag{7.6}$$

Six eigensolutions can be found. Three of them represent displacement dominated acoustic waves, the others are rather dominated by the microdisplacements [60]. In the scope of this thesis, only the first are of relevance. The general analytical solution is quite lengthy and only little physical insights can be drawn from that. Yet, for wave propagation in z-direction and assuming the long wavelength limit $k_z \to 0$, the following simple solutions were derived [60]

$$\omega_{1,2} = \sqrt{\frac{C_{44}}{2\rho}} k_z \pm \frac{B_{44}}{2\sqrt{2\rho C_{44}}} k_z^2 \qquad \text{for } k_z \to 0, \tag{7.7}$$
$$\omega_3 = \sqrt{\frac{C_{11}}{\rho}} k_z - \sqrt{\frac{1}{\rho C_{11}}} \frac{B_{11}^2}{4C_{47}} k_z^3 \qquad \text{for } k_z \to 0. \tag{7.8}$$

Again, a longitudinal mode with frequency ω_3 and two transverse modes with frequencies $\omega_{1,2}$ are found. In contrast to the Cauchy continuum, all modes are dispersive for $\mathbf{B} \neq 0$. More importantly, in this case even the degeneracy between the two transversal modes is lifted. However, B_{44} is only nonvanishinging for a chiral medium (see section 2.3). This means that elastic waves in a micropolar medium are dispersive for chiral media even in this long wavelength approximation, , i.e. the phase velocities $v_i = \omega_i / k$ are k-dependent.

Yet, chirality not only influences the eigenvalues, but also the eigenvectors. For $\mathbf{B} \neq 0$, the transverse modes are no longer linearly polarized plane waves. Instead, they are polarized circularly. Thereby, the displacement vector

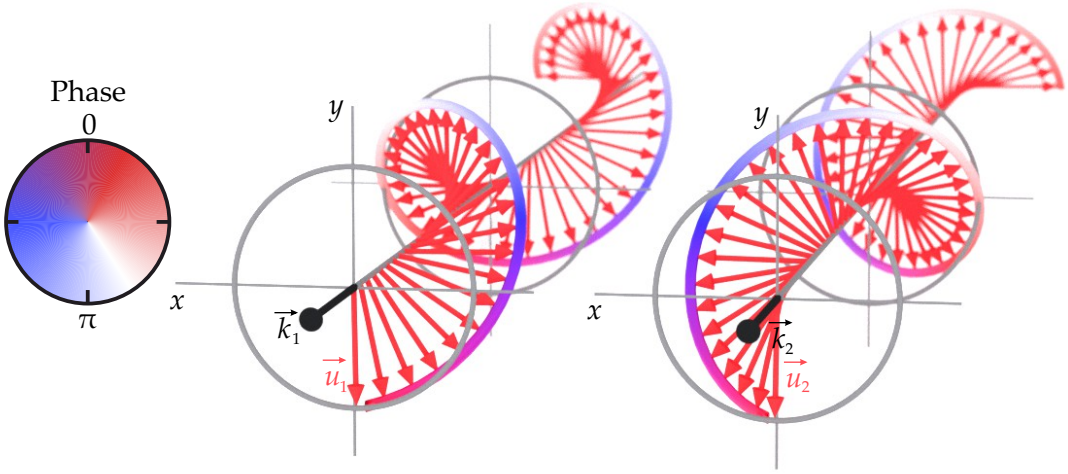

Figure 7.1: Snapshot of two circularly polarized eigenmodes. For these modes, the displacement vector $\vec{u}$ at a given position z_0 rotates around its reference point as a function of time. Since the degeneracy between the two modes is lifted, the modes propagated with distinct wave vectors $\vec{k}_1$ and $\vec{k}_2$. The phase $k_i z$ is indicated by the false colors.

$\vec{u}_{1,2}$ rotates clockwise or counterclockwise around its reference position. Consequently, the displacement vectors on a line in the propagation direction form a helix for a fixed time t_0. An illustration of two circularly polarized plane waves is given in Figure 7.1.

For extremely long wavelengths ($k_z \approx 0$), the k_z^2 terms can also be neglected. Therefore, the two transverse modes are again degenerate and their eigenvectors can be represented as two linear transverse waves. This means that for $k_z \approx 0$ the Cauchy limit is recovered (compare section 7.1). Together with the findings of section 2.3, this can be summarized as follows: Cauchy mechanics is only valid in the large sample limit, which can be defined as $\lambda/a \to \infty$ and $L/a \to \infty$. Violating one of these assumptions can lead to effects that go beyond the scope of Cauchy's theory. As will be shown in chapter 10, violating both assumptions at the same time will have the largest effects.

It is worth noting that these circularly polarized modes are only guaranteed to occur for selected propagation directions in a crystal. It can be shown that at least threefold rotational symmetry along the propagation direction is required [60, 148, 149]. Therefore, rather elliptical or even linear polarizations

are observed for most directions in a crystal. For chiral cubic crystals, the circular polarized eigenmodes are ensured to appear along the principle cubic axes and the space diagonals [60]. Yet, isotropic properties can be achieved by exploiting accidental degeneracies. Thereby, the structure is systematically adjusted, such that the numerical values of the entries of an arbitrary elasticity tensor become equal to those of an isotropic elasticity tensor. In [150], nearly isotropic chiral properties were achieved by using quasi crystals.

Circularly polarized eigenstates are not only predicted by the micropolar elasticity. Similar results are derived in theories based on spatial dispersion [34, 36], as well as in Willis elasticity [67, 68].

7.3 Acoustical Activity

Acoustical activity is the elastic counterpart of the better known optical activity [151]. In both effects, the polarization direction of a linearly polarized, transverse wave rotates upon propagation around the propagation direction. Thereby, the rotation angle is independent of the incident angle of the linear polarization and proportional to the propagation distance. Both effects are fundamentally linked to the notion of chirality and require two nondegenerate transverse circular polarized eigenstates. How these lead to a rotation of the polarization is derived in the following.

Mathematically, these circular polarized modes of the displacement vector can be described by the polarization vectors

$$\vec{p}_{1,2} = \frac{1}{\sqrt{2}} \begin{pmatrix} 1 \\ \pm \mathrm{i} \\ 0 \end{pmatrix}. \tag{7.9}$$

Note that the sign of the second components of $\vec{p}_{1,2}$ also depends on the sign of B_{44} and B_{47}. The whole displacement field $\vec{u}_{1,2}$ of a single mode is then given by

$$\vec{u}_{1,2} = A_{1,2} \begin{pmatrix} 1 \\ \pm \mathrm{i} \\ 0 \end{pmatrix} . \exp(\mathrm{i}(k_z z - \omega_{1,2} t)), \tag{7.10}$$

with the scalar amplitudes A_1 and A_2.

When exciting a wave with frequency ω_0 that is linearly polarized along the x-direction at $z = 0$ and propagating along z, a superposition of these

eigenmodes is excited

$$\begin{pmatrix} u_x \\ 0 \\ 0 \end{pmatrix} \exp(-\mathrm{i}\omega_0 t)) = \frac{u_x}{2\sqrt{2}} \left[\begin{pmatrix} 1 \\ \mathrm{i} \\ 0 \end{pmatrix} + \begin{pmatrix} 1 \\ -\mathrm{i} \\ 0 \end{pmatrix} \right] \exp(-\mathrm{i}\omega_0 t). \tag{7.11}$$

Keep in mind that the two modes are degenerate. Hence, they propagate with distinct wave vectors k_1 and k_2 for a given frequency of ω_0. Therefore, the wave at an arbitrary position z is given by

$$\vec{u}(z,t) = \frac{u_x}{2\sqrt{2}} \left[\begin{pmatrix} 1 \\ \mathrm{i} \\ 0 \end{pmatrix} \exp(\mathrm{i}k_1 z) + \begin{pmatrix} 1 \\ -\mathrm{i} \\ 0 \end{pmatrix} \exp(\mathrm{i}k_2 z) \right] \exp(-\mathrm{i}\omega_0 t). \tag{7.12}$$

Using $\Delta k = k_2 - k_1$ and $k_0 = (k_1 + k_2)/2$, this can be simplified

$$\vec{u}(z,t) = \frac{u_x}{2\sqrt{2}} \left[\begin{pmatrix} 1 \\ \mathrm{i} \\ 0 \end{pmatrix} \exp(-\mathrm{i}\Delta k\, z/2) + \begin{pmatrix} 1 \\ -\mathrm{i} \\ 0 \end{pmatrix} \exp(\mathrm{i}\Delta k\, z/2) \right] \exp(\mathrm{i}(k_0 z - \omega_0 t)), \tag{7.13}$$

$$\iff \vec{u}(z,t) = u_x \begin{pmatrix} \cos(\Delta k\, z/2) \\ \sin(\Delta k\, z/2) \\ 0 \end{pmatrix} \exp(\mathrm{i}(k_0 z - \omega_0 t)). \tag{7.14}$$

As a result, the wave is always polarized in a plane perpendicular to the propagation direction. Furthermore, the polarization is linear at any position z. Yet, the direction of the polarization is rotated by an angle ϕ, given by

$$\phi = \frac{\Delta k}{2} z. \tag{7.15}$$

It can be shown that ϕ is independent of the incident polarization, indeed.

As a result, acoustical activity can be observed, when a material exhibits two non-degenerate circular polarized eigenmodes. In the scope of the second part of this thesis, acoustical activity is studied in mechanical metamaterials in detail. Apart from the wave vector difference Δk, the rotation angle ϕ of the polarization will be the most important quantity.

The phenomenon of acoustical activity has already been verified experimentally decades ago. Pine was able to observe it in a chiral atomic crystal in 1970 [151]. Yet, the effect was comparatively small and frequencies in

the gigahertz regime are required to achieve reasonable rotations of the polarization. Using metamaterials, the frequency range can easily be tailored by simply scaling the lattice constant [60]. Therefore, metamaterials could smoothen the path towards real world applications and might exhibit rotational powers, which is the rotation angle per centimeter, exceeding the ones measured by Pine.

7.4 Waves in Periodic Structures

7.4.1 Bloch Waves

Bloch waves are a specific set of wave functions $\psi_{n\vec{k}}$, which are solutions of the Hamilton operator for periodic potentials. Originally, Bloch waves emerged in solid-state physics to describe electrons in a crystal. Yet, their implications can be generalized to any wave propagation in a periodic potential. Their general form is given by [152, 153]

$$\psi_{n\vec{k}} = \exp(\mathrm{i}\vec{k}\cdot\vec{x})u_{n\vec{k}}(\vec{x}). \tag{7.16}$$

In that, $\vec{k}$ denotes the wave vector, n describes the band index, and $u_{n\vec{k}}(\vec{x})$ is a function with the same periodicity as the crystal lattice. If $\vec{R}_{lnm}$ is a translation vector that connects a single lattice point to every other, then $u_{n\vec{k}}(\vec{x})$ obeys

$$u_{n\vec{k}}(\vec{x}) = u_{n\vec{k}}(\vec{x}+\vec{R}_{lnm}). \tag{7.17}$$

Consequently, the eigenstate $\psi_{n\vec{k}}$ can be chosen as

$$\psi_{n\vec{k}}(\vec{x}+\vec{R}_{lnm}) = \exp(\mathrm{i}\vec{k}\cdot\vec{R}_{lnm})\psi_{n\vec{k}}(\vec{x}). \tag{7.18}$$

This means that the eigenstate of a periodic system at two equivalent lattice sites $\vec{x}$ and $\vec{x}+\vec{R}_{lnm}$ differs by a phase factor $\exp(\mathrm{i}\vec{k}\cdot\vec{R}_{lnm})$.

Specifically, for the displacement vector $\vec{u}$ in a classical Cauchy continuum, this translates to

$$u_i(\vec{x}) = \exp(\mathrm{i}\vec{k}\cdot\vec{R}_{lnm})u_i(\vec{x}+\vec{R}_{lnm}). \tag{7.19}$$

In a micropolar continuum the Bloch conditions read [154]

$$u_i(\vec{x}) = \exp(\mathrm{i}\vec{k}\cdot\vec{R}_{lnm})u_i(\vec{x}+\vec{R}_{lnm}), \tag{7.20}$$

$$\phi_i(\vec{x}) = \exp(\mathrm{i}\vec{k}\cdot\vec{R}_{lnm})\phi_i(\vec{x}+\vec{R}_{lnm}). \tag{7.21}$$

As a result, the problem of solving the wave equation for an infinite crystal reduces to finding the periodic function $u_{n\vec{k}}(\vec{x})$ for a given wave vector $\vec{k}$.

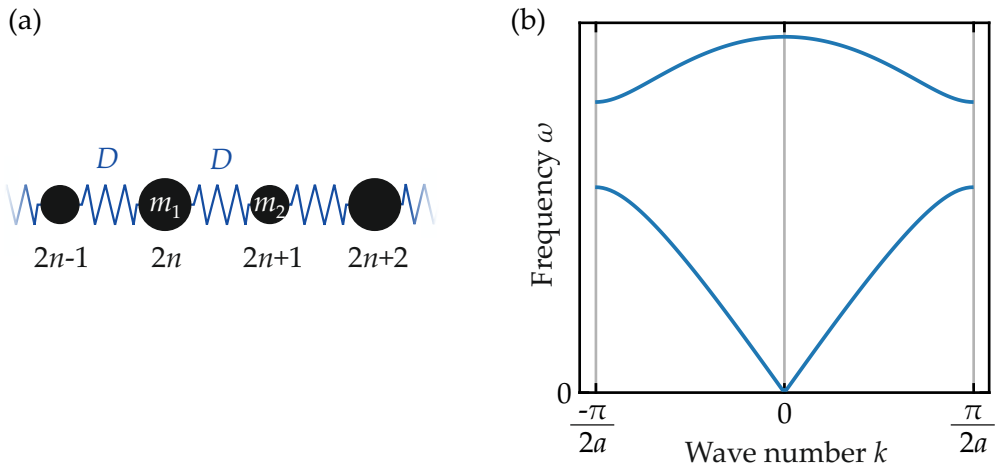

Figure 7.2: (a) Illustration of a 1D diatomic chain. (b) Bandstructure of 1D diatomic chain.

7.4.2 1-Dimensional Diatomic Crystal

To get used to the particularities of periodically structured materials, the simple case of a 1D diatomic crystal is discussed here. More details can be found in [9]. This crystal should be built up of two atoms with mass m_1 and m_2 in an alternating fashion. The interaction is modeled by Hooke springs with spring constant D. An illustration of this model is depicted in Figure 7.2(a). Atoms with odd numbers have the mass m_1 and atoms with even numbers have the mass m_2. Furthermore, $m_1 > m_2$ is chosen and the spacing between atoms is given by a. Hence, the crystal periodicity is $2a$.

For this system, the equations of motion with respect to the adjacent atoms are given by

$$m_1 \ddot{u} = D(u_{2n+1} - u_{2n} + u_{2n-1}), \tag{7.22}$$
$$m_2 \ddot{u} = D(u_{2n+2} - u_{2n+1} + u_{2n}), \tag{7.23}$$

wherein u_n denotes the displacement of the n-th atom. In accordance with the Bloch waves of the previous subsection, the following ansatz is applied

$$u_{2n} = A \exp(\mathrm{i}(2kna - i\omega t)), \tag{7.24}$$
$$u_{2n+1} = B \exp(\mathrm{i}(2k(n+1)a - i\omega t)). \tag{7.25}$$

Note that distinct complex amplitudes A and B were chosen for the odd and

even atoms. Inserting these into the equations of motion yields

$$(2D - m_1\omega^2)A - 2D\cos(ka)B = 0, \tag{7.26}$$

$$-2D\cos(ka)A + (2D - m_2\omega^2)B = 0. \tag{7.27}$$

This eigenwert problem can be solved by demanding

$$\det\left(\begin{pmatrix} 2D - m_1\omega^2 & 2D\cos(ka) \\ -2D\cos(ka) & 2D - m_2\omega^2 \end{pmatrix}\right) = 0. \tag{7.28}$$

From that, the following solution is derived

$$\omega_{1,2}^2 = D\left(\frac{1}{m_1} + \frac{1}{m_2}\right) \pm \sqrt{D^2\left(\frac{1}{m_1} + \frac{1}{m_2}\right)^2 - \frac{4D^2}{m_1 m_2}\sin^2(ka)}. \tag{7.29}$$

These are the dispersion relations for a longitudinal elastic wave in a 1D diatomic crystal. They are plotted in the band structure depicted in Figure 7.2. Obviously, the solution has periodicity of π/a. Therefore, the solutions are represented in the interval $[-k/(2a), k/(2a)]$, the so-called first Brillouin zone.

Interestingly, two solutions ω_1 and ω_2, the so-called bands, are found for every k. This is caused by the two atomic basis of the unit cell. Generally, the number of bands is proportional to the number of atoms per unit cell, as well as to the number of degrees of freedom per atom. Therefore, a 3D crystal with a mono-atomic basis exhibits three bands, the same crystal with a di-atomic base has 6 bands [155].

Chapter 8

8 Numerical Methods for Elastodynamic Problems

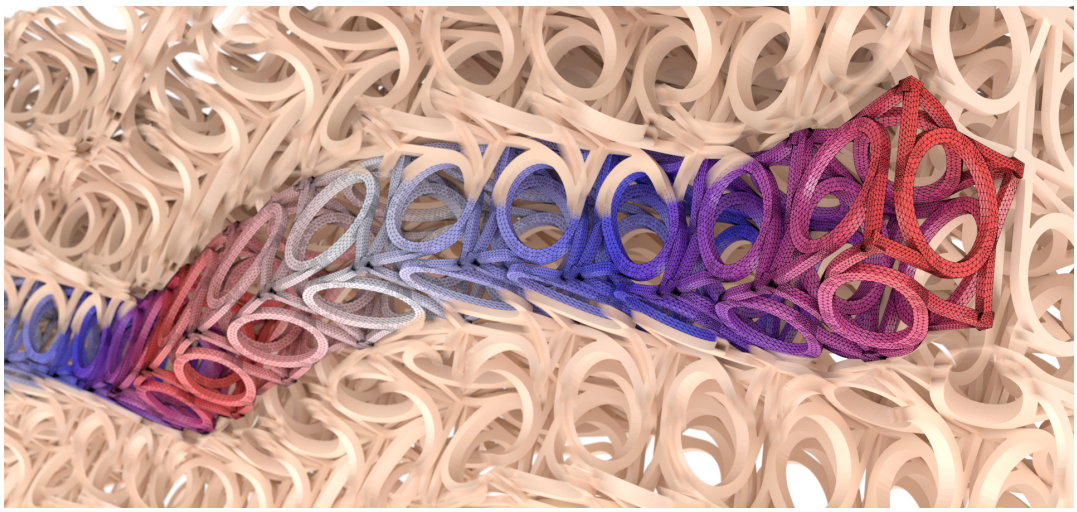

Artistic rendering of a chiral phonon mode

For the numerical calculations, I will again fall back on the finite element method, which was already introduced in the first part of this thesis. Here, I zoom in on a couple of techniques, which are particularity helpful when considering wave propagation in periodic structures. First, I will pick up on Bloch's Theorem. Subsequently, this theorem is exploited for the implementation of band structure calculations. Finally, the so-called frequency domain is introduced.

8.1 Finite Elements Band Structure Calculations

Eigenfrequency Analysis

As has been illustrated in the example for the 1D diatomic crystal in the previous section, calculating band structures is equivalent to an eigenvalue problem. Here, the derivation of the eigenvalue problem in finite elements for a Cauchy continuum is sketched. As in section 3.2, the weak form of the differential equations is calculated. Yet, this time the time derivatives are considered nonvanishing. Using the same ansatz functions as in section 3.2, this yields [111]

$$\int_\Omega \rho \frac{\partial^2 u_i}{\partial t^2} \delta v_i \mathrm{d}V + \int_\Omega C_{ijkl} u_{i,j} \delta v_{i,j} \mathrm{d}V - \int_\Omega b_i \delta v_i \mathrm{d}V - \int_{\partial\Omega} t_i \delta v_i \mathrm{d}A = 0. \tag{8.1}$$

In analogy to section 3.2, this can be expressed as

$$M_{ab} \frac{\partial^2 c_{bi}}{\partial t^2} + K_{aibk} c_{bk} - F_{ai} = 0, \tag{8.2}$$

with the stiffness matrix K_{aibk} and the mass density matrix M_{ab}. Assuming plane harmonic waves and neglecting external forces $F_{ai} = 0$, the following eigenvalue problem is found [111]

$$(-M_{ab}\omega^2 + K_{aibk}) c_{bk} = 0. \tag{8.3}$$

In COMSOL, these equations are already implemented when using the eigenfrequency analysis study in the solid mechanics module [113]. To solve this eigenvalue problem, the direct solver MUMPS was used in the scope of this thesis.

Bloch-Periodic Boundaries

In section 7.4, it has been shown that the eigensolution $\psi_{n\vec{k}}$ of an infinite crystal is the product of a lattice-periodic term $u_{n\vec{k}}$ and a phase given by $\exp(\mathrm{i}\vec{k} \cdot \vec{x})$. Since $u_{n\vec{k}}$ has the same periodicity as the crystal, the eigensolutions $\psi_{n\vec{k}}$ are completely defined, when a solution for $u_{n\vec{k}}$ is found in the domain of a single unit cell. In other words, the band structure can be

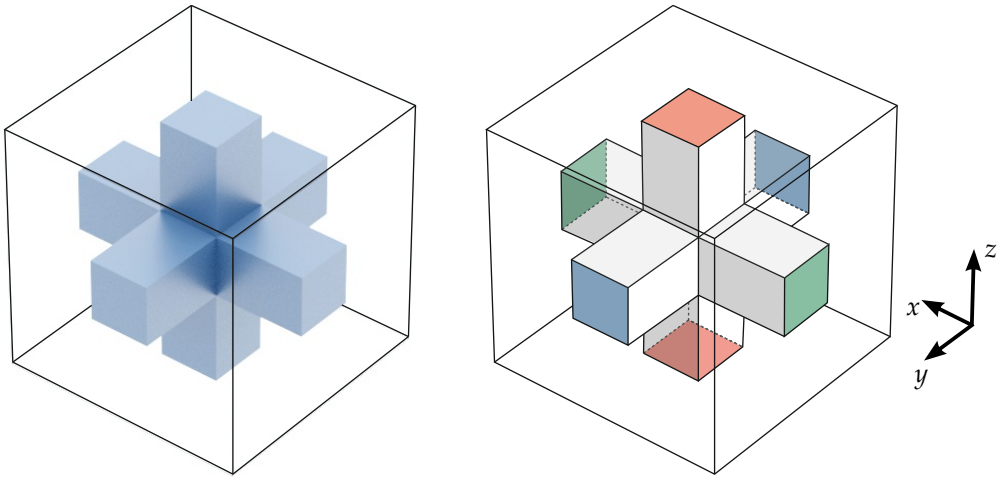

Figure 8.1: Illustration of an exemplary cubic unit cell with Bloch periodic boundaries. On the right hand side, the displacements on the outer surfaces of the unit cell with equal colors (red, blue, and green) are linked via the Bloch conditions. For example for the blue boundaries, they yield $\vec{u}(x, y, z) = \exp(ik_y a)\vec{u}(x, y + a, z)$.

calculated by finding the eigenfunction $u_{n\vec{k}}$ and its eigenvalue for a single unit cell for a given $\vec{k}$.

Therefore, an eigenfrequency analysis as introduced before is conducted with Bloch periodic boundary conditions assigned to equivalent points of the unit cell's outer surface. These boundary conditions simply state that the displacement of these equivalent points are linked by

$$u_i(\vec{x}) = \exp(\mathrm{i}\vec{k} \cdot \vec{R}_{lnm}) u_i(\vec{x} + \vec{R}_{lnm}). \tag{8.4}$$

An example for a simple unit cell is depicted in Figure 8.1. The planes of equal color at the outer surfaces of the cubic unit cell (green, blue, red) are connected via the Bloch periodic boundaries. For a point in the green plane this means

$$\vec{u}(x, y, z) = \exp(\mathrm{i}k_x a)\vec{u}(x + a, y, z), \tag{8.5}$$

with a being the lattice constant.

8.2 Finite Elements Frequency Domain Calculations

The frequency domain is another method to simplify the partial differential equation. In that it is assumed that the motion of all nodes is time harmonic and that all nodes oscillate with the same frequency ω [113]. Hence, frequency domain calculations compute the stationary state of an oscillation for a given frequency ω. The ansatz for the i-th component of the displacement of a node is given by

$$u_i(\vec{x}, t) = U_i(\vec{x}) \exp(-\mathrm{i}\omega t). \tag{8.6}$$

In that, every node has a different complex amplitude $\vec{U}(\vec{x})$. Information both about magnitude and phase of the oscillation is contained. Plugging this ansatz into the equations of motions yields a problem comparable to the one already discussed in section 3.2. Hence, it is solved in a similar fashion.

In COMSOL, the equations for frequency domain studies are already implemented in the solid mechanics module [113]. Note, prescribing a displacement in frequency domain implies a time harmonic excitation, not a static displacement. The same holds true for boundary loads.

Chapter 9

9 Dynamic Measurement Setup and Fabrication Methods

Rendering of tuning forks under stroboscopic illumination

In this chapter, I will present the self-build measurement setup to measure the rotation of the polarization vector due to acoustical activity. Before that, I will discuss that a standing wave pattern does not influence this rotation angle. Therefore, it will not be necessary to observe transient waves. Finally, I will present a measurement of the constituent material's Young's modulus, which is needed to compare the numerical and experimental data.

9.1 Propagating versus Standing Waves

The optical rotation of an optically active medium is usually measured using a polarimeter. In that, linear polarized light is sent through an optically active media of finite length. The light leaves the sample and is analyzed by a polarizer in air. By rotating the polarizer, the angle of maximum transmission is deduced and thereby, the direction of the linear polarization.

Unfortunately, this measurement method is not easily transferable to elasticity. Not least, because these transverse elastic waves do not propagate in vacuum or air, in contrast to electromagnetic waves. Hence, to investigate transient waves, a measurement would have to take place in the middle of an elongated sample. It should be long enough, so the reflections at the end do not reach the point of observation before the measurement is finished. This would lead to unfeasibly large samples and long fabrication times.

Luckily, it can be shown that a standing wave in a sample with finite length exhibits the same polarization rotation as the transient wave. Consider an acoustically active material, infinitely extended along x- and y-direction, but with finite length H along the z-direction. At one end ($z = 0$), a wave polarized along x is launched into the $+z$-direction. According to Equation 7.14, at the other end of the sample the polarization direction is given by

$$\begin{pmatrix} \cos(\Delta k\, H/2) \\ \sin(\Delta k\, H/2) \\ 0 \end{pmatrix}. \tag{9.1}$$

In that, the wave vector difference is defined as $\Delta k = k_1 - k_2$. For simplicity, it should be assumed that $k_1 > k_2$. Therefore, the phase velocity v_1 of the first band is smaller than the one of the second band v_2. Additionally, k_1 shall correspond to a right-handed circular polarized wave, and k_2 to the left-handed one.

At the other end, the wave is reflected back. Hence, the wave vector's z-component k_0' of the reflected wave is given by $k_0' = -k_0$. Equivalently, the wave vectors of the circularly polarized eigenstates revert their signs, yielding $k_1' = -k_1$ and $k_2' = -k_2$. At the same time, the handedness of the waves is reversed. Meaning, the right-handed wave is reflected as a left-handed wave and vice versa. Thereby, the former fast traveling mode with phase velocity v_2 is reflected as a slow mode with v_1. As a result, the phase difference between the right- and left-handed mode reduces upon further propagation. Therefore, the polarization direction of the backwards

propagating wave is given by

$$\begin{pmatrix} \cos(\Delta k(H-z)/2) \\ \sin(\Delta k(H-z)/2) \\ 0 \end{pmatrix}. \tag{9.2}$$

Hence, the backward propagation wave exactly reverses the polarization rotation (Note that the coordinate system's z-component of the reflected wave is chosen to point in the propagation direction. Thus, z goes from $z = 0$ to $z = H$). As a consequence, incident and reflected wave have the same polarization direction at $z = 0$. When considering multiple reflections at both ends, the argument above still holds true.

In conclusion, the polarization rotation of a standing wave pattern after a certain propagation distance is the same as for transient waves. Nevertheless, due to interference, the amplitude of the oscillations might be amplified or reduced. Consequently, the acoustical rotation can be measured by comparing the polarization direction of a standing wave pattern at both ends of a sample with finite length.

9.2 Measurement Setup

The acoustical activity of metamaterial samples, that were fabricated using the same 3D printing technique as in the previous part, shall be measured. Therefore, a measurement setup needs to satisfy the following requirements:

1) Excite standing waves at a defined frequency f in the metamaterial sample within the frequency range of $20 - 200\,\mathrm{kHz}$.

2) Extract the polarization vector at both ends of the metamaterial sample with nanometer precision.

Despite these demanding requirements, the realized setup is surprisingly simple. Its key components are depicted in Figure 9.1 and its basic working principle is the following: A piezoelectric element is driven time-harmonically and excites the metamaterial sample. Two near infrared light emitting diodes (LED) illuminate the sample stroboscopically. The frequency of this illumination is slightly detuned with respect to the excitation of the piezoelectric element. Thereby, the oscillations can be observed in slow motion without the need of ultrafast cameras. In fact, the utilized microscope setup and

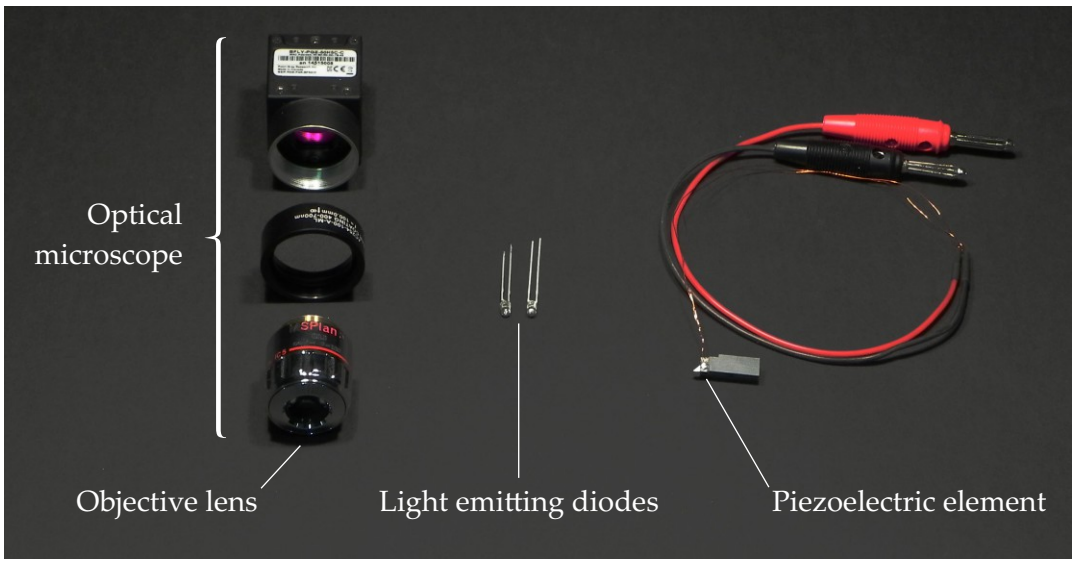

Figure 9.1: Depiction of the key components of the measurement setup. Two optical microscopes were used to monitor the sample. Using a piezoelectric element, harmonic waves were excited. Two infrared light emitting diodes (LED) were used to stroboscopically illuminate the samples. Thereby, the frequency of the illumination was detuned by 0.75 Hz with respect to the frequency of the harmonic waves. In that fashion, slow motion films of the oscillation were recorded, which were used to deduce the displacement vectors.

cameras are similar to the ones discussed in section 4.2. Using the same image-cross correlation algorithms as introduced in section 4.3, the displacement can be measured as a function of time. From that, the polarization vectors are calculated. More details on the individual components are given in the following.

Piezoelectric Transducer

Due to the small lattice constant of the metamaterial, relatively high frequencies in the range of 20 to 200 kHz are needed for characterization. At the same time, reasonably large displacements are desirable to facilitate the measurement. Therefore, a piezoelectric element was the natural choice. A multilayer piezoelectric transducer was used (Physik Instrumente, PICMA Chip Actuator) with outer dimension of $3 \times 5 \times 2\,\mathrm{mm}^3$. When mounted, resonances around 300 kHz and 500 kHz were deduced by impedance mea-

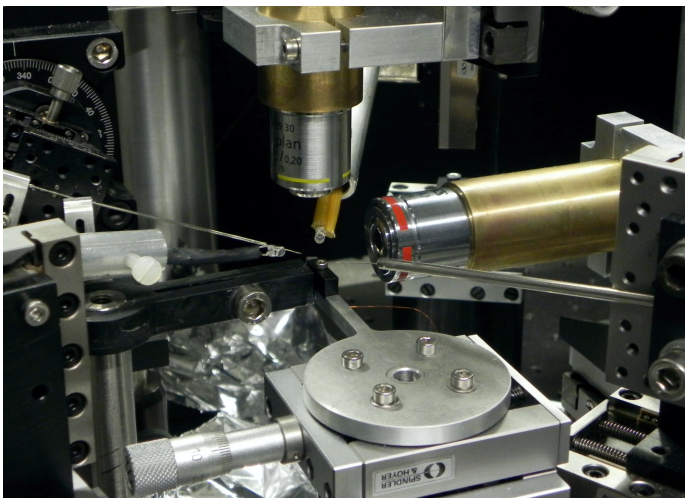

Figure 9.2: Photograph of the measurement setup. The sample was monitored both from the top and from the side using two microscopes. Two glass fibers mounted on micrometer stages were used to position the sample on the piezoelectric transducer.

surements. By design, the dominant oscillation is a thickness mode in the direction of the smallest dimension. To excite a transverse wave in the metamaterial sample, the piezoelectric element was mounted vertically and an aluminum wedge was attached to it. This additional mass reduces the resonance frequency significantly and was found experimentally to be around 120 kHz. The piezoelectric transducer was driven by a 4-quadrant voltage amplifier (Hubert, A 1230-01).

Stroboscopic Illumination

For the stroboscopic illumination, two light-emitting diodes (Vishay, VSLY 3850) with a center wavelength of 850 nm were used. These are capable of emitting light-pulses as short as FWHM = 70 ns. The current for the diodes was supplied using a custom-built driver.

Electrical Layout

Both the signal for the piezoelectric element and the LED were sent by a frequency generator. For the LED, a step function with a duty cycle 1.5% and an amplitude of 2 V was generated. An amplifier provided the necessary current to drive the LEDs. As depicted in Figure 9.3, the emitted light pattern is slightly smeared out compared to the sharp step function received from the frequency generator.

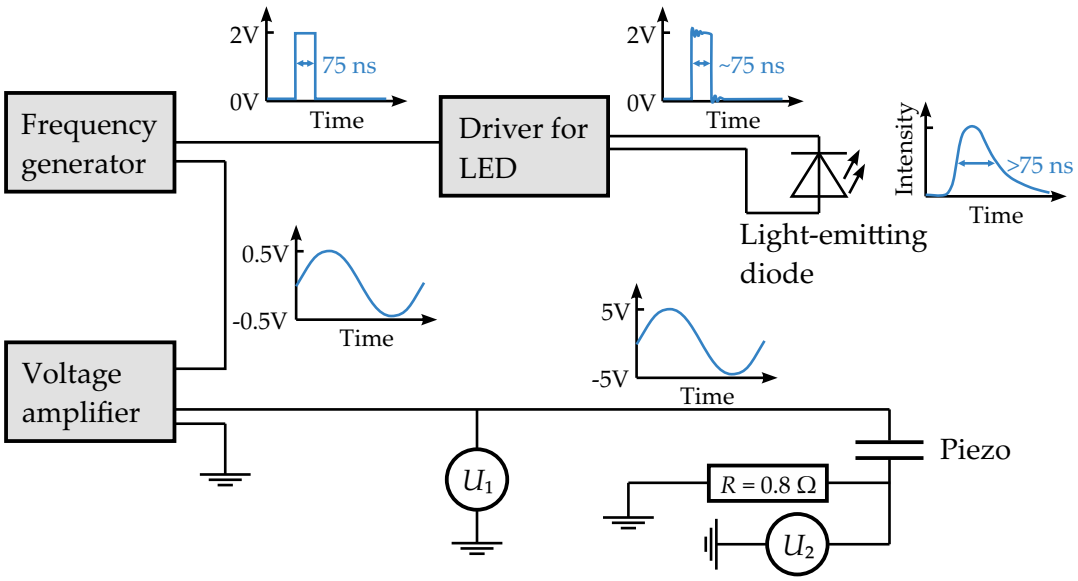

Figure 9.3: Electrical layout of the self-built measurement setup. A frequency generator was used to generate the signals both for stroboscopic illumination and the piezoelectric transducer. The pulse shapes are schematically plotted next to the different devices. The values for the pulse lengths refer to a frequency of 200 kHz and a step function's duty cycle of 1.5%.

A second, sinusoidal signal was created by the frequency generator in parallel and sent to the voltage amplifier. This increased the voltage by a factor of 10. For the experiments, the piezoelectric element was driven with an amplitude of $\pm 5\,\mathrm{V}$. The frequency of the signal sent to the LED was detuned by 0.75 Hz with respect to the frequency sent to the piezoelectric element.

Additionally, the voltage drop U_2 at the piezoelectric element was measured with an oscilloscope. Exploiting a resistor with $R = 0.8\,\Omega$, the current through the piezoelectric element was deduced by measuring the voltage drop U_1. Thereby, the frequency-dependend impedance of the piezoelectric element can be determined. The entire scheme of the electrical layout is depicted in Figure 9.3. The frequency generator, the oscilloscope, and the voltage amplifier are addressed by a personal computer using MATLAB.

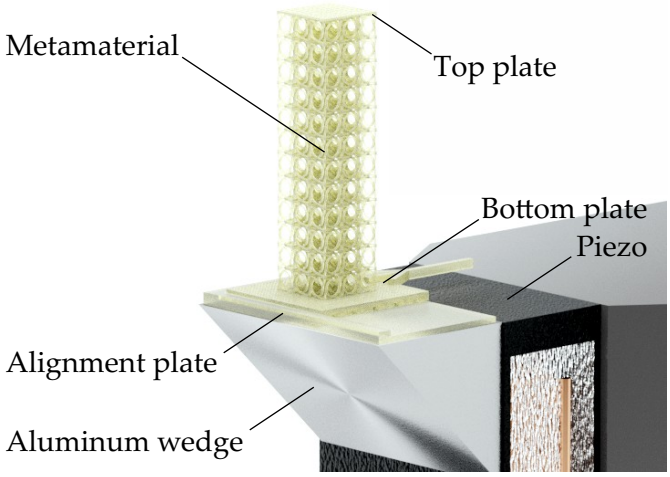

Figure 9.4: Illustration of the piezoelectric transducer with the mounted sample. To excite a transverse mode in the metamaterial, an aluminum wedge was attached to the piezo's surface. To facilitate the alignment, a plate was printed onto this wedge with edges that guide the sample's bottom plate to the proper position.

Sample Holder

Putting large masses on the piezoelectric element, like the glass substrate necessary for printing, would result in low amplitudes of the excited wave. Hence, the samples were taken off the substrate after fabrication. Therefore, unsilanized cover slips were used. To facilitate the handling, the samples were printed onto a bottom plate with an arm attached to it, which can be grabbed by a tweezer.

Afterwards, the sample is placed on the aluminum wedge attached to the piezoelectric element. To facilitate the alignment and ensure proper contact to the piezoelectric element, a plate was also printed on the aluminum wedge. The whole arrangement is sketched in Figure 9.4. Two glass fibers were used to move the sample and clamp it, before it was glued to the piezoelectric element (Uhu plast special Modellbau-Kleber). Channels at the bottom of the plate distributed the glue evenly. After the measurement, the samples were removed using acetone.

9.3 Characterization of the Constituent Material

To compare the numerical and experimental data, the constituent material's Young's modulus needs to be determined. Although the material is the same one as in the previous chapter, the effective Young's modulus for a given frequency might differ from the static case due to its viscoelastic properties. Therefore, an additional experiment was conceived to measure the Young's

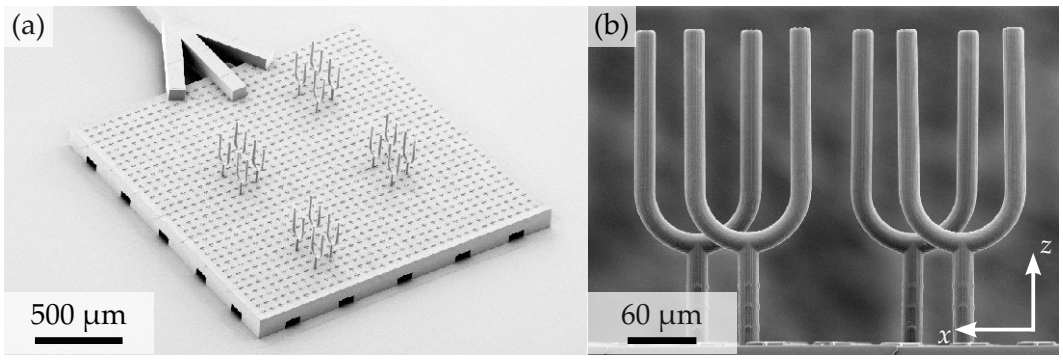

Figure 9.5: Scanning electron micrographs of the fabricated tuning forks. (a) Overview of a whole array of tuning forks, that were printed on a bottom plate. The close up in (b) impressively illustrates the fabrication accuracy. These tuning forks were fabricated from the same constituent material that was used for the dynamic experiments on the metamaterial. By characterizing one of the fundamental asymmetric modes, the complex constituent's Young's modulus was determined. This figure is adapted from [122] (CC BY 4.0).

modulus for the relevant frequency range.

Conceptually, the eigenfrequency of an elastic eigenmode is proportional to the square root of the real part of the constituent material's Young's modulus. Furthermore, the ratio between the amplitude of the excitation and the amplitude of the oscillation for a given frequency is determined by the material's damping. For harmonic waves, the damping is captured by the imaginary part of the Young's modulus. As a consequence, by studying the resonance of a known elastic system, the real and imaginary part of the Young's modulus can be deduced.

In [122] and in the scope of Erik Jung's bachelor thesis, Erik Jung and Julian Köpfler studied one of the fundamental antisymmetric resonances of tuning forks. Thereby, they 3D printed micro-tuning forks using the Nanoscribe instrumentation and characterized them using the setup introduced in section 9.2. In contrast to the experiment shown later, these tuning forks were excited along the z-direction, whereas the arms of the tuning forks oscillated along the x-direction. Scanning electron micrographs of the fabricated samples are depicted in Figure 9.5. Using image-cross correlation, both the enhancement of the amplitude and the phase shift with respect to the excitation was determined as a function of frequency. The results were compared to finite-element calculations of the tuning forks. Via a

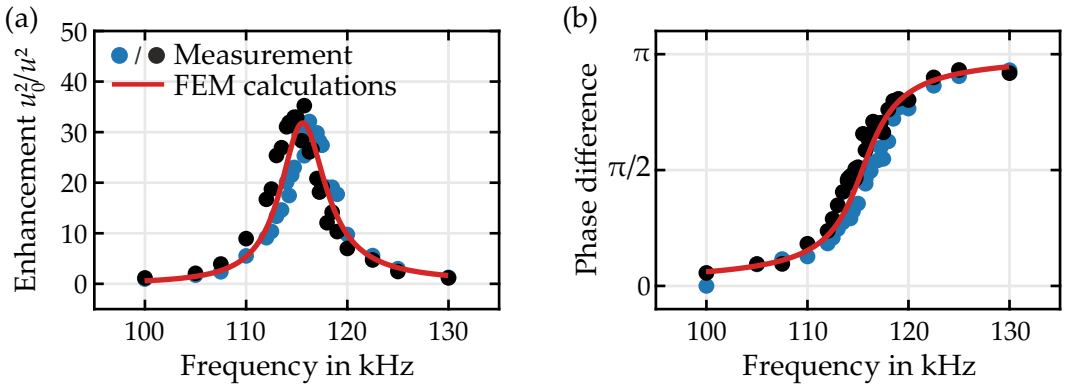

Figure 9.6: Characterization of a tuning fork's antisymmetric resonance mode. (a) the amplitude enhancement u_0^2/u^2 and (b) the phase difference between excitation and response of the samples depicted in Figure 9.5 were measured as a function of frequency. The experimental results and two nominally identical tuning forks are depicted as blue and black points. These are compared to finite element calculations of the tuning forks. Via a least-squares approach, the best fitting complex Young's modulus was deduced. This figure is adapted from [122] (CC BY 4.0).

least-squares approach, the best fitting material parameters were deduced. According to [122], the complex Young's modulus $E = E' + \mathrm{i}E''$ is given by

$$E' \pm \Delta E'_{\text{sys.}} \pm \Delta E'_{\text{stat.}} = (4.18 \pm 0.32 \pm 0.07)\,\text{GPa}, \tag{9.3}$$

$$E'' \pm \Delta E''_{\text{sys.}} \pm \Delta E''_{\text{stat.}} = (0.21 \pm 0.02 \pm 0.01)\,\text{GPa}, \tag{9.4}$$

whilst assuming a mass density of $\rho_0 = 1.15\,\text{g}\,\text{cm}^{-3}$.

Interestingly, this is nearly twice as high as the static Young's module measured in [104]. On top of that, the ratio between real and imaginary part is approximately 5%. This means that the damping is quite pronounced in this polymer. Previous studies on cured epoxies, poly(methyl methacrylate), poly(dimethyl siloxane), and SU8 yielded qualitatively similar results [156, 157].

Chapter 10

10 Acoustical Activity in Metamaterials

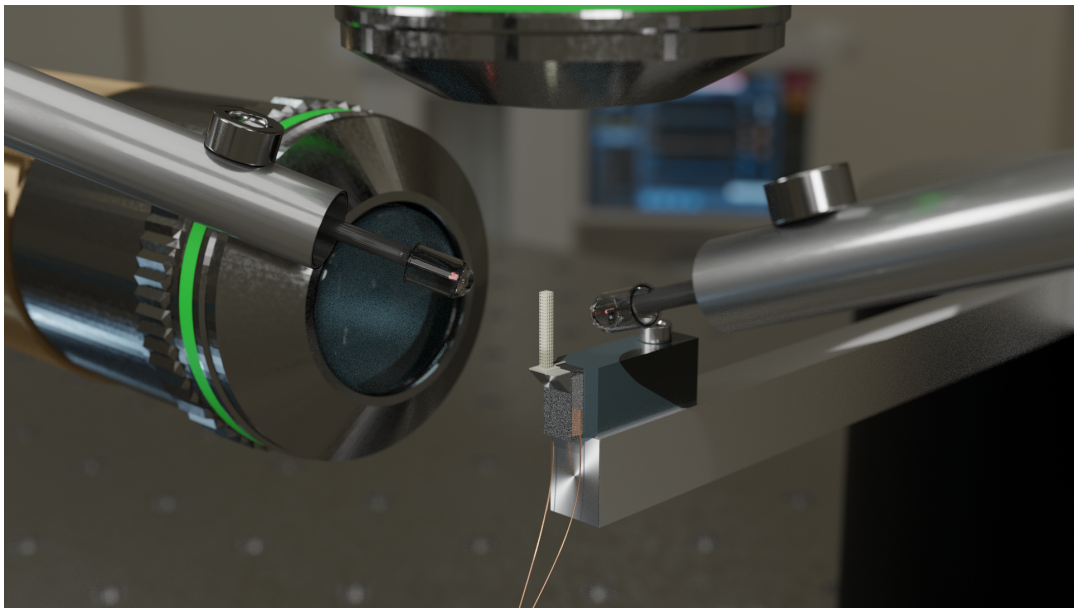

Rendering of the measurement setup

As has been shown in chapter 7, acoustical activity is a paradigm of chirality. More precisely, for $B_{44} \neq 0$, we expect a rotation of a linear polarization upon propagation. In this chapter, I will go back to the cubic unit cell introduced in chapter 5 and will find that the metamaterial exhibits pronounced acoustical activity in both numeric calculations and in the experiments. Additionally, I put our results into perspective by comparing them to micropolar continuum calculations by Yi Chen. In closing, I will show results obtained from a different metamaterial design which have been obtained by Janet Reinbold in the wake of her bachelor thesis.

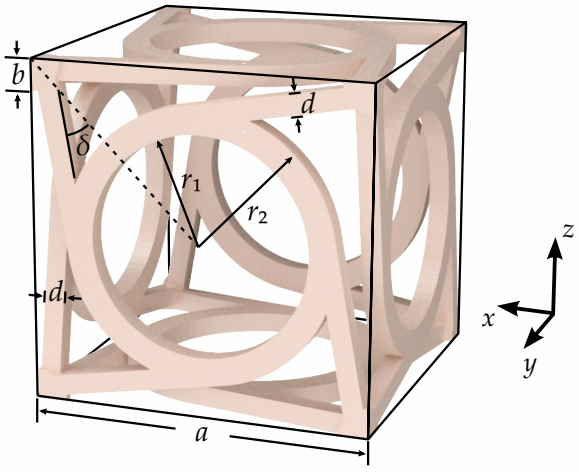

Figure 10.1: Blueprint of the cubic unit cell with lattice constant $a = 250\,\mu\text{m}$. The unit is equal to the one that was studied in the first part of this thesis. The geometrical parameters are given by $d = 0.06a$, $r_2 = 0.4a$, $\delta = \delta_{\max} \approx 35°$, $b = \sqrt{2}d$, and $r_1 = 0.32a$. Crucially, when setting $\delta = 0$, the unit cell becomes achiral. This figure is adapted from [122] (CC BY 4.0).

10.1 Calculated Acoustical Activity

The unit cell depicted in Figure 10.1, which was already introduced in chapter 5, has proven to show a push-to-twist coupling. As discussed in chapter 3, this coupling is a paradigm of chiral elastic materials. Here, an other paradigm, namely acoustical activity, shall be studied in this metamaterial.

10.1.1 *Bandstructures of Infinite Crystals*

As a start, the bulk properties of an infinite crystal was studied numerically. Therefore, the bandstructure and the corresponding eigenmodes were calculated using COMSOL Multiphysics. The unit cell was implemented with periodic boundaries (compare section 7.4) at all outer surfaces, which would be connected to neighboring unit cells. Bandstructures were calculated both for the metamaterial depicted in Figure 10.1 and an achiral control structure with $\delta = 0°$. The results for the propagation along the z-direction are depicted in Figure 10.2. The frequency scale on the left corresponds to a lattice constant $a = 250\,\mu\text{m}$, a constituent's Young's modulus of $E = 4.18\,\text{GPa}$, Poisson's ratio of $\nu = 0.4$, and mass density of $\rho = 1.15\,\text{g}\,\text{cm}^{-3}$. In contrast, the normalized frequency a/λ_0 on the right scale does not depend on both the properties of the constituent material and the unit cell size. Hence, this representation is suitable to compare different geometries. In that, λ_0 denotes the wavelength of the pressure wave in the bulk constituent, which is given

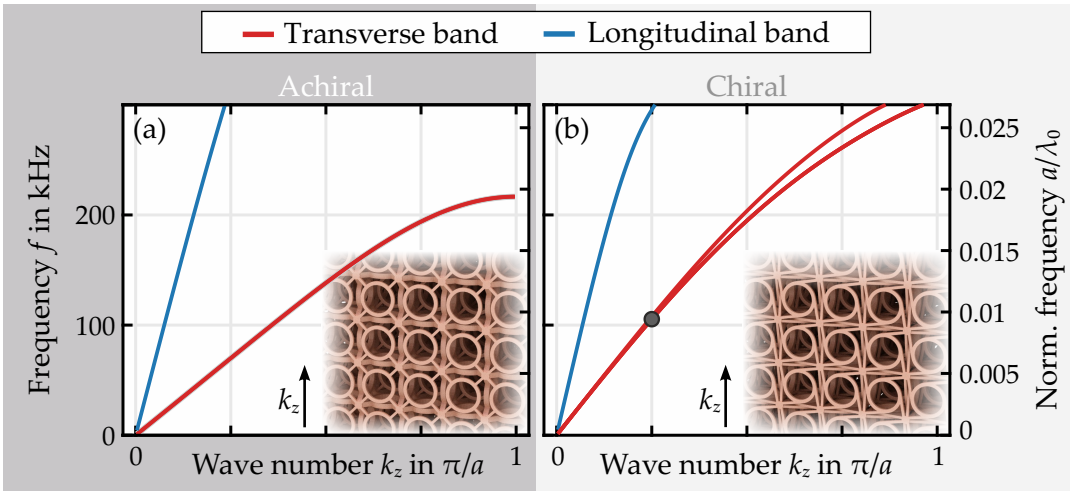

Figure 10.2: Phonon bandstructures of an (a) achiral and (b) chiral cubic metamaterial crystal. The first two bands depicted in red are polarized transversely. The third band colored in blue is of longitudinal character. The degeneracy of transverse modes in the achiral case is lifted when introducing chirality. A circular polarized eigenstate corresponding the wave number and frequency indicated by the gray dot is depicted in Figure 10.3. This figure is adapted from [122] (CC BY 4.0).

by $\lambda_0 = c_{\text{long.}}/f$, with the phase velocity of the longitudinal wave

$$c_{\text{long.}} = \sqrt{\frac{E(1-\nu)}{\rho(1-2\nu)(1+\nu)}}. \tag{10.1}$$

For both the chiral and achiral structure, three bands emerge from the center of the Brillouin zone in Figure 10.2: one with longitudinal polarization (blue), and two exhibiting a transverse polarization (red). In the achiral case, the latter are degenerate. As predicted by the micropolar continuum theory (see section 7.2), chirality lifts the degeneracy between the transverse bands. The resulting splitting Δk between these bands generally increases with increasing k_z. In the center of the Brillouin zone $k \to 0$, the bands are dispersive (also compare Figure C.1). This is in contrast to achiral structures, which show no dispersion near the center of the Brillouin zone.

Examining the shape of the eigenmodes of the chiral metamaterial shows that indeed the transverse bands are circularly polarized. A snapshot of such a mode is depicted in Figure 10.3(a). For illustration purposes, the infinite

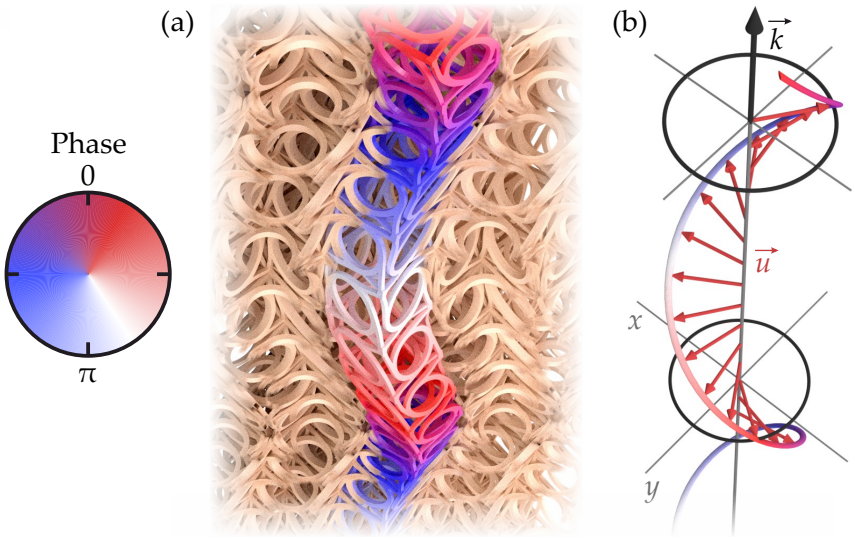

Figure 10.3: Phonon eigenmode of an infinitely extended chiral crystal. (a) shows a snapshot of a circular polarized eigenmode with $k_z = \pi/(4a)$, corresponding to a wavelength of $\lambda = 8a$. For clarity, the crystal was cut in half and a single column was highlighted. The mean displacement vectors of a unit cell are depicted in (b). The typical helical deformation can be seen nicely in both cases. This figure is adapted from [122] (CC BY 4.0).

crystal is cut in half and one metamaterial beam is highlighted. The false colors illustrate the phase of the wave. This eigenmode corresponds to the wave number k_z and frequency f marked by a gray point in Figure 10.2(b). In Figure 10.3(b), only the displacement vectors $\vec{u}$ of the center of mass of the unit cells are depicted. When connecting them, they form a helix for a fixed time t_0. Hence, the center of mass of a unit cell rotates around its rest position, when a circular polarized wave is excited. Additional calculations showing higher bands and more propagations directions are given in Appendix C. Alternative representations of the eigenmodes can be found there as well.

As a result, the chiral metamaterial exhibits two non-degenerate circularly polarized eigenmodes. Therefore, it is expected to be acoustically active (see section 7.3). From these bandstructures, the splitting Δk can be deduced easily. Using Equation 7.15, the rotation angle of a linear polarization can be calculated. Exemplary rotation angles for a given propagation distance of $z = N_z a = 12a$ are plotted as a function of the frequency f in Figure 10.12(a) and compared to experiments and calculations of finite samples.

10.1.2 *Bandstructures of Infinite Bars*

Obviously, all real world samples are finite. Hence, it should be checked, how the finite dimensions influence acoustical activity or whether the effect persists at all. In a first step, bandstructure calculations for bars of finite footprint, but with infinite length, were performed. Therefore, planes of the metamaterial were implemented containing $N_x \times N_y \times 1$ unit cells, with $N_x = N_y = 1, 2, 3, 5$. This time, periodic boundaries were only applied to those surfaces of the metamaterial that are in the bottom and top boundary of the unit cells (boundaries parallel to the x-y-plane). The boundaries to the side were intentionally left open. In Figure 10.4, exemplary bandstructures with $N_x = 1, 3$ are depicted for both a chiral and an achiral structure. As before, the frequency scale on the left corresponds to a lattice constant $a = 250\,\mu\text{m}$, a constituent's Young's modulus of $E = 4.18\,\text{GPa}$, Poisson's ratio of $\nu = 0.4$, and mass density of $\rho = 1.15\,\text{g}\,\text{cm}^{-3}$.

Instead of the three bands in the case of the infinite crystal, four bands emerge from the center of the Brillouin zone, both for the chiral and achiral structure. In the achiral case, three of them are of similar nature as the bands of the infinite crystal. Two transverse bands (red) and a longitudinal band (blue) can be identified. The fourth band (black) has a twist character. Thereby, the metamaterial's cross section rotates around its center of mass in the plane perpendicular to the propagation direction. In the presence of chirality, the blue and black bands are of mixed character. The blue band is predominantly longitudinally polarized, whereas the black band rather twists. This character mixing is the dynamic counterpart of the push-to-twist coupling discussed in the first part of this thesis. For $N_x \to \infty$, the black band vanishes, since the twisting motion is forbidden by the periodic boundary conditions.

For all cases, the transverse bands (red) are dispersive in the center of the Brillouin zone. They emerge quadratically, which is to be expected for flexural waves. With increasing bar thickness, hence increasing N_x, the quadratic onset gets smaller.

Again, by introducing chirality the degeneracy between the transverse bands is lifted. Compared to the bandstructures of the infinite crystal, the resulting splitting Δk between these bands is much more pronounced. The largest Δk was observed for $N_x = 1$. For higher N_x, the splitting decreases and the bands converge towards the bands of the infinite crystal. Again, the splitting generally increases as a function of k_z, before the splitting

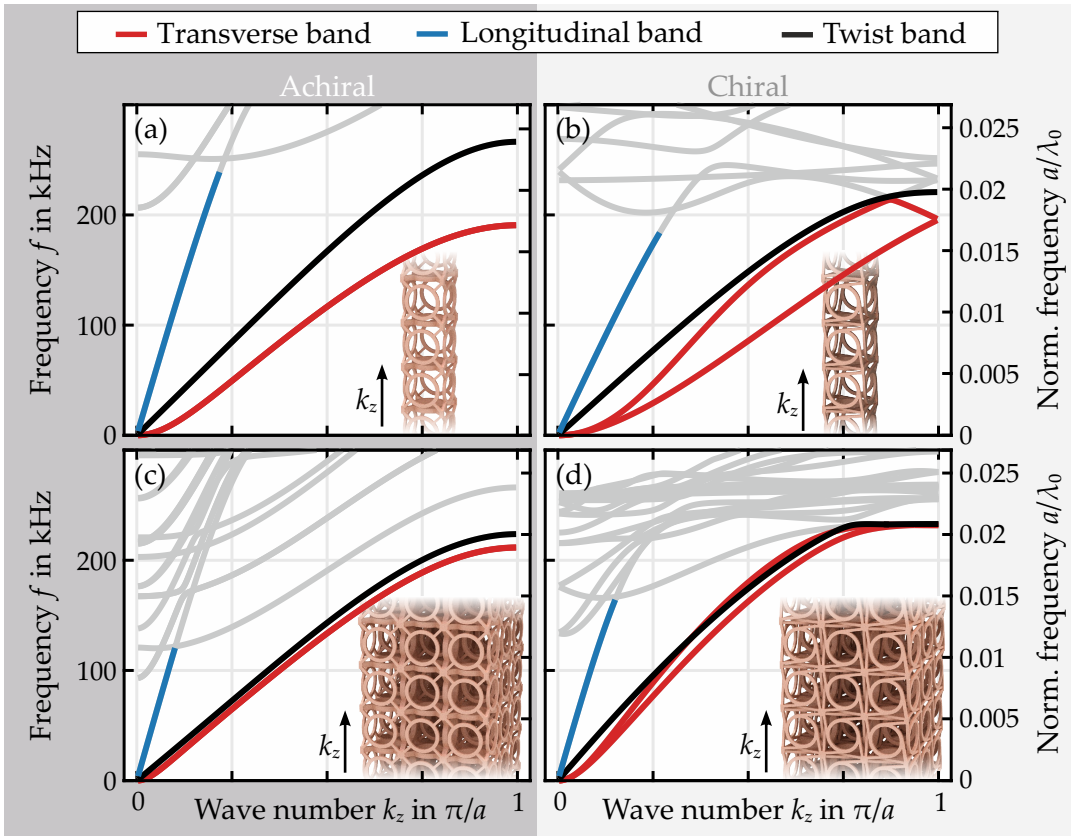

Figure 10.4: Phonon bandstructures for an infinitely extended bar with finite footprint. In the left column, the bandstructures of the achiral control structures are plotted. In the right column, results of the chiral structures are depicted. Panels (a) and (b) show bandstructures for bars with $N_x = N_y = 1$. (c) and (d) display the cases of $N_x = N_y = 3$. Again, the two transverse modes are depicted in red and the longitudinal one in blue. Additionally, a fourth band (black) with a twist character emerges from the center of the Brillouin zone. Small depictions of the corresponding sample geometry are shown in the bottom right corner of every panel. This figure is adapted from [122] (CC BY 4.0).

vanishes at the edge of the Brillouin zone ($k_z = \pi/a$). This is due to the four-fold rotational symmetry around the propagation axis. At the edge of the Brillouin zone, k_z is equal to $-k_z$. Yet, by replacing k_z with $-k_z$ turns a left-handed into a right-handed mode and vice versa. As a consequence, both modes have the same frequency at the edge of the Brillouin zone.

As a result of these bandstructure calculations, acoustical activity persists

even in infinitely long bars. The splitting between the circular polarized eigenmodes generally increases as a function of k_z and decreases with N_x. Hence, effects beyond Cauchy elasticity generally increase when either the wavelength λ or the sample side length $L = N_x a$ becomes comparable to the material's lattice constant a (i.e. N_x is of order 1).

10.1.3 Finite Sized Samples

Finally, the sample dimensions are also considered finite in z-direction. For a harmonic excitation, these lead to the formation of standing waves. Therefore, the following simulations were performed in the frequency domain. In that, samples containing $N_x \times N_x \times N_z$ unit cells were implemented with a lattice constant of $a = 250\,\mu\text{m}$. A linear elastic material with a complex Young's modulus of $E = 4.18 + \text{i}0.21\,\text{GPa}$, a mass density of $\rho = 1.15\,\text{g}\,\text{m}^{-3}$, and Poisson's ratio of $\nu = 0.4$ was assumed. As in the experiments, a plate was added to the top with a thickness of $10\,\mu\text{m}$. At the bottom, a displacement was prescribed along the y-direction. An illustration on the implemented geometry is depicted in Figure 10.5.

The polarization direction at the top of the sample was calculated by averaging the displacement vector components u_x and u_y over a square with side length $3/4a$. This averaging region is comparable to the area that was observed in the experiments. Exemplary data of a sample with $N_x = 3$ and $N_z = 12$ for an excitation frequency of $f = 160\,\text{kHz}$ is depicted in Figure 10.5. In that, the amplitude of the excitation was scaled to match the excitation in the experiments. Obviously, the polarization direction at the top of the sample is rotated with respect to the polarization of the excitation. Hence, acoustical activity is preserved even in these finite samples, whilst considering standing waves.

A systematical study of the rotation angle as a function of frequency is depicted in Figure 10.6. Samples with $N_x = 3$ and $N_z = 6, 12, 18$ unit cells were simulated for excitation frequencies between 100 and 190 kHz. Additionally, the material damping was varied. Calculations assuming no damping ($E'' = 0\,\text{GPa}$, solid line) and finite damping ($E'' = 0.21\,\text{GPa}$, points) are depicted. The value of the finite damping is equal to the material parameters deduced in section 9.3. For comparison, the rotation angles calculated from the bandstructure of the infinite bar with $N_x = 3$ is also depicted (dashed line).

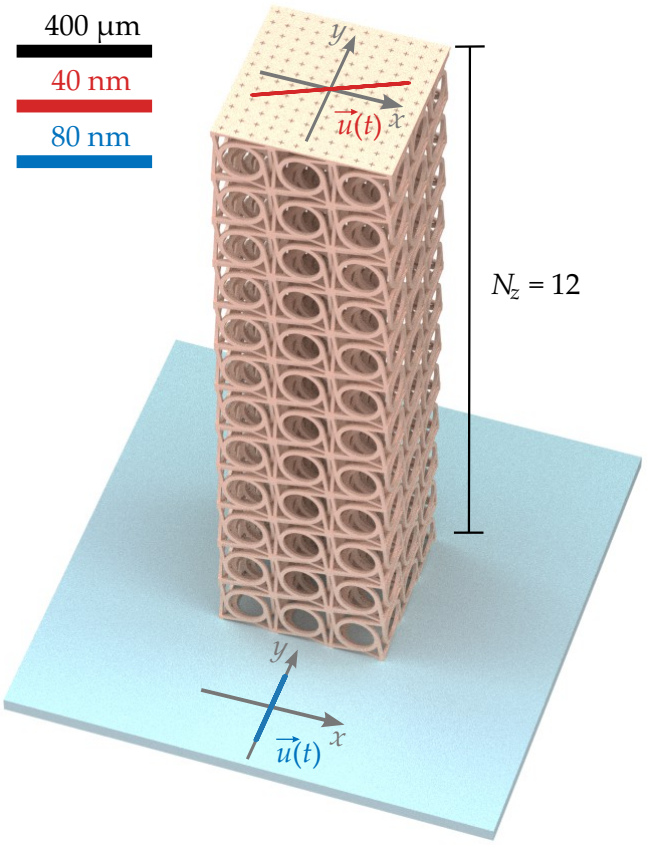

Figure 10.5: Illustration of a sample with $N_x = N_y = 3$ and $N_z = 12$ unit cells. The displacements $\vec{u}(t)$, deduced using frequency domain calculations, for an excitations frequency of $f = 160\,\text{kHz}$ are plotted at the top and the bottom of sample. For better visibility, the displacements were scaled. The blue scale bar corresponds to the displacements at the bottom, the red one to the displacements at the top. Due to acoustical activity, the direction of the linear polarization is rotated by approximately 65°. This figure is adapted from [122] (CC BY 4.0).

The qualitative trends are comparable for all simulations depicted. The rotation angle generally increases both as a function of the frequency and of the propagation distance $N_z a$. Yet, the frequency domain calculations show features that are not present in the bandstructure calculations. These can be traced back to a resonant excitation of a rotational mode of the top plate . This mode is depicted in Figure 10.7 for a sample with $N_x = 2$ and $N_z = 12$ at a frequency of $f = 166\,\text{kHz}$, which is close to the resonance frequency.

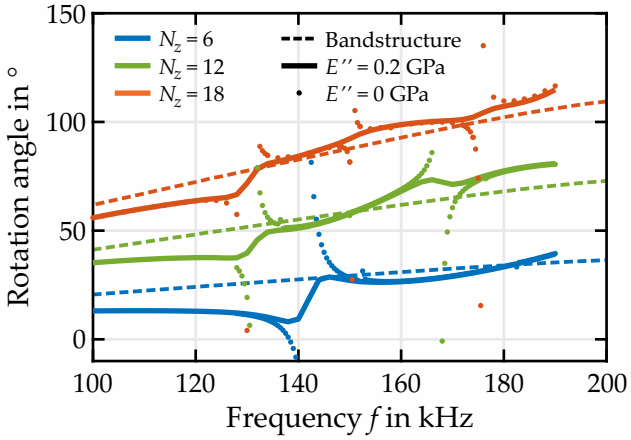

Figure 10.6: Acoustical rotation from finite-element frequency domain calculation. Calculated rotation angles are plotted as a function of the excitation frequency for $N_x = N_y = 3$ and different sample lengths. Both the cases of finite damping (Young's modulus $E = E' + E'' = 4.18\,\text{GPa} + \text{i}0.21\,\text{GPa}$) and zero damping ($E = 4.18\,\text{GPa}$) are depicted. Apart from the vicinity of the resonances at the sample top, the damping has no influence on the rotation angle. This figure is adapted from [122] (CC BY 4.0).

The z-component of the displacement vector u_z is depicted in false colors. For illustration purposes, the deformation has been exaggerated. Close to this resonance, u_z is drastically enhanced. In fact, is becomes much larger than the transverse components u_x and u_y.

In an achiral bar, this oscillation would not influence the direction of the polarization. The rotation axis would simply be perpendicular to the polarization of the transverse modes. Yet, when introducing chirality, the longitudinal and transverse degrees of freedom mix at the boundary. This can be explained as follows. For such a rotational mode, one side of the metamaterial bar is effectively compressed, whereas the other is elongated. In the first part of this thesis it has been shown that an axial strain induces a rotation. Loosely speaking, this means that the bottom half of the sample depicted in Figure 10.7(b) wants to rotate clockwise, whereas the upper parts wants to turn counterclockwise. This is illustrated by the red arrows. Concerning symmetry, these rotations $u_c(t)$ add up to a displacement parallel to the rotation axis. Therefore, this additional displacement is perpendicular to the wave that drives the rotational mode in the first place. This leads to an effective rotation of the measured polarization vector.

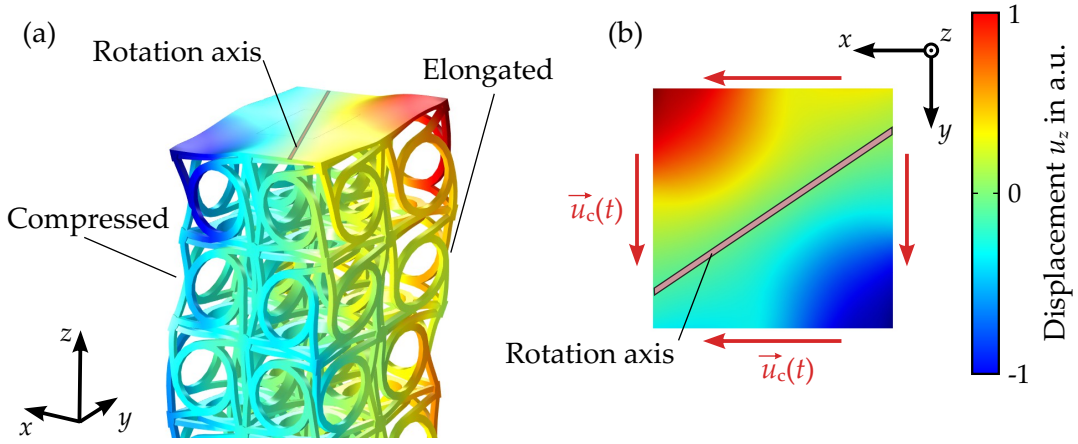

Figure 10.7: Eigenmode of a sample with $N_x = N_y = 2$ and $N_z = 12$ at $f = 166\,\mathrm{kHz}$. The excitation frequency is in close vicinity to one of the twisting resonances of the sample's top facet. The z-component of the displacement u_z is plotted in false colors. For clarity, the deformation is exaggerated. The top plate exhibits a rotation oscillation around the indicated axis. Due to the push-to-twist coupling, an additional transverse displacement component u_c is initiated.

This contribution to the polarization of the oscillations is relatively small for frequencies that are far away from the resonance frequency. They can become dominant close to the resonance frequency. In the case of a lossless material, the resonances even lead to divergence of the rotation angle. Unfortunately, there is no simple way to circumvent this problem. Yet, the unavoidable internal material damping eases the situation, in which the displacement enhancement is finite and therefore no divergences occur in Figure 10.6. Aside the resonance frequency, damping does not affect the deduced rotation angle, making acoustical activity a robust phenomenon [122].

Finally, it can be shown that even for the finite samples the rotation angle of the polarization angle does not depend on the direction of the incident polarization. Exemplary calculations for a structure with $N_x = 3$ and $N_z = 6, 12, 18$ at an excitation frequency of $120\,\mathrm{kHz}$ are plotted in Figure 10.8. Within the margins of errors, the rotation angle is constant.

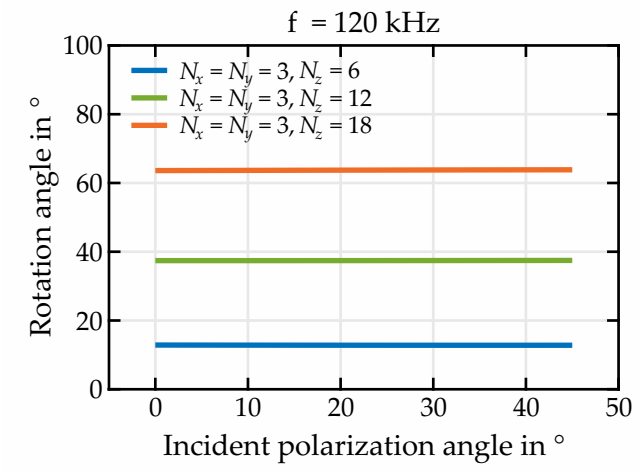

Figure 10.8: Acoustical rotation as a function of the in plane incident angle. For a fixed excitation frequency of $f = 120\,\mathrm{kHz}$, the rotation angle was calculated for samples with $N_x = N_y = 3$ and various sample lengths $H = N_z a$. Obviously, the acoustical rotation does not depend on the direction of the incident polarization. This figure is adapted from [122] (CC BY 4.0).

10.2 Experimental Results

Eventually, the rotation of the polarization, and hence the acoustical activity, was measured experimentally on finite-sized 3D printed samples. In this section, the fabricated samples are presented first. Afterwards, the method of extracting the rotation angle from the raw measurement data is presented. Finally, the measured rotation angles are shown as a function of frequency for various sample heights and sample footprints.

10.2.1 Fabricated Samples

All samples in this section were printed using the Nanoscribe instrumentation, which was already introduced in section 4.4. To study the influence of the sample's side length, samples containing $N_x = 1, 2, 3, 5$ unit cells in a side were fabricated. At the same time, several sample heights $H = N_z a$ were realized with $N_z = 6, 12, 18$. The lattice constant of $a = 250\,\mu\mathrm{m}$ was chosen. All samples were printed on a thick bottom plate with a bar attached. Both are needed to transfer the sample from the substrate to the measurement setup without damage. Additionally, markers were printed on both the bottom and top plate to assist the image cross-correlation. A gallery of scanning electron micrographs of the printed exemplary samples is presented in Figure 10.9. These images illustrate the generally high quality of the fabricated structures nicely.

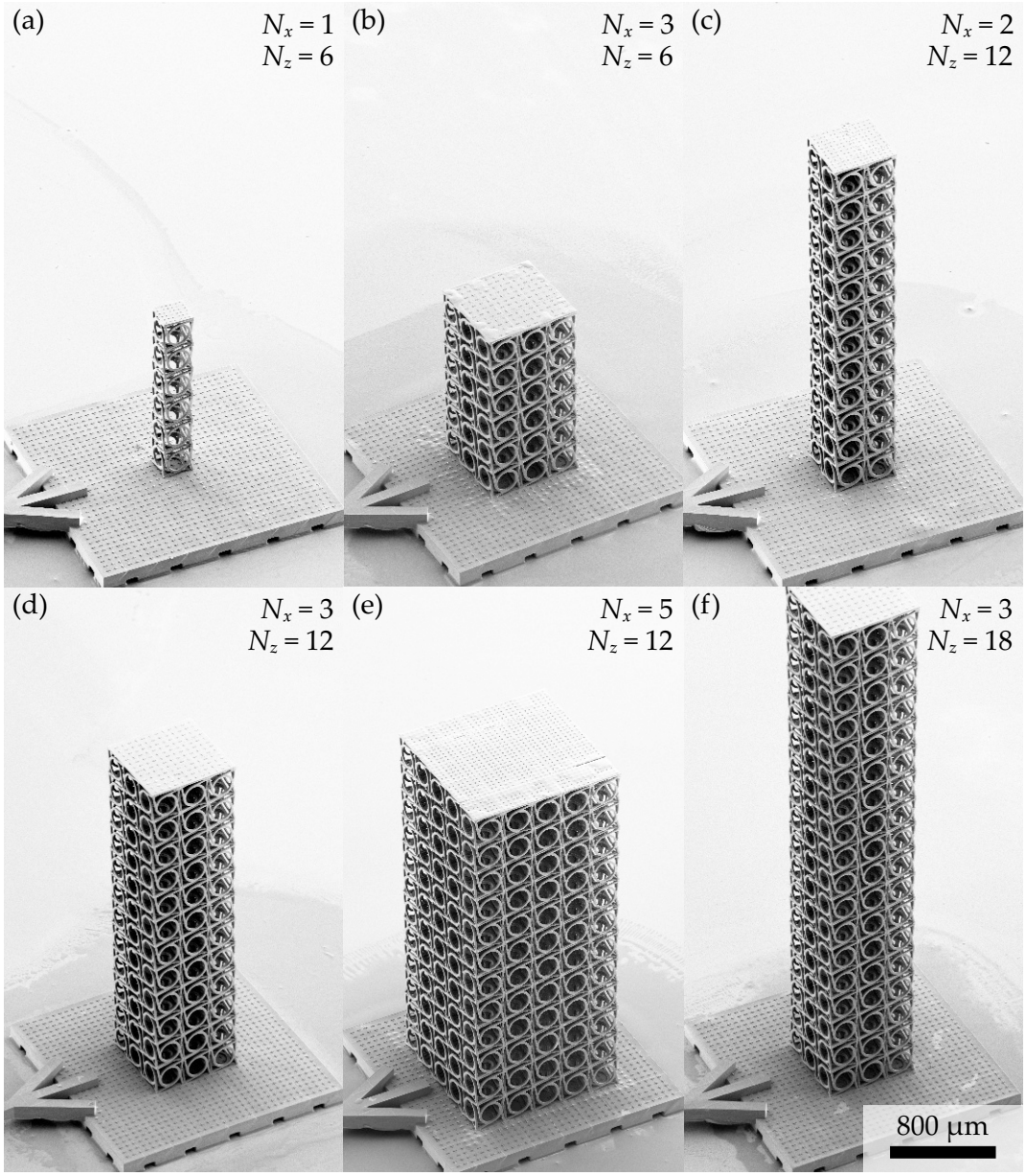

Figure 10.9: Gallery of 3D printed samples with lattice constant $a = 250\,\mu\text{m}$. Scanning electron micrographs of selected for samples with various sample footprints $N_x \times N_y$ and sample heights N_z are depicted. All pictures are shown on the same scale. This figure is adapted from [122] (CC BY 4.0).

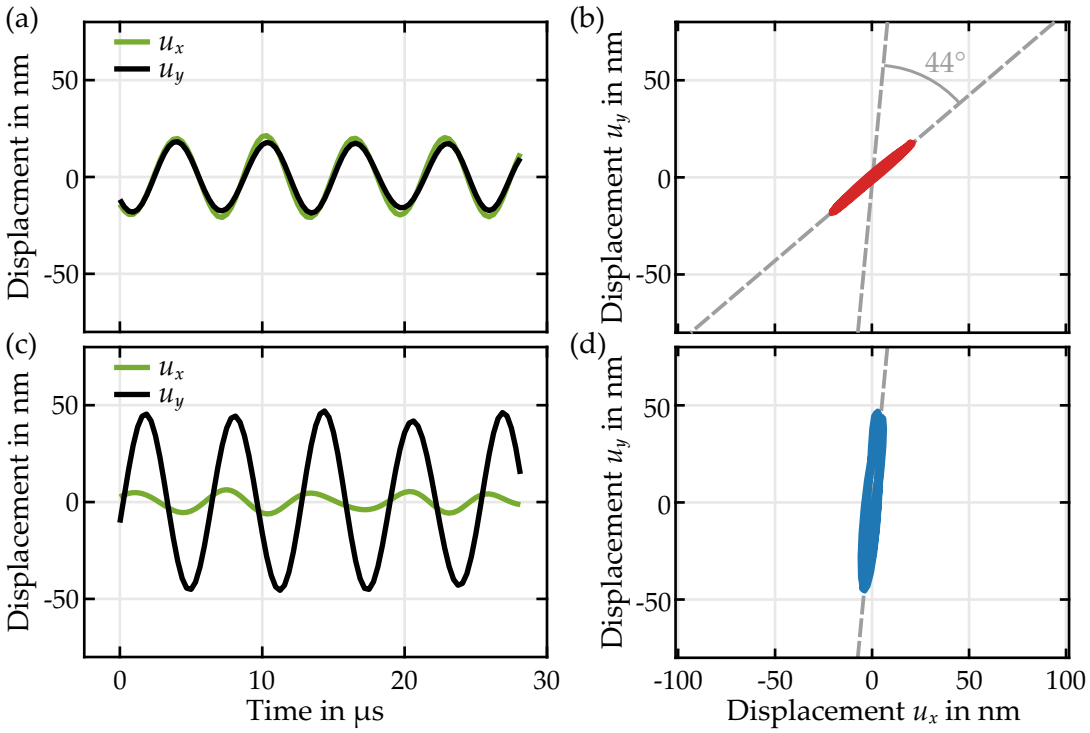

Figure 10.10: Measured data for a sample with $N_x = N_y = 3$ and $N_z = 12$ for an excitation frequency of $f = 160\,\mathrm{kHz}$. (a) and (b) show the displacement components $u_x(t)$ and $u_y(t)$ measured at the sample's top. In (c) and (d), the displacement components of the excitation are depicted. To eliminate drifts, a bandpass filter was applied to the data. From that, a rotation angle of 44° was deduced. Five periods of the signal are depicted to demonstrate the generally good data quality and reproducibility. This figure is adapted from [122] (CC BY 4.0).

10.2.2 *Extracting the Polarization Directions Using Image Cross-Correlation*

Using the microscope that was aligned with the z-axis of the sample, two films were recorded subsequently for a fixed excitation frequency. For the first film, the microscope was focused on the markers at the bottom plate. For the other one, the markers at the top of the sample were in focus. Due to the stroboscopic near-IR illumination (compare section 9.2), the high frequency oscillation of the sample can be seen in slow motion. Therefore, regular cameras are sufficient to capture the movement. Using

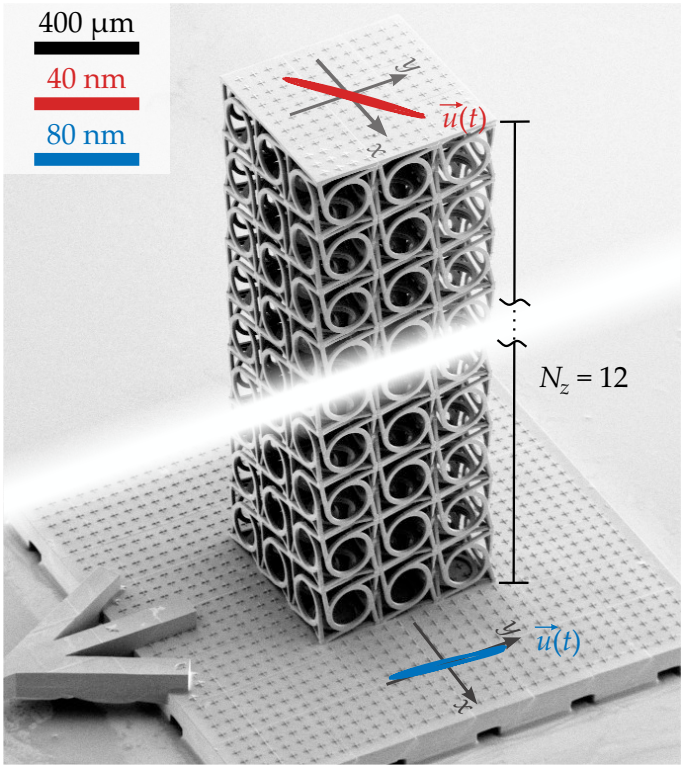

Figure 10.11: Overlay of measured data and scanning electron micrograph. The same data as depicted in Figure 10.10 is shown at the position where the underlaying film was shot. The data corresponds to a sample containing $3 \times 3 \times 12$ unit cells and an excitation frequency of $f = 120\,\mathrm{kHz}$. This figure is adapted from [122] (CC BY 4.0).

the previously introduced digital image cross-correlation section 4.3, the in-plane displacement components were deduced. Between 10 and 20 ROI were tracked for each measurement. It is fair to assume that the plates are stiff compared to the sample and hence, do not deform. Therefore, all markers exhibit the same movement. Following [120], the average displacement of the markers is calculated to improve the precision. Subsequently, a band-pass filter was applied, which attenuated all frequencies above 200 kHz and below 15 kHz. Thereby, drifts and excitations of higher harmonics were eliminated. In this fashion, the raw data plotted in Figure 10.10 was acquired. The displacements depicted in the top row were measured at the samples's top, the bottom row at the bottom plate. This is once again illustrated in Figure 10.11, where the measured data is superimposed on a scanning

electron micrograph. The positions where the data is depicted corresponds to the positions the films were shot. In both cases, five consecutive oscillations are depicted illustrating the good reproducibility of the measurement.

To deduce the direction of the polarization, the sinusoidal functions

$$u_x = U_x \sin(\omega_0 t + \Delta_x), \tag{10.2}$$
$$u_y = U_y \sin(\omega_0 t + \Delta_y), \tag{10.3}$$

were fitted to the data. Due to imperfections, the polarizations are going to be elliptical in general. Therefore, the direction of the semi-major axis was taken as a measure for the polarization direction. This can be calculated by

$$\phi = \frac{1}{2}\text{atan}\left(2\cos(\Delta_x - \Delta_y)\frac{U_x/U_y}{1 - U_x^2/U_y^2}\right). \tag{10.4}$$

Consequently, the rotation angle of the polarization is then given by the difference of the direction ϕ measured at the top and at the bottom of the sample. For the exemplary data depicted in Figure 10.10, a rotation angle of 44° was deduced.

10.2.3 Measured Acoustical Activity

Experiments were performed to systematically study acoustical activity in the metamaterial. Therefore, the rotation angle was studied: 1) as a function of frequency, 2) as a function of the sample's side length $L = N_x a$, and 3) as a function of the sample height $H = N_z a$. All measurement results are plotted in Figure 10.12. Illustrations of the corresponding samples are shown next to the data. The samples are dyed in the same color as the corresponding data points. For comparison, both the results from bandstructure calculations and finite structure calculations are depicted.

Generally, the measurement and the simulations show good agreement. Especially, all trends are reproduced nicely. For all samples, the rotation angle increases as a function of the excitation frequency. Figure 10.12 also clearly indicates that the rotation angle is proportional to the propagation distance and hence, proportional to N_z. Furthermore, the data shows that the acoustical activity generally increases with decreasing N_x, i.e., decreasing sample foot print. Most importantly, all chiral samples showed acoustic activity. Whereas for the achiral structures, rotations angles below $\pm 10°$

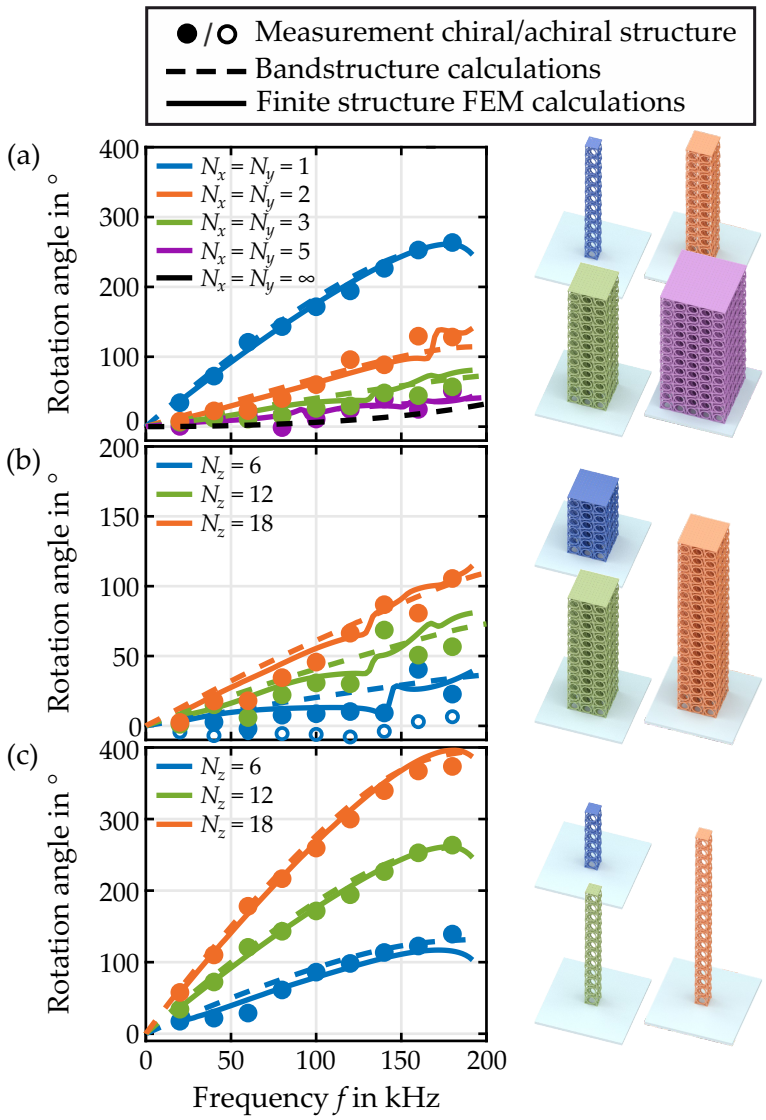

Figure 10.12: Summary of all numerically and experimentally determined rotation angles of a linearly polarized transverse wave as a function of the excitation frequency f. The measurement data of the chiral (achiral) samples are plotted as dots (circles). Additionally, the rotation angles deduced from bandstructure calculations (dashed lines) and finite-structure calculations (solid lines) are shown. For the latter, a complex Young's modulus of $E = 4.18\,\mathrm{GPa} + \mathrm{i}0.21\,\mathrm{GPa}$ was assumed. (a) Rotation angles for a fixed sample height of $N_z = 12$ and various footprints. (b) Rotation angles for fixed sample side length of $N_x = 3$, but various sample heights N_z. (c) same as (b) but with $N_x = 1$. Illustrations of the samples dyed in the corresponding color are depicted on the right. This figure is adapted from [122] (CC BY 4.0).

were measured. These residual rotation angles are most likely due to sample imperfections and imperfect excitation. Yet, these errors can be considered small, especially compared to the maximum rotations angles measured for $N_x = 1$ and $N_z = 18$ that even exceeded 360°.

This maximum rotation angle of more than 360° near the edge of the Brillouin zone ($f \approx 180\,\text{kHz}$) equals a rotation of more than 20° per unit cell. For the same structure with $N_x = 1$, rotation angles of about 10° are observed at the center of the Brillouin zone ($f \approx 20\,\text{kHz}$).

10.3 Effective Micropolar Material Parameters

To be able to call the observed scaling behavior versus N_x a material property, it is important to reproduce the previously discussed results using an effective medium description. It has been shown in section 7.2 that the notion of acoustical activity itself is reproduced correctly by the micropolar theory of elasticity. Whether the scaling versus N_x can be mimicked by the theory, is yet to be shown

In [60], Yi Chen did exactly that by performing band structure calculations for a micropolar medium. The effective material parameters he used are given in section B.2 and [60]. These were partially deduced by comparison to analytical solutions of the wave equation for directions of high symmetry for a cubic material in the long wavelength limit. Parameters that could not be determined analytically, were deduced in a numerical optimization. His results for infinite extended bars and infinite extended crystals are plotted in Figure 10.13. Additionally, the results are compared to the achiral Cauchy theory.

The bandstructures of the micropolar continuum depicted in Figure 10.13 reproduce the qualitative trends of the bandstructures depicted in Figure 10.2 and Figure 10.4 astonishingly well. Most importantly, it predicts an increased splitting for small N_x. Even quantitatively, the splittings predicted in the center of the Brillouin zone agree reasonably well.

Chen also shows that the symmetries of the eigenmodes are reproduced by the micropolar medium description [60]. More precisely, he showed that both the effective medium and the metamaterial structure exhibit circular polarizations along the principle axis and the volume diagonal. In contrast, more or less linear polarizations occur for all other direction.

Obviously, this theory cannot be expected to yield reasonable results at

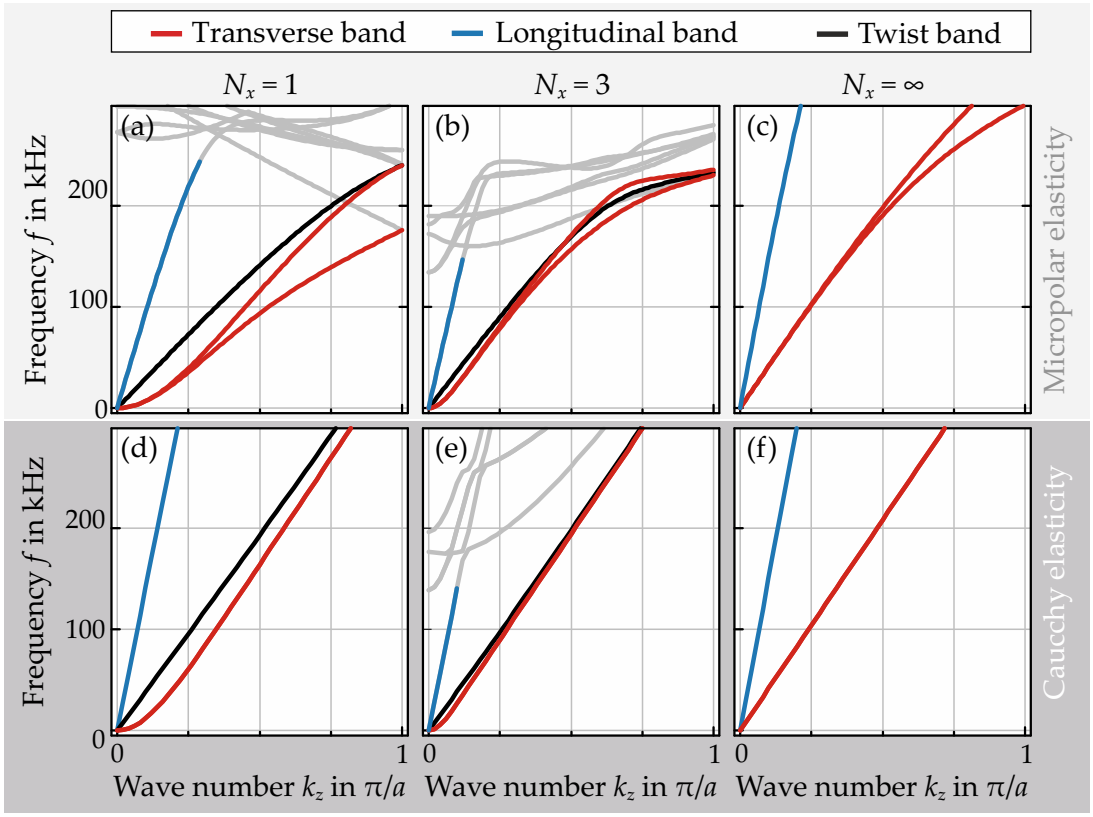

Figure 10.13: Phonon dispersions calculated from continuum theories. Using Bloch periodic boundary conditions, the dispersion relation of phonons in a chiral micropolar medium were calculated for (a) $N_x = 1$, (b) $N = 3$, and (c) infinite crystals. In (d)-(f), corresponding dispersions assuming a classical Cauchy continuum are depicted. The material parameters used for the micropolar continuum are given in section B.2. Qualitatively, the splittings of the transverse bands in the micropolar continuum resemble the results obtained from bandstructure calculations of the metamaterial. This figure is adapted from [60].

the edge of the Brillouin zone ($k_z = \pi/a$). Due to symmetry, the bands are degenerate in the structural calculations depicted in Figure 10.4. In the effective medium description, the periodicity along the z-direction is a numerical trick and not physical reality. In fact, the effective medium description does not "know" about any periodicity at all. Therefore, the bandstructures of the effective medium represent the metamaterial correctly only for wavelengths much bigger than the lattice constant a.

Note that the effective material parameters given in Figure 10.2 and Figure 10.4 not only grasp the dynamic behavior correctly, but also the static push-to-twist coupling discussed in the first part of this thesis. In fact, the parameters given in subsection B.1.2 and Figure 10.2 are equal. The first parameter set was only scaled to match the respective constituent material's Young's modulus and the metamaterial's lattice constant.

10.4 Discussion

Acoustical activity was demonstrated both numerically and experimentally in chiral mechanical metamaterials. Thereby, rotation angles of the linear polarization as large as 22° per unit cell were observed. For the used lattice constant of $a = 250\,\mu\text{m}$, this corresponds to a rotational power of approximately $15\,\text{rad}\,\text{cm}^{-1}$. This is between three and five times larger than the rotational power reported on α-quartz [151] for gigahertz frequencies. For the bulk metamaterial, rotation angles as large as 2.6° per unit cell were calculated.

Slender beams exhibit generally larger rotation angles. This agrees well with the findings of the first part of this thesis, which observed that effects generally become more prominent for small sample side lengths $N_x a = L$. Yet, in contrast to the static push-to-twist coupling, acoustical activity does not vanish for $N_x \to \infty$. This is related to the fact that the lattice constant a is still finite compared to the wavelength λ. The Cauchy limit of "point mechanics" is only recovered when both a/L and a/λ tend to zero.

Generally, bandstructure calculations, finite structure calculations, and experiments fit together nicely. The finite sample length led to resonances at the end facet of the sample, which influenced the polarization direction additionally. Away from these resonances, the finite length had only little influence on the polarization direction. The same holds true for the damping of the constituent material, making acoustical activity a robust phenomenon in mechanical metamaterials.

For all chiral structures, noticeable rotation angles were measured, whereas the rotation angles of the achiral structures scattered around zero. Hence, they effectively showed no rotation, which is expected for achiral structures. The measured rotation angles of the chiral structure scatter with a tolerable spread around the simulated curves. These deviations are comparable for the chiral and achrial samples. Most likely, these are caused by small sample imperfections. These tend to increase for bigger structures. Due to the

limited field of view of the objective lens in the Nanoscribe system, large samples are split up into smaller blocks. This stitching procedure causes defects at the interfaces between consecutively printed structures. This can break symmetry or introduce local resonances, which are not taken into account in the simulations.

Due to different resonance modes of the piezoelectric transducer, the excitation varied slightly as a function of frequency. For some frequencies, the excitation was rather elliptical. Furthermore, the amplitude of the excitation varied by more than a factor of 10. In itself, neither the ellipticity nor the amplitude should have an influence on the measured polarization rotation. Yet, together with the sample's imperfections, this could lead to the observed small deviations of the measurement with respect to theoretical prediction. Despite these deviations, acoustical activity was unambiguously verified in the experiments, both qualitatively and quantitatively.

Furthermore, the scaling behavior of the rotation angle as a function of N_x was qualitatively reproduced by a micropolar continuum theory. Therefore, the observed effects can be considered material properties indeed, and not just effects related to the finite sample sizes.

10.5 Towards Maximum Acoustical Activity

In this last section, fundamental bounds on the maximum achievable acoustical rotation in metamaterials are derived. Furthermore, yet another metamterial is studied showing even larger rotation angles than the design of the previous chapter. The experimental and numerical results were obtained by Janet Reinbold in the wake of her bachelor thesis, which was supervised by the author. The same methods and instrumentations as in the previous section were used. The results of this section were also published in [149].

10.5.1 Fundamental Bounds

The bandstructures of the metamaterial in the previous section (compare Figure 10.4 and Figure 10.2) all exhibited a degeneracy of the the two transverse modes both in the center of the Brillouin zone ($k_z = 0$) and at the edges ($k = \pi/a$). The latter is caused by the threefold or higher rotational symmetry along the propagations direction. This can be understood as follows. According to Bloch's theorem, the wave numbers $k_z = \pi/a$ and $k_z = -\pi/a$ are equivalent, hence the respective eigenmodes must have equal

energies. Yet, replacing $k_z \rightarrow -k_z$, turns a left-handed into a right-handed mode and vice versa. Therefore, left- and right-handed modes have to exhibit the same energy at the edge of the Brillouin zone.

Having these predetermined degeneracies in mind, the modulus of the splitting Δk is bounded by the size of the Brillouin zone [149]. Therefore, the upper bound for the rotation angle ϕ is given as

$$|\phi(\omega)| \leq \frac{\pi}{2}\frac{L_z}{a}, \tag{10.5}$$

with propagation distance L_z and lattice constant a. This means that the rotation angle per unit cell cannot exceed 90°.

10.5.2 Unit Cell Design

The unit cell that is depicted in Figure 10.14 is inspired by [142] and was already introduced in section 5.2. Yet, the cube in the middle was replaced by a framework to reduce mass. Thereby, the frequency of the transverse modes at the edge of the Brillouin zone is increased. This resulted in generally higher rotation angles of the linear polarization. The other geometrical parameters were systematically varied to show large acoustical rotation, whilst maintaining a feasible geometry. More details are provided in [149]. In order to match the metamaterial to the frequency range that is accessible with the measurement setup, the lattice constant was set to $a = 250\,\mu\text{m}$. The exact geometrical parameters are given in the caption of Figure 10.14.

10.5.3 Finite Element Simulations

The bandstructure calculations were carried out in the same fashion as presented in the previous chapter. For the bandstructure of the infinite crystal, Bloch periodic boundary conditions were prescribed to all outer surfaces of a single unit cell. For the bandstructures of the infinite bars, a plane of $N_x \times N_y$ unit cells was implemented with $N_x = N_y$. Periodic boundaries were only applied to surfaces at the top and at the bottom of this plane. All remaining boundaries were left open. The calculated bandstructures for $N_x = 2, 4$, and the infinite crystal ($N_x = \infty$) are depicted in Figure 10.15. The constituent material was modeled by an isotropic Cauchy

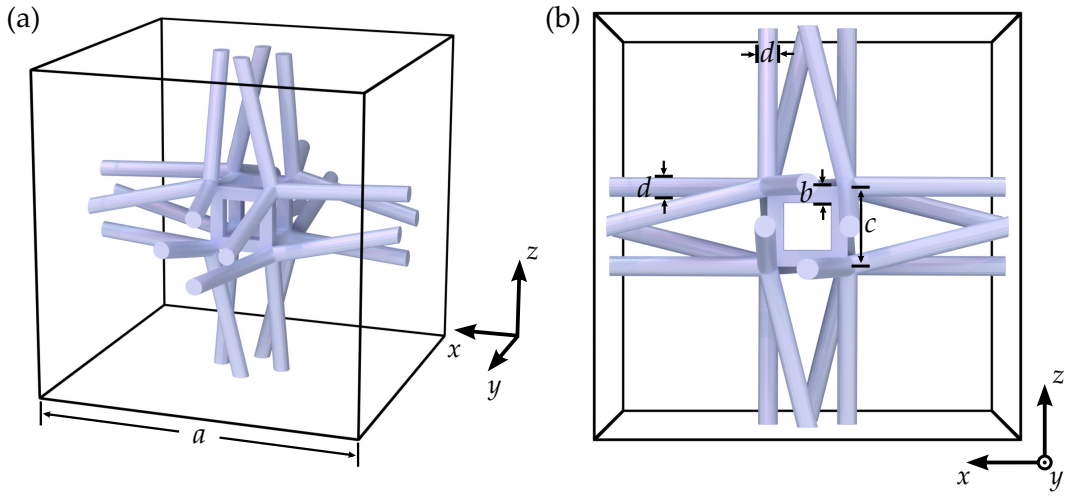

Figure 10.14: Illustration of a cubic, chiral unit cell. The design was inspired by [142]. An oblique view of the unit cell is depicted in (a) and a side view in (b). The unit cell was optimized to exhibit large acoustical rotation. The geometrical parameters are $a = 250\,\mu\text{m}$, $b = 0.04a$, $c = 0.2a$, and $d = 0.025a$. This figure is adapted from [149] (CC BY 4.0).

material with Young's modulus $E = 4.18\,\text{GPa}$, Poisson's ration $\nu = 0.4$, and mass density $\rho = 1.15\,\text{g}\,\text{cm}^{-3}$.

Obviously, the splitting Δk is drastically increased compared to splittings in the previous bandstructures (compare Figure 10.2 and Figure 10.4). Even for $N_x = \infty$, the maximum splitting covers more than 40% of the Brillouin zone. The splitting is even larger for $N_x = 2$. Therefore, rotation angles as large as 45° per unit cell can be expected.

As before, simulations of the finite sample containing $N_x \times N_y \times N_z$ unit cell were performed in the frequency domain. The extracted rotation angles are plotted in Figure 10.17.

10.5.4 Samples

The printing of this metamaterial design is significantly more difficult than the geometries presented previously. Due to the fragility of the unit cell, only structures with $N_x \geq 2$ could be fabricated. Various samples with $N_x = 2, 3, 5$ and $N_z = 6, 12, 18$ were printed onto a bottom plate. Yet, no plate was added to the top.

The bars sticking out to the sides of the unit cell impose the same problems

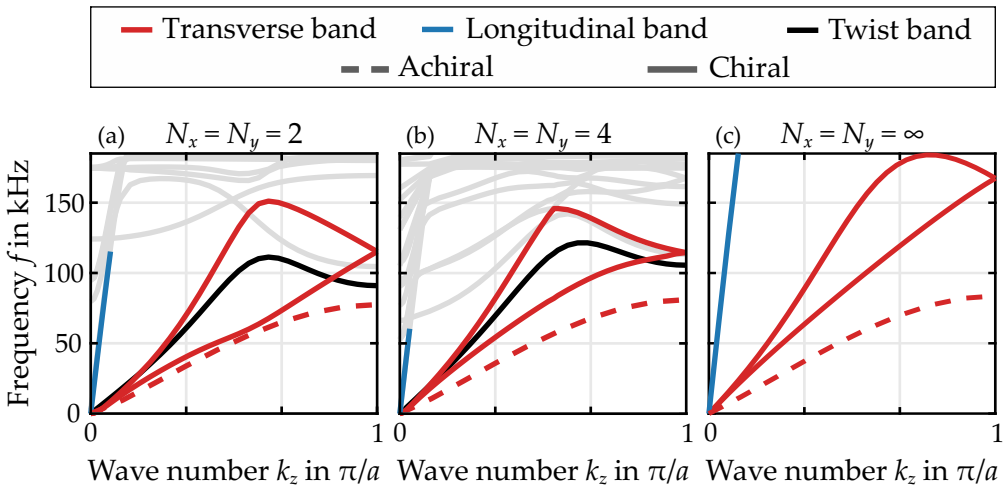

Figure 10.15: Phonon bandstructure calculations of the metamaterial depicted in Figure 10.14. Both calcuations assuming a finite cross section with side lengths (a) $N_x = N_y = 2$ and (b) $N_x = N_y = 4$, as well as the bandstructure of the infinite crystal (c) are depicted. The degeneracy of the two transverse bands (red) is lifted in all cases. The longitudinal mode is plotted in blue. For the bars with finite cross section, an additional fourth band with twist character (black) emerges form the center of the Brillouin zone. For comparison, the degenerate transverse bands of the achiral control structure (red dashed line) are also depicted. This figure is adapted from [149] (CC BY 4.0).

as the long horizontal bars of the unit cell discussed in chapter 6. These overhanging and even flying structures tend to drift away during the printing process, leading to significant defects. This issue was addressed in the same manner as before (compare chapter 6), in that the vertical bars as well as the central cube were printed in a first step. In a subsequent step, the horizontal bars were added in between. Special care had to be taken for the bars at the outer surfaces of the sample. When considering only static experiments, their contribution could be neglected. Yet, in the dynamic regime, their mass and inertia influence the polarization significantly. Therefore, they were added in a third printing step. Depending on their orientation, these bars were printed either from top to bottom or vice versa.

Scanning electron micrographs of an exemplary structure with $N_x = 5$ and $N_z = 12$ are depicted in Figure 10.16. Especially the close up (b) reveals the high structural quality. It turned out that this geometry is very susceptible for dirt. This might be related to the fact that parts of the structure easily fall

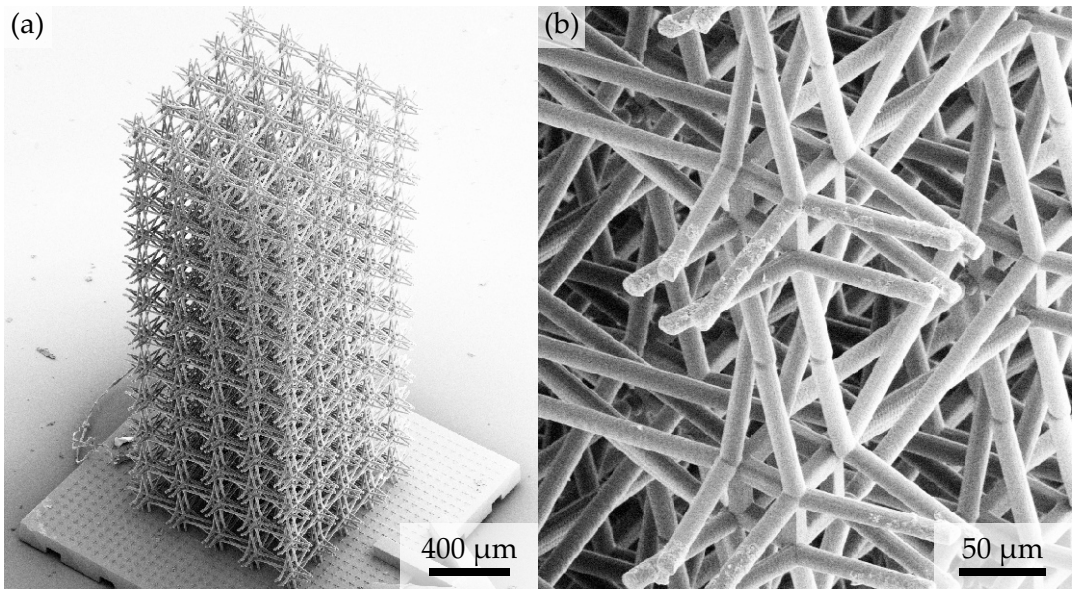

Figure 10.16: Exemplary scanning electron micrograph of a sample containing $5 \times 5 \times 12$ unit cells. An overview of the fabricated sample including the bottom plate is depicted in (a). A close up of a single unit cell is shown (b). The micrographs prove the generally high printing quality. This figure is adapted from [149] (CC BY 4.0).

dry even during the printing process. Therefore, residue of the photoresist is not as efficiently washed away in the development step, but rather sticks to the sample.

10.5.5 Results and Discussion

The experiments and the evaluation of the experimental data was conducted in the same way as in subsection 10.2.3. The measured rotation angles of the linear polarization, as well as the results from bandstructure calculations and finite structure calculations, are summed up in Figure 10.17.

Generally, the rotation angle increases with frequency, and decreases as a function of N_x. Hence, the behavior of this metamaterial design is quantitatively similar to the one discussed in the previous section. Yet, even for the infinite crystal ($N_x = \infty$) rotation angles exceeding 20° per unit cell are found. This is already comparable and even surpasses some of the values extracted in subsection 10.2.3 for finite sample footprints. For

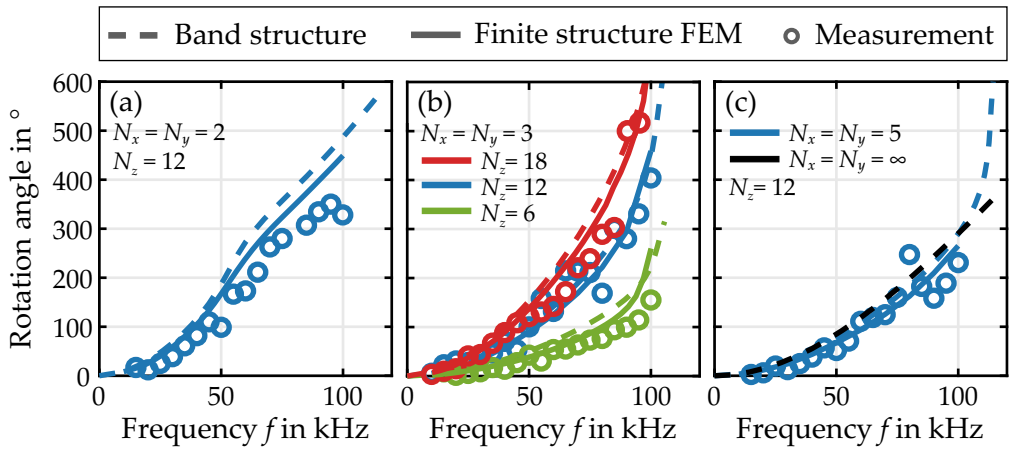

Figure 10.17: Summary of the numerically and experimentally determined rotation angles as a function of the excitation frequency. Samples with side lengths of (a) $N_x = N_y = 2$, (b) $N_x = N_y = 3$, and (c) $N_x = N_y = 5$ are depicted. Experimental data (circles), finite structure calculations (solid lines), and rotations angles from bandstructure simulations (dashed line) are depicted. Experimentally, rotation angles exceeding 500° were found. This figure is adapted from [149] (CC BY 4.0).

$N_x = 2$, rotation angles approaching 30° per unit cell were determined experimentally.

Frequency domain calculations and bandstructure calculations show good agreement. Remarkably, the resonances on the top surface of the sample do not seem to play as much of a role as in the previous experiments. This might be attributed to the lacking top plate. Systematically, smaller rotation angles were measured in the experiments than predicted numerically. Most certainly, this is related to residual structural defects. Bandstructure calculations showed that the results depend quite sensitively on both the bar thickness d and the cube size c. Additionally, the Young's modulus of the constituent material might be slightly different for the samples fabricated here. Although the same setup with the identical photoresist was used for fabrication, the printing strategy itself differed vastly. Especially the scanning speed of the laser beam and the laser intensity were chosen differently. As has been shown previously [76], this influenced the crosslinking of the polymer drastically. Hence, differences in the resulting Young's modulus seem feasible. Both structural defects and uncertainties in the constituent's Young's modulus can easily account for the small deviations observed.

As a result, the metamaterial design presented here approaches the funda-

mental limit of 90° rotation per unit cell. Especially for the case of the infinite crystal, a vast increase of the rotation angle was observed. Furthermore, the rotation angles of the linear polarization exceeding the results from the previous section were also experimentally obtained.

In conclusion, chiral metamaterials are an unprecedented and tailorable tool to manipulate the linear polarization direction of a transverse elastic wave. By scaling the lattice constant, the operation frequency of a material can easily be adjusted to the desired frequency range. The demonstrated rotation angles exceeding 360° are more than sufficient for most engineering applications. Thereby, these metamaterials pave the road towards completely controlling the polarization of elastic waves.

Chapter 11

11 Conclusions and Outlook

In this thesis, I have successfully designed, fabricated, modeled, and characterized chiral mechanical metamaterials. Due to their additional degrees of freedom, these so called Cosserat or micopolar materials exhibit properties that go well beyond the scope of the classical Cauchy theory. I demonstrated the presence of these new degrees of freedom by characterizing a quasi-static push-to-twist coupling and acoustical activity in these metamaterials. Thereby, both effects have been examined experimentally and numerically using finite element calculations. The push-to-twist coupling and acoustical activity are paradigms of chirality in mechanics, hence cannot be modeled using the classical theory.

In the following, I will briefly summarize the key findings and put them into perspective. In doing so, I will touch upon publications and applications that have been inspired by the work presented in this thesis. In closing, I will also shine a light on open prospects and challenges.

In Part I, starting from classical Cauchy continuum theory, I argued that chirality played only a minor role in mechanics for decades. In fact, it has been neglected altogether in the classical theory. It turned out that this is deeply rooted in the underlying continuum assumption, which imagines materials to be build up out of infinitesimal points. Yet, points are always centrosymmetric objects making the Cauchy continuum inherently centrosymmetric, hence achiral. I showed in chapter 2 that a fundamental generalization of the Cauchy continuum, the micropolar continuum theory, is required to treat chirality in mechanics. In that, the infinitesimal points of the Cauchy continuum are replaced by finite sized point particles. This leads to a break down of scale invariance and to the occurrence of characteristic length scales in these micropolar materials. I reiterated that significant deviations from the Cauchy continuum are expected when these characteristic lengths

become comparable to sample dimensions. Most importantly, I presented a push-to-twist coupling as a qualitatively new deformation mode that only occurs in chiral material. It predicts that a bar from a chiral constituent material twists when being subjected to an axial compression. Thereby, the rotation occurs in the plane orthogonal to the compression axis.

In chapter 3 and chapter 4, I established the numerical and experimental methods needed to study these push-to-twist couplings in metamaterials. In doing so, I presented a sample design that forgoes sliding boundaries in the experiments. Furthermore, I introduced the 3D printing techniques used for the fabrication of the metamaterial samples.

Subsequently, I laid down mechanisms and unit cell blueprints for metamaterials exhibiting said push-to-twist coupling in chapter 5. From those blueprints, I picked a feasible candidate for a cubic unit cell and optimized the geometry numerically. An easily accessible measure for the strength of this coupling is twist angle per axial strain. Therefore, I studied this angle for metmaterial samples containing $N \times N \times 2N$ unit cells both numerically and experimentally. Thereby, I determined twist angles exceeding 2° per percent axial strain. As predicted by the micropolar continuum theory, the twist angle is not constant, but rather depends on the scaling factor N. When increasing the scaling factor from 1 to 5, the twist angle only decreases by a factor of 2. This indicates that the relevant characteristic length scale is on the order of the unit cell size. For large N, i.e. for sample dimensions much larger than the characteristic length scale, the twist angle per percent axial strain decreases proportional to N^{-1}. Additionally, I showed that the observed deformation is indeed a material property by finding the same behavior in simulations of a homogeneous bar made out of a micropolar material.

Our mechanism driven design guarantees by no means to find an optimum design. Therefore, it is even more surprising that an approach based on topology optimization yielded a remarkably similar geometry with comparable twist per axial strain [81].

In in 2016 and 2017, these push-to-twist mechanical metamaterials were proposed more or less simultaneously by Lakes in [142] and by us [2]. Since then, these publications triggered a multitude of new chiral unit cell designs and structures [116, 158–166]. Some of them exhibit even larger characteristic lengths and twist angles per axial strain. Even applications like a laser beam scanner based on a topological protected edge state [106] or auxetic actuators [167] have been proposed.

In chapter 6, I presented our very own approach to systematically increase and tailor the characteristic length of chiral metamaterials. Therefore, I introduced a simple analytical model which is capable of describing the scaling of the twist per axial strain. Exploiting the physical insights of this model, we modified the cubic unit cell presented in chapter 5. We mitigated the influence of neighboring unit cells in a plane by introducing coupling elements. Thereby, the modified unit cell has tetragonal symmetry. As a result, both the twist angles and the characteristic length were drastically increased. The largest twist angles even exceeded 10° per percent axial strain. Even for the largest samples with $N = 27$, we found twist angles of about 5° per percent axial strain. This surpasses all twist angles found on the cubic structure before. Other approaches exploiting tetragonal unit cells have also been reported and have shown comparable results [158–160]. Yet, the unprecedented hight number of unit cells, both in the numerical calculations and experiments, makes our work unique.

In Part II, I focused on studying wave propagation in chiral metamaterials. As a consequence of chirality, the phonon eigenstates are circularly polarized and propagate with different phase velocities. In chapter 7, I showed that this leads to acoustical activity, the rotation of the polarization direction of a linear transversed polarization elastic wave upon propagation. This can be considered the elastic counterpart of the well know optical activity.

Subsequently, I introduced the experimental and numerical methods to characterize acoustical activity in chapter 8 and chapter 9. In the latter, I laid out an experimental setup to excite waves in 3D printed microstructures in the ultrasound frequency range. Therein, the displacements are measured as a function of time using a stroboscopic illumination, which is slightly detuned with respect to the excitation. The data obtained was later used to determine the polarization direction, both of the excitation oscillation and of the wave after propagating through the sample.

In chapter 10, I first presented band structure calculations of the cubic metamaterial that has already been characterized in the static regime in chapter 5. These showed consistently two nondegenerate, circularly polarized transverse eigenstates along the principle axis - the prerequisites for acoustical activity. The splitting between these two eigenstates generally increased with frequency and decreasing samples size. Therefore we concluded that effects beyond Cauchy elasticity are most prominent when either the wavelength or the sample size becomes comparable to the characteristic lengths. Achieving both at the same time will yield the biggest effects. Furthermore, I

showed both numerically and experimentally that the metamaterial is acoustically active, even for finite sample sizes. Thereby, rotation angles of the linear polarization exceeding 360° have been determined. This is more than sufficient for any desirable engineering applications. Hence, by choosing the right lattice constant or sample heights, arbitrary directions of the linear polarization in the plane orthogonal to the propagation direction can be realized. Finally in this chapter, I addressed the issue of bounds on the maximum achievable rotation angle in crystalline structures. I argued that this is bound to be smaller than 90° per unit cell by symmetry. Consequently, we optimized a unit cell that has been proposed by Lakes in order to approach this fundamental limit. Thereby, rotation angles of about 30° per unit cell were found experimentally.

It should be noted that all results presented in this thesis relate to certain directions in the metamaterial crystal. Small deviations from these directions might already drastically change the response of the material. Whilst for some applications this anisotropy might be useful, it also requires good alignment. Therefore, isotropic material properties would be desirable and could increase the metamaterial's applicability. Yet, getting isotropic material parameters is notoriously difficult in mechanics when using crystalline structures. This presents a sharp contrast to optics, where the isotropic case and the cubic case are formally equal in the long wavelength limit. Theoretically, it should be possible to tailor a cubic unit cell to exhibit isotropic properties. Though, since the isotropy is not protected by symmetry, it will critically depend on precisely controlling all geometry parameters. Especially in experiments, implementing such effective isotropic crystals will be challenging. Another approach to achieve isotropy has been publish recently [150]. There, the authors propose to use chiral quasi crystals. Nevertheless, the proposed geometry stretches todays 3D printing capabilities to its limits. It will be interesting to see whether one could achieve a reasonable isotropy with feasible geometries.

Characterizing large characteristic lengths scales as in chapter 6 numerically requires simulating a large number of unit cells. As we became painfully aware, this goes along with long computation times and excessive memory consumption. Whilst in the dynamic regime Bloch periodic boundaries ease this problem, comparable boundaries are currently lacking for the static case. Having these would be a major improvement for the study of these metamaterials with internal degrees of freedom. Especially design approaches based on topological optimization would profit from such boundary conditions.

In chapter 2 I argued that metamaterials turn the traditional approach of material science on its head, in the sense that they pose a creative challenge to envision new structures having the desired material properties. Therefore, finding routines to retrieve material parameters uniquely will be the major challenge. Solving it could potentially speed up development cycles of metamaterials and thereby bringing metamaterials closer to everyday applications. Ideally, one would even find analytical expression linking certain geometry parameters to the effective material properties. In that regard, two rather recent publications [145, 168], which established analytical expression, could serve as role models.

Appendix A

A Sample Directory

Here, all input parameters for the fabrication of the metamaterial samples are given. This includes geometrical parameters of the unit cell design and printing settings.

A.1 Elastostatic: Push-to-Twist Coupling

A.1.1 Cubic Metamaterial

All structures in chapter 5 were printed using the Nanoscribe instrument. The printing parameters are given in Table A.1.

As has been discussed in chapter 5, the geometry data needs to be corrected for the finite voxel size. Especially the relatively large height of the voxel

Parameter	Value
Slicing mode	Fixed
Slicing distance in µm	0.5
Contour count	0
Hatching distance in µm	0.2
Hatching angle in °	90
Hatching angle offset °	90
Laser power in %	45
Scan speed in $\mathrm{m\,s^{-1}}$	0.1

Table A.1: List of printing parameters used to print the cubic metamaterial samples with the Nanoscribe instrument.

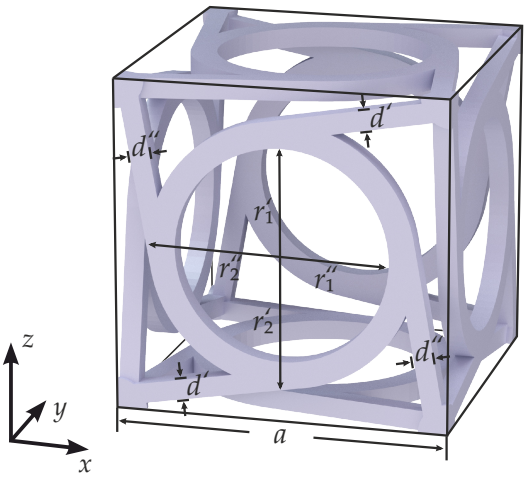

Figure A.1: Illustration of the cubic metamaterial unit cell. To account for the finite voxel size, the geometry parameters need to be adapted. The individual geometry parameters are defined as indicted. This figure is adapted from [2].

N	d' in µm	d'' in µm	r_1' in µm	r_1'' in µm	r_2' in µm	r_2'' in µm
1	28.5	29.5	162.0	160.0	198.0	200.0
2	13.5	14.5	82.0	80.0	98.0	100.0
3	5.5	9.0	55.3	53.3	64.7	66.7
4	2.2	6.7	42.0	40.0	48.0	50.0
5	1.2	5.3	34	32	38	40

Table A.2: List of geometry parameters used to correct the finite voxel size of the Nanoscribe instrument. The parameters are defined in Figure A.1.

leads to considerable deviations, when not taken into account properly. Therefore, the geometry parameters depicted in Figure A.1 were optimized for every N to bring the fabricated dimensions close to the targeted geometry. This was done for every scaling factor N individually. All parameters are summarized in Table A.2.

A.1.2 Tetragonal Metamaterial

For the samples printed using the Nanoscribe system, the printing and geometry parameters are given in Table A.3 and Table A.4. The different parameters are defined in Figure A.1 and Figure A.2.

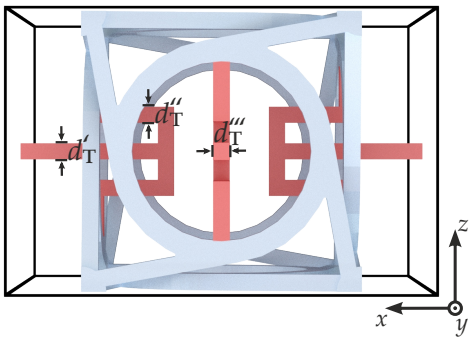

Figure A.2: Illustration of the tetragonal metamaterial unit cell. To account for the finite voxel size, the geometry parameters need to be adapted. The individual geometry parameters are defined as indicted. The parameters of the blue parts are defined in Figure A.1. This figure is adapted from [118].

d' in µm	d'' in µm	r'_1 in µm	r''_1 in µm	r'_2 in µm	r''_2 in µm
3.5	6.5	34.0	32.0	41.0	41

d'_T in µm	d''_T in µm	d'''_T in µm
1.8	2.9	6.0

Table A.3: List of geometry parameters of the tetragonal unit cell used to correct for the finite voxel size of the Nanoscribe instrumentation. The parameters are defined in Figure A.2.

Parameter	Value
Slicing mode	Fixed
Slicing distance in µm	0.7
Contour count	0
Hatching distance in µm	0.3
Hatching angle in °	90
Hatching angle offset °	90
Laser power in %	50
Scan speed in $\mathrm{m\,s^{-1}}$	0.1

Table A.4: List of printing parameters used to print the tetragonal metamaterial samples using the Nanoscribe instrument.

d' in µm	d'' in µm	r_1' in µm	r_1'' in µm	r_2' in µm	r_2'' in µm
1.6	2.8	16.5	15.8	18.7	19.7

d_T' in µm	d_T'' in µm	d_T''' in µm
1.2	1.2	2.8

Table A.5: List of geometry parameters of the tetragonal unit cell used to correct for the finite voxel size of the Nanoscribe instrument. The parameters are defined in Figure A.2.

Parameter	Value
Slicing distance in µm	0.3
Hatching distance in µm	0.2
Scan speed in $\mathrm{m\,s^{-1}}$	0.4

Table A.6: List of printing parameters used to print the tetragonal metamaterial samples using the multifocus setup.

Both the voxel size and the lattice constant were different in the multifocus setup. Therefore, other printing parameters and voxel corrections were used. These are given in Table A.5 and Table A.6.

A.2 Elastodynamics: Acoustical Activity

Here, all parameters used for the fabrication of the samples presented in the second, elastodynamic part of the thesis are presented. The additional parameters of the tetragonal unit cell are defined in Figure A.1. The ones used for the fabrication are equal to the parameters given in Table A.2 for the case of $N = 2$.

B Appendix B
Effective Material Parameters

B.1 Elastostatic: Push-to-Twist Coupling

The effective material parameters of a micropolar continuum used to characterize the static push-to-twist coupling are given here.

B.1.1 Isotropic Micropolar Material Parameters

This parameter set was already published in [2]. As discussed in the chapter 5, these material parameters do not satisfy the conditions for passive materials. Data derived with these parameters are presented and discussed in chapter 5.

For isotropic material, the elasticity tensors **C**, **A**, and **B** are given by

$$\begin{aligned} C_{klmn} &= C_1\delta_{kl}\delta_{mn} + C_2\delta_{km}\delta_{ln} + C_3\delta_{kn}\delta_{lm}, \\ A_{klmn} &= A_1\delta_{kl}\delta_{mn} + A_2\delta_{km}\delta_{ln} + A_3\delta_{kn}\delta_{lm}, \\ B_{klmn} &= B_1\delta_{kl}\delta_{mn} + B_2\delta_{km}\delta_{ln} + B_3\delta_{kn}\delta_{lm}. \end{aligned}$$

In that, the material parameters are given as: $C_1 = -6.14\,\mathrm{MPa}$, $C_2 = 97.41\,\mathrm{GPa}$, $C_3 = -97.37\,\mathrm{GPa}$, $A_1 = 0.42\,\mathrm{N}$, $A_2 = -1.85\,\mathrm{N}$, $A_3 = 3.11\,\mathrm{N}$, $B_3 = -7500\,\mathrm{N/m}$, $B_1 = B_2 = 0$.

B.1.2 Cubic Micropolar Material Parameters

This parameter set was presented by Yi Chen in [60]. Yet, the parameters were scaled to match the constituent's Young's modulus of $E = 2.6\,\mathrm{GPa}$ and

a lattice constant of $a = 500\,\mu\text{m}$. Note that the definition of Voigt's notation in the first part of the thesis differs from the one used in [60] and for the parameters given here. Instead, the notation is defined by

$$\begin{aligned} &\bar{\varepsilon}_1 = \varepsilon_{11}, \quad \bar{\varepsilon}_2 = \varepsilon_{22}, \quad \bar{\varepsilon}_3 = \varepsilon_{33}, \quad \bar{\varepsilon}_4 = \varepsilon_{23}, \quad \bar{\varepsilon}_5 = \varepsilon_{31}, \\ &\bar{\varepsilon}_6 = \varepsilon_{12}, \quad \bar{\varepsilon}_4 = \varepsilon_{32}, \quad \bar{\varepsilon}_8 = \varepsilon_{13}, \quad \bar{\varepsilon}_9 = \varepsilon_{21}. \end{aligned} \tag{B.1}$$

$$\begin{aligned} C_{11} &= 6.4 \times 10^7\,\text{Pa} & A_{11} &= 1.3\,\text{N} \\ C_{12} &= 1.7 \times 10^7\,\text{Pa} & A_{12} &= 1.2\,\text{N} \\ C_{44} &= 9.8 \times 10^6\,\text{Pa} & A_{44} &= 4.7 \times 10^{-2}\,\text{N} \\ C_{47} &= -5.3 \times 10^4\,\text{Pa} & A_{47} &= 3.0 \times 10^{-2}\,\text{N} \end{aligned}$$

$$\begin{aligned} B_{11} &= -5.6 \times 10^3\,\text{N/m} \\ B_{12} &= -4.6 \times 10^3\,\text{N/m} \\ B_{44} &= 135\,\text{N/m} \\ B_{47} &= -169\,\text{N/m} \end{aligned}$$

Data derived with these parameters are presented and discussed in chapter 5.

B.1.3 Tetragonal Metamaterial

This parameter set was deduced by Patrick Ziemke and is published in [118]. Note that the definition of Voigt's notation in the first part of the thesis differs from the one used in [118] and for the parameters given here. Instead, the notation is defined by

$$\begin{aligned} &\bar{\varepsilon}_1 = \varepsilon_{11}, \quad \bar{\varepsilon}_2 = \varepsilon_{22}, \quad \bar{\varepsilon}_3 = \varepsilon_{33}, \quad \bar{\varepsilon}_4 = \varepsilon_{23}, \quad \bar{\varepsilon}_5 = \varepsilon_{31}, \\ &\bar{\varepsilon}_6 = \varepsilon_{12}, \quad \bar{\varepsilon}_4 = \varepsilon_{32}, \quad \bar{\varepsilon}_8 = \varepsilon_{13}, \quad \bar{\varepsilon}_9 = \varepsilon_{21}. \end{aligned}$$

$C_{11} = 1.5 \times 10^5\,\mathrm{Pa}$
$C_{12} = 1.9 \times 10^4\,\mathrm{Pa}$
$C_{13} = -1.7 \times 10^4\,\mathrm{Pa}$
$C_{22} = C_{11}$
$C_{23} = C_{13}$
$C_{33} = -13.7 \times 10^5\,\mathrm{Pa}$
$C_{44} = 9.1 \times 10^6\,\mathrm{Pa}$
$C_{47} = -52\,\mathrm{Pa}$
$C_{55} = C_{44}$
$C_{58} = C_{47}$
$C_{66} = 6.2 \times 10^3\,\mathrm{Pa}$
$C_{69} = -45\,\mathrm{Pa}$
$C_{77} = 5.7 \times 10^3\,\mathrm{Pa}$
$C_{88} = C_{77}$
$C_{99} = C_{66}$

$A_{11} = 1.4 \times 10^{-5}\,\mathrm{N}$
$A_{12} = 1.1 \times 10^{-8}\,\mathrm{N}$
$A_{13} = 1.0 \times 10^{-6}\,\mathrm{N}$
$A_{22} = A_{11}$
$A_{23} = A_{13}$
$A_{33} = 2.7 \times 10^{-3}\,\mathrm{N}$
$A_{44} = 4.9 \times 10^{-3}\,\mathrm{N}$
$A_{47} = -9.8 \times 10^{-7}\,\mathrm{N}$
$A_{55} = A_{44}$
$A_{58} = A_{47}$
$A_{66} = 7.4 \times 10^{-5}\,\mathrm{N}$
$A_{69} = 1.4 \times 10^{-7}\,\mathrm{N}$
$A_{77} = 1.0\,\mathrm{N}$
$A_{88} = A_{77}$
$A_{99} = A_{66}$

$B_{11} = 3.7 \times 10^{-2}\,\mathrm{N/m}$
$B_{12} = 2.4 \times 10^{-3}\,\mathrm{N/m}$
$B_{13} = 0.9\,\mathrm{N/m}$
$B_{22} = B_{11}$
$B_{23} = B_{13}$
$B_{31} = -8.2 \times 10^{-2}\,\mathrm{N/m}$
$B_{32} = B_{31}$
$B_{33} = 51\,\mathrm{N/m}$
$B_{44} = 7.8 \times 10^{-3}\mathrm{N/m}$

$B_{47} = -1.5 \times 10^{-2}\,\mathrm{N/m}$
$B_{55} = B_{44}$
$B_{58} = B_{47}$
$B_{66} = -78\,\mathrm{N/m}$
$B_{69} = 7.9 \times 10^{-5}\,\mathrm{N/m}$
$B_{74} = 1.5 \times 10^{-3}\mathrm{N/m}$
$B_{77} = 1.3\,\mathrm{N/m}$
$B_{88} = B_{66}$.

Data derived using these parameters are presented and discussed in chapter 6.

B.2 Elastodynamics: Acoustical Activity

The effective material parameters used to characterize the acoustical activity are given here. Results derived from these parameters are presented and discussed in chapter 10.

This parameter set was deduced by Yi Chen and is published in [60]. Note that the definition of Voigt's notation in the first part of the thesis differs from the one used in [60] and for the parameters given here. Instead, the notation is defined by

$$\begin{aligned} &\bar{\varepsilon}_1 = \varepsilon_{11}, \quad \bar{\varepsilon}_2 = \varepsilon_{22}, \quad \bar{\varepsilon}_3 = \varepsilon_{33}, \quad \bar{\varepsilon}_4 = \varepsilon_{23}, \quad \bar{\varepsilon}_5 = \varepsilon_{31}, \\ &\bar{\varepsilon}_6 = \varepsilon_{12}, \quad \bar{\varepsilon}_4 = \varepsilon_{32}, \quad \bar{\varepsilon}_8 = \varepsilon_{13}, \quad \bar{\varepsilon}_9 = \varepsilon_{21}. \end{aligned}$$

The material parameters were found to be:

$$\begin{aligned} C_{11} &= 6.4 \times 10^7\,\mathrm{Pa} & A_{11} &= 0.50\,\mathrm{N} \\ C_{12} &= 1.7 \times 10^7\,\mathrm{Pa} & A_{12} &= 0.47\,\mathrm{N} \\ C_{44} &= 9.8 \times 10^6\,\mathrm{Pa} & A_{44} &= 1.9 \times 10^{-2}\,\mathrm{N} \\ C_{47} &= -5.3 \times 10^4\,\mathrm{Pa} & A_{47} &= 1.2 \times 10^{-2}\,\mathrm{N} \end{aligned}$$

$$\begin{aligned} B_{11} &= -4.5 \times 10^3\,\mathrm{N/m} \\ B_{12} &= -3.7 \times 10^3\,\mathrm{N/m} \\ B_{44} &= 108\,\mathrm{N/m} \\ B_{47} &= -136\,\mathrm{N/m} \end{aligned}$$

Appendix C

Bandstructures of Infinite Crystal

In the bandstructure calculation for the infinite crystall shown in section 10.1, only propagations along the z-direction were considered. Calculations for a path through the first Brillouin zone are depicted in Figure C.1. Clearly, the degeneracy is lifted for the Γ-R direction. This is to be expected, since this direction exhibits a three-fold rotational symmetry around the propagation axis. Along the borders of the Brillouin zone, the transversal bands are again degenerate. Both findings are in agreement with the reasoning in section 10.1. In the lower panel, the ratio between the phase velocities of the the two transverse bands v_1 and v_2 is given. It also shows that the bands are degenerated in the center and at the edges of the Brillouin zone.

The corresponding eigenmodes for wave propagation along one of the principle axes are depicted in Figure C.2. Additionally, the mean displacement vector of a single unit cell $\vec{u}$ is plotted. For both transverse modes, the mean displacement vector is a complex quantity. The real and imaginary part are of equal magnitude, yet they include an angle of 90°. Both are in a plane perpendicular to the wave vector $\vec{k}$. An investigation of the eigenmodes along the Γ-R direction would yield similar results.

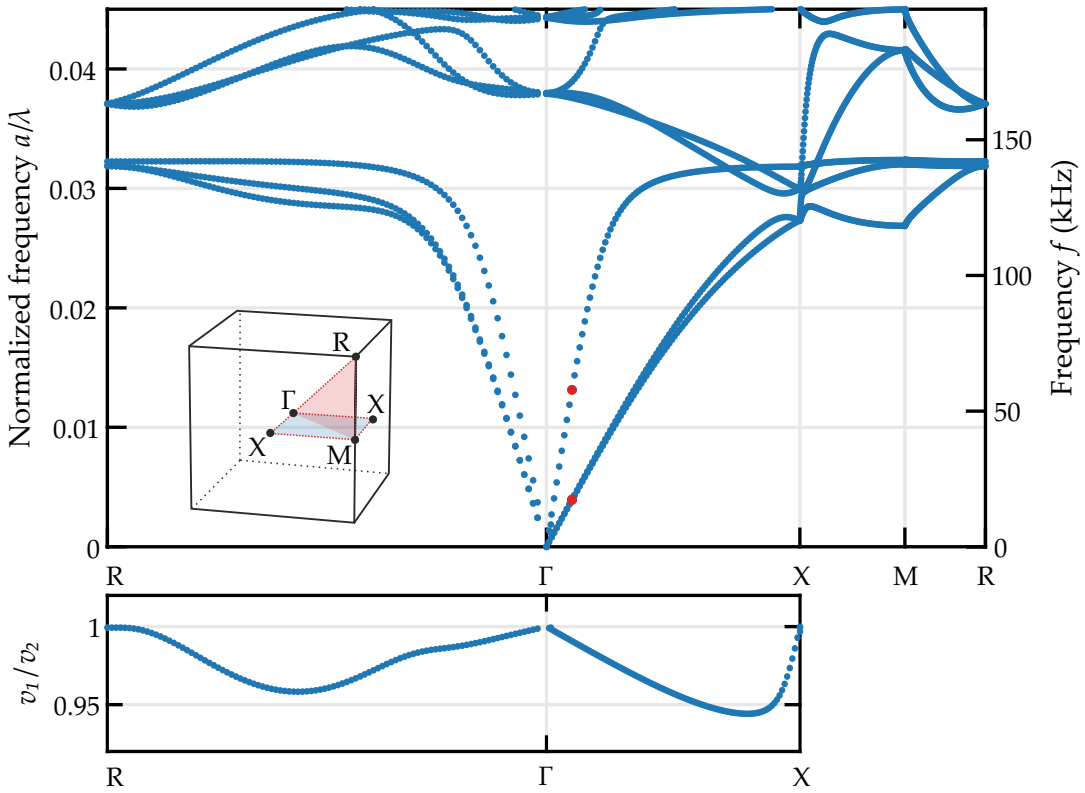

Figure C.1: Phonon bandstructure of the metamaterial crystal. The bandstructure is depicted not only for wave propagation along the z-axis, but also for some selected high-symmetry directions. Additionally, the relative frequency splitting along the z-direction and along the volume diagonal are plotted at the bottom. The red dots correpsond to the modes depicted in Figure C.2. This figure is adapted from [2].

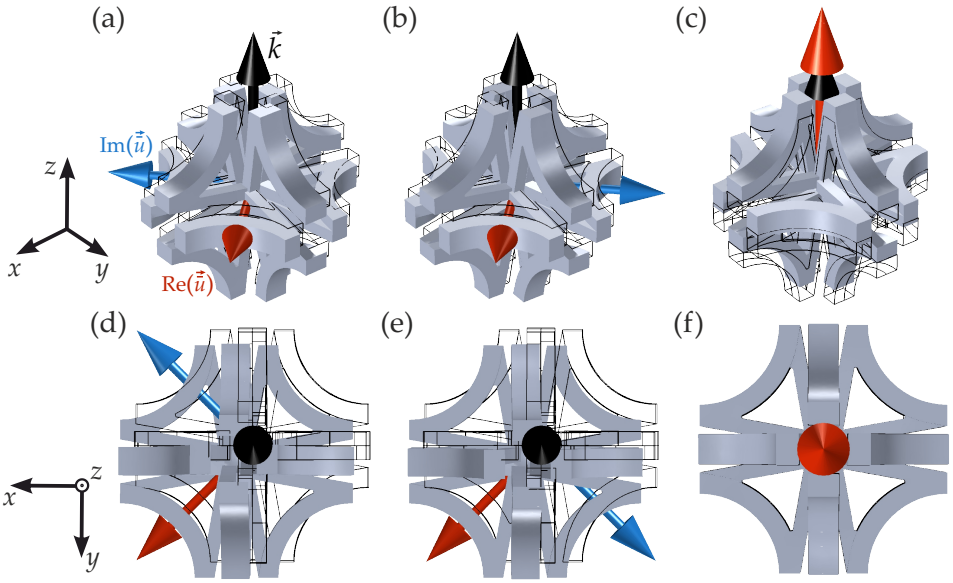

Figure C.2: Phonon eigenmodes. The three lowest phonon eigemodes corresponding to the red points in Figure C.1 are depicted. Additionally, the real (red) and imaginary part (blue) of the mean displacement vector $\vec{u}$ is depicted. For the circular polarized transversal modes (a), (b), (d), and (e), the real and imaginary parts of the displacement vector is in a plane orthogonal to wave vector $\vec{k}$ (black). Also, they include an angle of 90°. Whereas the longitudinal mode is linearly polarized. Hence, the imaginary part of the displacement vector is zero. This figure is adapted from [2].

Bibliography

[1] G. W. Milton and N. Phan-Thien, "New bounds on effective elastic moduli of two-component materials", Proc. Roy. Soc. London Ser. A **380**, 305–331 (1982) (cited on pages 6, 39).

[2] T. Frenzel, M. Kadic, and M. Wegener, "Three-dimensional mechanical metamaterials with a twist", Science **358**, 1072–1074 (2017) (cited on pages 6, 55, 58, 59, 67, 71–73, 75, 77–79, 84–86, 88, 90–93, 101, 174, 180, 183, 188, 189).

[3] T. Renner, *Quantities, units and symbols in physical chemistry* (Royal Society of Chemistry, 2007) (cited on page 6).

[4] C. M. Soukoulis and M. Wegener, "Past achievements and future challenges in the development of three-dimensional photonic metamaterials", Nat. Photonics **5**, 523–530 (2011) (cited on pages 7, 44, 62).

[5] R. S. Kshetrimayum, "A brief intro to metamaterials", IEEE Potentials **23**, 44–46 (2004) (cited on page 7).

[6] H. Chen, C. T. Chan, and P. Sheng, "Transformation optics and metamaterials", Nat. Mater. **9**, 387–396 (2010) (cited on page 7).

[7] D. R. Smith, J. B. Pendry, and M. C. Wiltshire, "Metamaterials and negative refractive index", Science **305**, 788–792 (2004) (cited on page 7).

[8] R. V. Craster and S. Guenneau, *Acoustic metamaterials: Negative refraction, imaging, lensing and cloaking*, Vol. 166 (Springer Science & Business Media, 2012) (cited on pages 7, 44).

[9] P. A. Deymier, *Acoustic metamaterials and phononic crystals*, Vol. 173 (Springer Science & Business Media, 2013) (cited on pages 7, 130).

[10] G. Ma and P. Sheng, "Acoustic metamaterials: From local resonances to broad horizons", Sci. Adv. **2**, e1501595 (2016) (cited on page 7).

[11] M. Kadic, T. Bückmann, R. Schittny, and M. Wegener, "Metamaterials beyond electromagnetism", Rep. Prog. Phys. **76**, 126501 (2013) (cited on pages 7, 44).

[12] R. Schittny, M. Kadic, S. Guenneau, and M. Wegener, "Experiments on transformation thermodynamics: molding the flow of heat", Phys. Rev. Lett. **110**, 195901 (2013) (cited on page 7).

[13] W. Cai and V. M. Shalaev, *Optical metamaterials*, Vol. 10, 6011 (Springer, 2010) (cited on page 7).

[14] K. Bertoldi, V. Vitelli, J. Christensen, and M. Van Hecke, "Flexible mechanical metamaterials", Nat. Rev. Mater. **2**, 1–11 (2017) (cited on pages 7, 44, 45).

[15] M. Kadic, G. W. Milton, M. van Hecke, and M. Wegener, "3D metamaterials", Nat. Rev. Phys. **1**, 198–210 (2019) (cited on pages 7, 43–45, 62, 90, 117, 119).

[16] A. A. Zadpoor, "Mechanical meta-materials", Mater. Horiz. **3**, 371–381 (2016) (cited on pages 7, 45).

[17] W. Cai, U. K. Chettiar, A. V. Kildishev, and V. M. Shalaev, "Optical cloaking with metamaterials", Nat. Photonics **1**, 224–227 (2007) (cited on page 7).

[18] T. Ergin, N. Stenger, P. Brenner, J. B. Pendry, and M. Wegener, "Three-dimensional invisibility cloak at optical wavelengths", Science **328**, 337–339 (2010) (cited on pages 7, 44).

[19] H. Hashemi, B. Zhang, J. D. Joannopoulos, and S. G. Johnson, "Delay-bandwidth and delay-loss limitations for cloaking of large objects", Phys. Rev. Lett. **104**, 253903 (2010) (cited on page 7).

[20] P. Alitalo and S. Tretyakov, "Electromagnetic cloaking with metamaterials", Mater. Today **12**, 22–29 (2009) (cited on page 7).

[21] H. M. Bernety and A. B. Yakovlev, "Reduction of mutual coupling between neighboring strip dipole antennas using confocal elliptical metasurface cloaks", IEEE Trans. Antennas and Propag. **63**, 1554–1563 (2015) (cited on page 7).

[22] A. Monti, J. Soric, A. Alu, F. Bilotti, A. Toscano, and L. Vegni, "Overcoming mutual blockage between neighboring dipole antennas using a low-profile patterned metasurface", IEEE Antennas Wirel. Propag. Lett. **11**, 1414–1417 (2012) (cited on page 7).

[23] R. Fleury and A. Alù, "Cloaking and invisibility: A review", in Forum for Electromagnetic Research Methods and Application Technologies (FERMAT), Vol. 1 (2014) (cited on page 7).

[24] A. Diatta, M. Kadic, M. Wegener, and S. Guenneau, "Scattering problems in elastodynamics", Phys. Rev. B **94**, 100105 (2016) (cited on page 7).

[25] E. Cosserat and F. Cosserat, *Théorie des corps déformables* (A. Hermann et fils, 1909) (cited on page 7).

[26] A. Diatta and S. Guenneau, "Controlling solid elastic waves with spherical cloaks", Appl. Phys. Lett. **105**, 021901 (2014) (cited on page 7).

[27] A. C. Eringen and E. Suhubi, "Nonlinear theory of simple micro-elastic solids—I", Int. J. Eng. Sci. **2**, 189–203 (1964) (cited on pages 7, 20, 27, 30, 32, 43).

[28] E. Suhubl and A. C. Eringen, "Nonlinear theory of micro-elastic solids—II", Int. J. Eng. Sci. **2**, 389–404 (1964) (cited on pages 7, 20, 27, 30, 32, 43).

[29] A. C. Eringen, *Foundations of micropolar thermoelasticity* (Springer, 1970) (cited on pages 7, 27, 30, 32, 43).

[30] A. Eringen, "Continuum physics, vol. 4: Polar and nonlocal field theories", New York, Academic Press (1976) (cited on pages 7, 27, 30, 32, 43).

[31] A. C. Eringen, *Microcontinuum field theories: I. Foundations and solids* (Springer Science & Business Media, 2012) (cited on pages 7, 20, 27, 30, 32, 36, 37).

[32] M. B. Rubin, *Cosserat theories: shells, rods and points*, Vol. 79 (Springer Science & Business Media, 2013) (cited on page 7).

[33] R. S. Lakes and R. L. Benedict, "Noncentrosymmetry in micropolar elasticity", Int. J. Eng. Sci. **20**, 1161–1167 (1982) (cited on pages 7, 26, 38, 39, 41, 75, 76, 78, 90, 92, 99).

[34] K. Bhagwat and R. Subramanian, "Acoustical activity of crystals: a comparative study of three descriptions", Acta Crystallogr. A **44**, 551–554 (1988) (cited on pages 7, 127).

[35] A. Lakhtakia, V. V. Varadan, and V. K. Varadan, "Elastic wave propagation in noncentrosymmetric, isotropic media: dispersion and field equations", J. Appl. Phys. **63**, 5246–5250 (1988) (cited on page 7).

[36] D. Portigal and E. Burstein, "Acoustical activity and other first-order spatial dispersion effects in crystals", Phys. Rev. **170**, 673 (1968) (cited on pages 7, 127).

[37] R. Hooke, *Lectures de potentia restitutiva, or of spring explaining the power of springing bodies* (John Martyn, London, 1678) (cited on page 11).

[38] T. Kelvin, "The second Robert Boyle lecture", J. Oxf. Univ. Jr. Sci. Club **18**, 25 (1894) (cited on page 12).

[39] B. Knoche and G. Blaschke, "Investigations on the in vitro racemization of thalidomide by high-performance liquid chromatography", J. Chromatogr. A **666**, 235–240 (1994) (cited on page 12).

[40] L. Whyte, "Chirality", Nature **180**, 513–513 (1957) (cited on page 13).

[41] L. Whyte, "Chirality", Nature **182**, 198–198 (1958) (cited on page 13).

[42] W. S. Slaughter, *The linearized theory of elasticity* (Springer Science & Business Media, 2012) (cited on pages 13, 39).

[43] S. P. Timoshenko and J. N. Goodier, *Theory of elasticity*, Engineering societies monographs (McGraw-Hill Education Pvt Limited, 2010) (cited on pages 13, 106).

[44] R. Toupin, "Elastic materials with couple-stresses", Arch. Ration. Mech. Anal. **11**, 385–414 (1962) (cited on pages 20, 43).

[45] R. Mindlin and H. Tiersten, "Effects of couple-stresses in linear elasticity", Arch. Rational Mech. Anal. **11**, 415–448 (1962) (cited on page 20).

[46] W. Koiter, "Couple-stresses in the theory of elasticity, I & II", Proc. K. Ned. Akad. Wet. (B) **67**, 17–4 (1969) (cited on page 20).

[47] J. Dyszlewicz, *Micropolar theory of elasticity*, Vol. 15 (Springer Science & Business Media, 2012) (cited on page 27).

[48] H. Altenbach, G. A. Maugin, and V. Erofeev, *Mechanics of generalized continua*, Vol. 7 (Springer, 2011) (cited on page 27).

[49] J. Yang and R. Lakes, "Transient study of couple stress effects in compact bone: torsion.", J. Biomech. Eng. **103**, 275–279 (1981) (cited on pages 27, 38).

[50] J. Yang and R. S. Lakes, "Experimental study of micropolar and couple stress elasticity in compact bone in bending", J. Biomech. **15**, 91–98 (1982) (cited on pages 27, 38).

[51] A. Askar and A. Cakmak, "A structural model of a micropolar continuum", Int. J. Eng. Sci. **6**, 583–589 (1968) (cited on page 27).

[52] C. Wożniak, "Bending and Stability Problems with Lattice Structures", Arch. Mech. Stosow **18**, 781–796 (1966) (cited on page 27).

[53] Z. Bažant and M. Christensen, "Analogy between micropolar continuum and grid frameworks under initial stress", Int. J. Solids Struct. **8**, 327–346 (1972) (cited on page 27).

[54] R. Gauthier and W. Jahsman, "A quest for micropolar elastic constants", J. Appl. Mech. **42**, 369–374 (1975) (cited on pages 37, 40, 75, 90).

[55] R. Lakes, "Experimental methods for study of Cosserat elastic solids and other generalized elastic continua", Continuum models for materials with microstructure **70**, 1–25 (1995) (cited on page 37).

[56] P.-Y. Tang, "Interpretation of bend strength increase of graphite by the couple-stress theory", Comput. Struct. **16**, 45–49 (1983) (cited on page 38).

[57] R. S. Lakes, "Size effects and micromechanics of a porous solid", J. Mater. Sci. **18**, 2572–2580 (1983) (cited on page 38).

[58] R. Lakes, "Experimental microelasticity of two porous solids", Int. J. Solids Struct. **22**, 55–63 (1986) (cited on page 38).

[59] X. Heng, "Inequalities for micropolar elastic constants: Cubic crystal classes O, Oh, Td and hemitropic solids", Int. J. Eng. Sci. **32**, 385–393 (1994) (cited on page 39).

[60] Y. Chen, T. Frenzel, S. Guenneau, M. Kadic, and M. Wegener, "Mapping acoustical activity in 3D chiral mechanical metamaterials onto micropolar continuum elasticity", J. Mech. Phys. Solids **137**, 103877 (2020) (cited on pages 39, 91–93, 125–127, 129, 163, 164, 183, 184, 186).

[61] G. W. Milton and A. V. Cherkaev, "Which elasticity tensors are realizable?", ASME J. Eng. Mater. Technol. **117**, 483–493 (1995) (cited on pages 39, 45).

[62] G. W. Milton and A. Sawicki, "Theory of composites. Cambridge monographs on applied and computational mathematics", Appl. Mech. Rev. **56**, B27–B28 (2003) (cited on page 39).

[63] C. S. Andreasen, E. Andreassen, J. S. Jensen, and O. Sigmund, "On the realization of the bulk modulus bounds for two-phase viscoelastic composites", J. Mech. Phys. Solids **63**, 228–241 (2014) (cited on page 39).

[64] R. D. Mindlin, *Microstructure in linear elasticity*, tech. rep. 98 (Columbia Univ. New York Dept. of Civil Engineering and Engineering Mechanics, 1964), pp. 51–78 (cited on page 43).

[65] R. D. Mindlin and N. Eshel, "On first strain-gradient theories in linear elasticity", Int. J. Solids Struct. **4**, 109–124 (1968) (cited on page 43).

[66] S.-A. Papanicolopulos, "Chirality in isotropic linear gradient elasticity", Int. J. Solids Struct. **48**, 745–752 (2011) (cited on page 43).

[67] J. Willis, "Polarization approach to the scattering of elastic waves—I. Scattering by a single inclusion", J. Mech. Phys. Solids **28**, 287–305 (1980) (cited on pages 43, 127).

[68] J. Willis, "A polarization approach to the scattering of elastic waves—II. Multiple scattering from inclusions", J. Mech. Phys. Solids **28**, 307–327 (1980) (cited on pages 43, 127).

[69] G. W. Milton and J. R. Willis, "On modifications of Newton's second law and linear continuum elastodynamics", P. Roy. Soc. A-Math. Phy. **463**, 855–880 (2007) (cited on page 43).

[70] M. Kadic, A. Diatta, T. Frenzel, S. Guenneau, and M. Wegener, "Static chiral Willis continuum mechanics for three-dimensional chiral mechanical metamaterials", Phys. Rev. B **99**, 214101 (2019) (cited on page 43).

[71] A. Lakhtakia, W. S. Weiglhofer, and I. J. Hodgkinson, "Complex mediums II: Beyond linear isotropic dielectrics", in SPIE, Vol. 4467 (2001) (cited on page 43).

[72] A. Ion, J. Frohnhofen, L. Wall, R. Kovacs, M. Alistar, J. Lindsay, P. Lopes, H.-T. Chen, and P. Baudisch, "Metamaterial mechanisms", in Proceedings of the 29th Annual Symposium on User Interface Software and Technology (2016), pp. 529–539 (cited on page 44).

[73] N. Engheta and R. W. Ziolkowski, *Metamaterials: physics and engineering explorations* (John Wiley & Sons, 2006) (cited on page 44).

[74] G. V. Eleftheriades and K. G. Balmain, *Negative-refraction metamaterials: fundamental principles and applications* (John Wiley & Sons, 2005) (cited on page 44).

[75] A. Alù and N. Engheta, "Guided modes in a waveguide filled with a pair of single-negative (SNG), double-negative (DNG), and/or double-positive (DPS) layers", IEEE Trans. Microw. Theory Tech **52**, 199–210 (2004) (cited on page 44).

[76] J. Qu, M. Kadic, A. Naber, and M. Wegener, "Micro-structured two-component 3D metamaterials with negative thermal-expansion coefficient from positive constituents", Sci. Rep. **7**, 40643 (2017) (cited on pages 44, 59, 171).

[77] M. Hippler, E. Blasco, J. Qu, M. Tanaka, C. Barner-Kowollik, M. Wegener, and M. Bastmeyer, "Controlling the shape of 3D microstructures by temperature and light", Nat. Commun. **10**, 1–8 (2019) (cited on page 44).

[78] A. Radman, X. Huang, and Y. Xie, "Topological optimization for the design of microstructures of isotropic cellular materials", Eng. Optim. **45**, 1331–1348 (2013) (cited on page 44).

[79] M. P. Bendsoe and O. Sigmund, *Topology optimization: theory, methods, and applications* (Springer Science & Business Media, 2013) (cited on page 44).

[80] J. U. Surjadi, L. Gao, H. Du, X. Li, X. Xiong, N. X. Fang, and Y. Lu, "Mechanical metamaterials and their engineering applications", Adv. Eng. Mater. **21**, 1800864 (2019) (cited on page 44).

[81] W. Chen and X. Huang, "Topological design of 3D chiral metamaterials based on couple-stress homogenization", J. Mech. Phys. Solids **131**, 372–386 (2019) (cited on pages 44, 94, 174).

[82] X. Chen, T. M. Grzegorczyk, B.-I. Wu, J. Pacheco Jr, and J. A. Kong, "Robust method to retrieve the constitutive effective parameters of metamaterials", Phys. Rev. E **70**, 016608 (2004) (cited on page 44).

[83] D. R. Smith and J. B. Pendry, "Homogenization of metamaterials by field averaging", J. Opt. Soc. Am. B **23**, 391–403 (2006) (cited on page 44).

[84] C. Menzel, C. Rockstuhl, T. Paul, F. Lederer, and T. Pertsch, "Retrieving effective parameters for metamaterials at oblique incidence", Phys. Rev. B **77**, 195328 (2008) (cited on page 44).

[85] M. Wegener, "Metamaterials beyond optics", Science **342**, 939–940 (2013) (cited on page 44).

[86] T. J. Cui, D. R. Smith, and R. Liu, *Metamaterials* (Springer, 2010) (cited on page 44).

[87] J. Li and C. T. Chan, "Double-negative acoustic metamaterial", Phys. Rev. E **70**, 055602 (2004) (cited on page 44).

[88] Y. I. Bobrovnitskii and T. Tomilina, "Sound absorption and metamaterials: A review", Acoust. Phys. **64**, 519–526 (2018) (cited on page 44).

[89] S. Brûlé, E. Javelaud, S. Enoch, and S. Guenneau, "Experiments on seismic metamaterials: molding surface waves", Phys. Rev. Lett. **112**, 133901 (2014) (cited on page 44).

[90] M. Miniaci, A. Krushynska, F. Bosia, and N. M. Pugno, "Large scale mechanical metamaterials as seismic shields", New J. Phys. **18**, 083041 (2016) (cited on page 44).

[91] A. Colombi, D. Colquitt, P. Roux, S. Guenneau, and R. V. Craster, "A seismic metamaterial: The resonant metawedge", Sci. Rep. **6**, 1–6 (2016) (cited on page 44).

[92] M. Briane and G. W. Milton, "Homogenization of the three-dimensional Hall effect and change of sign of the Hall coefficient", Arch. Ration. Mech. Anal. **193**, 715–736 (2009) (cited on page 44).

[93] M. Kadic, R. Schittny, T. Bückmann, C. Kern, and M. Wegener, "Hall-effect sign inversion in a realizable 3D metamaterial", Phys. Rev. X **5**, 021030 (2015) (cited on page 44).

[94] C. Kern, M. Kadic, and M. Wegener, "Experimental evidence for sign reversal of the hall coefficient in three-dimensional metamaterials", Phys. Rev. Lett. **118**, 016601 (2017) (cited on page 44).

[95] C. Kern, M. Kadic, and M. Wegener, "Parallel Hall effect from three-dimensional single-component metamaterials", Appl. Phys. Lett. **107**, 132103 (2015) (cited on page 44).

[96] M. Kadic, T. Bückmann, N. Stenger, M. Thiel, and M. Wegener, "On the practicability of pentamode mechanical metamaterials", Appl. Phys. Lett. **100**, 191901 (2012) (cited on page 45).

[97] T. Bückmann, M. Thiel, M. Kadic, R. Schittny, and M. Wegener, "An elasto-mechanical unfeelability cloak made of pentamode metamaterials", Nat. Commun. **5**, 1–6 (2014) (cited on pages 45, 58, 59).

[98] X. Ren, R. Das, P. Tran, T. D. Ngo, and Y. M. Xie, "Auxetic metamaterials and structures: a review", Smart Mater. Struct. **27**, 023001 (2018) (cited on page 45).

[99] I. Masters and K. Evans, "Models for the elastic deformation of honeycombs", Compos. Struct. **35**, 403–422 (1996) (cited on page 45).

[100] T. Bückmann, R. Schittny, M. Thiel, M. Kadic, G. W. Milton, and M. Wegener, "On three-dimensional dilational elastic metamaterials", New J. Phys. **16**, 033032 (2014) (cited on pages 45, 58, 70).

[101] X. Zheng, H. Lee, T. H. Weisgraber, M. Shusteff, J. DeOtte, E. B. Duoss, J. D. Kuntz, M. M. Biener, Q. Ge, J. A. Jackson, et al., "Ultralight, ultrastiff mechanical metamaterials", Science **344**, 1373–1377 (2014) (cited on page 45).

[102] T. A. Schaedler, A. J. Jacobsen, A. Torrents, A. E. Sorensen, J. Lian, J. R. Greer, L. Valdevit, and W. B. Carter, "Ultralight metallic microlattices", Science **334**, 962–965 (2011) (cited on page 45).

[103] S. Shan, S. H. Kang, J. R. Raney, P. Wang, L. Fang, F. Candido, J. A. Lewis, and K. Bertoldi, "Multistable architected materials for trapping elastic strain energy", Adv. Mater. **27**, 4296–4301 (2015) (cited on page 45).

[104] T. Frenzel, C. Findeisen, M. Kadic, P. Gumbsch, and M. Wegener, "Tailored buckling microlattices as reusable light-weight shock absorbers", Adv. Mater. **28**, 5865–5870 (2016) (cited on pages 45, 58, 145).

[105] B. Florijn, C. Coulais, and M. van Hecke, "Programmable mechanical metamaterials", Phys. Rev. Lett. **113**, 175503 (2014) (cited on page 45).

[106] J. Köpfler, T. Frenzel, M. Kadic, J. Schmalian, and M. Wegener, "Topologically protected twist edge states for a resonant mechanical laser-beam scanner", Phys. Rev. Appl. **11**, 034059 (2019) (cited on pages 45, 174).

[107] A. S. Meeussen, J. Paulose, and V. Vitelli, "Geared topological metamaterials with tunable mechanical stability", Phys. Rev. X **6**, 041029 (2016) (cited on page 45).

[108] B. G. Chen, B. Liu, A. A. Evans, J. Paulose, I. Cohen, V. Vitelli, and C. Santangelo, "Topological mechanics of origami and kirigami", Phys. Rev. Lett. **116**, 135501 (2016) (cited on page 45).

[109] K.-J. Bathe, *Finite element procedures* (Klaus-Jurgen Bathe, 2006) (cited on page 48).

[110] M. A. Neto, A. Amaro, L. Roseiro, J. Cirne, and R. Leal, *Engineering computation of structures: the finite element method* (Springer, 2015) (cited on page 48).

[111] A. F. Bower, *Applied mechanics of solids* (CRC press, 2009) (cited on pages 48–50, 134).

[112] J. Jeong, H. Ramézani, I. Münch, and P. Neff, "A numerical study for linear isotropic Cosserat elasticity with conformally invariant curvature", J. Appl. Math. Mech. **89**, 552–569 (2009) (cited on pages 50, 51).

[113] A. COMSOL, "COMSOL multiphysics reference manual, version 5.3", COMSOL AB (2018) (cited on pages 50, 51, 134, 136).

[114] J. Jeong and H. Ramezani, "Implementation of the finite isotropic linear cosserat models based on the weak form", strain **2**, 4 (2008) (cited on page 51).

[115] J. Jeong, P. Mounanga, H. Ramézani, and M. Bouasker, "A new multi-scale modeling approach based on hygro-Cosserat theory for self-induced stress in hydrating cementitious mortars", Comput. Mater. Sci. **50**, 2063–2074 (2011) (cited on page 51).

[116] P. Ziemke, T. Frenzel, M. Wegener, and P. Gumbsch, "Tailoring the characteristic length scale of 3D chiral mechanical metamaterials", Extreme Mech. Lett. **32**, 100553 (2019) (cited on pages 55, 101–104, 106, 174).

[117] J. R. Davis, *Tensile testing* (ASM international, 2004) (cited on page 55).

[118] T. Frenzel, V. Hahn, P. Ziemke, J. L. G. Schneider, C. Yi, P. Kiefer, P. Gumbsch, and M. Wegener, "Large characteristic lengths in 3D chiral elastic metamaterials: modeling and experiments", submitted (2020) (cited on pages 58, 59, 65, 95–97, 99, 104, 106–110, 113, 114, 116, 118, 181, 184).

[119] R. Schittny, T. Bückmann, M. Kadic, and M. Wegener, "Elastic measurements on macroscopic three-dimensional pentamode metamaterials", Appl. Phys. Lett. **103**, 231905 (2013) (cited on page 58).

[120] T. Frenzel, J. Köpfler, A. Naber, and M. Wegener, "Detecting atomic-scale displacements by optical-image cross-correlation analysis and 3D printed marker arrays", submitted (2020) (cited on pages 59, 61, 62, 160).

[121] J. Qu, A. Gerber, F. Mayer, M. Kadic, and M. Wegener, "Experiments on metamaterials with negative effective static compressibility", Phys. Rev. X **7**, 041060 (2017) (cited on page 59).

[122] T. Frenzel, J. Köpfler, E. Jung, M. Kadic, and M. Wegener, "Ultrasound experiments on acoustical activity in chiral mechanical metamaterials", Nat. Commun. **10**, 1–6 (2019) (cited on pages 59, 144, 145, 148–150, 152, 154–160, 162).

[123] C. Eberl, D. Gianola, and S. Bundschuh, *Free digital image correlation and tracking functions*, (2010) www.mathworks.com/matlabcentral/fileexchange/12413 (cited on page 59).

[124] (2010) https://en.wikipedia.org/wiki/File:Culinary_fruits_top_view.jpg (cited on page 60).

[125] J. Qu, "On thermoelastic and poroelastic metamaterials", Karlsruhe, Karlsruher Institut für Technologie (KIT), PhD thesis (Karlsruhe, 2018) (cited on pages 60, 61).

[126] V. Hahn, F. Mayer, M. Thiel, and M. Wegener, "3-D laser nanoprinting", Opt. Photonics News **30**, 28–35 (2019) (cited on pages 62, 75).

[127] V. Hahn, P. Kiefer, T. Frenzel, J. Qu, E. Blasco, C. Barner-Kowollik, and M. Wegener, "Rapid assembly of small materials building blocks (Voxels) into large functional 3D metamaterials", Adv. Funct. Mater., 1907795 (2020) (cited on pages 62, 65, 66).

[128] H.-B. Sun, S. Matsuo, and H. Misawa, "Three-dimensional photonic crystal structures achieved with two-photon-absorption photopolymerization of resin", Appl. Phys. Lett. **74**, 786–788 (1999) (cited on page 62).

[129] S. Kawata, H.-B. Sun, T. Tanaka, and K. Takada, "Finer features for functional microdevices", Nature **412**, 697–698 (2001) (cited on page 62).

[130] C. N. LaFratta, J. T. Fourkas, T. Baldacchini, and R. A. Farrer, "Multiphoton fabrication", Angew. Chem. **46**, 6238–6258 (2007) (cited on page 62).

[131] F. Klein, B. Richter, T. Striebel, C. M. Franz, G. v. Freymann, M. Wegener, and M. Bastmeyer, "Two-component polymer scaffolds for controlled three-dimensional cell culture", Adv. Mater. **23**, 1341–1345 (2011) (cited on page 62).

[132] A. M. Greiner, B. Richter, and M. Bastmeyer, "Micro-engineered 3D scaffolds for cell culture studies", Macromol. Biosci. **12**, 1301–1314 (2012) (cited on page 62).

[133] J. Fischer, "Three-dimensional optical lithography beyond the diffraction limit", Karlsruhe, Karlsruher Institut für Technologie (KIT), PhD thesis (Karlsruhe, 2012) (cited on page 63).

[134] J. B. Mueller, J. Fischer, F. Mayer, M. Kadic, and M. Wegener, "Polymerization Kinetics in Three-Dimensional Direct Laser Writing", Adv. Mater. **26**, 6566–6571 (2014) (cited on page 63).

[135] Nanoscribe GmbH, (2015) www.nanoscribe.de (cited on page 64).

[136] M.-S. Kang, H. Ma, H.-L. Yip, and A. K.-Y. Jen, "Direct surface functionalization of indium tin oxide via electrochemically induced assembly", J. Mater. Chem. **17**, 3489–3492 (2007) (cited on page 65).

[137] R. Lakes, "Deformation mechanisms in negative Poisson's ratio materials: structural aspects", J. Mater. Sci. **26**, 2287–2292 (1991) (cited on page 70).

[138] D. Prall, R. Lakes, et al., "Properties of a chiral honeycomb with a Poisson's ratio of-1", Int. J. Mech. Sci. **39**, 305–314 (1997) (cited on page 70).

[139] J. N. Grima, R. Gatt, and P.-S. Farrugia, "On the properties of auxetic meta-tetrachiral structures", Phys. Status Solidi B **245**, 511–520 (2008) (cited on page 70).

[140] C. E. Marshall, *Introduction to crystal optics* (Cooke, Troughton & Simms, 1953) (cited on page 70).

[141] C. S. Ha, M. E. Plesha, and R. S. Lakes, "Chiral three-dimensional lattices with tunable Poisson's ratio", Smart Mater. Struct. **25**, 054005 (2016) (cited on page 72).

[142] C. S. Ha, M. E. Plesha, and R. S. Lakes, "Chiral three-dimensional isotropic lattices with negative Poisson's ratio", Phys. Status Solidi B **253**, 1243–1251 (2016) (cited on pages 72, 167, 168, 174).

[143] E. H. Waller and G. Von Freymann, "Spatio-temporal proximity characteristics in 3D μ-printing via multi-photon absorption", Polymers **8**, 297 (2016) (cited on page 75).

[144] T. Belytschko, W. K. Liu, B. Moran, and K. Elkhodary, *Nonlinear finite elements for continua and structures* (John Wiley & sons, 2013) (cited on page 106).

[145] S. Duan, W. Wen, and D. Fang, "A predictive micropolar continuum model for a novel three-dimensional chiral lattice with size effect and tension-twist coupling behavior", J. Mech. Phys. Solids **121**, 23–46 (2018) (cited on pages 117, 177).

[146] D. Royer and E. Dieulesaint, *Elastic waves in solids I: Free and guided propagation* (Springer Science & Business Media, 1999) (cited on page 124).

[147] C. Malgrange, C. Ricolleau, and M. Schlenker, *Symmetry and Physical Properties of Crystals* (Springer, 2014) (cited on page 124).

[148] I. Fernandez-Corbaton, "Forward and backward helicity scattering coefficients for systems with discrete rotational symmetry", Opt. Express **21**, 29885–29893 (2013) (cited on page 126).

[149] J. Reinbold, T. Frenzel, A. Münchinger, and M. Wegener, "The Rise of (Chiral) 3D Mechanical Metamaterials", Materials **12**, 3527 (2019) (cited on pages 126, 166–171).

[150] Y. Chen, M. Kadic, S. Guenneau, and M. Wegener, "Isotropic Chiral Acoustic Phonons in 3D Quasicrystalline Metamaterials", Phys. Rev. Lett. **124**, 235502 (2020) (cited on pages 127, 176).

[151] A. Pine, "Direct observation of acoustical activity in α quartz", Phys. Rev. B **2**, 2049 (1970) (cited on pages 127, 128, 165).

[152] A. W, N. Ashcroft, N. Mermin, N. Mermin, and B. C. P. Company, *Solid State Physics*, HRW international editions (Holt, Rinehart and Winston, 1976) (cited on page 129).

[153] C. F. Klingshirn, *Semiconductor optics* (Springer Science & Business Media, 2012) (cited on page 129).

[154] N. Guarin-Zapata, J. Gomez, C. Valencia, G. F. Dargush, and A. R. Hadjesfandiari, "Finite element modeling of micropolar-based phononic crystals", Wave Motion **92**, 102406 (2020) (cited on page 129).

[155] M. Razeghi, "Phonons and Thermal Properties", in *Fundamentals of Solid State Engineering* (Springer, 2019), pp. 203–250 (cited on page 131).

[156] J. Le Rouzic, P. Delobelle, P. Vairac, and B. Cretin, "Comparison of three different scales techniques for the dynamic mechanical characterization of two polymers (PDMS and SU8)", Eur. Phys. J. Appl. Phys. **48** (2009) (cited on page 145).

[157] M. R. VanLandingham, N.-K. Chang, P. Drzal, C. C. White, and S.-H. Chang, "Viscoelastic characterization of polymers using instrumented indentation. I. Quasi-static testing", J. Polym. Sci., Part B: Polym. Phys. **43**, 1794–1811 (2005) (cited on page 145).

[158] M. Fu, F. Liu, and L. Hu, "A novel category of 3D chiral material with negative Poisson's ratio", Compos. Sci. Technol. **160**, 111–118 (2018) (cited on pages 174, 175).

[159] R. Zhong, M. Fu, X. Chen, B. Zheng, and L. Hu, "A novel three-dimensional mechanical metamaterial with compression-torsion properties", Compos. Struct. **226**, 111232 (2019) (cited on pages 174, 175).

[160] L. Wang and H.-T. Liu, "3D compression-torsion cubic mechanical metamaterial with double inclined rods", Extreme Mech. Lett., 100706 (2020) (cited on pages 174, 175).

[161] W. Wu, D. Qi, H. Liao, G. Qian, L. Geng, Y. Niu, and J. Liang, "Deformation mechanism of innovative 3D chiral metamaterials", Sci. Rep. **8**, 1–10 (2018) (cited on page 174).

[162] W. Wu, W. Hu, G. Qian, H. Liao, X. Xu, and F. Berto, "Mechanical design and multifunctional applications of chiral mechanical metamaterials: A review", Mater. Design **180**, 107950 (2019) (cited on page 174).

[163] S. Duan, L. Xi, W. Wen, and D. Fang, "A novel design method for 3D positive and negative Poisson's ratio material based on tension-twist coupling effects", Compos. Struct. **236**, 111899 (2020) (cited on page 174).

[164] D. T. Farrell, C. McGinn, and G. J. Bennett, "Extension twist deformation response of an auxetic cylindrical structure inspired by deformed cell ligaments", Compos. Struct. **238**, 111901 (2020) (cited on page 174).

[165] X. Li, Z. Yang, and Z. Lu, "Design 3D metamaterials with compression-induced-twisting characteristics using shear–compression coupling effects", Extreme Mech. Lett. **29**, 100471 (2019) (cited on page 174).

[166] W. Chen, D. Ruan, and X. Huang, "Optimization for twist chirality of structural materials induced by axial strain", Mater. Today Commun. **15**, 175–184 (2018) (cited on page 174).

[167] J. I. Lipton, R. MacCurdy, Z. Manchester, L. Chin, D. Cellucci, and D. Rus, "Handedness in shearing auxetics creates rigid and compliant structures", Science **360**, 632–635 (2018) (cited on page 174).

[168] C. Coulais, C. Kettenis, and M. van Hecke, "A characteristic length scale causes anomalous size effects and boundary programmability in mechanical metamaterials", Nat. Phys. **14**, 40–44 (2018) (cited on page 177).

Acknowledgments

Of course, this thesis and the results presented in it are not the work of just one single person. Instead, multiple people contributed to this work with only a few being mentioned in the main part of this work. Therefore, I want to take the chance and express my thankfulness and gratitude to all of them here.

First and foremost, I want to thank Prof. Dr. Martin Wegener for the opportunity to work on this fascinating field of physics. Especially for his outstanding support during the whole time and for the opportunities to present and discuss our research on international conferences. He was always keen to see the latest results and provided plenty of helpful hints and suggestions.

I also want to thank Prof. Dr. Peter Gumbsch, not only for the longstanding and fruitful cooperation, but also for kindly agreeing to co-referee this thesis.

Here, I want to the use the opportunity to explicitly thank and show my gratitude to those I work with on a daily basis. First, I want to thank Prof. Dr. Muamer Kadic. He supported me from the beginning of my Master's thesis and continued doing so through my time as a PhD student. I am grateful for our discussions and for his help in solving the unfathomable mysteries of COMSOL.

I am also indebted to thank Yi Chen, who boosted my understanding of the micropolar continuum and found suitable material parameters for our metamaterials. I further want to express my gratitude to Patrick Ziemke, who brought new impulses and computation capabilities for metamaterials with enhanced characteristic length scales to our group. Also, I want to thank Alexander Münchinger, for always enthusiastically engaging in discussions and thereby solving some fundamental issues, as well as Julian Köpfler and Erik Jung, who characterized the constituent material for ultrasound frequencies. I would also like to thank Vincent Hahn, who enabled the 3D printing of the large metamaterial samples and assisted me with the fabrication.

Furthermore, I want to thank Janet Reinbold, Jonathan Ludwig Günter Schneider, and Jannis Weinberger for the enthusiasm and hard work they

put in during their Bachelor theses. I have very much enjoyed our common projects.

Additionally, there many people in the background who keep everything running and are vital for our research, but unfortunately are only mentioned seldomly on the publications. Therefore, I want to thank our technician Johann Westhauser, who has drawn most of the parts of the experimental setups. Furthermore, I am deeply indebted to the members of the electronic workshop Michael Hippe, Helmuth Lay, and Werner Gilde, who took care of the electrical layout of the setups and helped managing the huge amount of data. I also want to thank Claudia Alaya, Monika Brenkmann, and Ursula Mösle from the secretary office for their constant assistance in the struggles with German bureaucracy.

Moreover, I want to thank all former and current members of the group. It is a great privilege to be able to work with the people I consider my friends and I am thankful for all the good times both during and after work.

I am also thankful to everybody, who went through the struggles of critically proofreading this thesis and thereby helped to remove the most severe errors. Namely, these are Julian Köpfler, Alexander Münchinger, Frederik Mayer, Vincent Hahn, Mark Hippler, Yi Chen, Muamer Kadic, Andreas Niemeyer, and Nicole Knopp.

Finally, I want to express my deepest gratitude and love to my family, especially to my parents Ursula and Uwe, and to my girlfriend Clara. Without your loving and unconditional support I would not have come so far.